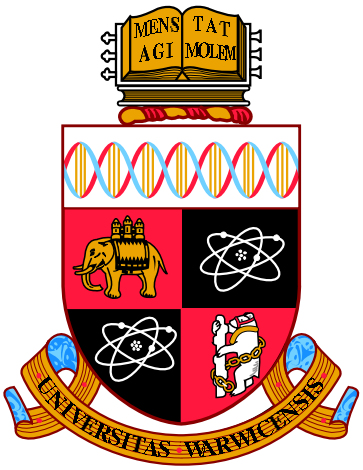

Structures and Properties of Perovskites and Pyrochlores from Hydrothermal Synthesis

by

Luke Mark William Daniels

Thesis

Submitted to the University of Warwick

for the degree of

Doctor of Philosophy

Department of Chemistry

May 2015

Contents

Acknowledgments

First and foremost, it is impossible to imagine a better supervisor than Professor Richard Walton. Thank you for the guidance, encouragement, endless opportunities, conference travels, and ultimately, a most enjoyable PhD. It has been marvellous.

To Dr Alex Hannon. Walking into Target Station 1 puts a huge smile on my face, and you have given me reason to make regular visits. I am immensely grateful for the time and expertise you provided on GEM experiments, and for showing me how to treat and analyse total scattering data.

Thanks to Dr Helen Playford for the utterly endless help, the guidance you continue to give, and for being my go-to person with all things neutron!

For providing answers to my many questions about magnetism, and helping with numerous measurements and helium transfers, I thank Dr Martin Lees.

I am grateful to Dr Reza Kashtiban for countless amazing STEM images. Thanks to Mads Weber for the education on Raman scattering, and Prof. Jens Kreisel and Dr Mael Guennou for your contributions. To Dr Andrew Grigg for showing me the intricacies behind t-o-f data in TOPAS. I thank Rodney Wesson, Dave Hammond, Dr Ben Douglas and all the technical and administrative staff working behind the scenes at Warwick, ISIS, Diamond, and SuperSTEM.

Thanks to the Waltons, past and present, for the laughs, lunchtime crosswords, and useful discussion (particularly Dr Craig Hiley). Thanks to everyone involved in PACMAN, PACLAN, and PACTA for making my time here memorable; Dan 'Daniel-san' Cook, Mohammed 'The Motivator' Saghir, Olli 'The Mad Hutter' Hutter, Dave 'The Great Dave' Burnett, Martin 'Brown Eyes' Tyler, and Kenny 'The Mad Dog' Marshall, to name a few.

Being a scientist requires an open mind and the ability to listen to people, even if they do enjoy solid state NMR... Thank you to my dearest friend Scott Sneddon, for always providing perspective, advice, and drama.

To the best Aunt that anyone could ask for! Thank you Laura and Louis for always taking an interest in my education and guiding me when needed.

To my Mum, Dad, and Sister, who, to this day, still don't know exactly what it is that I do. It doesn't matter, because you're the reason I'm here! Thank you for your endless support, love, and encouragement.

Finally, I thank my fiancée, Emelie. The tireless patience and understanding you have had for my love of my work has been nothing short of remarkable. Thank you for the support and devotion that you continue to give, and for making the past four years the best of my life.

It is to my family and family-to-be that I dedicate this thesis.

Declarations

All of the work presented in this thesis was carried out by the author, except when stated otherwise in the text, at the University of Warwick under the supervision of Professor Richard Walton. This thesis has been composed by myself and has not been submitted at any other academic institution in any application for a higher degree.

Parts of this thesis have been published, as listed below, and it is anticipated that further parts will be submitted for publication in due course.

1. L. M. Daniels, M. C. Weber, M. R. Lees, M. Guennou, R. J. Kashtiban, J. Sloan, J. Kreisel and R. I. Walton, *Inorg. Chem.*, 2013, **52**, 12161.
2. L. M. Daniels, H. Y. Playford, J.-M. Grenèche, A. C. Hannon and R. I. Walton, *Inorg. Chem.*, 2014, **53**, 13197.

In addition, the following publications arose through collaboration where the author performed data measurement and analysis during the course of the work described herein:

1. K.-L. Zhang, Z.-Y. Zhong, L. Zhang, C.-Y. Jing, L. M. Daniels and R. I. Walton, *Dalton Trans.*, 2014, **43**, 11597.
2. L. Mitchell, P. Williamson, B. Ehrlichová, A. E. Anderson, V. R. Seymour, S. E. Ashbrook, N. Acerbi, L. M. Daniels, R. I. Walton, M. L. Clarke and P. Wright, *Chem. Eur. J.*, 2014, **20**, 17185.
3. A. S. Munn, S. Amabilino, T. W. Stevens, L. M. Daniels, G. Clarkson, F. Millange, M. Lenox, T. Düren, S. Bourrelly, P. L. Llewellyn and R. I. Walton, *Cryst. Growth Des.*, 2015, **15**, 891.

Luke M. W. Daniels
April 2015

Abstract

The hydrothermal syntheses of new complex pyrochlore and perovskite oxide materials have been explored. Disorder is prevalent in these materials, so their structures and properties were investigated using a wide range of techniques.

New pyrochlore oxides with compositions $(Na_{0.60}Bi_{1.40})(Fe_{1.06}Mn_{0.17}Bi_{0.77})O_{6.87}$ and $(K_{0.24}Bi_{1.51})(Fe_{1.07}Mn_{0.15}Bi_{0.78})O_{6.86}$ were hydrothermally produced in solutions of NaOH or KOH, respectively, at 200 °C for 6 hours. These pyrochlores are metastable, decomposing at *ca* 400 °C, suggesting their formation would be impossible through conventional solid state synthesis. Their average structures were studied and are described by $Fd\overline{3}m$ symmetry, with considerable disorder present in the A_2O' network. Investigation of their local structures through total scattering confirms the extent of disorder within these materials, showing significant deviation from the average structure. RMC was used to model accurately this disorder; resulting in interesting atomic arrangements for the A and O′ sites. The presence of Fe^{3+} and Mn^{4+} within these disordered structures leads to spin-glass type magnetic behaviour, with no observed long-range ordering interactions, typical of geometrically frustrated pyrochlores.

A new mixed rare-earth chromite $La_xSm_{1-x}CrO_3$ perovskite solid solution (x = 0.0, 0.25, 0.5, 0.625, 0.75, 0.875, and 1.0) was prepared by single-step hydrothermal reaction at 370 °C for 6 hours. The distorted perovskite structures are described by orthorhombic space group *Pnma*, whilst XRD and Raman scattering confirms the increasing structural distortion towards $SmCrO_3$. The hydrothermal treatment results in dendritic-type crystallites, shown by STEM, offering greater homogeneity of particle size over solid state methods. Magnetometry reveals the onset of antiferromagnetic ordering of Cr^{3+} spins below room temperature, with magnetic interactions below these temperatures greatly dependent upon the structural distortion and samarium content. Spin-phonon coupling effects and switchable polarisations were observed at temperatures corresponding to magnetic events, suggesting these phenomena are spontaneously induced by magnetic interactions.

A study of A site cation size variance effects in mixed rare-earth orthochromites was performed on $Y_{0.5}Ho_{0.5}CrO_3$, $La_{0.5}Sm_{0.5}CrO_3$, and $La_{0.5}Tb_{0.5}CrO_3$ solid solutions, prepared through both hydrothermal and solid state methods. Increased variance in the La-Tb system resulted in separation of the two rare-earths in local layers, observed by atomically-resolved EELS, whilst attempts to make La-Ho solid solutions were not possible as the A site radius variance was too great. Separate rare-earth regions were observed in the solid state sample on the nano-scale, showing that greater homogeneity was achieved through hydrothermal synthesis. The homogeneity of rare-earth cation mixing also influenced the magnetic properties of these materials, with dramatic changes being observed upon annealing the layered hydrothermal material.

Abbreviations

ABF	Annular bright field
ADPs	Anisotropic displacement parameters
BFO	Bismuth ferrite ($BiFeO_3$)
BMO	Bismuth manganite ($BiMnO_3$)
BZN	$(Bi, Zn)_2(Zn, Nb)_2O_7$ ceramic pyrochlores
CMR	Colossal magnetoresistance
CSI	Cornell spectrum imaging
EDX	Energy dispersive X-ray spectroscopy
EELS	Electron energy loss spectroscopy
EXAFS	Extended X-ray absorption fine structure
FCC	Field-cooled cooling
FT-IR	Fourier transform - infrared spectroscopy
GEM	GEneral Materials diffractometer
GOF	Goodness-of-fit
HAADF	High-angle annular dark field
ICP-OES	Inductively coupled plasma - optical emission spectroscopy
ICSD	International crystal structure database
LCPL	Linear combination of power laws
MPMS	Magnetic property measurement system
NIST	National institute of standards and technology
PDF	Pair distribution function
PPMS	Physical property measurement system
PXRD	Powder X-ray diffraction
RM	Remanent magnetisation
RMC	Reverse Monte Carlo modelling
SAED	Selected area electron diffraction
SDS	Sodium dodecyl sulfate
SEM	Scanning electron microscopy
SOFC	Solid oxide fuel cell
SQUID	Semiconducting quantum interference device
STEM	Scanning transmission electron microscopy
TEM	Transmission electron microscopy
TGA/DSC	Thermogravimetric analysis/differential scanning calorimetry
t-o-f	Time-of-flight
XANES	X-ray absorption near edge structure
XRD	X-ray diffraction
XRF	X-ray fluorescence spectroscopy
ZFCW	Zero field-cooled warming

Chapter 1

Introduction

1.1 Pyrochlores

The $A_2B_2O_6O'$ pyrochlores are a family of ternary oxides that acquire their name from the mineral pyrochlore, $(Na,Ca)_2Nb_2O_6(OH)$. It is due to the wide range in composition that can be adopted by the structure, with the A site occupied by either a rare-earth or lone-pair cation, and the B site by a transition metal or post-transition metal, that the pyrochlores possess a plethora of interesting properties considered useful for application.[1]

It is because of this appeal, that current work involving pyrochlore materials rivals that of systems adopting the widely-known ABO_3 perovskite structure, also famous for the incorporation of many different metals. The mechanisms that lead to local structural distortions, paramount to material properties, are comparable in both structure types.[2]

1.1.1 The Pyrochlore Structure

The now well-known nomenclature of $A_2B_2O_7$ pyrochlore systems was first proposed in 1977 by Hogarth.[3] For charge neutrality to be obeyed, the most common pairings of cations encountered in stoichiometric pyrochlore systems are $A_2^{III}B_2^{IV}O_7$ and $A_2^{II}B_2^{V}O_7$. Pyrochlores generally adopt the cubic space group $Fd\bar{3}m$ with eight formula units of $A_2B_2O_6O'$ enclosed in each unit cell.

As with perovskites, considered further into this chapter, the A site cation is larger than the B site cation, typically greater than 1 Å in radius, and usually occupies an eight-coordinate environment. The smaller B site cation which is nominally $\sim$ 0.6 Å in radius, is six-coordinate, occupying the central position of an octahedron.[4]

The four crystallographically unique atoms, and their fractional coordinates are listed in Table 1.1. Only a single positional parameter in the whole structure (the 48*f* O *x* parameter) can be refined, and it can be easily thought of as a simple structure. However, slight variations in this single parameter have a significant effect on the structure as it links both the A site polyhedral and B site octahedral networks.[1]

Table 1.1: Unique atoms in the pyrochlore structure and their fractional atomic coordinates for space group $Fd\bar{3}m$. The B site is set as the origin.

Site	Wyckoff position	Coordinates (x, y, z)
A	16*d*	$\frac{1}{2}$, $\frac{1}{2}$, $\frac{1}{2}$
B	16*c*	0, 0, 0
O	48*f*	x, $\frac{1}{8}$, $\frac{1}{8}$
O′	8*b*	$\frac{3}{8}$, $\frac{3}{8}$, $\frac{3}{8}$

Due to the variability of the O 48*f* x parameter, it is possible to describe the pyrochlore structure in several ways. Fundamentally, it can be depicted as a network of BO_6 octahedra that share all vertices, with the A site atoms occupying an interstitial site.[5] However, the most common description of the structure is to think of it as a cubic fluorite (BO_2) derivative, or an anion-deficient fluorite lattice.[6] Half of the tetravalent B^{4+} cations are replaced by trivalent A^{3+} ions, resulting in the formula $A_2B_2O_8$. To charge compensate, this is accompanied by the removal of $\frac{1}{8}$ of the anions in an ordered fashion, producing the more familiar $A_2B_2O_7$.[7] In this fluorite form, the cations form a face-centred arrangement and the anions occupy the tetrahedral sites between the cations. There are three tetrahedral sites that the anions can occupy, all of which are summarised below, and two of which are shown in Figure 1.1:

- The 48*f* position, bridging A site and B site nearest neighbour pairs.
- The 8*b* site, bridging two A site nearest neighbour pairs.
- The 8*a* site, bridging two B site nearest neighbour pairs.

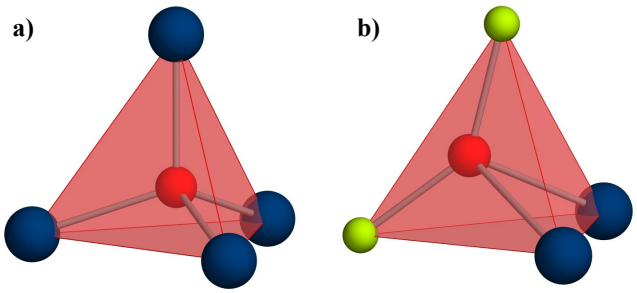

Figure 1.1: a) A_4O' tetrahedron with central O′ 8*b* anion, and b) A_2B_2O tetrahedron displaying off-central O 48*f* anion. A atoms are blue, B are green, and oxygen are red.

Using the definition in Table 1.1, both the 48*f* and 8*b* sites are occupied and it is the 8*a* position from which the anions are removed. The cations are ordered into an alternating ABAB pattern, meaning that the unit cell length is doubled from the fluorite value of ~ 5 Å to ~ 10 Å.[8] Therefore, to fill a single pyrochlore unit cell, it would require a total of eight fluorite units (or rather, eight $A_2B_2O_7$ units), giving the structure its other known description of "fluorite supercell", shown in Figure 1.2. The figure illustrates how the B site cations are coordinated by only six anions due to the vacant 8*a* site, whilst the A site cations retain the eight-coordinate environment of the fluorite structure. The 8*b* O′ anions bridge the distances between two pairs of neighbouring A cations and do not form part of the BO_6 octahedral network, so the B site cations are coordinated only by 48*f* O positions. The A site cations are coordinated by six 48*f* O ions and two 8*b* O′ ions. These AO_8 'cubes' share edges with the BO_6 octahedra, and are corner connected to neighbouring AO_8 coordinations through the 8*b* O′ ions.[9]

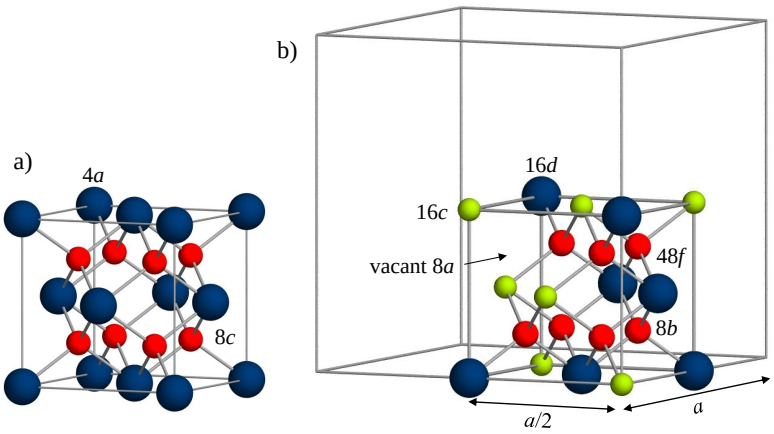

Figure 1.2: Equivalence of a) AO_2 fluorite unit cell to the b) pyrochlore unit cell, highlighting the doubled cell length and vacant 8*a* positions of the latter. A cations are shown in dark blue, the B cations in green, and the oxide ions in red.

The absence of the $8a$ anions exposes neighbouring B site cations to one another, however they achieve some shielding from the $48f$ oxide ion which undergoes a displacement, x, away from the centre of its tetrahedral environment in order to be closer to the B site cation.[1] The flexibility in the x parameter allows the $48f$ O ions to move away from their ideal fluorite position ($x = 0.375$), in which they are perfectly ordered, towards the vacant $8a$ site. The value of x can be anywhere within the range of 0.3125 to 0.375, and the structural consequences of this are illustrated in Figure 1.3.

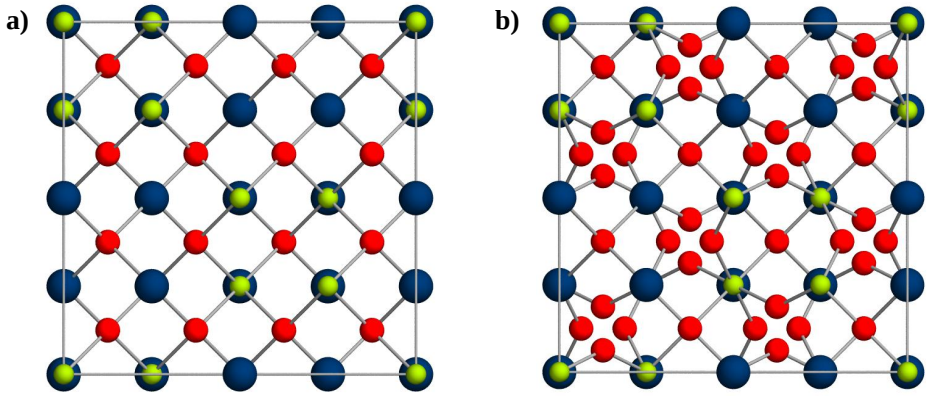

Figure 1.3: Pyrochlore structures with a) $x = 0.375$ where $48f$ O ions are ordered analogous to a fluorite lattice, and b) $x = 0.3125$ showing the extent of displacement in the $48f$ anions as they migrate towards the vacant $8a$ site. A site atoms are blue spheres, B site atoms are green spheres, and oxide ions as red spheres.

When x is equal to 0.3125 ($\frac{5}{16}$) the B site cation occupies a perfect six-coordinate octahedron where the B—O($48f$) bonds are equidistant and the angles between them (O—B—O) are 90°. The A site, however, is in a distorted eight-coordinate, or 'distorted cubic', environment that consists of six equally spaced A—O($48f$) bonds and two slightly shorter A—O′($8b$) bonds, shown in Figure 1.4 a). When x is equal to 0.375 ($\frac{3}{8}$) then the situation becomes reversed. The A site cation now occupies the centre of a perfect eight-coordinate cube with all A—O bonds being equidistant, whilst the B site cation is in a distorted six-coordinate environment resembling an irregular octahedron, shown in Figure 1.4 b). The B—O bonds remain of equal length, but the angles between them change, with half decreasing below 90° and half increasing above 90°.

Therefore the conditions required for perfect A site cubic coordination and perfect B site octahedra cannot be satisfied simultaneously due to this displacement of the $48f$ oxygen. Although the value of x can be anywhere along this range, it is far

more common to find pyrochlores with values of x that are closer to 0.3125, because of the shielding requirements discussed earlier and the preference for most B site cations to be in a perfect octahedral environment.

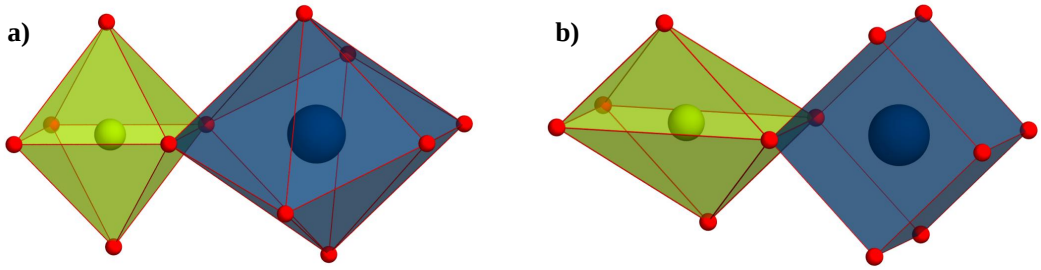

Figure 1.4: Illustration of how the A (blue) and B (green) site coordination polyhedra share edges. In a) $x = 0.3125$ so the A site cation has a distorted eight-coordinate environment alongside a perfect BO_6 octahedron. Conversely in b) $x = 0.375$ therefore the A site cation occupies a perfect AO_8 cube akin to the fluorite structure, whilst the B site cation resides in an irregular octahedral environment.

1.1.1.1 Possible disorder in pyrochlore systems

Although the $A_2B_2O_6O'$ pyrochlore can be thought of as a simple structure, it often can be very complex. It has an ability to accommodate high levels of structural disorder that can be introduced by various means.

The majority of this disorder comes from potential deficiencies of the O′ site, which can be fully or partially occupied, or completely unoccupied to give $A_2B_2O_6$, allowing for the formation of many mixed valence pyrochlore systems.[2] It is possible for the O′ site to be occupied by other anionic species, such as hydroxide or halide ions, or even neutral species like water. Fluorite-like ordering of the oxygen and metal positions can also occur as the O′ site can migrate onto the $8a$ site resulting in compositions based on $A_2B_2O_6O'_xO''_y$.[6]

The structure may tolerate vacancies on the A site leading to $A_{2-x}B_2O_7$ compositions, and AB_2O_6 is classed as a 'defect pyrochlore', with examples of such phases like KTa_2O_6.[10] It is possible for some metals to mix and occupy both the A and B sites.[8]

Pyrochlores can accommodate cations with stereochemically active electron lone pairs, such as Pb^{2+} and Bi^{3+}, that cause off-centring of the metal or distortion in the local oxygen environment, generating disorder in the A_2O' network. It is also possible for the A site and oxide ions to occupy other crystallographic sites like the $32e$ or $8a$ positions, whilst the overall symmetry of the unit cell is maintained.

Pyrochlores in which the A site cation occupies the O′ site instead of the AO_8 environment are known as β-pyrochlores, with the composition $\square_2B_2O_6A$, where $\square$ represents a vacancy.[11]

Ultimately by randomly distributing both the cation and anion sublattices, the pyrochlore structure can be transformed into the disordered defect fluorite structure.[7]

1.1.2 Properties of Pyrochlores

Owing to the wide range of metal ions that the pyrochlore structure can accommodate and also with the potential for nonstoichiometry and disorder, their properties can span a wide spectrum of applications.

The inclusion of transition metals in the structure leads to many interesting and unusual electronic, magnetic and ionic properties. The transition metal ion present can lead to widely varying electronic behaviour from insulating, through semiconducting, to metallic,[1] with a few compounds exhibiting metal-insulator transitions also.[12,13] For example, in $A_2Ru_2O_7$ pyrochlores, the structural modifications that lead to metallic or semiconducting behaviours are very small, and a clear relationship between the ionic radius of the A cation and the resulting electrical behaviour has been found.[14] $Bi_2Ru_2O_7$, unlike the rare-earth ruthenates, has a metallic ground state, due to the mixing of the $6s^2$ lone-pair of Bi^{3+} and d-orbitals of the transition metal. This is also applicable to the equivalent pyrochlores of Rh and Ir.[2]

At room temperature the $Cd_2Nb_2O_7$ pyrochlore is a dielectric insulator, however, below 185 K ferroelectric behaviour is exhibited.[15]

The related pyrochlore $Cd_2Re_2O_7$ contains the unusual oxidation state of Re^{V} and shows a number of complex low-temperature electronic and structural behaviours, culminating in superconductivity below 1.4 K.[16] The defect pyrochlore KOs_2O_6, with the β-pyrochlore structure, has attracted major attention within the last decade due to it exhibiting superconductivity with a T_C of 9.6 K.[17]

Colossal magnetoresistance (CMR), where a material undergoes a large change in electrical resistance in response to an applied magnetic field, is a property displayed by manganese pyrochlores, such as $Tl_2Mn_2O_7$ and doped derivatives.[18,19]

Pyrochlore materials that are useful dielectric materials typically have cation substitutions on both the A and B sites, such as the widely studied $(Bi,Zn)_2(Zn,Nb)_2O_7$ or BZN ceramics. These materials possess high dielectric

constants with low loss that are tunable with an applied voltage; properties useful for application in high-frequency multilayer capacitors.[20] It has been shown that the further the Bi^{3+} cation is displaced away from the ideal $16d$ site, then the greater the dielectric constant of the material,[21] without any significant degradation of dielectric loss.[22] A combination of EXAFS and bond valence analysis, used by Krayzman *et al.*, showed that these dielectric properties are intimately linked with the static disorder caused by Bi^{3+} off-centring.[23] Through careful modelling, it was indicated that the displacement of the O′ anion is directed towards coordinated Zn^{2+} cations, and away from the Bi^{3+} cations.

The phenomenon of frustrated magnetism, or *spin ice* systems, has been extensively studied in lanthanide titanate pyrochlore systems, and is also under investigation in equivalent stannate, iridate, manganate, ruthenate, and molybdate materials.[24] It is widely accepted that the corner-connected A_4 and B_4 tetrahedral sublattices of the pyrochlore structure can result in magnetic frustration when either the A or B site metals are magnetic.[14] Due to this geometric frustration, these materials lack long-range magnetic ordering, and instead, exhibit spin-glass behaviour which results in a *freezing* of the magnetic spins.

Pyrochlore materials are attracting large amounts of interest due to the possibility of them being useful as solid electrolytes or oxygen electrodes in fuel cells and batteries. The ability of the structure to accommodate high levels of oxide deficiencies on the O′ site ultimately provides a pathway for ion conduction, with the transport of O^{2-} ions through the structures of materials such as $Sr_2Os_2O_{6.4}$ and $Bi_2Rh_2O_{6.8}$.[2] The pyrochlore $Gd_2Zr_2O_7$ and other doped derivatives carry an intrinsic ionic conductivity that is comparable to that of yttria-stabilised zirconia, the most predominant electrolyte used in fuel cells.[25]

Catalysis is also a field in which pyrochlores are being investigated, particularly those that contain cerium due to the excellent redox properties of Ce^{3+}/Ce^{4+}. The study of such materials is being guided towards applications such as depollution catalysts in the automotive industry, and the water gas shift reaction for the production of CO-free hydrogen for fuel cells.[8]

Photoluminescence is another property in which a few pyrochlores could be suitable for application, with Eu-doped $KLuTa_2O_7$ being useful as red phosphors in white LEDs,[26] and Yb-doped $Ln_2Sn_2O_7$ having strong broad emission bands applicable for scintillator detectors.[27]

The stoichiometry of the oxide-nitride pyrochlores $Ca_{1-x}La_xTaO_{2-x}N_{1+x}$ makes for a useful pigment as the colour of the material changes from bright yellow to

deep red depending on the O to N ratio.[28] Many others are being studied with the view of replacing the toxic cadmium-based pigments currently in use.

One of the many ongoing investigations with regards to applicable properties of pyrochlores is that into the immobilisation of actinide elements for nuclear waste disposal.[1] This is because of the structure's high tolerance of accommodating defects and disorder. Ion irradiation from a nuclear material will generate defects causing disorder in the cations across the A and B sites, as well as the oxygen sites. The pyrochlore undergoes an order-disorder transition from its ideal structure into a defect fluorite structure. One example of such a material is $La_2Zr_2O_7$ which is an ordered pyrochlore at ambient conditions, but upon irradiation easily changes to a disordered fluorite structure because of its low formation energy ($\sim$ 2 eV).[29] The ease at which this happens indicates that the material should exhibit high resistance to radioactive materials, however, it is the only lanthanide zirconate that is easily amorphised on irradiation, with the others having higher formation energies.

1.2 Perovskites

Named after the Russian mineralogist Count Lev Aleksevich von Perovski, the perovskite mineral ($CaTiO_3$) was discovered in 1839 by Gustav Rose from rock samples taken from the Ural mountains.[30,31] Although the term *perovskite* is used to denote any ternary inorganic crystal structure that has the general formula ABO_3, strictly the structure was related to $CaTiO_3$.

It is thought that the ternary perovskite structure is one of the most common materials to make up the solid earth, with (Mg,Fe)SiO_3 and $CaSiO_3$ being the predominant compounds found in the Earth's lower mantle.[32,33]

Renowned for its structural versatility, the perovskite structure receives tremendous amounts of interest due to the wide selection of elements that it can incorporate, that drive various types of structural distortions, ultimately leading to interesting and useful properties.[34]

1.2.1 The Perovskite Structure

Perovskites have the general formula ABO_3, where A and B are both cations and O is typically an oxide (O^{2-}) or halide (X^-). It is well known that the diverse range of properties that perovskites can exhibit derive from the fact that almost 90 % of the metallic natural elements in the Periodic Table are known to be stable within

the structure,[35] with possible combinations listed in Table 1.2.

Table 1.2: Potential elemental combinations for the perovskite system ABO_3 and possible valence pairings that conform to charge neutrality.

Site	Occupant	Valence
A	Alkali, alkaline-earth, post-transition, or rare-earth metal	A^{+}, A^{2+}, or A^{3+}
B	Transition metal	B^{5+}, B^{4+}, or B^{3+}
O	Oxide or halide anions	O^{2-}, or X^{-}

In its most basic form, the ideal perovskite structure can be described by the cubic space group $Pm3m$, with one formula unit (Z=1) enclosed within the unit cell. The A site cation is the larger of the two metals and requires twelve-fold coordination to neighbouring anions, whereas the B site is much smaller and occupies the central position of a six-coordinate octahedron.

The cubic structure of this unit cell is perhaps thought of most simply consisting of a network of BO_6 octahedra with the larger A site cation residing in the interstitial site, as shown by Figure 1.5. The cubic arrangement means that either the A or B site can be treated as the origin of the unit cell, with the BO_6 octahedron or the A site cation occupying the body centre of the unit cell, respectively. This equivalency is shown in Figure 1.5. Alternatively, the structure can be described as the A cation being close-packed in layers with oxide ions, with the smaller B site metal situated in octahedrally coordinated holes between these AO_3 layers.[36]

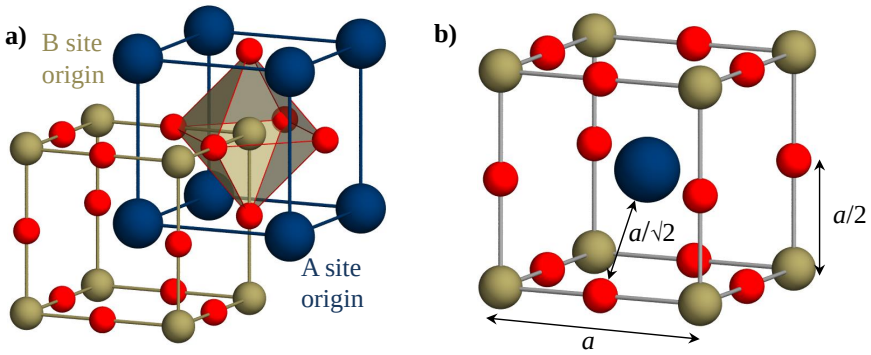

Figure 1.5: Ideal cubic perovskite structure a) showing the equivalence of both the A and B site cations as the origin. The dimensions of the cubic unit cell, including bond lengths, are shown in b). The A site is shown in blue, the B site in beige, and oxide ions in red.

The ideal structure is shown in Figure 1.5 b) and with A–O and B–O bonds at equilibrium distances the ions are treated as hard spheres and can be thought of

as *touching* one another. This therefore makes the B–O distance equal to half of the unit cell length, $a/2$, where a is the cubic lattice parameter. The A–O distance diagonally across the face of the unit cell is longer and is equal to $a/\sqrt{2}$, producing the following relationship between the ionic radii of the A and B site cations:

$$r_A + r_O = \sqrt{2}(r_B + r_O) \tag{1.1}$$

First observed by Goldschmidt in 1926 it was used to show that the A site cations fit precisely into the twelve-coordinate site when they are of equal size to the anions. The O–A–O distance from one cell edge to the other would be exactly equal to $\sqrt{2}$ times that of the cubic cell length.[34] Goldschmidt realised that, by taking the ratio between the two, it was possible using just the ionic radii of the two cations to quantify the deviation away from the ideal structure.[37] This ratio, known as the *tolerance factor*, is shown by Equation 1.2:

$$t = \frac{r_A + r_O}{\sqrt{2}(r_B + r_O)} \tag{1.2}$$

For the ideal cubic perovskite t is unity, with any size mismatch between the ionic radii of the A and B cations generating structural distortion that produces a value of $t < 1$. Stable perovskite compounds generally lie within the range of 0.8 to 1. As one approaches unity then distortion decreases and the structure adopts the higher symmetry cubic phase, as cubic structures can be retained even when t does not equal 1.[35] It is known that as t decreases, rhombohedrally distorted unit cells are adopted, and lower symmetry orthorhombic structures occur at even smaller values.[38]

Though it is important to note that the tolerance factor t provides no detailed structural information, such as space group, it can be used as a reasonable gauge of the deviation away from the ideal structure.[34] A minimum t value of 0.77 was assigned to perovskite compounds of valence configuration $A^{2+}B^{4+}O_3$ by Keith and Roy,[39] however $CaUO_3$ has a value of 0.71, considerably less than the value proposed.[40]

The tolerance factor shows that there is some deviation away from the ideal structure in $CaTiO_3$, with $t = 0.968$. The naturally occurring mineral perovskite was originally thought to adopt the aristotype cubic unit cell, but was later shown by Megaw to be of orthorhombic *Pnma* symmetry.[41] This deviation is driven by the mismatch in size between the B site Ti^{4+} and undersized A site Ca^{2+} ions.[42] It is in fact $SrTiO_3$, with a tolerance factor of exactly 1.00, that adopts the ideal

cubic structure under ambient conditions.

For values of t above 1, hexagonal close-packed structures are commonly adopted over cubic ones.[34] This also occurs for many polar perovskites that have off-centre B sites, such as $YMnO_3$. If the radii of the cations sufficiently deviate from the ideal ratio, then the formation of hexagonal structures with $P6_3cm$ symmetry is observed. Such phases are known as *perovskite variants* as both A and B sites occupy seven- and five-coordinate environments from the increased distortions.[43]

This is perhaps a good point to redefine the earlier definition of perovskites that describes them as ternary oxides with the general formula ABO_3. Care must be taken when using this definition as the formula is shared also by the closely-related ilmenite ($FeTiO_3$) structure, the difference being that both A and B site cations have an octahedral coordination and a structure based on A_2O_3 corundum sesquioxide.[40,44] A small alteration is therefore required, based upon the architecture of the perovskite structure, whereby the A cation occupies a higher coordination environment than the always-octahedral B cation.[45]

1.2.2 Distortions of the Perovskite Structure

It is the flexibility of the perovskite structure that leads to many diverse and unique properties. The three main types of structural distortion are categorised and discussed herein, and are summarised by Figure 1.6, which is adapted from Guennou *et al.*,[46] with a few extensively-studied materials as examples.

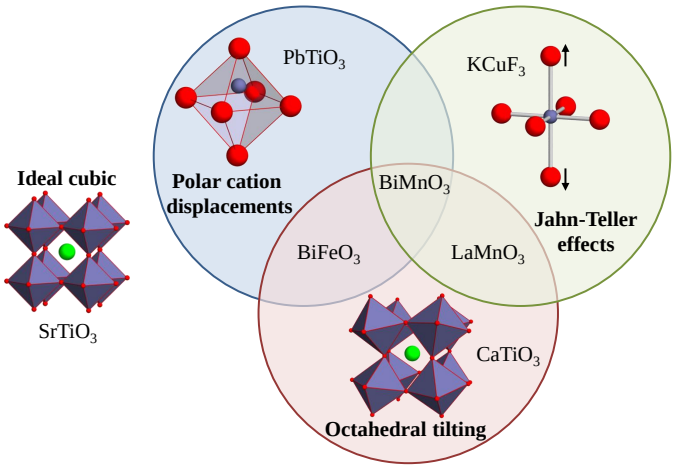

Figure 1.6: The three main distortions of the perovskite structure, adapted from Guennou *et al.*[46] On the left is the aristotype cubic perovskite structure of $SrTiO_3$. The distortions of cation displacements, octahedral tilts, and first-order Jahn-Teller effects, each with example materials, are highlighted by circles. Those in overlapping regions are materials that adopt multiple distortions, with $BiMnO_3$ being one of the few materials to exhibit all three.

1.2.2.1 Cation Displacements

The first type of distortion arises from the displacement of cations from their central positions within their local coordination environment. These displacements can be parallel where both the structure and space group remain centrosymmetric, or anti-parallel where the structure is non-centrosymmetric and the space group becomes a sub-group of that particular tilt system.[47] Displacements of the A cation off-centre are rare since the bonding with neighbouring anions is ionic in character, with lower valence electron orbital overlap.[48] Off-centring of the A cation occurs more frequently when the cation is a lone-pair species such as Pb^{2+} and Bi^{3+}. The B site cations exhibit much more covalent bonding with their neighbouring anions and are therefore more readily polarised, especially when the metal is undersized and carrying a high charge, e.g. Nb^{5+} in $NaNbO_3$.[8] Cation displacements are intimately linked with bulk properties such as ferroelectricity; the off-centring of the cation induces a polarisation within the material, for example the highly displaced Ti^{4+} cations are what leads to $BaTiO_3$ being such a useful ferroelectric.[49]

1.2.2.2 Jahn-Teller Distortions

The second form that can lead to further functionalities is the distortion of the octahedra themselves, due to the central position being occupied by a Jahn-Teller active ion. Both first- and second-order interactions can have an effect on the BO_6 octahedron. The multiferroic $TbMnO_3$ system, as well as other lanthanide manganites, have Mn^{3+} ions occupying the B site positions. The energies of the four *d*-shell electrons become separated to give a three t_g and one e_g orbital configuration, which causes an elongation of some of the Mn–O bonds, generating irregularly shaped octahedra.[50]

1.2.2.3 Octahedral Tilting

More common than the above two forms of distortion, however, is the tilting of BO_6 octahedra, a process that has a much larger effect on structural symmetry and unit cell than the former types. Octahedral tilting occurs when there is mismatch between the sizes of the A and B site cations. When the A site cation is undersized and too small for the 12-fold coordination, the A–O bonds are placed under tension and the B–O bonds under compression. The stresses produced from this are minimised by the BO_6 octahedra undergoing a correlated tilting around the pseudocubic axes.[45,50] As a result the A–O distance is altered, and the coordination number lowered. The A–O distances are no longer equal, and some

anions are now too far away from the cation to be considered part of the coordination sphere.[34]

Ultimately, these processes lead to the lowering of the unit cell symmetry away from the ideal cubic structure, and the mismatch in cation size causes a concomitant decrease in the tolerance factor of the system away from the value of unity along with the symmetry of the unit cell. Lower symmetry space groups like the common $GdFeO_3$-type orthorhombic *Pnma* typically have A sites that are eight- or nine-coordinate. For example, $CaTiO_3$ actually has a Ca^{2+} coordination number of eight which reduces the tension in the Ca–O bonds and increases the lattice energy.[42]

As a result of the octahedral tilting, the B–O–B bond angles decrease from the cubic 180°, reducing the distance between the B site metals.[49] This has a large effect on the potential magnetic interactions introduced from the incorporation of transition metals on the B site. For example, for larger lanthanides in rare-earth ferrites and chromites, this bond angle is close to 180°, resulting in a strong negative exchange interaction along the metal-oxide pathway. Such interactions lead to the formation of two separate magnetic sublattices whose moments are antiparallel in arrangement.[51] As the A site rare-earth ionic radius contracts, the bond angle deviates from this and the small angle between the two produces a weak ferromagnetic component.

When coupled with another type of distortion an enhancement or reduction of the properties is observed, either through cooperation or competition. If bismuth becomes the A site element in rare-earth ferrites, then the BO_6 network is magnetic as in other ferrites, whilst the stereochemistry of the lone pair gives rise to the ferroelectric properties exhibited by $BiFeO_3$. More often than not the tilting of octahedra competes with ferroelectricity and also affects the dielectric response.[50] The magnetoelectric $BiMnO_3$ system possesses all three types of distortion, giving rise to the multiferroic properties that it exhibits below room temperature.

Glazer's notation is the most widely used system to describe the nature of octahedral distortions within orthorhombic perovskites.[49] A total of twenty-three different tilt systems were derived by Glazer and shown to be adopted by orthorhombic perovskites. The depiction is based upon the rotation of octahedra around three Cartesian axes *a*, *b*, *c*, correspondent to the *x*, *y*, and *z* axes of the unit cell. The notation takes on the form $x^a y^b z^c$, the meaning of which is summarised below:

- The letter used indicates the relative magnitude of rotation about that axis. Different letters signify unequal magnitudes.
- The assigned superscript denotes the phase of tilting of neighbouring octahedra along that particular direction; in-phase and out-of-phase tilting would be denoted by positive and negative symbols, respectively, whereas a superscript of 0 signifies no tilting about that axis.

So the notation $a^0a^0a^0$ can be used to describe the aristotype cubic $SrTiO_3$, for example, as there are no tilts about any of the axes. The prototype for orthorhombic systems is $GdFeO_3$ described by $a^-b^+a^-$ where there are two out-of-phase tilts of equal magnitude along both the x and z directions, and a different in-phase tilt along the y axis.[49]

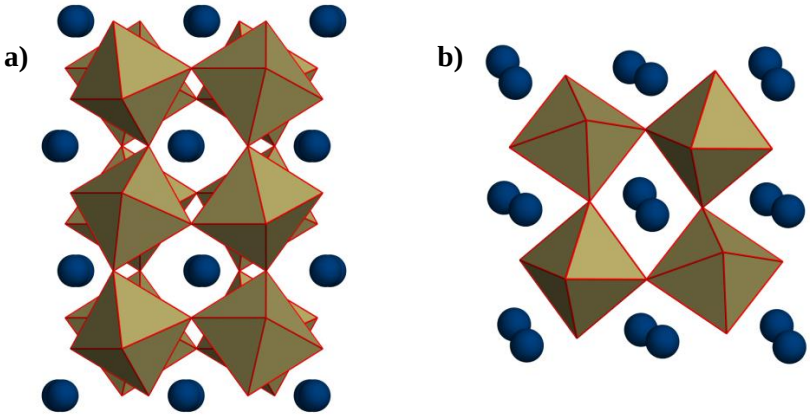

Figure 1.7: The prototype orthorhombic structure of $GdFeO_3$ of tilt system $a^-b^+a^-$. Orientation a) shows the primitive $[100]_p$ direction and demonstrates the anti-phase tilting of octahedra along that direction. The view along the [010] direction in b) highlights the in-phase tilt of different magnitude.

It is entirely possible to calculate the tilt angles of the octahedra, most simply by using the unit cell dimensions which assumes the octahedral units themselves are undistorted. A more accurate method is to use the atomic coordinates of the crystal structure, as the octahedra themselves are not always perfect. As two of the tilts share equal magnitude in the *Pnma* system ($a^-b^+a^-$), the tilt angles can be sufficiently described by just two parameters θ and ϕ, which are the rotations around the [101] and [010] axes, respectively.

The two formulations for the *Pnma* space group are written in Zhao notation in

Equations 1.3 and 1.4 below:[52]

$$tan\theta = \frac{4\sqrt{u_{O1}^2 + w_{O1}^2}}{b} \tag{1.3}$$

and

$$tan\phi = \frac{4\sqrt{u_{O2}^2 + w_{O2}^2}}{\sqrt{c^2 + a^2}} \tag{1.4}$$

where u and w are atomic displacements of the anions away from their special positions in the ideal cubic structure, to the new positions of the orthorhombic structure. These values are determined using Table 1.3.

Table 1.3: Displacements of ions away from special positions for the orthorhombic *Pnma* space group. The fractional displacements (u, v, w) must be converted into real distances (in Å), before implementing into the equations above.

	x	y	z
A	1-u_A	0.25	v_A
B	0	0	0.5
O(1)	0.5-u_{O1}	0.25	w_{O1}
O(2)	0.25+u_{O2}	v_{O2}	0.75-w_{O2}

It is observed for many perovskite systems which exhibit a distorted structure at room temperature, that on heating the structure will eventually achieve the cubic symmetry of the ideal perovskite, but may pass through increasingly less distorted intermediate phases first.[35] This means that on heating, the octahedral tilts observed in orthorhombic systems will decrease in magnitude as the symmetry increases towards the ideal cubic structure.[51] Often observed for many orthorhombic perovskites is the transition to a tetragonal symmetry before reaching the ideal cubic symmetry, which occurs if the value of θ goes to zero before that of ϕ. The structure then results in the cubic phase when the tilt of ϕ is diminished.[52]

It is sometimes necessary to follow these transitions using both diffraction that describes the average structure, as well as a method that probes the local structure as well. For example, in $LaMnO_3$ it is observed by diffraction techniques that the Jahn-Teller distortions of the MnO_6 octahedra in the orthorhombic phase do not survive the transition to the higher symmetry rhombohedral structure. However, when studying the local structure, it is clear that the irregularly-shaped octahedra are present in the higher temperature phase, and that this information becomes

more difficult to extract from the large thermal parameters of the oxide ions in the average model, as a result of the increased thermal motion introduced into the system.[53,54]

1.2.2.4 Variance from Size Disparity

Another factor that is useful to consider regarding disorder in perovskite structures is the effect of size disparity which results when two different metals that share the same crystallographic position.[38] For example, with two cations of different size on the A site of the structure, the random disorder introduced could have an effect on the structure, and therefore the properties of the perovskite. In order to quantify such effects, the statistical variance (σ^2) is used, with a higher variance referring to a larger difference between the cation radii, and therefore a high level of disorder. Variance, which is the difference between the mean-squared value and the square of the mean, is calculated by Equation 1.5 for the case of atomic radii:

$$\sigma^2(r) = \sum_i y_i r_i^2 \; - \; \left(\sum_i y_i r_i \right)^2 \tag{1.5}$$

where r_i is the radius of the cation, and y_i is the concentration of that particular cation in the structure. As is simply observed from the above relationship, when only one cation is present on the structural site, or in the event that both ions have the same radii, then the variance is equal to zero.

It is assumed that the distribution of the two cations throughout the structure will be random, and can be quantified by the variance, however, it is possible to obtain an ordered distribution of the cations, which are most probable when there are large differences between their charges or ionic radii.[36] When the different preferred coordination environments of the cations differ sufficiently, an ordered arrangement can occur, and is particularly common for metals on the B site of the perovskite structure, with the well known family of Brownmillerite materials providing prime examples.[55] Ordered arrangements on the A site are rather rare and often involve vacancies as the second cationic species, such as $Th_{0.25}\square_{0.75}NbO_3$,[56] and it is thought that the increased covalent character of the BO_6 network leads to this.[50] When the segregation between the cations is sufficiently large, it is expected that solid solutions will often separate into a mixture of multiple phases.

The random distribution of the cations will generate disorder in their local oxygen environments, so these are often displaced away from their ideal positions. For the

material $A_xA'_{1-x}BO_3$, the variance changes with the value of x, and the maximum variance is observed at $x = 0.5$. These effects have been found to greatly affect the magnetoresistive properties of materials such as $La_{1-x}Sr_xMnO_3$, and also the superconducting properties of $La_{2-x}Sr_xCuO_4$.[38] For both the doped-lanthanide manganite materials and cuprate superconductors, it was found that the metal-insulator transition temperature and critical temperature, respectively, display a inverse proportionality to variance, with higher temperatures observed for lower variance compositions.

1.3 Magnetoelectric Multiferroics

For a material to be categorised as multiferroic, it must exhibit at least two of the three ferroic phenomena; ferroelectricity, ferromagnetism, or ferroelasticity.[57,58]

The reliance of modern technology upon the use of materials that exhibit magnetic or polar electric ordering is immense; data stored in hard drives in the form of binary makes use of layers of oppositely polarised ferromagnetic or ferroelectric orientations,[59] whilst transducers, actuators, and capacitors all function due to their ferroelectric components.[60] These uses alone make the separate ferroic behaviours interesting to study for both the underlying physics as well as for technological application, so the combination of two such properties within a single phase is even more attractive. Current data storage devices depend upon a high write current between several magnetic layers. In contrast, a multiferroic device would not require the colossal magnetoresistance (CMR) read/write head, only an electric field, so its energy consumption would be dramatically reduced, whilst retaining the long-term stability of the existing magnetic memory.[61]

Multiferroic materials such as ferroelectric ferroelastics exist and form the basis of piezoelectric transducers, however, the term "multiferroic" is used more commonly to describe the phenomena of magnetoelectric coupling. A single ferroic property can usually be modified by its conjugate field; for example, the application of an electric field to a ferroelectric material modifies the polarisation of the material. Whereas in a material that exhibits magnetoelectric coupling, it is possible for a magnetic field to alter the electric polarisation and for an electric field to tune the magnetisation of the material. This effect leads to much more interest in such materials because, not only are the separate parent properties maintained, but the coupling effects between the two can lead to further functionalities.[62] The possibility of being able to alter magnetisation with an electric field and vice versa, could lead to a revolution in the current design of data-storage or memory

devices.[63]

It is noted that the properties of magnetic and electric polar ordering often tend to be mutually exclusive, explaining why magnetoelectric materials are rare, and this is due to the contradicting driving mechanisms on the atomic level for each. Ferroelectricity usually arises from nonmagnetic cations with empty d orbitals (d^0) due to the competition between the energy-lowering covalent bond formation, which is larger for d^0 cations, and the energy-raising electronic Coulomb repulsion, which is larger for cations with d electrons. This balance favours the off-centring that is observed for d^0 cations, leading to polar ordering in ferroelectric materials, such as the Ti^{4+} ions in barium titanate and lead titanate as described in the above section on perovskites.[59] In contrast, magnetic behaviour results from the unpaired localised electrons in cations with partially filled d orbitals (d^n), typically transition metals. So the property of ferroelectricity requires the absence of d electrons, whilst it is the presence of unpaired d electrons that leads to the property of magnetism.

One of the more promising ways to bypass the above described problems is through the production of complex oxides. As a class of materials they contain most of the systems that are currently known to be multiferroic, and are attractive because they are both chemically inert and nontoxic. The idea behind being able to *tailor* the properties of the material is with the incorporation of two different types of cation; one that provides the ferroelectricity, and one that provides the magnetism. The ionic-covalent nature of the bonds between a transition metal and oxygen leads to a strong polarisability, which is desirable for ferroelectrics, whilst the highly-localised unpaired d electrons of the transition metal lead to the spin correlations associated with magnetic ordering.

One such prototypical material is bismuth ferrite ($BiFeO_3$), where the A site Bi^{3+} induces the ferroelectricity due to its stereochemically active $6s^2$ electron lone pair that does not partake in bonding, but instead, often causes the atom to sit off-centre, whilst the $3d^5$ electron configuration of the B site Fe^{3+}, particularly if in high-spin configuration, provides the magnetism. The lone-pair effects described here also play an important role in piezoelectric $PbTiO_3$ which contains the stereochemically active Pb^{2+} cation that enhances the effects of the d^0 Ti^{4+} cation,[64] and the lone pair effects of Bi^{3+} have also been attributed to the multiferroic properties observed in $BiMnO_3$.[65]

The second recognised mechanism of inducing ferroelectricity in materials containing magnetic cations, alternatively to using lone-pair cations, is geometric

ferroelectricity. This is where the structural instability is driven by size effects between the incorporated ions resulting in polar-ordered states. An example of such a material is the hexagonal phase of $YMnO_3$.[66]

What has also become clear from the recent advances in the study of multiferroic materials is that two separate classes of multiferroics can be distinguished:

- Materials in which the ferroelectricity results from structural effects, and are driven by hybridisation and covalency, described above.
- Materials where the ferroelectricity is driven by some other form of primary ordering, such as magnetism.

The first category consists of materials in which the polar and magnetic order are both primary order parameters, and coupling can occur between the two. The latter case involves ferroelectricity which has arisen as a secondary effect due to coupling with a primary ordering, such as magnetic or charge ordering.[67] This means that it is entirely possible for polar ordering to exist within a structure that is centrosymmetric, because it is being driven by something other than structural effects.

In order for the materials to be considered for possible technological application, their properties need to be maintained both at and above room temperature.[68] One of the few known multiferroics to do this is $BiFeO_3$ (BFO), which displays antiferromagnetic ordering of the Fe^{3+} spins at $T_N \sim 640$ K, and ferroelectric behaviour below $T_C \sim 1100$ K.[69,70] BFO displays a distinct ferroelectric hysteresis loop with large saturation polarisation and remanent polarisation of 24 μC cm^{-2}.[71] Bismuth manganite (BMO) is one of the few *true* ferroelectric ferromagnetic materials, with a ferroelectric T_C of $\sim$ 450 K, and ferromagnetic T_C of $\sim$ 100 K.[72,73] The varied bond lengths of the irregularly-shaped MnO_6 octahedra lead to a ferromagnetic spin configuration as the preferred type of ordering, compared to the antiferromagnetic lattice of BFO.

The two materials are often thought of as prototypical magnetoelectrics, however, each has drawbacks. BFO, for example, exhibits a high leakage current density, whilst the properties of BMO are only exhibited below room temperature, rendering it less useful for real-world application.

It is widely recognised that chemical substitution, or cation doping, are methods used to tailor and enhance the magnetic and electric properties of functional materials.[74] In the case of BFO, the substitution of trivalent rare-earth ions, such as lanthanum or neodymium, on the A site have been used to control the volatility

of bismuth, suppressing the formation of oxygen vacancies.[75–77] The idea of making a solid solution of the two systems, in an effort to produce an above-room-temperature ferroelectric ferromagnetic material, is not a novel one.[68,78,79] The doping of manganese into BFO was investigated with the aim of inducing ferromagnetic or ferrimagnetic interactions in the material, whilst retaining the ferroelectric ordering. This incorporation of manganese within the structure increases magnetic hysteresis, and also improves the dielectric properties, however, it is noted that the ferroelectric transition temperature decreases with increasing manganese content.[80] It can be concluded that the substitution of iron by manganese has beneficial effects on the observed magnetoelectric properties, whilst several studies show that the ferroelectric properties remain unaffected by the doping, but small enhancements to the magnetisation are observed.[79,81] It was suggested that the statistical distribution of Fe^{3+} ions alongside Mn^{4+} on the B site produces charge-balancing lattice defects, which can lead to bulk magnetisation.[82] Manganese-doped BFO thin films have also been shown to have superior properties in terms of leakage current density.[77]

1.3.1 Magnetism

A magnetic field H produces lines of force which are known as the magnetic flux density B. The flux density can either decrease or increase when a material is placed in an applied magnetic field; a diamagnetic material will reduce the density of the lines of force within the material, whilst a paramagnetic material will increase the flux density. Such interactions result in the material producing a magnetic field of its own, known as the magnetisation M, and this is related to the magnetic flux density and applied field through Equation 1.6:

$$B = \mu_0(H + M) \tag{1.6}$$

However in magnetic materials, the magnetisation is usually discussed in terms of the magnetic susceptibility χ, which is equivalent to:

$$\chi = \frac{M}{H} \tag{1.7}$$

As electrons carry a spin of $\frac{1}{2}$, an element exhibits magnetic behaviour if it possesses an odd number of electrons, as the total spin won't be zero.[83] The individual electronic spins can interact cooperatively, resulting in magnetic ordering. If the individual spins do not interact with each other, they exhibit

paramagnetism where the spins are unordered and random but do produce a positive contribution to the magnetic susceptibility. As the spins do not interact with one another, when a field is applied to the material the spins align with the direction of the field, giving a positive contribution. However, this effect is opposed by thermal energy which randomises the spins, meaning that the susceptibility of a paramagnetic material will increase as the temperature, and therefore thermal energy, decreases.[84] The relationship between the applied field and thermal randomisation can be described by the Curie law:

$$\chi = \frac{C}{T} \tag{1.8}$$

where C is the Curie constant and T the temperature in Kelvin.

When there are cooperative interactions between the individual electron spins, then different temperature dependencies are observed, and these are summarised in Figure 1.8. For a ferromagnetic material, all of the spins are in an ordered arrangement and align along the same direction, as seen in Figure 1.8 a), resulting in a net spontaneous moment in the material, even in the absence of an applied field. This behaviour occurs below a certain temperature, known as the Curie temperature T_C, below which quantum mechanical exchange energy causes electrons with parallel spins to have a lower energy than those with antiparallel spins.[60] Above this temperature, the thermal energy $k_B T$, is larger than that of the exchange energy, and the ordered arrangement disappears and the spins become paramagnetic. Below T_C a sharp upturn in the susceptibility is observed due to alignment of the spins with the applied field.

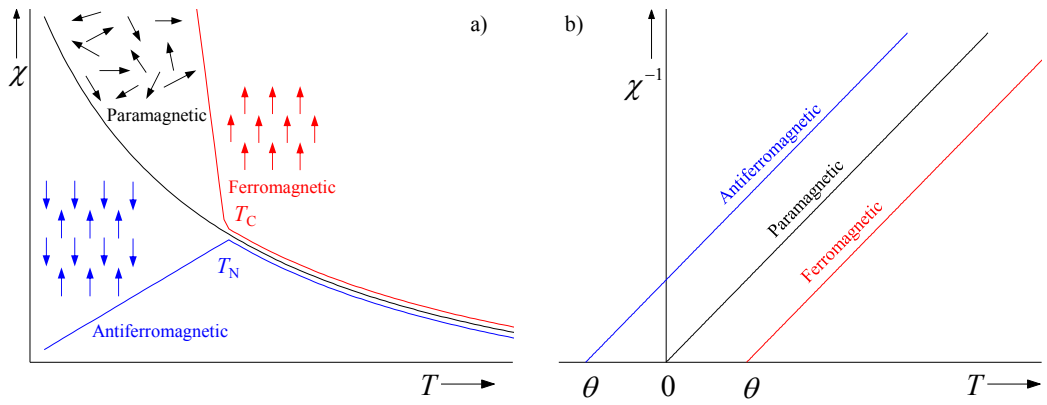

Figure 1.8: a) Temperature dependence of magnetic susceptibilities from paramagnetic, ferromagnetic and antiferromagnetic materials. b) Inverse susceptibility dependence for each type where ferromagnets give a positive Weiss temperature θ, and antiferromagnets give a negative one.

The other common type of spin arrangement is antiferromagnetic, where the moments are ordered in an antiparallel fashion to each other, resulting in no net magnetic field produced by the material. Like ferromagnetism, this behaviour occurs below a certain temperature, characterised by the Néel temperature T_{N}. Again, above this the spins are paramagnetic so the susceptibility slowly increases as the temperature decreases, however, below T_{N} a rapid drop is observed due to the absence of magnetisation produced by the sample.

The modified version of the Curie law for both ferro- and antiferromagnetic materials can be described by the Curie-Weiss law shown in Equation 1.9.

$$\chi = \frac{C}{T - \theta} \tag{1.9}$$

The Weiss temperature θ, is used to determine what type magnetic of ordering a material exhibits, by fitting the paramagnetic region of the inverse susceptibility data, as shown in Figure 1.8 b). If the value of θ is positive, then the behaviour of the spins are predominantly ferromagnetic. If it is negative, then the spins order with a predominantly antiferromagnetic arrangement.

For metal oxides that exhibit antiferromagnetism, the interactions between individual spins normally occur through the mechanism of *superexchange*, which involves the bridging oxide ions.[85] The overlapping d orbitals of the transition metal and p orbitals of the oxygen each carry an electron with antiparallel spins, shown in Figure 1.9. The following transition metal will have an electron that is antiparallel again to the oxygen p orbital that it overlaps, meaning that its d electron will be aligned antiparallel to that on the original metal atom, giving an antiferromagnetic arrangement of the spins.

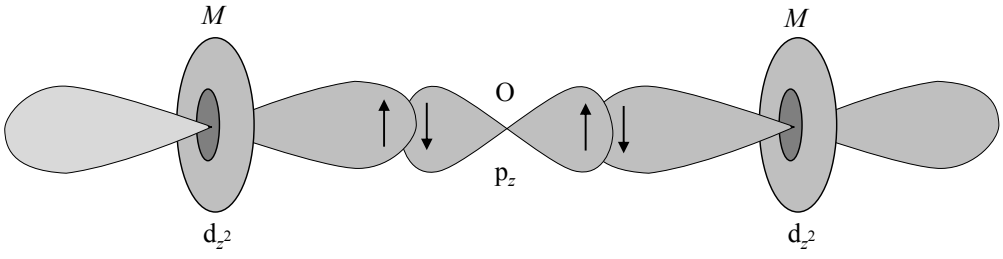

Figure 1.9: Overlap between metal M d_{z^2} orbitals and O p_z orbitals in a metal oxide, showing how the antiparallel spins of neighbouring electrons leads to antiferromagnetic arrangement of metal spins.

In complex oxides, it is possible to discuss the susceptibility in terms of magnetic moments of the metals that are present. These do not have a dependence on

temperature unlike the susceptibility, and depend upon the angular momentum of the unpaired electrons. Electrons possess both spin and orbital angular momentum, and except for the triply degenerate ground states of d^1 or d^2 electron configurations, the orbital angular momentum is usually negligible for first row transition metals. It is therefore possible to determine the theoretical magnetic moment (μ_S) using spin-only momentum through Equation 1.10:

$$\mu_S = 2\sqrt{S(S+1)} \tag{1.10}$$

where S is the spin quantum number, and the units of μ_S are in Bohr magnetons. The value of S is related to the number of unpaired electrons ($S = \frac{1}{2}$ for each unpaired electron; *i.e.* for 3 unpaired electrons, $S = \frac{3}{2}$).

For heavier elements such as the lanthanides, the orbital angular momentum is no longer negligible, and so must be taken into account in the total angular momentum **J**, which is the vector sum of the orbital **L** and spin **S** angular momenta, so the magnetic moment is now given by:

$$\mu = g\sqrt{J(J+1)} \tag{1.11}$$

where g is the Landé g-factor and is calculated by Equation 1.12.

$$g = 1 \ + \frac{J(J+1) + S(S+1) - L(L+1)}{2J(J+1)} \tag{1.12}$$

This can lead to a wide range of magnetic moments, particularly for the lanthanides with partially filled f orbitals, which have values ranging from 0 μ_B for Eu^{3+}, to 10.63 μ_B for Dy^{3+}.

1.3.2 Ferroelectricity

In the case of ferroelectric materials, the *ferro* part of the name arises from the similarity of their electrical properties to the magnetic properties of iron-based ferromagnets. Most ferroelectric materials are not ferrous, however, as they do not contain iron.[82]

One of the earliest observations of ferroelectricity, or more specifically piezoelectricity, was in Rochelle's salt,[86] and was claimed to be a property analogous to the hysteresis of ferromagnets. The desire for such materials to be ready for application lead to a huge increase in interest after the observation of similar properties in materials such as α-quartz and $BaTiO_3$.[87,88]

A ferroelectric material is defined to be a material with a spontaneous electric polarisation that can be switched by the application of an electric field.[60] Ferroelectrics exhibit an electric dipole moment even in the absence of an external electric field, akin to a ferromagnetic material retaining its magnetic moment without an applied magnetic field. Again, like magnetisation, the ferroelectric polarisation decreases with increasing temperature up to a phase transition point where the material becomes unpolarised or paraelectric, defined as T_C.

It is the noncentrosymmetric arrangement of the ions that leads to the production of an electric dipole. Described above, this lowering of symmetry is often the result of cation off-centring being driven by the formation of lower-energy covalent bonds for d^0 cations, or even the stereochemical effect of lone pair cations.

1.4 Synthesis of Pyrochlores & Perovskites

The traditional preparative technique used for the synthesis of the complex oxide materials described above, is that of conventional solid state synthesis. Also known as the ceramic method, this involves the mixing and heating of separate oxide precursors to temperatures usually in excess of 1000 °C for long periods of time, often requiring numerous cycles of regrinding to ensure homogeneity of the product.[55] These high-temperature solid state reactions rely upon atomic diffusion which, at ambient temperatures is very slow, so the technique is often thought of as a brute force method, making use of the high temperatures in order to obtain a thermodynamic product. This is often paired with high pressure in some cases, or performed under various oxidising or reducing atmospheres, depending on the oxidation states of the metals required. The resulting products are highly crystalline but the method offers poor control over crystallite size and morphology, and only the most thermodynamically stable phases are formed.[8] Many methods are able to overcome one or two of these difficulties, such as sol-gel or co-precipitation techniques that achieve homogeneous mixing, however these still rely on a final annealing step in order to crystallise the desired material. The use of solution chemistry, or *soft* chemistry, performed under much milder conditions is able to overcome many of the difficulties encountered through conventional techniques, by giving homogeneous mixing of the reagents, enhanced control over particle size and shape, the ability to stabilise new, metastable phases that are not formed at high temperatures, and most importantly allowing much more freedom with regards to the possible reaction conditions, chemistry, and therefore potential products.[89]

Hydrothermal synthesis consists of a one-step reaction, or "one-pot synthesis", of appropriate reagents in solution under much milder conditions and can directly produce a variety of complex crystalline products.[90] The use of much lower temperatures (between 100 to 240 °C) means that the technique is easier, more environmentally friendly, and cost-effective. Various solvents, or mineralisers, are used in high concentrations to promote the solubility of the starting materials. Of particular relevance to the work in this thesis, the behaviour of the solvent under these moderate temperatures and pressures gives rise to the possibility of synthesising metastable compounds or phases that can include elements in exotic oxidation states.[89] Regulation of the pH, type of solvent, and temperature of the reaction medium allows for considerable control over the shape and size of the crystallites produced. The hydrothermal route can be thought of as a *synthesis* method, rather than a *processing* step as part of a more complicated technique.

The use of hydrothermal and solvothermal synthesis techniques to produce mixed-metal oxide materials, although well-established, is still being explored for the syntheses of both existing and new materials. The use of hydrothermal synthesis to produce materials like pyrochlores and perovskites is rapidly increasing, with the production of stoichiometric pyrochlores such as $Ca_2M_2O_7$ (where M = Nb and Ta),[91] as well as novel and complex phases that contain metals in unusual oxidation states. Materials such as $(Na_{0.33}Ce_{0.67})_2Ti_2O_7$ and $KLuTa_2O_7$ are both produced hydrothermally and are metastable in that they phase separate on heating, showing that they cannot be produced through traditional solid state synthesis.[26,92] Hydrothermal synthesis under different conditions used for the production of perovskite phases like $BaTiO_3$, has resulted in excellent control over crystal morphology for the well-known ferroelectric material. Crystallite morphologies such as porous spheres,[93] nanospheres,[94] plate-like crystals,[95] dendritic particle shapes,[96] and even structured nanotubes,[97] have all been observed as a result of different hydrothermal growth techniques. This variability in morphology has even allowed for the fabrication of hydrothermally grown thin-films on kapton substrates.[98]

1.5 Aims and Overview of this Project

The work presented in this thesis is concerned with the synthesis of new complex oxides with properties associated with magnetism, along with the study of their structures in relation to their properties. There are no previous reports of the materials discussed herein, and the hydrothermal synthesis method is developed to

isolate phase-pure samples for detailed structural analysis. Although the materials described in each chapter of this thesis differ considerably in chemical composition, it is the presence of structural distortions or disorder that lead to the properties that they exhibit, so the interpretation of this disorder is vital to the understanding of their properties. The study of such complex materials is made difficult by the presence of this disorder, so a large number of techniques, complementary to one another, are used alongside conventional diffraction analysis to probe the structures and properties of these materials.

This thesis is comprised of six chapters that each describe the synthesis and study of new materials.

Chapter 1 introduces the type of materials studied in this work, providing a detailed overview of their structures and potential properties, whilst Chapter 2 discusses the theory behind the synthetic and analytical techniques used to produce and study these materials; including hydrothermal synthesis, X-ray and neutron diffraction, total scattering techniques, and Raman spectroscopy. The results of using such methods to synthesise and study new materials such as Bi-Fe-Mn pyrochlore oxides and rare-earth chromite perovskites will be discussed in Chapters 3 and 4, respectively. Chapter 5 will form a follow-up study of variance effects in several mixed rare-earth chromite materials. Finally, Chapter 6 summarises the work presented in the previous three chapters in a wider context, and includes predictions and discussions of experiments that will lead to further study.

References

[1] M. A. Subramanian, G. Aravamudan and G. V. Subba Rao, *Prog. Solid St. Chem.*, 1983, **15**, 55.

[2] M. T. Weller, R. W. Hughes, J. Rooke, C. S. Knee and J. Reading, *Dalton Trans.*, 2004, **19**, 3032.

[3] D. D. Hogarth, *Am. Mineral.*, 1977, **62**, 403.

[4] D. Atencio, M. B. Andrade, A. G. Christy, R. Gieré and P. M. Kartashov, *Can. Mineral.*, 2010, **48**, 673.

[5] A. Byström, *Ark. Kemi Min. Geol.*, 1945, **A18**, 8.

[6] E. Aleshin and R. Roy, *J. Am. Ceram. Soc.*, 1962, **45**, 18.

[7] C. Jiang, C. R. Stanek, K. E. Sickafus and B. P. Uberuaga, *Phys. Rev. B*, 2009, **79**, 104203.

[8] D. R. Modeshia and R. I. Walton, *Chem. Soc. Rev.*, 2010, **39**, 4303.

[9] H. Nyman, S. Andersson, B. G. Hyde and M. O'Keeffe, *J. Solid State Chem.*, 1978, **26**, 123.

[10] G. K. L. Goh, S. M. Haile, C. G. Levi and L. F. F., *J. Mater. Res.*, 2002, **17**, 3168.

[11] R. Galati, C. Simon, C. S. Knee, P. F. Henry, B. D. Rainford and M. T. Weller, *Chem. Mater.*, 2008, **20**, 1652.

[12] J. Yamaura, K. Ohgushi, H. Ohsumi, T. Hasegawa, I. Yamauchi, K. Sugimoto, S. Takeshita, A. Tokuda, M. Takata, M. Udagawa, H. Harima, T. Arima and Z. Hiroi, *Phys. Rev. Lett.*, 2012, **108**, 247205.

[13] S. Fujimoto, *Phys. Rev. Lett.*, 2002, **89**, 226402.

[14] M. W. Gaultois, P. T. Barton, C. S. Birkel, L. M. Misch, E. E. Rodriguez, G. D. Stucky and R. Seshadri, *J. Phys.: Condens. Matter*, 2013, **25**, 186004.

[15] W. R. Cook and H. Jaffe, *Nature*, 1953, 1297.

[16] H. Sakai, K. Yoshimura, H. Ohno, H. Kato, S. Kambe, R. E. Walstedt, T. D. Matsuda, Y. Haga and Y. Onuki, *J. Phys.: Condens. Matter*, 2001, **13**, 785.

[17] Y. Kasahara, Y. Shimono, T. Shibauchi, Y. Matsuda, S. Yonezawa, Y. Muraoka and Z. Hiroi, *Phys. Rev. Lett.*, 2006, **96**, 247004.

[18] Y. Shimakawa, Y. Kubo and T. Manako, *Nature*, 1996, **379**, 53.

[19] P. Velasco, J. A. Alonso, V. G. Tissen, W. G. Marshall, M. T. Casais, M. J. Martinez-Lope, A. de Andres, C. Prieto and J. L. Martinez, *Phys. Rev. B*, 2003, **67**, 104403.

[20] R. L. Withers, T. R. Welberry, A.-K. Larsson, Y. Liu, L. Norén, H. Rundlöf and F. J. Brink, *J. Solid State Chem.*, 2004, **177**, 231.

[21] B. Melot, E. E. Rodriguez, T. Proffen, M. A. Hayward and R. Seshadri, *Mater. Res. Bull.*, 2006, **41**, 961.

[22] Y. Liu, R. L. Withers, T. R. Welberry, H. Wang, H.-L. Du and X. Yao, *J. Electroceram.*, 2008, **21**, 401.

[23] V. Krayzman, I. Levin and J. C. Woicik, *Chem. Mater.*, 2007, **19**, 932.

[24] J. S. Gardner, M. J. P. Gingras and J. E. Greedan, *Rev. Mod. Phys.*, 2010, **82**, 53.

[25] J. Lian, L. M. Wang, S. X. Wang, J. Chen, L. A. Boatner and R. C. Ewing, *Phys. Rev. Lett.*, 2001, **87**, 145901.

[26] M. Nyman, M. A. Rodriguez, L. E. Shea-Rohwer, J. E. Martin and P. P. Provencio, *J. Am. Chem. Soc.*, 2009, **131**, 11652.

[27] D. Jin, X. Yu, H. Yang, H. Zhu, L. Wang and Y. Zheng, *J. Alloys Compd.*, 2009, **474**, 557.

[28] M. Jansen and H. P. Letschert, *Nature*, 2000, **404**, 980.

[29] F. X. Zhang, M. Lang, Z. Liu and R. C. Ewing, *Phys. Rev. Lett.*, 2010, **105**, 015503.

[30] M. Hu, H.-R. Wenk and D. Sinitsyna, *Am. Mineral.*, 1992, **77**, 359.

[31] A. R. Chakhmouradian and P. M. Woodward, *Phys. Chem. Miner.*, 2014, **41**, 387.

[32] J.-S. Zhou and J. B. Goodenough, *Phys. Rev. B*, 2008, **77**, 132104.
[33] T. Ishihara, *Perovskite Oxide for Solid Oxide Fuel Cells*, Springer, New York, 2009.
[34] R. H. Mitchell, *Perovskites: Modern and Ancient*, Almaz Press Inc., Thunder Bay, ON, Canada, 2002.
[35] M. A. Peña and J. L. G. Fierro, *Chem. Rev.*, 2001, **101**, 1981.
[36] F. Galasso and W. Darby, *J. Phys. Chem.*, 1962, **66**, 131.
[37] V. M. Goldschmidt, *Naturwissenschaften*, 1926, **14**, 477.
[38] J. P. Attfield, *Chem. Mater.*, 1998, **10**, 3239.
[39] M. L. Keith, *Am. Mineral.*, 1954, **39**, 1.
[40] R. S. Roth, *J. Res. Nat. Bur. Stand.*, 1957, **58**, 75.
[41] H. D. Megaw, *Proc. Phys. Soc.*, 1946, **58**, 133.
[42] M. W. Lufaso and P. M. Woodward, *Acta Crystallogr.*, 2001, **B57**, 725.
[43] M. R. Levy, B. C. H. Steel and R. W. Grimes, *Solid State Ionics*, 2004, **175**, 349.
[44] B. A. Wechsler and C. T. Prewitt, *Am. Mineral.*, 1984, **69**, 176.
[45] J. B. Goodenough, *Rep. Prog. Phys.*, 2004, **67**, 1915.
[46] M. Guennou, P. Bouvier, G. S. Chen, B. Dkhil, R. Haumont, G. Garbarino and J. Kreisel, *Phys. Rev. B*, 2011, **84**, 174107.
[47] A. M. Glazer, *Acta Cryst. A*, 1975, **31**, 756.
[48] Z. L. Wang and K. C. Kang, *Functional and Smart Materials: Structural Evolution and Structure Analysis*, Plenum Press, New York; 1st Ed., 1998.
[49] A. M. Glazer, *Acta Cryst. B*, 1972, **28**, 3384.
[50] P. K. Davies, H. Wu, A. Y. Borisevich, I. E. Molodetsky and L. Farber, *Annu. Rev. Mater. Res.*, 2008, **38**, 369.
[51] A. S. Verma and V. K. Jindal, in *Perovskites: Structure, Properties and Uses*, ed. M. Borowski, Nova Science Publishers, Inc., Hauppauge, NY 11788-3619, USA, 2010, ch. 11, pp. 463–479.
[52] Y. Zhao, D. J. Weidner, J. B. Parise and D. E. Cox, *Phys. Earth Planet. Inter.*, 1993, **76**, 17.
[53] J. Rodríguez-Carvajal, M. Hennion, F. Moussa and A. H. Moudden, *Phys. Rev. B*, 1998, **57**, R3190.
[54] X. Qui, T. Proffen, J. F. Mitchell and S. J. L. Billinge, *Phys. Rev. Lett.*, 2005, **94**, 177203.
[55] C. N. R. Rao and J. Gopalakrishnan, *Acc. Chem. Res.*, 1987, **20**, 228.
[56] A. R. Chakhmouradian, R. H. Mitchell and P. C. Burns, *J. Alloys Compd.*, 2000, **307**, 149.
[57] H. Schmid, *Bull. Mater. Sci.*, 1994, **17**, 1411.
[58] D. I. Khomskii, *J. Magn. Magn. Mater.*, 2006, **306**, 1.
[59] N. A. Spaldin, S.-W. Cheong and R. Ramesh, *Physics Today*, 2010, 38.
[60] N. A. Hill, *J. Phys. Chem. B*, 2000, **104**, 6694.
[61] M. Bibes and A. Barthélémy, *Nat. Mater.*, 2008, **7**, 425.
[62] N. A. Spaldin and M. Fiebig, *Science*, 2005, **309**, 391.
[63] J. F. Scott, *Nat. Mater.*, 2007, **6**, 256.
[64] R. E. Cohen, *Nature*, 1992, **358**, 136.
[65] R. Seshadri and N. A. Hill, *Chem. Mater.*, 2001, **13**, 2892.
[66] B. B. Van Aken, T. T. M. Palstra, A. Filippetti and N. A. Spaldin, *Nat. Mater.*, 2004, **3**, 164.
[67] S. Picozzi and C. Ederer, *J. Phys.: Condens. Matter*, 2009, **21**, 303201.
[68] D. Kothari, V. R. Reddy, A. Gupta, D. M. Phase, N. Lakshmi, S. K. Deshpande and A. M. Awasthi, *J. Phys.: Condens. Matter*, 2007, **19**, 136202.
[69] G. Catalan and J. F. Scott, *Adv. Mater.*, 2009, **21**, 2463.
[70] D. H. Wang, W. C. Goh, M. Ning and C. K. Ong, *Appl. Phys. Lett.*, 2006, **88**, 212907.
[71] J. R. Sahu and C. N. R. Rao, *Solid State Sci.*, 2007, **9**, 950.
[72] A. A. Belik, K. Kodama, N. Igawa, S.-I. Shamoto, K. Kosuda and E. Takayama-Muromachi, *J. Am. Chem. Soc.*, 2010, **132**, 8137.

[73] A. Moreira dos Santos, S. Parashar, A. R. Raju, Y. S. Zhao, A. K. Cheetham and C. N. R. Rao, *Solid State Commun.*, 2002, **122**, 49.
[74] K. Takahashi and M. Tonouchi, *J. Magn. Magn. Mater.*, 2007, **310**, 1174.
[75] H. Uchida, R. Ueno, H. Funakubo and S. Koda, *J. Appl. Phys.*, 2006, **100**, 014106.
[76] S.-H. Lee, C.-H. Yang, Y. H. Jeong and N. O. Birge, *Physica B*, 2006, **383**, 31.
[77] S. K. Singh, H. Ishihwara and K. Maruyama, *Appl. Phys. Lett.*, 2006, **88**, 262908.
[78] A. A. Belik, A. M. Abakumov, A. A. Tsirlin, J. Hadermann, J. Kim, G. Van Tendeloo and E. Takayama-Muromachi, *Chem. Mater.*, 2011, **23**, 4504.
[79] V. R. Palkar, D. C. Kundaliya and S. K. Malik, *J. Appl. Phys.*, 2003, **93**, 4337.
[80] J. R. Sahu, C. R. Serrao, N. Ray, U. V. Waghmare and C. N. R. Rao, *J. Mater. Chem.*, 2007, **17**, 42.
[81] M. Azuma, H. kanda, A. A. Belik, Y. Shimakawa and M. Takano, *J. Magn. Magn. Mater.*, 2007, **310**, 1177.
[82] W. Prellier, M. P. Singh and P. Murugavel, *J. Phys.: Condens. Matter*, 2005, **17**, R803.
[83] C. Kittel, *Introduction to Solid State Physics*, John Wiley & Sons Ltd, Hoboken, NJ, 8th Ed., 2005.
[84] L. E. Smart and E. A. Moore, *Solid State Chemistry: An Introduction*, CRC Press Taylor & Francis Group, Boca Raton, USA, 3rd Ed., 2005.
[85] P. W. Anderson, *Phys. Rev.*, 1950, **79**, 350.
[86] J. Valasek, *Phys. Rev.*, 1921, **17**, 475.
[87] L. H. Dawson, *Phys. Rev.*, 1927, **29**, 532.
[88] A. von Hippel, R. G. Breckenridge, F. G. Chesley and L. Tisza, *Ind. Eng. Chem.*, 1946, **38**, 1097.
[89] A. Rabenau, *Angew. Chem. Int. Ed.*, 1985, **24**, 1026.
[90] R. E. Riman, W. L. Suchanek and M. M. Lencka, *Ann. Chim. Sci. Mat.*, 2002, **27**, 15.
[91] J. T. Lewandowski, I. J. Pickering and A. J. Jacobson, *Mater. Res. Bull.*, 1992, **27**, 981.
[92] C. S. Wright, J. Fisher, D. Thompsett and R. I. Walton, *Angew. Chem. Int. Ed.*, 2006, **45**, 2442.
[93] Y. Wang, H. Xu, X. Wang, X. Zhang, H. Jia, L. Zhang and J. Qiu, *J. Phys. Chem. B*, 2006, **110**, 13835.
[94] I. J. Clark, T. Takeuchi, N. Ohtori and D. C. Sinclair, *J. Mater. Chem.*, 1999, **9**, 83.
[95] W. Feng, M. Hirasawa and K. Yanagisawa, *Chem. Mater.*, 2001, **13**, 290.
[96] F. Maxim, P. Ferreira, P. M. Vilarinho and I. Reaney, *Cryst. Growth Des.*, 2008, **8**, 3309.
[97] Y. Yang, X. Wang, C. Sun and L. Li, *Nanotechnology*, 2009, **20**, 055709.
[98] R. Z. Hou, A. Wu and P. M. Vilarinho, *Chem. Mater.*, 2009, **21**, 1214.

Chapter 2

Experimental Approach

2.1 Synthesis

2.1.1 Hydrothermal Synthesis

Of geological origin, the term *hydrothermal* was first used to describe the formation of rocks and minerals under the effects of water at elevated temperatures and pressures; a natural geological process that is almost as old as the Earth itself and is the origin of a vast range of minerals.[1]

The solvothermal technique involves the formation (usually crystallisation) of inorganic solids by heating reactants in solution at temperatures above the boiling point of the solvent, usually in a sealed container under autogeneous pressure. In this instance, the solvent is water, hence hydrothermal.

The first reported use of the hydrothermal process in the laboratory dates back to 1845 when Schafhaütl observed the formation of quartz microcrystals in a Papin's digestor (high-pressure steam cooker). Three years later, Robert Bunsen produced single crystals of $BaCO_3$ and $SrCO_3$ in thick-walled glass tubes. For the next seventy years, all manner of minerals, from oxides to silicates, were produced using sealed glass ampoules and it wasn't until 1913 that a closed reaction system that resembles anything of the modern day autoclave, was developed by Morey.[2] The technique begun to properly gain commercial interest after the Second World War, and this was largely driven by the demand for zeolites and large-sized quartz crystals.[1]

Since then the hydrothermal method has been fine-tuned into a versatile approach for the crystallisation of inorganic materials directly from solution.[3] For ceramic materials, the technique offers multiple advantages when compared to the

conventional solid state synthetic technique, the most common preparative method used for the synthesis of multinary oxides.[4–6]

The scalability of the method has been highlighted by a commercially-developed pilot plant that has successfully mass produced a wide range of metal oxides using hydrothermal synthesis on an industrial scale.[7,8] The scaled-up processes are precisely controlled and can continuously produce nano-particulate materials.

2.1.1.1 Experimental details

In this work, hydrothermal reactions were performed in Teflon®-lined stainless-steel autoclaves with internal volumes of 20 ml. Depending on the reaction, the volume of water used was varied from 6 ml to 10 ml, never exceeding a 50 % fill. The sealed vessels were heated in forced-air ovens (Genlab MINO/40) that were pre-heated to the desired temperature, and autoclaves were then allowed to cool naturally to room temperature. The mineralisers that were used were solutions of NaOH, KOH and NH_4OH of various concentrations. The polycrystalline powders were removed from solution through suction filtration, washed several times with deionised water, and dried at 75 °C in air for characterisation.

2.1.2 High-temperature High-pressure Hydrothermal Synthesis

Some of the materials discussed in this thesis require higher synthesis temperatures and pressures than those achievable in the Teflon®-lined vessels. It is not possible to achieve such conditions using the stainless-steel Teflon®-lined autoclaves due to the Teflon® dissociating around 300 °C and deforming under autogeneous pressure.[1] Instead a specially-designed custom-built hydrothermal autoclave system made from Inconel® superalloy was used. A general description of the apparatus used for such syntheses is given here, with details specific to each material provided in their respective chapters.

The system, manufactured by Baskerville Reactors & Autoclaves Ltd, is designed to achieve solution temperatures of 600 °C and contain pressures of up to 300 bar, and is shown in Figure 2.1. It consists of five individual Inconel® vessels, each of 30 ml internal volume that can be heated independently using a five-heater heating block. Each vessel houses an Inconel® well that is immersed in solution enabling a thermocouple to measure the temperature in situ, shown in detail in Figure 2.1. The pressure is also measured throughout the reaction and is digitally displayed alongside the temperature.

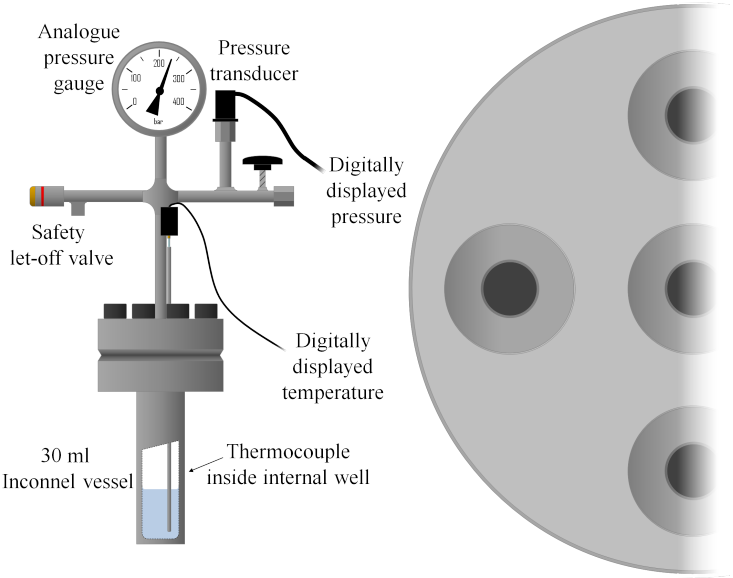

Figure 2.1: The Inconel® high-pressure vessel, along with heating block, highlighting the features discussed in the text.

Although the absence of a Teflon® liner allows for higher temperatures to be achieved, it means that the reaction solution is in direct contact with the Inconel®. Caution is therefore required when deciding on the contents of the vessels in order to minimise corrosion on the internal walls and thermo-well. Close-to-neutral pH was maintained by precipitating amorphous hydroxide precursors containing the appropriate metals, which were then added to the vessels along with water, before being heated. These amorphous precursors are produced by dissolving the required metal salts into water, before adding base to the solution, which resulted in the precipitation of a mixed-metal hydroxide gel. The gel was stirred for 15 minutes to ensure a homogeneous mixture, before being separated from solution by suction filtration, washed copiously with deionised water, and dried at 75 °C. The precipitate was ground into a fine powder before being placed inside the vessels to undergo hydrothermal treatment.

The above method of coprecipitation is well known for enhancing the chemical homogeneity of metals in many complex oxides, especially when the materials possess electronic and magnetic properties which are greatly affected by composition and homogeneity.[9]

Variation of the volume of water inside the vessels, or the *fill fraction*, not only greatly affects the pressure achieved, but also determines the maximum temperature achievable without exceeding the safety limits of the apparatus. As

can be seen in Figure 2.2, increasing the fill fraction from 40% to 70% increases the achievable pressure ten-fold, but limits the maximum solution temperature to 400 °C, compared to 600 °C at a 40 % fill. This range of accessible conditions proved to be quite useful for some materials discussed in this thesis which require high pressure to form, whilst it is only possible to form other materials using lower fill fractions and higher temperatures.

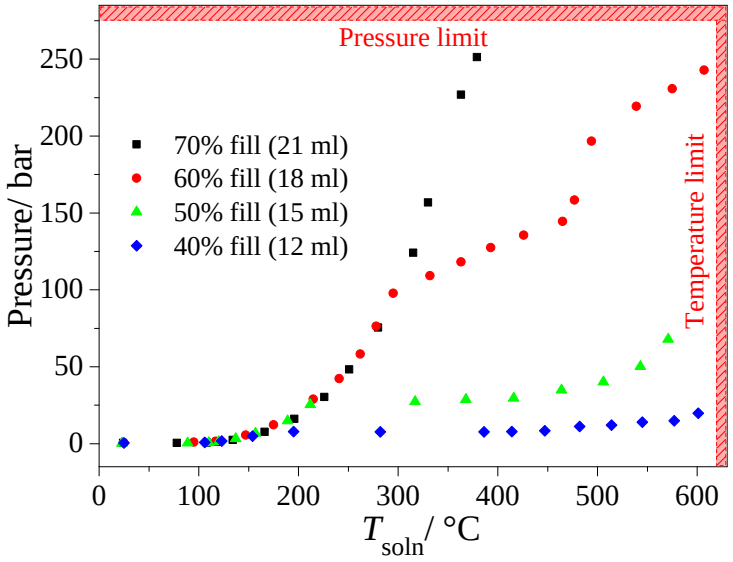

Figure 2.2: Measured pressure-temperature curves showing the effect of fill fraction (pure water) on the internal pressure and temperature achieved during reactions.

2.2 Characterisation

2.2.1 X-ray Diffraction

X-ray diffraction has become the most widely used technique for the determination of crystal structures, and is ubiquitous in the study of crystalline materials.

"*By crystal we mean any solid having an essentially discrete diffraction diagram, and by a periodic crystal we mean any crystal in which three-dimensional lattice periodicity can be considered to be absent*" –International Union of Crystallography definition of a crystal in 1992.[10]

2.2.1.1 Background

It was realised in 1912 by Von Laue, and later shown by Friedrich and Knipping, that crystals can act as diffraction gratings for radiation of an appropriate wavelength.[11] An incident ray is diffracted if its wavelength is of the same order of magnitude as the

grating spacing, which for the case of a crystal, is the distance between neighbouring atoms within the lattice. This was shown to be the case with X-rays in 1914 by the father and son, William Henry Bragg and William Lawrence Bragg.[12]

The Bragg's theory of diffraction considers a crystal to be made up of parallel planes of atoms from which the incident radiation is *reflected*. It is constructive interference of the scattered X-rays that leads to diffraction, illustrated in Figure 2.3.

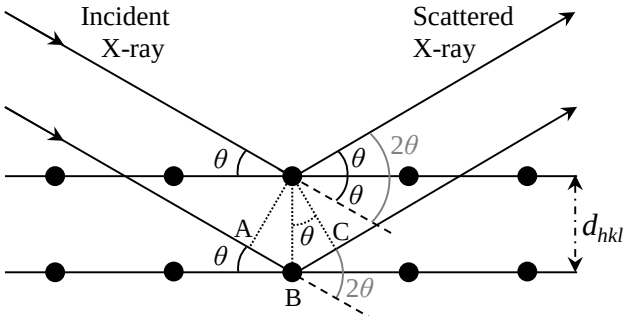

Figure 2.3: Diffraction of X-rays incident upon parallel planes of atoms separated by distance d_{hkl}. The angle between the incident and diffracted beams is 2θ.

The incident waves are in phase when entering the crystal, however, some penetrate deeper than others. Constructive interference and therefore diffraction only occurs when the waves that have been scattered are in phase, and this would only happen if the extra distance travelled by the deeper penetrating waves is equal to an integer number of wavelengths $n\lambda$. This path difference is demonstrated in Figure 2.3 by the sum of the distances between points A and B and points B and C, giving Equation 2.1:

$$n\lambda = \mathrm{AB} + \mathrm{BC} \tag{2.1}$$

As the angle of incidence is known and the distance between the two atomic planes, known as d-spacing, is given by d_{hkl}, then the path length AB + BC is equal to:

$$\mathrm{AB} + \mathrm{BC} = 2d_{hkl}\sin\theta = n\lambda \tag{2.2}$$

The above relationship is known as Bragg's Law, and it shows that constructive interference will occur at different incident angles θ for different plane separations d_{hkl}.

An ideal ground powder sample consists of a large number of small crystallites, all with random orientations to each other. When in the path of monochromatic X-ray radiation there are enough crystallites in every orientation to fulfill the Bragg

condition, and this will occur for all lattice spacings. Ultimately, this gives rise to each lattice spacing producing a "cone" of diffraction, with 2θ being the angle between the incident and diffracted beams, as illustrated in Figure 2.4.[13]

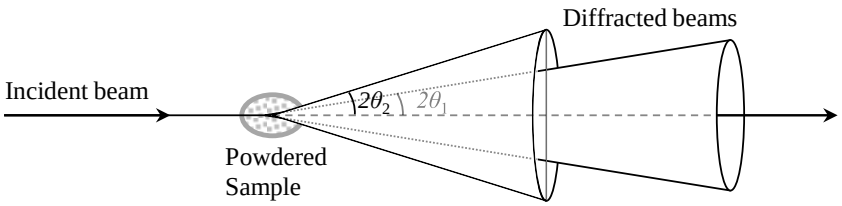

Figure 2.4: Diffraction of X-rays from an isotropic powdered sample resulting in *diffraction cones* that are at an angle 2θ from the incident beam.

For structural information to be extracted from powder diffraction, the data are collected in the format of diffracted intensity as a function of their position, or 2θ. At angles that satisfy the Bragg condition, intense peaks are observed producing a diffraction pattern, each one corresponding to an individual lattice plane.

Using the Bragg equation, it is possible to determine the d-spacing value for each reflection as both the position in 2θ and the wavelength of monochromatic radiation are known. The method of assigning each reflection with Miller indices relating that particular lattice plane to the unit cell so that the cell dimensions can be determined is known as indexing. An example of this is given in Figure 2.5 which provides a diffraction pattern of NIST (National Institute of Standards and Technology) crystalline ceria and highlights the (111) diffraction plane for the cubic system.

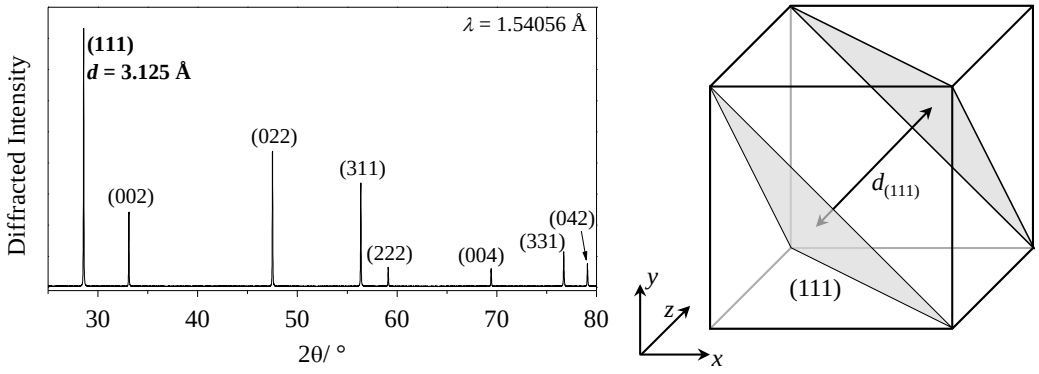

Figure 2.5: X-ray diffraction pattern of NIST CeO_2 using Cu Kα_1 radiation ($\lambda = 1.54056$ Å) and Miller indices for each Bragg reflection. A structural representation of the (111) lattice plane for the cubic system is also shown.

Miller indices, labelled as h, k, and l, are represented by integer numbers. Each refers to the reciprocal of the fractional value where the lattice plane intercepts the x, y, and z axes of the unit cell.

For a simple cubic system, the relationship between unit cell parameter a and d-spacing is given by Equation 2.3:

$$d_{hkl} = \frac{a}{\sqrt{h^2 + k^2 + l^2}} \tag{2.3}$$

and when combined with Bragg's law, and rearranged, this produces:

$$\sin^2\theta = \frac{\lambda^2}{4a^2}(h^2 + k^2 + l^2) \tag{2.4}$$

The unit cell is the simplest representation of the ordered arrangement of atoms that can be repeated by translation, making up the crystal. The positions of the atoms within the unit cell are described using fractional coordinates. The unit cell and its contents describe the entire symmetry of the crystal structure through the assignment of a space group, and has dimensions of a, b, and c with internal angles of α, β, and γ. There are seven different types of crystal class, ranging from cubic where $a{=}b{=}c$ and $\alpha{=}\beta{=}\gamma{=}90°$, through to the lowest symmetry triclinic system where $a{\neq}b{\neq}c$ and $\alpha{\neq}\beta{\neq}\gamma{\neq}90°$.

The lattice is a three-dimensional array of points that describe the translational symmetry of the structure. The simplest lattice, containing a single lattice point located on the corners of the unit cell, is called *primitive*. The second is *body-centred* where there is an additional lattice point at the centre of the unit cell. When there are lattice points in the centre of each face as well as the corners of the unit cell, this is a *face-centred* structure. In face-centred lattices that have lattice points in the centre of only one pair of opposite faces, these are assigned the symbol A, B, or C, depending on the face upon which it resides, as depicted in Figure 2.6.

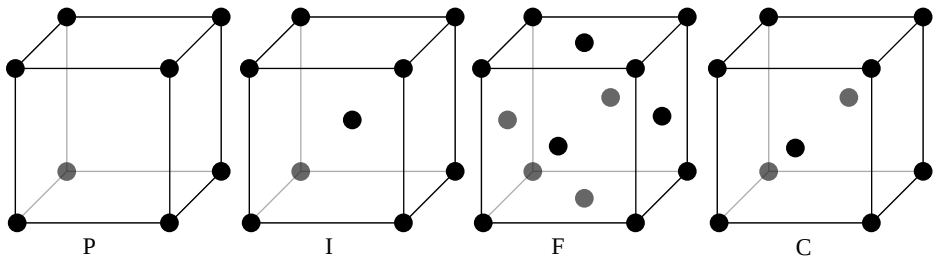

Figure 2.6: Four different types of lattice point arrangements for a cubic unit cell. From left to right: primitive (P), body-centred (I), face-centred (F), and C face-centred (C).

When these four types of lattice are combined with the seven different crystal classes, it gives rise to fourteen different variations, known as *Bravais lattices*.

Only an orthorhombic unit cell can adopt each of the four different lattices, as some of the combinations do not lead to a unique Bravais lattice. For example, a cubic system which is C face-centred actually loses its cubic symmetry as only two of the faces have lattice points at their centres. For tetragonal systems, the C face-centred lattice can be described by a primitive lattice with a smaller volume, meaning that only primitive and body-centred lattices are adopted by the tetragonal class.

The position and number of reflections observed in a powder diffraction pattern are used to determine the crystal class, lattice type, unit cell size and overall symmetry, described by the space group of the structure. Generally, the lower symmetry the structure then the more reflections there are in the powder pattern, and systematic absences can allude to the lattice type. Systematic absences describe reflections that are technically allowed by the crystal system, but have zero intensity due to certain centrings resulting in destructive interference. For example, the 200 plane in a face-centred cubic lattice diffracts X-rays that are exactly out of phase with those from the 100 plane, so no 100 reflection is observed, and this can be deduced from the structure factor. When all of the planes in a face-centred cubic system are considered, such as CeO_2 in Figure 2.5, the Miller indices of the plane have to be either *all odd* or *all even* for a reflection to be observed.

However, knowledge of the atom types and their positions inside the unit cell are only gained once the intensities of the reflections have been determined, something which Bragg's law does not achieve.

X-rays are scattered by the electron cloud surrounding the nucleus of the atom. The electric field of the incident wave causes the electron to oscillate about its position, and in doing so, it emits a new scattered wave of identical wavelength to the incident wave, so the scattering process is said to be *coherent*. As all elements have a different number of electrons Z or *scatterers*, then each atom therefore has its own scattering factor f_j:

$$f_j = \frac{\text{amplitude of the wave scattered by the atom } j}{\text{amplitude of the wave scattered by a single electron}} \tag{2.5}$$

The incident X-rays have a wavelength of similar magnitude to the size of the electron cloud and as the scattering angle 2θ increases, the intensity of the reflections drops off rapidly due to more of the scattered waves being out of phase. The electron cloud is not a perfect *point scatter* and so X-rays scattered at

different points in the cloud are out of phase. At $2\theta = 0$, the scattering factor f_j is equal to Z, however, this rapidly decreases with increasing angle.

The unit cell contains multiple atoms, each of which will have its own scattering factor f_j that affects the amplitude of the diffracted wave. The separate atoms of the unit cell will give different contributions to the observed intensity of the reflection, depending on which particular *hkl* plane it resides upon and its position within the unit cell. The sum of each of these atomic scattering factors f_j leads to the structure factor F_{hkl}, given by the expression:

$$F_{hkl} = \sum_j f_j e^{2\pi i(hx_j + ky_j + lz_j)} \tag{2.6}$$

where x_j, y_j, and z_j are the atomic coordinates of the jth atom and h, k, and l refer to the Miller indices of the reflection.

It is worth noting that the intensity of a *hkl* reflection is proportional to the square of the structure factor, and the electron density for a particular atom is the Fourier transform of its structure factor. Bearing this in mind, measuring the observed intensity allows one to determine the structure factor, calculate the electron density distribution, or *Fourier map*, for the unit cell and thus the positions of each atom.

2.2.1.2 Experimental details

The powder XRD data shown in this thesis were recorded from three different laboratory X-ray diffractometers.

Phase identification and preliminary characterisation were performed using a Siemens D5000 diffractometer equipped with Cu Kα radiation (Kα_1 λ = 1.54056 Å, Kα_2 λ = 1.54443 Å). Typically, data were collected over a 2θ range of 8 to 60° with a step size of 0.02° and 1.1 second per step measurement.

High-resolution powder XRD data were collected using a Panalytical X'pert Pro MPD, equipped with monochromatic Cu Kα_1 radiation and a PIXcel solid state detector. Data were collected over a 2θ range of 20 to 100°, sufficient enough for refinement. Some of the metals used in the work described in this thesis are known to fluoresce when illuminated by radiation of Cu Kα wavelength. The effects of sample fluorescence were minimised by placing a thin (0.02 mm) nickel filter in the diffracted beampath between the sample and detector. The effects of preferred orientation were reduced by spinning the powders at a rate of 4 revolutions per second during data collection.

Variable temperature measurements were made using a Bruker D8 Advance diffractometer equipped with bichromatic Cu Kα radiation and a VÅNTEC-1 high-speed detector. Samples were heated at a rate of 0.2 °C per minute inside an Anton Paar XRK 900 reaction chamber controlled through a TCU 750 temperature unit. Temperatures ranged from 30 to 900 °C, with data collected at sample-specific temperatures. Powders were held at these temperatures for at least 5 minutes in order to thermally equilibrate before data collection commenced.

2.2.2 Neutron Diffraction

2.2.2.1 Background

Discovered in 1932 by James Chadwick,[14] the neutron would later become a valuable tool used in the study of condensed matter. Over the following years the technique of neutron scattering was rapidly developed by many scientists, including Brockhouse and Shull.[15] Unlike X-ray diffraction where the incoming photon is scattered by the electron cloud surrounding the atom, the neutron with neutral charge, is instead scattered by the nucleus of the atom. The neutron scattering power, or cross-section, of each element does not hold a relationship to the atomic number, unlike X-rays where it scales as Z^2. This means that neutron diffraction holds several advantages over X-ray diffraction, two of which are applicable to the work described in this thesis. The first is that compared to X-rays, neutrons are scattered relatively more strongly from 'light' atoms such as hydrogen and oxygen; particularly useful when the presence of heavier elements dominate the XRD pattern. The second is that the haphazard variation in neutron scattering cross-sections between neighbouring elements,[16] such as manganese and iron, allows for them to be distinguished from each other. These two advantages are both illustrated in Figure 2.7.

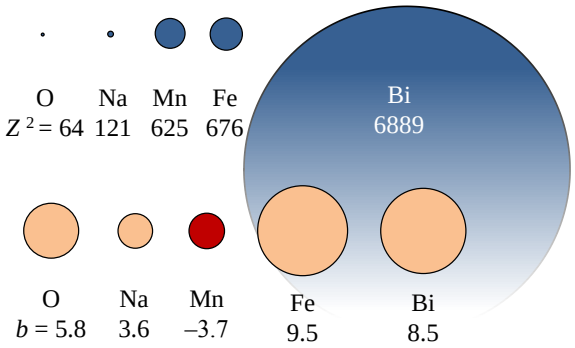

Figure 2.7: X-ray (top) and neutron (bottom) scattering cross-sections (units of fm) drawn to scale as circles for a select group of elements encountered in this work, showing the random neutron cross-sections compared to the Z^2 relationship for X-rays.

One further advantage that neutron diffraction holds over XRD is that there is no form factor for neutrons. The form factor of X-rays, as described above, originates from the size of the electron cloud surrounding the nucleus, so with the nucleus effectively being a point scatterer due to its size relative to the neutron wavelength, the scattering length b does not depend upon the scattering angle. Practically, this means that the range of useful data in reciprocal space that can be obtained from a diffraction experiment is increased for neutrons.

In order for diffraction to occur, like with X-rays, the wavelengths of the incoming neutrons have to be of a similar order of magnitude to the interatomic distances in crystalline materials. Using the semi-classical approach, the de Broglie relationship given in Equation 2.7, shows that it is possible to alter the wavelength (λ) of the neutrons by changing the speed (v) at which they are travelling.

$$\lambda \;=\; \frac{h}{m_{\mathrm{n}} v} \tag{2.7}$$

where h is Planck's constant, and m_{n} is the mass of the neutron.

The process by which the speed, or energy, of neutrons is controlled is known as *moderation*, and the degree of moderation is usually given by the temperature of the moderating medium. Once moderated, thermal neutrons have wavelengths that are suitable for performing diffraction experiments, and this can be shown when considering their kinetic energy given by Equation 2.8.

$$\tfrac{1}{2} m_{\mathrm{n}} v^2 \;=\; k_{\mathrm{B}} T \tag{2.8}$$

Through Equation 2.8, thermal neutrons produced at room temperature (290 K) have a speed of 2200 ms^{-1}, and this corresponds to a wavelength of approximately 1.8 Å, similar to the metal-oxygen distances found in many crystalline materials.[17]

The scattering of a neutron by a sample is characterised by the change in momentum involved in the process.[18] The vector quantity $\mathbf{Q}$ is commonly referred to as the "diffraction vector" or "momentum transfer" (strictly speaking, momentum transfer actually equates to $\hbar\mathbf{Q}$) and expresses the change in momentum as such:

$$\mathbf{Q} \;=\; \mathbf{k}_i \;-\; \mathbf{k}_f \tag{2.9}$$

where $\mathbf{k}_i$ and $\mathbf{k}_f$ are the incident and final wavevectors, respectively. In the case of elastic scattering, where there is no exchange of energy between the incident neutron and the sample, then the magnitude of $\mathbf{Q}$ can be related to the wavelength

and scattering angle by Equation 2.10.

$$|\mathbf{Q}| \; = \; Q \; = \; \frac{4\pi \sin\theta}{\lambda} \tag{2.10}$$

The quantity that is being measured in a neutron experiment is typically the differential cross-section, defined by Equation 2.11:

$$\frac{\mathrm{d}\sigma}{\mathrm{d}\Omega} \; = \; \frac{\text{No. neutrons scattered into solid angle d}\Omega \text{ at angle } 2\theta,\phi}{N\Phi \mathrm{d}\Omega} \tag{2.11}$$

where Φ is the flux of incident neutrons, and N the number of atoms in the sample. The solid angle $\mathrm{d}\Omega$ refers to the area (in units of steradians) perpendicular to the beam direction, typically the area of a detector placed in the diffracted beam path, and is described through Figure 2.8.

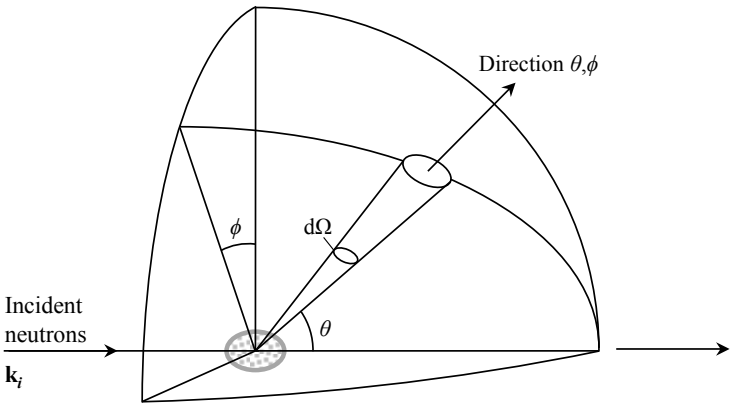

Figure 2.8: Geometry of a neutron scattering experiment, illustrating solid angle $\mathrm{d}\Omega$.

The total scattering cross-section, which refers to the number of neutrons scattered in all directions can therefore be defined as:

$$\sigma_{\mathrm{tot}} \; = \; \frac{\text{Total number of neutrons scattered per second}}{N\Phi} \tag{2.12}$$

The coherent scattering cross-section σ_{coh} is given by Equation 2.13, and is proportional to the square of the scattering amplitude, in the same way that the intensity of scattered X-rays is proportional to the square of the form factor.

$$\sigma_{\mathrm{coh}} \; = \; 4\pi\bar{b}^2 \tag{2.13}$$

However, unlike for X-rays, the coherent scattering length $\bar{b}$ is invariant of both the scattering angle and wavelength, and therefore energy, of the incident

neutrons. Instead, the magnitude of $\bar{b}$ depends upon the target nucleus. Their values can be positive, or negative as is the case for the elements of H, Ti, and Mn. A positive scattering length means that the incident and scattered waves are 180° out of phase, whereas a negative value means that both the incident and scattered waves are in phase.

Sources of neutrons can be separated into two different types; reactor-based sources, and accelerator-based sources. Reactor sources such as the Institut Laue Langevin (ILL) in Grenoble, France, rely on the production of neutrons for scattering based purposes as a direct result of the fission reaction of ^{235}U nuclei in a reactor core. High energy neutrons are produced, too high in fact for the fission reaction to continue as the absorption cross-section for ^{235}U is low at such energies. Thus, the neutrons are slowed down through the moderation process in order to both sustain the fission reaction, and to produce neutrons of a suitable wavelength for scattering purposes.

An example of the second type, the accelerator-based source, is ISIS, U.K. These type of sources are based upon the collision of high energy charged particles with a heavy metal target. At ISIS, a linac (linear accelerator) is used to feed H^- ions of 70 MeV energy through an alumina foil, removing the electrons, and into a synchrotron as protons. Once accelerated further to 800 MeV, the protons are extracted from the synchrotron and directed towards a tungsten target, where on impact, neutrons are produced through the spallation process. This is where the violent collision between high-energy charged particles causes the emission of neutrons from the heavy metal nuclei. A proton current of up to 200 μA can be achieved and they are fired at the target every 20 ms (frequency of 50 Hz).

The moderation process involves passing the produced neutrons through a considerable number of nuclei with low mass, such as hydrogen. The neutrons undergo inelastic collisions, and the energy transferred in these collisions is maximised due to the mass of the moderating atom being very close to that of the incident neutron. Example moderating materials include H_2O, D_2O, CH_4, and graphite.

All of the neutron scattering data included and analysed in this thesis were collected at ISIS, which as a pulsed source makes use of the time-of-flight method.

2.2.2.2 Time-of-flight neutron diffraction

As the flux of neutrons is constant at reactor-based sources, it is necessary to monochromate the incident beam in order to perform diffraction measurements.

This results in large amounts of the initial neutron flux being wasted and only small amounts being used. This is one advantage of pulsed spallation sources, as they are ideally suited for time-of-flight (t-o-f) scattering, whereby a wide range of neutron energies is used. The wavelengths are calculated based upon the time taken for the neutrons to travel from the moderator to the detector, via the sample. For example, shorter wavelength neutrons have higher energies and therefore traverse this distance in a shorter amount of time. The distance and scattering angle are typically known, such that the wavelengths can be calculated through Equation 2.14:

$$t = \frac{m_{\mathrm{n}}}{h} L\lambda \tag{2.14}$$

where L is the total flight path of the neutron. Through combination with Bragg's Law, t-o-f is proportional to d-spacing by:

$$t = 505.56\, L \sin\theta\, d \tag{2.15}$$

and through Equation 2.10, it is possible to plot the neutron counts as a function of Q.

Ultimately, this technique utilises the majority of the neutron flux in the scattering experiment, making the total number of detected neutrons a comparable order of magnitude to that in a reactor-based experiment. Also, this method allows for the collection of an entire diffraction pattern from just a single fixed-angle detector.

2.2.3 Fitting of Diffraction Data

As mentioned above, crystal structures are determined from structure factors, the magnitudes of which are derived from the integrated intensities of peaks in a diffraction pattern. It is typical to solve an unknown structure from single crystal diffraction, involving the determination of space group and unit cell from hundreds of individually measured diffraction peaks, or "spots". The intensities of each peak can be directly converted into structure factor magnitudes, which are used to determine a list of atomic coordinates, occupancies, and displacement parameters for the crystal under study.

For powder diffraction data, structure solution is made increasingly more difficult due to the information contained within the data being compressed into the one-dimensional powder pattern.[19] For powdered materials of high symmetry, the reflections are resolved enough such that the integrated intensities of them can be extracted and used to produce an end structure. However, the majority of

powdered materials display Bragg reflections that overlap with one another in the powder pattern, rendering these techniques much less amenable.

2.2.3.1 Rietveld refinement

Proposed in the late 1960s by Hugo Rietveld,[20] the technique of Rietveld refinement overcame the problem presented by reflection overlap in a powder pattern by considering each data point as an individually observed intensity. At the time, it was thought that powder diffraction methods were inferior to those of single crystal diffraction, however, the Rietveld method is now widely recognised as a valuable step in the structural study of powdered crystalline materials.[21]

In Rietveld refinement, each observed data point y_{oi} is treated individually, and the overall quantity that is calculated is the residual which describes the difference between the observed data and calculated model:

$$S_y = \sum_i w_i (y_{oi} - y_{ci})^2 \tag{2.16}$$

where y_{ci} is the calculated intensity at the ith data point, and w is a weighting defined as the reciprocal variance of the measured values which is equal to $1/\sigma^2(y_{oi})$. During the refinement, it is the residual that is minimised through least-squares refinement until the best fit between the observed powder pattern and calculated pattern is obtained.

It is at this point that the requirement of not only a starting model, but one that already suitably resembles that of phase being studied, becomes obvious. Fortunately, many crystal structures are currently known and are available through the inorganic crystal structure database (ICSD) for such use. Many inorganic materials have structures related to those already known, so suitable starting models can often be deduced. The Rietveld process allows the simulated pattern to be compared with the observed pattern, before altering the model slightly, and recalculating until the simulated pattern matches the observed data as much as possible.

The model structure has various degrees of freedom including the choice of space group, unit cell dimensions, atomic positions, site occupancy, and thermal displacement parameters (both isotropic and anisotropic) that can be altered or *refined* against the observed data in order to improve the fit. Once the refined model produces a pattern that agrees well with the observed data, the refined crystallographic parameters may give a good representation of the unknown

structure, but chemical sense and information from other techniques is likely also needed. It is perhaps at this point important to acknowledge that the Rietveld technique is a structure *refinement* method, and not a structure *solution* method.

Non-structure specific effects that arise need to be considered also, such as instrumental effects, background, profile shape, diffuse scattering, and the Lorentz-polarisation factor. It is commonplace for corrections such as a zero and height offset of the sample to be applied during refinements made against observed powder patterns. The former results in a linear offset, and the latter a cosinusoidal offset to the peak position in the observed data. Refinements made against powder XRD data collected from the instruments described above made it necessary to apply a Lorentz-Polarisation correction to the model as such an effect has an effect on the observed intensities of Bragg reflections.

It was realised by Rietveld that in order to extract the maximum information from a measured diffraction pattern, it is necessary to put in as much knowledge about the structure, instrument, and conditions to begin with.[19]

An example Rietveld refinement made against neutron diffraction data collected on bank 5 of the GEneral Materials diffractometer (GEM), at ISIS, from NIST (National Institute of Standards and Technology) CeO_2 is shown in Figure 2.9. A total of eleven degrees of freedom were refined; five structural, and six instrumental.

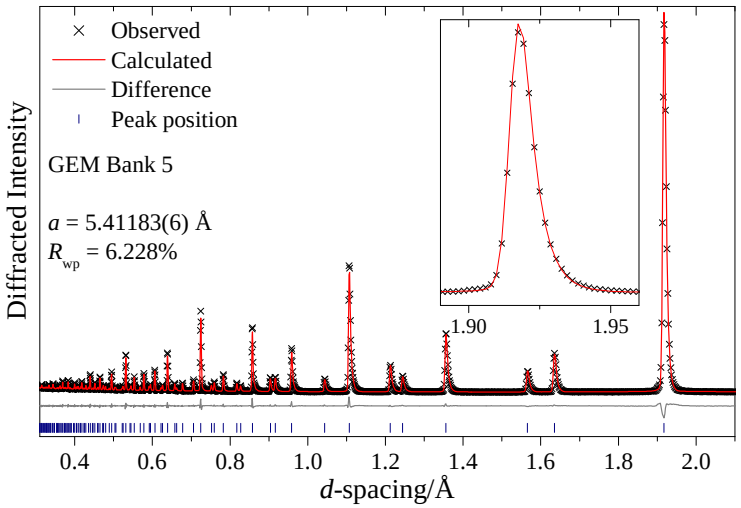

Figure 2.9: Rietveld refinement against time-of-flight neutron data recorded from a NIST CeO_2 standard. The refinement converged with $R_{wp} = 6.288\%$, defined in Equation 2.17. The inset highlights the asymmetric profile of the peaks.

Peak shapes for X-ray diffraction are generally described through the use of a pseudo-Voigt function, comprised of a convolution between a Gaussian term and a Lorentzian term. For time-of-flight neutron diffraction, peak profiles are more complicated, since the peak appears asymmetric with a sharp leading edge and a trailing edge that decays more slowly, as shown in the inset of Figure 2.9. The sharp leading edge is a result of the large neutron flux that comes rapidly from the proton beam colliding with the target. The slow decay of the tail represents neutrons that have been slowed down through interactions with the moderator that is in between the target and sample. The Ikeda-Carpenter function is commonly used to model this asymmetrical peak shape, and is comprised of two functions: the first is the "slowing down" term and describes the flux of neutrons that emerge before reaching thermal equilibrium with the moderator, and the second is the "storage" term which describes the number of neutrons that remain in the moderator and become thermalised, before decaying away.[22] The Ikeda-Carpenter function is convoluted with a Gaussian term that describes the instrumental contribution to the peak resolution.

For the neutron data presented in this thesis, refinements were made simultaneously against data from more than one detector bank, often banks 3, 4, and 5 (mean scattering angles of 35.14°, 62.39°, and 92.83°, respectively).[23] This was done to exploit the different ranges in d-spacing provided by each bank so as to include more Bragg peaks in the refinement. As a result of each bank having different scattering angles and resolutions, the refinement used different background terms, scale factors, and profile parameters for each. These values were initially refined for each bank using the data for NIST CeO_2, shown in Figure 2.9, and once determined, were fixed for the subsequent refinement of the materials studied in this work.

Wherever neutron data are presented in this thesis, the refinements also used X-ray diffraction data recorded from the same material. The incorporation of high-resolution monochromated X-ray diffraction data in the refinements, alongside the neutron data, ensures that accurate and precise lattice parameters are obtained. Once this was achieved, both the neutron and X-ray data were used to refine the structure.

The simultaneous refinements of both X-ray and neutron diffraction data presented in this thesis were performed using the program TOPAS-Academic (Version 4.1) implemented with jEdit (Version 4.3.1).[24] TOPAS-Academic handles all of the corrections, peak shape functions, background fitting, as well as the

structural and instrumental effects mentioned above, through means that are described in the TOPAS technical reference.[25]

It is possible to monitor the progress of the refinement through both graphical visualisation of the simulated and observed diffraction patterns, and also through the various statistical quantities that are calculated during the refinement process. Though there are several, all of which give different statistical weightings on the quality of fit, the two used in this thesis are the weighted profile R-factor, R_{wp}, which gives a measure of how well the calculated pattern fits the observed pattern, based on the differences summed over each step:

$$R_{\mathrm{wp}} = \sqrt{\frac{\sum_i w_i(y_{oi} - y_{ci})^2}{\sum_i w_i(y_{oi})^2}} \tag{2.17}$$

and the expected R-factor, R_{exp}, which calculates the best fit possible from the number of steps N and number of degrees of freedom P:

$$R_{\mathrm{exp}} = \sqrt{\frac{N - P}{\sum_i w_i(y_{oi})^2}} \tag{2.18}$$

where w_i is a weighting factor for the ith data point.[26] Ideally R_{wp} and R_{exp} would be equal on convergence, but for a refinement of a real system, the former is always higher than latter.

Of course one must always critically examine the results from Rietveld refinement to check that certain parameters refined during the process have not become unrealistic. For example, a refinement of a model against experimental data could look statistically good, but on closer inspection, one might find that parameters such as site occupancies or thermal displacement parameters have refined to unreasonable values. It is always important to therefore check these parameters, as well as the errors on them, after refinement.

As mentioned above, the importance of a starting model of known space group and with similar lattice parameters to the unknown phase is paramount. The dimensions of the unit cell as well as a scale factor are the first parameters to be refined. If profile fitting preceded the Rietveld refinement, then these values should already be known with some accuracy. The profile and instrument terms are then refined; again with the possibility of prior knowledge of these from profile fitting. Once these parameters have stabilised, it is then possible to focus more on the structural details of the model by refining the atomic positions. Refining the

positions of the heavier elements first is sensible, particularly if the refinement involves only X-ray diffraction data. Once these parameters have converged individually, then it is possible to refine them all simultaneously. The refinement of site occupancies is problematic as these can be affected by very slight changes in the background, much like the thermal displacement parameters, to which they are correlated. Akin to the atomic positions, thermal displacement parameters should be refined starting with the heavier elements. Refinements of both the site occupancy and thermal displacement parameters become more reliable if neutron data are incorporated. Only once the structural parameters are satisfactorily stable can the background be modelled.
Numerous cycles are performed between each of the above steps to ensure that the refinement is stable and does not diverge, and also that the end point is not a false minimum. Ultimately, if the refinement is robust, it is usually possible to refine all the parameters simultaneously.

2.2.3.2 Pawley fitting

In instances where there are no models that would act as a suitable place from which to start the Rietveld refinement, it is possible to extract the intensities of reflections and other parameters important to the Rietveld process through profile fitting.[27] An example Pawley refinement made against XRD data collected from NIST CeO_2 is shown in Figure 2.10.

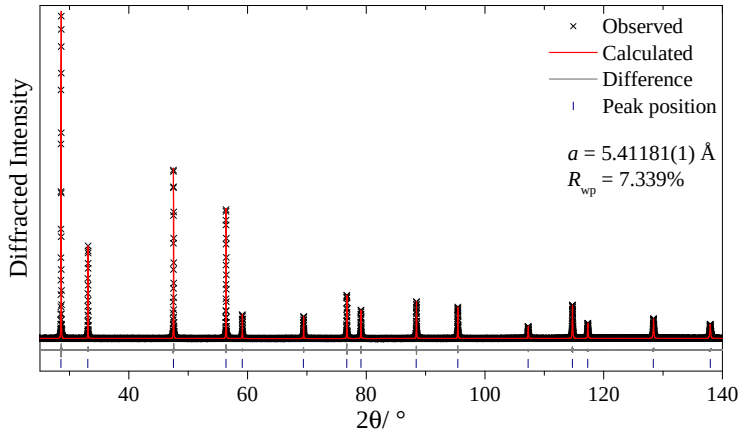

Figure 2.10: Pawley refinement made against powder XRD data of NIST CeO_2.

Where the Rietveld procedure is a least-squares fitting of the diffraction pattern including variable parameters that depend upon the peak area, the Pawley method is a structure-free least-squares approach in which the calculated reflections are

adjusted to fit the observed intensities to allow for the extraction of peak areas.[26,28] As mentioned in the section above, parameters such as the unit cell dimensions, scale factor, background, profile parameters, and instrumental parameters can all be refined through this process, providing a set of highly accurate intensities and peak positions that then are transferable across to Rietveld.

2.2.4 Total Scattering

Total scattering refers to an experiment in which both the Bragg and *diffuse scattering* are simultaneously included in the analysis of the data. The diffuse scattering typically resides in the "background" of the diffraction pattern and is widely spread across Q-space, compared to Bragg reflections which are confined to particular reciprocal lattice points. The diffuse scattering often contains important information regarding deviations on the local scale away from the Bragg-described average structure. It is common for the diffuse scattering to dominate the higher-Q region where Bragg peaks are minimised or non-existent due to the Debye-Waller factor, and is shown in Figure 2.11 a), which shows the scattering data for crystalline GeO_2 quartz, taken from Hannon *et al.*[29]

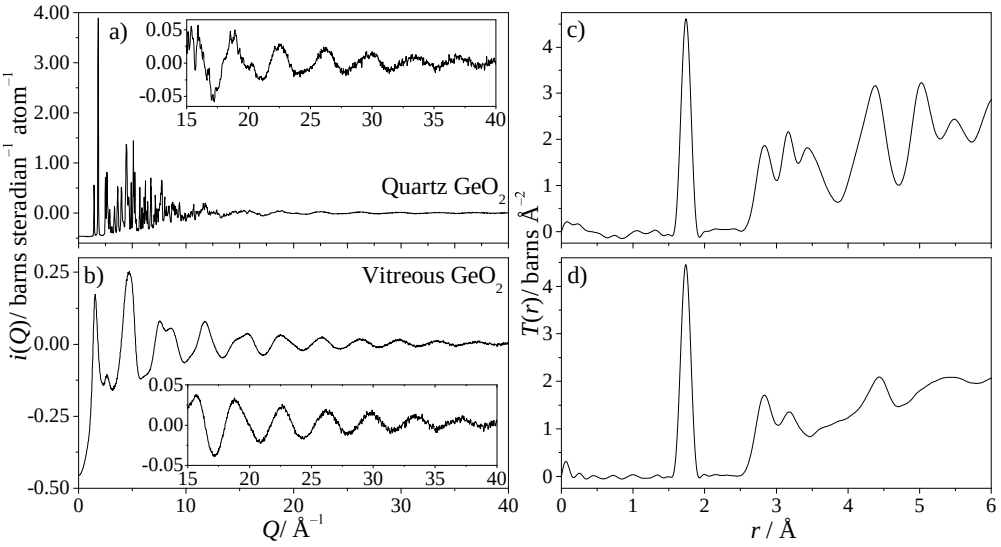

Figure 2.11: Measured $i(Q)$ for a) crystalline quartz GeO_2 and b) vitreous GeO_2, and the results of their Fourier transformation into $T(r)$, c) for crystalline GeO_2 and d) vitreous GeO_2. Data were provided by Dr Alex Hannon.

In a typical Rietveld study this diffuse scattering is treated as the background and is simply fitted using polynomial functions in order to improve the fit statistics; no information is obtained from fitting the background in a Rietveld refinement. In the total scattering technique, the extra information included in the background is

used to further study the structure.

Total scattering has been used extensively to study materials that do not have an ordered crystalline structure, such as amorphous materials, liquids, and gases. Such materials do not produce diffraction patterns that contain Bragg peaks, only the diffuse scattering as shown in the distinct scattering data for vitreous GeO_2 in Figure 2.11. It is possible through Fourier transformation to take the reciprocal space diffraction pattern and obtain the so-called correlation function which shows real space interatomic correlations. For amorphous materials, such as glasses and liquids, this can provide detailed information on the disordered structure by displaying the first few well defined correlations in r. Conversely, for crystalline materials the atomic correlations will be resolved out to much larger distances in r, and can be used to study local deviations away from the average structure that are not accounted for in the refinement of Bragg data alone. Panels c) and d) of Figure 2.11 show that a correlation function is produced from Fourier transformation whether or not Bragg peaks are present in the distinct scattering, showing that short range order is always present in the material, whether or not it has long range order.

The term "correlation function" is used extensively in this thesis to describe data that display the number of atoms situated at a distance r from the average atom placed at the origin. It is, however, possible to Fourier transform the distinct scattering into several different types of correlation function, the details of which will be discussed further into this chapter.

Figure 2.12 displays the correlation function for crystalline GeO_2 with the quartz-type structure, along with a structural representation of a single GeO_2 tetrahedron. It is clear to see that the first observed peak, or correlation, corresponds to the Ge–O distance within the crystal structure and the second is due to the next-nearest neighbour distance of the O–O correlation. Although the correlations continue out to further r, the assignment and analysis becomes more difficult due to the overlap between these types of bonding distances and the inclusion of others such as Ge–Ge distances.

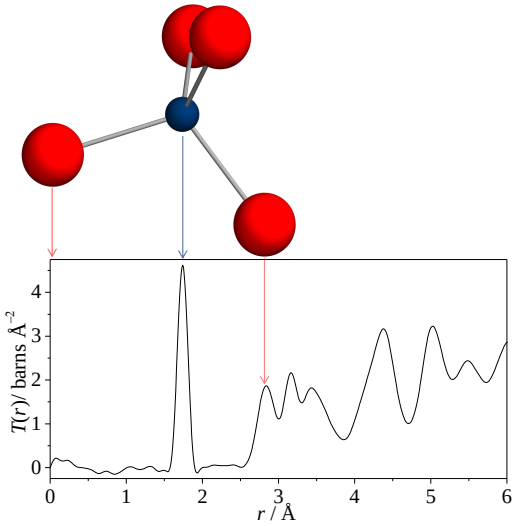

Figure 2.12: Measured correlation function of crystalline GeO_2 quartz, assigning the first two distances. Data were provided by Dr Alex Hannon.

As stated by Equation 2.11, it is the differential cross section that is being measured in a total scattering experiment. This can be broken down into two components that express the self scattering $I^S(Q)$ and the distinct scattering $i(Q)$, where Q is the magnitude of the momentum transfer.

$$\frac{\mathrm{d}\sigma}{\mathrm{d}\Omega} = I(Q) = I^S(Q) + i(Q) \tag{2.19}$$

It is the distinct scattering containing information on the interatomic distances, that we wish to Fourier transform into the correlation function. The self scattering, which can be calculated from knowing the composition of the sample, temperature, and several instrument parameters, is subtracted from the total scattering data to yield the distinct scattering, which undergoes Fourier transformation to produce the total correlation function, $T(r)$, given in Equation 2.20:

$$T(r) = T^0(r) + \frac{2}{\pi}\int_0^\infty Qi(Q)M(Q)\sin r(Q)\mathrm{d}Q \tag{2.20}$$

where $T^0(r)$ is a linear function of r and is the average density contribution, and $M(Q)$ is a modification function that is discussed further in this chapter.

$$T^0(r) = 4\pi r g^0 \left(\sum_l c_l \bar{b}_l\right)^2 \tag{2.21}$$

Where g^0 is the average atomic number density of the sample (equal to N/V), c_l is the atomic fraction of element l, and $\overline{b}_l$ is the bound coherent scattering length of element l.[23]

2.2.4.1 GEneral Materials diffractometer - GEM

All of the total neutron scattering data shown in this thesis were collected using the GEneral Materials diffractometer (GEM) at the ISIS pulsed neutron source.[23]

GEM is well suited for both Bragg scattering as well as total neutron scattering. A large component of its success is due to the array of detectors which, grouped into eight different banks ranging in scattering angle from 1.2° to 171.4°, shown in Figure 2.13, cover a very large solid angle with a total area of 7.270 m^2. This large area gives a very high count rate meaning that it is possible to make high-resolution diffraction measurements in relatively short periods of time. The wide scattering angle covered also ensures that the Q-range of the data is maximised, ranging from 0.1 to 60 $Å^{-1}$. GEM receives neutrons from a liquid methane moderator at temperature 110 K, and the long flight path of 17 m from the moderator to the sample contributes to the excellent resolution in reciprocal space, with $\Delta Q/Q = 0.34\%$ for backscattering banks. A series of beam choppers are used to prevent frame overlap between pulses and also to reduce the background produced by very fast neutrons.

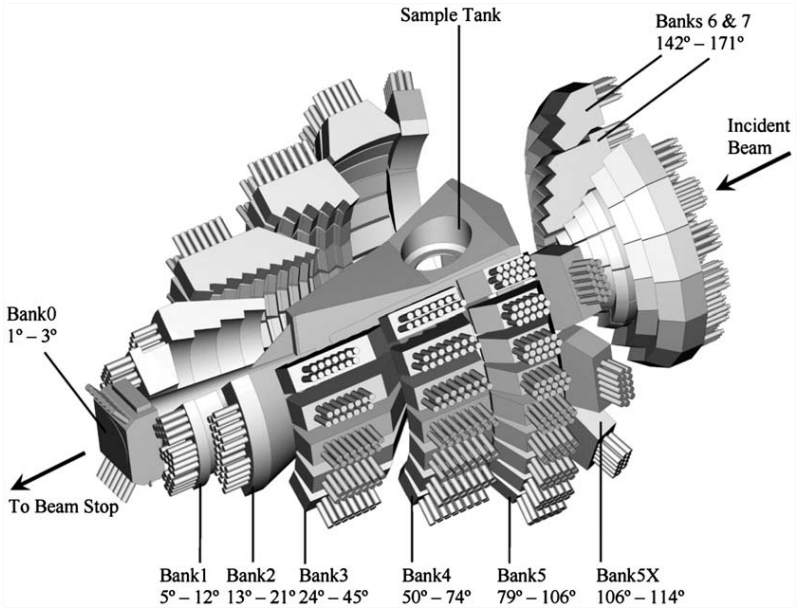

Figure 2.13: The GEM time-of-flight diffractometer, showing all eight detector banks. The beam direction is from top-right to bottom-left.

For total scattering experiments on GEM, powders were loaded into thin-walled vanadium cylindrical cans. Different sizes of can were used depending upon the sample size, but the most common can dimensions had an inner diameter of 0.6 cm, with a wall thickness of 0.004 cm. Other can sizes include 0.83 cm inner diameter with an identical wall thickness, and 0.5 cm diameter cans with a wall thickness of 0.0025 cm.

Once loaded, the cans were heated under reduced pressure to 80 °C in a ThermoScientific Heraeus Kelvitron T vacuum oven to drive off any residual moisture in the powders, before being placed in the neutron beam. This negates the effects that arise from the presence of hydrogen which, due to its large incoherent scattering cross-section ($\sigma_{\text{inc}} = 80.26$ barns)[16], tends to lead to a high sloping background, especially towards low Q values. In order to achieve a high statistical quality, data were recorded for 6 hours from each powder. The dimensions of the incident beam were set to 4 cm high by 1.5 cm across.

Data were also collected from an empty vanadium can, the empty instrument, and a solid vanadium rod of 0.834 cm diameter. The reasons for this are explained in the next section.

2.2.4.2 From raw data to correlation function

Since GEM, or any scattering instrument, measures the differential cross section, defined by Equation 2.11 as the *total* number of neutrons scattered at a particular angle, not just neutrons scattered by the sample, it is therefore necessary to correct the data. Neutrons are detected from various types of scattering that take place along the beam path such as: scatter from the inside of the instrument or vacuum tank, scatter from the sample container, and also scatter from the air (either in the sample environment if the measurement is not performed in a vacuum, or from the air in between the vacuum tank and detector). The necessary measurements to accurately correct the data are summarised below:

- A dataset measured from a vanadium rod (0.834 cm diameter) is used to normalise the data to the flux distribution of the moderator and place the data onto an absolute scale, whilst also taking account of the different solid angle covered by each detector.
- Data collected from an empty sample container (same type and size as those used in the experiment) are used for background subtraction.
- Data collected from the empty instrument (if samples were measured under vacuum, the empty tank must be evacuated also) for further background

subtraction.

Further corrections would have to be made as a result of performing measurements in unusual sample environments, such as a furnace or cryostat. It is necessary to know the packing density of the sample within the vanadium can, and also how much of the sample is actually illuminated by the beam (size 4 cm by 1.5 cm) for normalisation purposes also.

The measured data are corrected by the simplified method given in Equation 2.22, producing normalised data that originates from the sample only.

$$\text{Corrected data} = \left(\frac{\text{sample} - \text{empty container}}{\text{vanadium rod} - \text{empty instrument}} \right) \tag{2.22}$$

Data were corrected using the program GudrunN,[30] which also takes into account effects such as attenuation, absorption, detector dead-time, and multiple scattering, the details of which are beyond the scope of this thesis.

It is particularly important to maximise the Q-range of the data used in the Fourier transform to obtain the best possible real-space resolution of the resultant correlation function.[31] In theory, the Fourier transform includes data from $Q = 0$ out to infinity, as given by Equation 2.20, however, in reality this is not possible. The low scattering angle banks of GEM allow for the measurement of Q down to very low values, whilst the maximum value of Q_{max} may be limited by the sample or the instrument, and a delicate balance is required with its selection. Endeavouring to choose a value of Q_{max} as high as possible is desirable in order to maximise the real-space resolution, however, a caveat comes with extending Q_{max} further than the data are statistically meaningful, as it leads to increased noise in the resultant correlation function, due to the statistical noise in the $i(Q)$ increasing also as a function of Q. The desired value of Q_{max} is therefore the point at which no extra information regarding the structure would be included in the Fourier transform if the value were taken higher, ultimately minimising the effects of statistical noise. The effect of varying the value of Q_{max} on a correlation function of GeO_2 quartz is shown in Figure 2.14 a). With increasing Q_{max}, the termination ripples on either side of the Ge–O peak are minimised by thermal broadening, and the resolution width decreases.

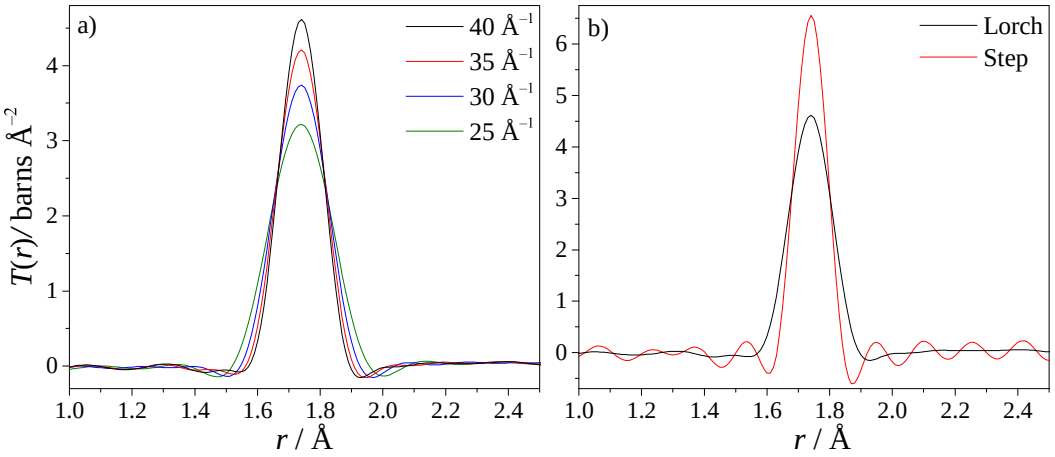

Figure 2.14: a) Effect of different values of Q_{max} used in the Fourier transform on the resulting correlation function. Data are treated using the Lorch modification function. b) Effect of different modification functions used in the Fourier transform on the resulting correlation function. Data treated using the Lorch (black) and step (red) modification functions both use a Q_{max} of 40 Å^{-1}.

The Fourier transformation of data using a finite value of Q_{max} has the effect of introducing *termination ripples* which oscillate away from the peaks in the correlation function. The term $M(Q)$ in Equation 2.20 refers to the modification function which describes how the value of Q_{max} is implemented in the Fourier transform.[32] This modification function is applied to the $i(Q)$ in order to take account of the finite momentum transfer (Q_{max}), and can be a standard method of suppressing the termination ripples.[33] There are two different forms that this modification function commonly takes; the first, known as the step function, simply terminates the data at Q_{max} such that for $Q > Q_{max}$ the data are equal to zero. This yields the best real-space resolution using all of the data up to Q_{max}, but amplifies the effect of termination ripples in the correlation function. The second form is the widely-used Lorch modification function,[34,35] described by Equation 2.23, which reduces the termination ripples through a gradual dampening of the data out towards Q_{max}, compared to the abrupt termination of the step function.

$$M(Q) = \begin{cases} \frac{sin(Q\Delta r)}{Q\Delta r} & \text{for } Q \leq Q_{max} \\ 0 & \text{for } Q > Q_{max} \end{cases} \tag{2.23}$$

where $\Delta r = \pi / Q_{max}$.

This improvement is detrimental to the resolution width however, which is increased when using the Lorch function. The effects of both the step and Lorch modification functions are highlighted clearly in Figure 2.14 b) showing the Ge–O bond length

in quartz GeO_2, where both datasets are treated using a Q_{max} of 40 $Å^{-1}$. In order to suppress the increased noise of the data treated using the step function, a much lower value of Q_{max} would have to be used to exclude much of the noise-containing high-Q data.

The correlation function produced can take on several different forms,[36] however the two main types encountered in this thesis are the total correlation function, $T(r)$, given by Equation 2.20 and the differential correlation function, $D(r)$, which are both shown in Figure 2.15. The differential correlation function is also known as the pair distribution function (PDF), and is related to the total correlation function through Equation 2.24:

$$T(r) = T^0(r) + D(r) \tag{2.24}$$

so by simply eliminating the term of $T^0(r)$ from Equation 2.20, it yields the differential correlation function given by Equation 2.25.

$$D(r) = \frac{2}{\pi}\int_0^\infty Qi(Q)M(Q)\sin r(Q)\mathrm{d}Q \tag{2.25}$$

The term $T^0(r)$ is a linear function of r, and is dependent upon the density and composition of the sample, as given by Equation 2.21, making the relationship between $T(r)$ and $D(r)$ linear through this function. This allows $D(r)$, unlike the $T(r)$, to be calculated without prior knowledge of sample density and composition.

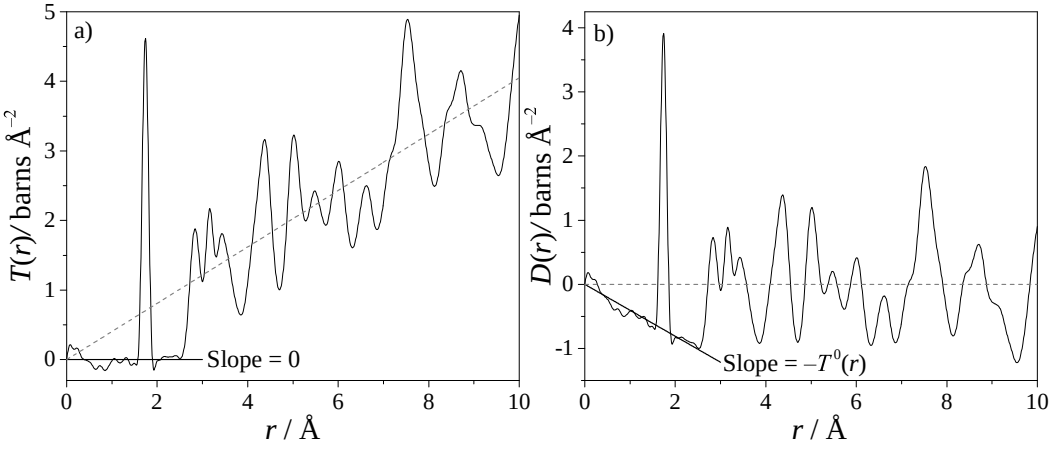

Figure 2.15: Calculated a) $T(r)$ and b) $D(r)$ for GeO_2 quartz. The two are related through the constant slope function $T^0(r)$.

The inclusion of $T^0(r)$ in $T(r)$ means that the low r region of the data is centred around zero but the rest of the data carry a $T^0(r)$ dependence, shown by the grey

dashed line in Figure 2.15 a). Conversely, for the $D(r)$ the low r region has a slope equal to $-T^0(r)$, and it is the rest of the data that oscillate about zero. The difference between $T(r)$ and $D(r)$ can be understood more easily through Figure 2.15, which shows both types of correlation function calculated for GeO_2 quartz.

2.2.4.3 Analysis of the Pair Distribution Function

As mentioned above, the pair distribution function contains a wealth of information regarding the local short range structure of the material under study. The first peak corresponds to the shortest nearest-neighbour distance in the material, shown in Figure 2.12, and its position in r gives the distance between the two bonded atoms. The area under this first peak can be used to determine the coordination number of the central atom. The coordination number, defined as the total number of neighbours (l') of the central atom (l), can be expressed as Equation 2.26.

$$n_{ll'} = \frac{r_{ll'} A_{ll'}}{(2 - \delta_{ll'}) c_l \bar{b}_l \bar{b}_{l'}} \tag{2.26}$$

Where $r_{ll'}$ is the peak position or distance between elements l and l', $A_{ll'}$ the area of the peak, and $\delta_{ll'}$ is the Kronecker delta.[37]

Fitting a resolution-broadened Gaussian to the first peak (or first few correlations in some cases) to obtain its area is a method commonly used for the study of amorphous materials like glasses and liquids.

For crystalline materials that exhibit structural order over greater length scales, it is possible to extract further information from both the first peak and the correlations out at higher r. Correlation functions, for crystal structures that have been determined through other methods such as Rietveld refinement, can be calculated and compared with the experimental data through a program called XTAL.[38] Parameters such as thermal broadening can be altered so as to improve the comparison between model and data.

It is possible to improve the comparison between data and model further by using a least-squares refinement, analogous to Rietveld refinement, in order to minimise the difference between the two, provided by programs such as PDFfit2 and PDFgui.[39] Figure 2.16 shows an example refinement made against PDF data obtained from powdered titanium metal, measured on GEM. The fitting of such data can be used to determine instrument-based resolution dampening and broadening parameters characteristic of GEM.

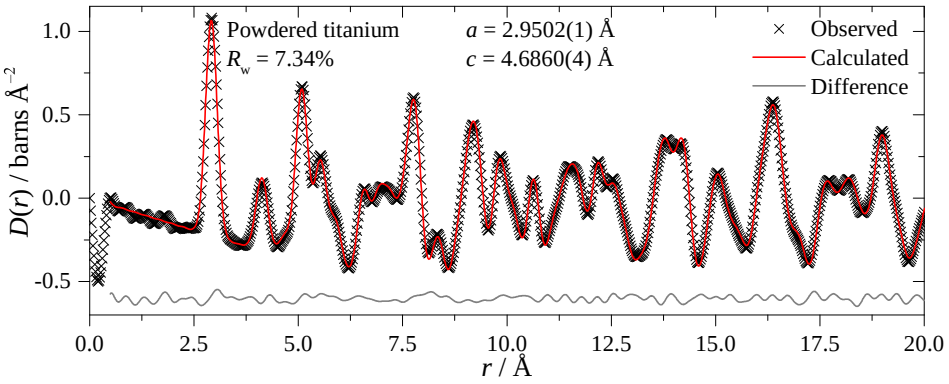

Figure 2.16: Fit to the PDF of powdered titanium metal, measured on GEM. Data were provided by Dr Alex Hannon.

Various structural and instrumental parameters can be refined in order to improve the fit to the data, again, analogous to Rietveld refinement. For a crystalline material, the structure obtained from Rietveld should agree well with the PDF, however for crystalline materials that contain disorder on a very local scale, the simulated PDF often deviates from the observed data in the low r region. It is often possible to achieve satisfactory agreement between the model and low r region by allowing various structural parameters to refine, however, this is not always the case for materials that contain high levels of local disorder, and in these instances other types of modelling are considered.

2.2.4.4 Reverse Monte Carlo modelling

Originally developed as a technique for studying the complex structures of glasses and liquids,[40] Reverse Monte Carlo (RMC) modelling has become a technique commonly used for the study of disordered crystalline materials, and even magnetic structures.[41]

Compared to the traditional Monte Carlo method which endeavours to minimise the overall energy of the system, RMC uses experimental data as the criterion to accept moves and seeks to minimise the difference between the experimentally observed data and the simulated data. The method works by employing an algorithm which selects a single atom from within a large configuration, referred to as the "box of atoms" herein, and moves this atom by a random amount in a random direction. The total scattering functions are then recalculated and compared against the experimental data. If the atom move improves the fit to the data, it is accepted. For atom moves that degrade the fit, a probability algorithm is used to decide whether it is accepted or rejected, in order to prevent the model

from becoming stuck in a false minimum. The data used to guide these configurations are typically the PDF and $i(Q)$.

A large configuration containing many atoms is required in order to improve the statistics of the simulated fit to the experimental data. The box of atoms used will typically contain tens of unit cells and thousands of atoms.

The program used to perform such simulations was RMCProfile.[42] It is possible to fit the model to several datasets simultaneously, for example; the Bragg scattering, the neutron or X-ray $i(Q)$, and also the neutron or X-ray PDF can all be modelled simultaneously. It is immensely useful to include both the PDF and Bragg data simultaneously such that the resulting model is consistent with both the local structure and the long-range average structure.

The use of various constraints in RMCProfile ensures that the random alterations of the atomic configuration result in a sensible outcome. In the absence of constraints such as density, closest approaches (cut-off distances for atom pairs), and coordination, then RMC modelling would be able to fit any dataset, but would result in an unrealistic model. The results from RMC included in this thesis make use of some of these constraints, and always make use of bond valence constraints; which are very useful when studying disordered crystalline structures and introduce some *chemical sense* into the simulation.[43] The simplicity of the bond valence sum approach lies within the assumption that the total valence of an atom i can be expressed as the sum of the valence contributions from the individual bonds to neighbouring atoms j, and can be determined from their lengths d_{ij}:[44]

$$V_i \;=\; \sum_j v_{ij} \;=\; \sum_j \exp\left[\frac{(R_{ij} - d_{ij})}{b}\right] \tag{2.27}$$

where b is a constant, and R_{ij} the atom-specific bond valence parameter.

These constraints ensure that the local environments of atoms do not become too disordered by guiding the model such that the total valence of all the bonds of the central atom remains realistic.

Unlike other techniques which struggle to model disorder in complex structures, it is made possible through RMC by removing the symmetry constraints put in place by crystallography and incorporating data that provide both local and average long range structural information into a single model.

The work involving RMC presented in this thesis was carried out with the helpful supervision of Dr Helen Playford.

2.2.5 Electron Microscopy

The majority of the electron microscope images included in this thesis were procured by Dr Reza Kashtiban.

2.2.5.1 Scanning Electron Microscopy

Scanning electron microscopy (SEM) images were used for studying bulk particle morphology, and were recorded using a Zeiss SUPRA 55VP FEG instrument with a working distance of 3 mm.

2.2.5.2 Transmission Electron Microscopy

Transmission electron microscopy (TEM) was used for examining particle morphology, observing secondary phases, and obtaining localised energy dispersive X-ray (EDX) spectra.

For TEM, samples were dispersed onto lacy carbon film reinforced on a copper grid from a suspension produced ultrasonically in methanol. Images and (EDX) spectra were recorded using a JEOL 2100 LaB_6 instrument operating at 200 kV equipped with an EDAX Genesis system.

2.2.5.3 Scanning Transmission Electron Microscopy

Scanning transmission electron microscopy (STEM) was used to obtain atomic resolution images.

A 3^{rd} order aberration corrected (C_3) JEOL ARM200F operating at 200 kV was used to acquire atomic resolution high-angle annular dark-field (HAADF) and annular bright-field (ABF) images.

2.2.5.4 Electron Energy Loss Spectroscopy

Electron energy loss spectroscopy (EELS) was used to study the distribution of metals within their crystal structures.

Measurements were performed at the SuperSTEM facility, Daresbury, U.K., using a Nion Ultrastem® 100 microscope with cold field emission gun operating at 100 kV. The microscope is 5^{th} order aberration corrected (C_5) giving a low energy spread of 0.3 eV, desirable for EELS.

Elemental maps were produced through integration of EELS edges after background subtraction, using ImageJ implemented with the Cornell Spectrum Imaging (CSI)

plugin.[45] Where the signal-to-noise is low, a background using a liner combination of power laws (LCPL) was subtracted, in place of using the conventional power-law background subtraction.

Dr Demie Kepaptsoglou and Professor Quentin Ramasse operated the microscope and obtained the images and spectra shown in this thesis.

2.2.6 Raman Spectroscopy

Bearing the name of its discoverer, Sir Chandrasekhara Raman, the phenomenon of Raman scattering was first observed in 1928 and is a powerful technique used to study the structures of materials.[46] The effect relies upon the inelastic scattering of monochromatic light incident on a sample. The majority of the incident light is scattered from elastic processes, known as Rayleigh scattering, however there are weak inelastic interactions that can provide chemical and structural information on the material under study. These inelastic components scatter light of a lower and higher frequency than the incident beam, and are known as Stokes and anti-Stokes lines, respectively. This process, displayed in Figure 2.17, shows that the frequency shift of the Stokes and anti-Stokes features is a direct relation to the vibrational energies of the material.[47]

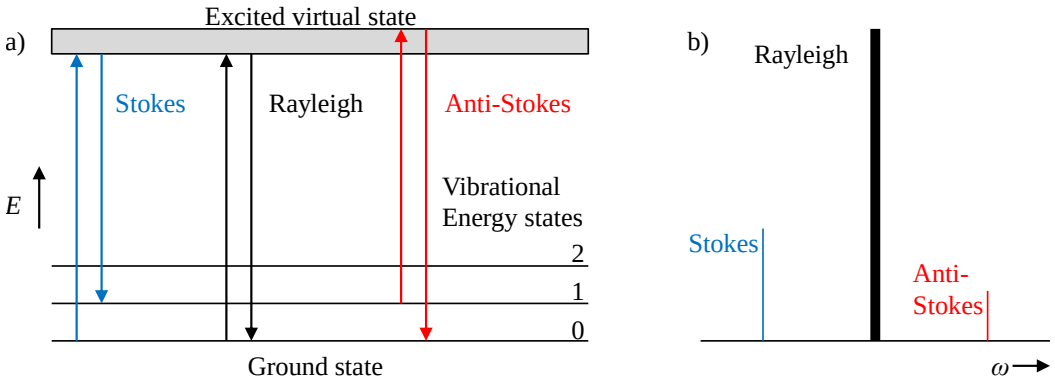

Figure 2.17: a) Simplistic energy level diagram illustrating the differences between Rayleigh, Stokes, and anti-Stokes scattering. b) Raman spectrum that shows these three types of scattering.

Typically a sample is illuminated by a laser beam of chosen wavelength such to minimise fluorescence from the sample. Scattered light of wavelengths close to the laser line resulting from Rayleigh interactions are ultimately filtered out, and it is the Stokes components showing the shift away from the incident wavelength that are measured and used to acquire the final spectrum displayed in wavenumbers (ω).[48]

2.2.6.1 Measurements under ambient conditions

Room temperature Raman spectra were collected using a Renishaw inVia Raman Microscope with a spectral cutoff of $\sim$ 120 cm^{-1}. The microscope was equipped with a Leica N Plan 50x/0.75 BD objective, and measurements were recorded in backscattering geometry. The laser used to study rare-earth orthochromites, chosen to minimise fluorescence from the sample, was a He-Ne laser of excitation wavelength 632.8 nm. Experiments were carried out using a laser power of 1 mW focused into a $\sim$ 1 μm^2 spot, to avoid local heating of the polycrystalline samples by the laser.

A few of the Raman spectra presented in this thesis were recorded by Mads Weber using an instrument at the Départment Sciences et Analyses des Matériaux, CRP Gabriel Lippmann, Luxembourg. This instrument is similar to the one described above and makes use of the same excitation wavelength, but has a much lower spectral cutoff of $\sim$ 10 cm^{-1}, useful for the observation of low wavenumber phonon modes, as will become clear in subsequent chapters of this thesis.

Phonon mode positions and line widths were extracted from the Raman spectra through profile fitting, performed using Wire 3.3 software. The spectra were fitted with an adequate number of separate modes that use a pseudo-Voigt function to describe peak shape.

2.2.6.2 Measurements under non-ambient conditions

Low-temperature measurements were performed to reduce thermal broadening of bands and allow the broadening due to static disorder be studied. For low temperature measurements, powders were placed in a Linkam THMS 600 sample stage and cooled to 123 K under liquid nitrogen. Long exposure times (30 minutes) were required to obtain data of good statistical quality. Owing to the increased working distance, a long focal length Olympus LMPlanFL 20x/0.40 objective was used.

For temperature-dependent measurements, spectra were recorded in steps of 10 K whilst warming over the temperature range of 113 to 333 K.

2.2.6.3 Shell model calculations

The shell model calculations included in this thesis were performed by Dr Mael Guennou (based at Départment Sciences et Analyses des Matériaux, CRP Gabriel Lippmann, Luxembourg).

Shell model calculations were performed using the program GULP,[49] on the series of

rare-earth orthochromites $La_xSm_{1-x}CrO_3$. The A and B site cations are represented by point cores carrying a charge Z, and the O^{2-} ions are represented as a charged core linked to a massless shell with charge Y through a spring constant k, which accounts for free ion polarisability. The calculations take into account the long-range Coulomb interactions between ions as well as a short-range repulsive potential energy, modelled by a Buckingham interatomic potential using a spherical cut-off radius of 12 Å, described in Equation 2.28.

$$V(r) = A\exp\left(\frac{-r}{\rho}\right) - \frac{C}{r^6} \tag{2.28}$$

Where A and ρ are constants specific to each ion pair obtained through fitting the available structural data, and C is a constant.

The Buckingham potential describes the exchange repulsion between ions and consists of an attraction and a repulsion term. For cation-anion short-range interactions, usually there is no attractive part so C becomes zero. The simulation of the $La_xSm_{1-x}CrO_3$ solid solutions (described in Chapter 4) follow a virtual ion approach and assume a random distribution of the A site cations.

2.2.7 X-ray Absorption Near-Edge Structure

X-ray absorption near-edge structure (XANES) spectroscopy was performed to determine the oxidation states of metals present in the complex oxides presented in this thesis. Experiments were performed on beamline B18 at the Diamond Light Source, with the assistance of Dr Giannantonio Cibin and Dr Silvia Ramos.[50] The double-crystal monochromator and collimating mirrors on the beamline provide a highly monochromatic and collimated X-ray beam whilst maintaining a high level of flux.

Powders, typically $\sim$ 12 mg once absorbance had been taken into account, mixed with $\sim$ 100 mg polyethylene binder, were ground in acetone until homogeneous mixture was achieved, and the solvent had evaporated off. The mixtures were pressed into 13 mm diameter pellets of thickness $\sim$ 1 mm.

Data were collected in transmission mode at edge energies of several metals, such as Cr, Mn, Fe, and Bi. Data were normalised by subtracting linear pre-edge and polynomial post-edge backgrounds using the software Athena.[51]

2.2.8 Mössbauer Spectrometry

The Mössbauer data presented in this thesis were collected as part of a collaboration with Dr Jean-Marc Grenèche based at the Institut des Molécules et des Matériaux du Mans, at the Université du Maine, France.

^{57}Fe Mössbauer spectrometry was performed using a conventional constant acceleration transmission spectrometer with a ^{57}Co radioactive source diffused into a rhodium matrix. Spectra were recorded at 300 and 77 K using a bath cryostat, and were fitted using the MOSFIT program,[52] using a discrete distribution of magnetic sextets and/or quadrupolar doublets based on lines with Lorentzian profiles. An α-Fe foil was used as the calibration sample, and isomer shifts are quoted relative to that of the α-Fe at 300 K.

2.2.9 Compositional Analysis

2.2.9.1 X-ray Fluorescence

X-ray Fluorescence (XRF) makes use of the same elemental phenomena as EDX, except it utilises high-energy X-rays as the excitation source in place of electrons. X-ray fluorescence spectroscopy was performed using a Panalytical Epsilon 3^{XL} energy dispersive X-ray fluorescence spectrometer with an X-ray tube operating at 50 kV and a silicon drift detector.

2.2.9.2 Inductively Coupled Plasma Optical Emission Spectroscopy

The relative compositions of metals were accurately determined using inductively coupled plasma optical emission spectroscopy (ICP-OES). This was performed by the external company MEDAC Ltd.

2.2.10 Thermal Analysis

For the work described in this thesis, thermogravimetric analysis (TGA) was used largely to determine the water content of reactants used in hydrothermal synthesis, and the resultant samples. Occasionally, differential scanning calorimetry (DSC) was used to accurately determine a transition or decomposition temperature.

Thermal analysis was performed using alumina crucibles under a constant flow of air or N_2 (50 ml/minute) on a Mettler Toledo Systems TGA/DSC 1 instrument. A typical experiment involved recording data from room temperature up to 1000 °C at a rate of 10 °C/minute.

2.2.11 Infrared Spectroscopy

Infrared spectroscopy was used to investigate the presence of water in a few materials in this thesis, made through the hydrothermal method.

Fourier transform infrared (FT-IR) spectra were recorded on a Bruker alpha platinum ATR-IR instrument. Each spectrum was collected over a wavenumber range of 450 to 4000 cm^{-1} and is the average of 32 measurements at 4 cm^{-1} resolution.

2.2.12 Pycnometry

Acquisition of the measured densities was essential for certain materials included in this thesis; firstly for comparison with the calculated densities from the solved crystal structures, and secondly for the determination of the function $T^0(r)$, useful in the analysis of total scattering data.

Densities of polycrystalline powders were measured using a Quantachrome Micropycnometer. Identical preparation conditions to the neutron scattering measurements were used, where the powders were placed in a vacuum oven at 80 °C to drive of residual moisture before measurement. The powders were purged under a constant flow of helium for fifteen minutes, and measurements were taken until six consecutive pressure readings (P_1/P_2) had stabilised within agreement of 0.001.

2.3 Material Property Investigation

2.3.1 Magnetic Measurements

Magnetisation data were collected using a Quantum Design Magnetic Property Measurement System (MPMS-5S) superconducting quantum interference device (SQUID) magnetometer. Powder samples (approx. 20 mg) were held in gel capsules inside the instrument and data were collected both on warming and on cooling over the temperature range of 2-400 K, whilst under applied magnetic fields of various magnitudes. Hysteresis loops were recorded at sample-specific temperatures in applied magnetic fields up to 50 kOe.

2.3.2 Physical Property Measurements

2.3.2.1 Pyroelectric Current and Electric Polarisation

Pyroelectric measurements were carried out with the assistance of Dr Martin Lees using a Quantum Design Physical Property Measurement System (PPMS), with a Keithley 6517A electrometer and Agilent 4294A precision impedance analyser. The $La_{0.25}Sm_{0.75}CrO_3$ powder was pressed into a pellet and sintered at 1000 °C before the measurements were made. The material was poled at room temperature in applied electric fields of +1.89 and –1.89 kV cm^{-1}, before being cooled to 10 K with the field still applied. The field was turned off, and the circuit allowed to short, before the pyroelectric current was measured on warming to room temperature. The electric polarisation was obtained by integrating the pyroelectric current with respect to time and dividing it by the sample area.

2.3.2.2 Heat Capacity

Specific heat data were collected with the assistance of Dr Martin Lees using a Quantum Design PPMS. Powders were pressed into pellets and cut into thin plates approximately $3 \times 3 \times 0.7$ mm^3, weighing 20-30 mg. Data were collected on warming from 1.85 K to 290 K whilst under applied magnetic fields of various magnitudes.

References

[1] K. Byrappa and M. Yoshimura, *Handbook of Hydrothermal Technology*, Noyes Publications: Park Ridge, New Jersey, USA, 2001.

[2] G. W. Morey and P. Niggli, *J. Am. Chem. Soc.*, 1913, **35**, 1088.

[3] A. Rabenau, *Angew. Chem. Int. Ed.*, 1985, **24**, 1026.

[4] R. E. Riman, W. L. Suchanek and M. M. Lencka, *Ann. Chim. Sci. Mat.*, 2002, **27**, 15.

[5] S. Sōmiya and R. R., *Bull. Mater. Sci.*, 2000, **23**, 453.

[6] D. R. Modeshia and R. I. Walton, *Chem. Soc. Rev.*, 2010, **39**, 4303.

[7] T. Adschiri, Y.-W. Lee, M. Goto and S. Takami, *Green Chem.*, 2011, **13**, 1380.

[8] E. Lester, P. Blood, J. Denyer, D. Giddings, B. Azzopardi and M. Poliakoff, *J. Supercrit. Fluids*, 2006, **37**, 209.

[9] P. S. Devi, *J. Mater. Chem.*, 1993, **3**, 373.

[10] International Union of Crystallography, *Acta Cryst. A*, 1992, **48**, 922.

[11] M. Etter and R. E. Dinnebier, *Z. Anorg. Allg. Chem.*, 2014, **460**, 3015.

[12] W. L. Bragg, *Proceedings of the Cambridge Philosophical Society*, 1913, **17**, 43.

[13] L. E. Smart and E. A. Moore, *Solid State Chemistry: An Introduction*, CRC Press Taylor & Francis Group, Boca Raton, USA, 3rd Ed., 2005.

[14] J. Chadwick, *Nature*, 1932, **129**, 312.

[15] E. O. Wollan and C. G. Shull, *Phys. Rev.*, 1948, **73**, 830.

[16] V. F. Sears, *Neutron News*, 1992, **3**, 26.

[17] G. L. Squires, *Introduction to the Theory of Thermal Neutron Scattering*, Cambridge University Press, Cambridge, U.K., 2012.

[18] D. S. Sivia, *Elementary Scattering Theory*, Oxford University Press, Oxford, U.K., 2011.

[19] *Principles and Applications of Powder Diffraction*, ed. A. Clearfield, J. Reibenspies and N. Bhuvanesh, Wiley-Blackwell, New Jersey, USA, 2008.

[20] H. M. Rietveld, *J. Appl. Cryst.*, 1969, **2**, 65.

[21] R. A. Young, *The Rietveld Method*, Oxford University Press, Oxford, U.K., 1993.

[22] S. Ikeda and J. M. Carpenter, *Nucl. Instrum. Methods Phys. Res., Sect. A*, 1985, **239**, 536.

[23] A. C. Hannon, *Nucl. Instrum. Methods Phys. Res., Sect. A*, 2005, **551**, 88.

[24] A. A. Coelho, *J. Appl. Cryst.*, 2000, **33**, 899.

[25] A. A. Coelho, *TOPAS Academic - Technical Reference, Version 4.1*, 2007.

[26] M. Ladd and R. Palmer, *Structure Determination by X-ray Crystallography*, Springer, London, U.K., 5th Ed., 2013.

[27] G. S. Pawley, *J. Appl. Cryst.*, 1981, **14**, 357.

[28] L. B. McCusker, R. B. Von Dreele, D. E. Cox, D. Louër and P. Scardi, *J. Appl. Cryst.*, 1999, **32**, 36.

[29] A. C. Hannon, D. Di Martino, L. F. Santos and R. M. Almeida, *J. Phys. Chem. B*, 2007, **111**, 3342.

[30] A. K. Soper, *GudrunN and GudrunX: programs for correcting raw neutron and X-ray diffraction data to differential scattering cross section*, Rutherford Appleton Laboratory technical report, RAL-TR-2011-013, 2011.

[31] X. Qui, E. S. Božin, J. Pavol, T. Proffen and S. J. L. Billinge, *J. Appl. Cryst.*, 2004, **37**, 110.

[32] S. J. Hibble, A. C. Hannon and I. D. Fawcett, *J. Phys.: Condens. Matter*, 1999, **11**, 9203.

[33] J. Waser and V. Schomaker, *Rev. Modern Phys.*, 1953, **25**, 671.

[34] E. Lorch, *J. Phys. C.: Solid State Phys.*, 1969, **2**, 229.

[35] A. K. Soper and E. R. Barney, *J. Appl. Cryst.*, 2012, **45**, 1314.

[36] D. A. Keen, *J. Appl. Cryst.*, 2001, **34**, 172.

[37] A. C. Hannon, in *Modern Glass Characterisation*, ed. M. Affatigato, John Wiley & Sons Ltd,

New York, 1st Ed., 2015, In Press.
[38] A. C. Hannon, *XTAL: A Program for Calculating Interatomic Distances and Coordination Numbers for Model Structures*, Rutherford Appleton Laboratory technical report, RAL-93-063, 1993.
[39] C. L. Farrow, P. Juhas, J. W. Liu, D. Bryndin, E. S. Božin, J. Bloch, T. Proffen and S. J. L. Billinge, *J. Phys.: Condens. Matter*, 2007, **19**, 335219.
[40] R. L. McGreevy, *J. Phys.: Condens. Matter*, 2001, **13**, R877.
[41] H. Y. Playford, L. R. Owen, I. Levin and M. G. Tucker, *Annu. Rev. Mater. Res.*, 2014, **44**, 429.
[42] M. G. Tucker, D. A. Keen, M. T. Dove, A. L. Goodwin and Q. Hui, *J. Phys.: Condens. Matter*, 2007, **19**, 335218.
[43] S. T. Norberg, M. G. Tucker and S. Hull, *J. Appl. Cryst.*, 2009, **42**, 179.
[44] N. E. Brese and M. O'Keeffe, *Acta Cryst. B*, 1991, **47**, 192.
[45] P. Cueva, R. Hovden, J. A. Mundy, H. L. Xin and D. A. Muller, *Microsc. Microanal.*, 2012, **18**, 667.
[46] C. V. Raman and K. S. Krishnan, *Nature*, 1928, **121**, 501.
[47] J. R. Ferraro, K. Nakamoto and C. W. Brown, *Introductory Raman Spectroscopy*, Academic Press, Amsterdam, 2nd Ed., 2003.
[48] D. A. Long, *The Raman Effect: A Unified Treatment of the Theory of Raman Scattering by Molecules*, John Wiley & Sons Ltd, Chicester, U.K., 2002.
[49] J. D. Gale and A. L. Rohl, *Molecular Simulation*, 2003, **29**, 291.
[50] A. J. Dent, G. Cibin, S. Ramos, A. D. Smith, S. M. Scott, L. Varandas, M. R. Pearson, N. A. Krumpa, C. P. Jones and P. E. Robbins, *J. Phys. Conf. Ser.*, 2009, **190**, 012039.
[51] B. Ravel and M. Newville, *J. Synchrotron Radiat.*, 2005, **12**, 537.
[52] F. Varret and J. Teillet, *unpublished*, MOSFIT Program; 1976.

Chapter 3

Studies of New Metastable Bismuth-Iron-Manganese Pyrochlores

3.1 Background

The chemistry of materials containing Bi^{3+} is interesting due to the non-bonding $6s^2$ electron lone pair that gives the cation an asymmetric coordination environment in many structures,[1,2] shown in Figure 3.1. The strong antibonding interaction between the $6s$ electrons and the filled $2p$ orbital of the oxygen results in 6s-6p hybridisation, driving down the energy of the $6s$ band. This hybridisation causes the lone pair to lose its spherical symmetry and projects it to one side of the cation resulting in a low symmetry environment for Bi^{3+}, often leading to unique properties. For example, the huge 1 S cm^{-1} ionic conductivity of the high temperature δ-phase of Bi_2O_3,[3] whose structure is based on a cubic fluorite unit cell,[4] is attributed to the intrinsic anion vacancies and off-centring of Bi^{3+} cations, which reduce the energy barriers involved in oxide ion mobility.[5]

Although there are many interesting materials that contain bismuth, the two most relevant to this work are the perovskites, $BiFeO_3$ (BFO) and $BiMnO_3$ (BMO). These both receive increased attention due to the multiferroic properties they exhibit, which are driven by the distortion mechanisms that were described in Chapter 1. The stereochemical activity of the lone pair on Bi^{3+} and Jahn-Teller interactions of Mn^{3+} in the case of BMO, give rise to the polarisability of these materials, whilst the presence of transition metals with partially-filled d orbitals on the B site leads to the magnetic properties that they exhibit.

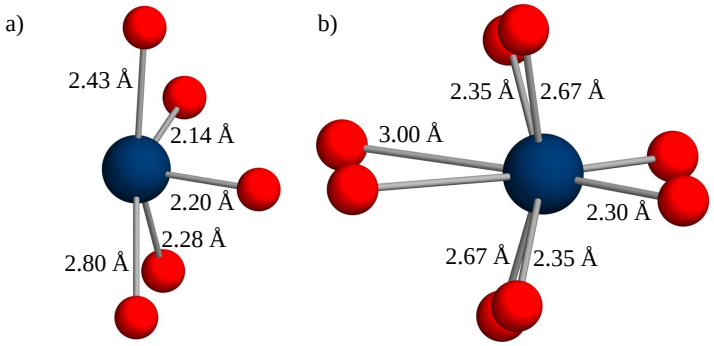

Figure 3.1: Asymmetric coordination of Bi^{3+} in a) α-Bi_2O_3, and in the eight-coordinate A site of stoichiometric pyrochlore $Bi_2Ti_2O_7$.

Although iron and manganese are neighbours in the Periodic Table, the properties and structures of oxides of the two vary greatly, with BFO and BMO adopting rhombohedral and monoclinic distorted perovskite structures, respectively.[6,7] The A site Bi^{3+} in both is displaced off-centre, such that it is coordinated by a lower number of oxide ions compared to the ideal ABO_3 structure, whilst there is extra distortion resulting from the Jahn-Teller effects of Mn^{3+}, which are absent for BFO, with the possibility also for oxygen nonstoichiometry in BMO.[8]

Because of their functionalities, the syntheses of these materials have been extensively explored; bismuth ferrite readily crystallises under mild hydrothermal conditions through reaction of metal nitrates in basic solution at 200 °C,[9] bypassing the problematic volatility of bismuth encountered through conventional solid state methods. The conventional technique results in the production of impurity phases, such as $Bi_2Fe_4O_9$ and $Bi_{25}FeO_{40}$, that are only removed through acid leaching.[10] The hydrothermal method also allows for a degree of control over the particle morphology, with nanowires,[11] millimetre-scale cubes,[7] and micron-scale spheres of $BiFeO_3$ being reported, depending upon the synthesis conditions and mineraliser used.[12,13]

In comparison, the formation of BMO is not possible through hydrothermal synthesis, and instead requires high-pressure solid state synthesis. This can result in either oxygen excess or deficiency, giving $BiMnO_{3\pm\delta}$, which ultimately can be detrimental to the properties of the material.[8,14]

Attempted syntheses of $BiFe_{1-x}Mn_xO_3$ solid solutions have been reported with ambiguous results. Some studies report the presence of impurity phases above $x = 0.2$,[6,15–17] whilst others produce phase-pure samples up to $x = 0.4$.[18] All of the studies suggest that the $R3c$ structure of $BiFeO_3$ is maintained up to $x = 0.4$,[19,20]

however, a more complete study of the entire solid solution was performed by Azuma *et al.*,[21] which showed that a new metastable orthorhombic phase is produced for solid solutions in the range of $0.2 \leq x \leq 0.6$, whilst the monoclinic structure of $BiMnO_3$ is yielded above $x = 0.6$. Overall, most of the studies show that the magnetic, and on occasion, both the dielectric and leakage current properties, were improved through the addition of manganese to BFO. Interestingly, Belik *et al.*[22] show that the precise structure of this compositional range is determined by the pressure at which the material is synthesised. For solid solutions produced under high pressure (6 GPa and 1400 K, sealed in Au capsules) an orthorhombic *Pnma* structure is adopted above $x = 0.1$, whilst samples made at ambient pressure retain the rhombohedral BFO-type structure up to $x = 0.25$. The magnetic properties were shown to be starkly different for both ambient- and high-pressure phases.

The hydrothermal chemistry of bismuth-containing oxides has been studied with the production of several different pyrochlore phases such as $Na_{0.32}Bi_{1.68}Ti_2O_{6.46}(OH)_{0.44}$,[23] and $Bi_2Sn_2O_7$.[24,25] The precursor sodium bismuthate ($NaBiO_3$), containing Bi^{5+}, has been used to form bismuth-containing pyrochlores, acting as an oxidiser and leading to interesting hydrothermal chemistry. The hydrothermal synthesis of bismuth-titanium oxides has been well explored with the reaction of $NaBiO_3$ and TiO_2 under aqueous basic conditions, resulting in the formation of $Bi_{1.43}Ti_2O_6(OH)_{0.29}$.[26] It is possible to form the stoichiometric $Bi_2Ir_2O_7$ pyrochlore through a single-step reaction under similar conditions, providing a novel route to the robust oxygen evolution catalyst.[27] Hydrothermal syntheses of bismuth pyrochlores have often resulted in phases that contain mixed valence Bi^{3+} and Bi^{5+} on the A and B sites of the structure, respectively, regardless of the oxidation state of the bismuth precursor. For example, $(K_{1.14}Bi^{3+}_{0.37}\square_{0.49})(Bi^{3+}_{0.27}Bi^{5+}_{1.73})O_{5.7}(OH)_{0.3}$ was made from Bi^{3+} reagents, whilst $(Na_{0.39}Bi^{3+}_{1.45}\square_{0.16})(Bi^{3+}_{0.37}Bi^{5+}_{1.63})O_7$ was made from Bi^{5+}, with $\square$ representing cation vacancies.[28,29] This suggests that the mild chemistry from hydrothermal conditions, along with the possibility of adding oxidising or reducing agents, have a significant influence the resulting oxidation states. The use of $NaBiO_3$ has also resulted in mixed-valence bismuth pyrochlores that are doped with small amounts of group II metals.[30]

The oxidising properties of $NaBiO_3$ are utilised in the formation of the layered bismuth manganese oxynitrate material $Bi_3Mn_4O_{12}(NO_3)$; one of the few reports of a material containing bismuth and manganese being produced from

hydrothermal synthesis.[31]

Many bismuth-containing pyrochlore oxides have properties that are potentially useful for application, with the most widely studied being the $(Bi,Zn)_2(Zn,Nb)_2O_7$ or BZN ceramics described in Chapter 1. There are several other examples that show interesting properties. It is possible to tune the band gap of Bi_2InNbO_7, when substituting the In^{3+} by Fe^{3+}, causing it to exhibit photocatalytic behaviour under UV irradiation.[32] These photocatalytic properties were explored further in Bi_2MNbO_7 pyrochlores (where M = Al, Fe, In, Sm), which were prepared by the sol-gel method, and exhibit greater activity over the established TiO_2 catalyst towards the photodegradation of methylene blue dye.[33] An in-depth structural study showed that the iron-containing analogue of these photocatalysts contains a considerable level of disorder, as well as the mixing of iron across both the A and B sites.[34] It is likely this disorder is the reason that the material is better than TiO_2 at photocatalysing the degradation of methyl orange dye.[35] In the form of thin films, $Bi_2Ti_2O_7$, with high permittivity and low leakage current, can be used to improve the electrical properties of the ferroelectric Aurivillius phase of $Bi_4Ti_3O_{12}$.[2,36]

The increased static disorder from the Bi^{3+}, as well as the random distribution of transition metals across both the A and B sites, lead to frustrated magnetic states in several bismuth-containing pyrochlores. This increased disorder is additional to the geometrical frustration often exhibited by pyrochlore systems. Several mixed-metal pyrochlores such as $(Bi_{1.89}Fe_{0.11})(Fe_{1.05}Nb_{0.95})O_7$ and $(Bi_{1.88}Fe_{0.12})(Fe_{1.42}Te_{0.58})O_{6.87}$ exhibit the spin-glass-like magnetic behaviour that is characteristic of many pyrochlores.[37] Occasionally, the mixture of metals produces both ferro- and antiferromagnetic interactions, and it is the interplay between these that results in the absence of long-range magnetic ordering.[38]

The Reverse Monte Carlo (RMC) method is a technique of modelling disordered crystalline structures that has been previously applied to many complex oxides, due to knowledge of the local structure being necessary to understanding their properties.[39]

For example, the results of RMC simulations alluded to the understanding of why δ-Bi_2O_3 displays one of the highest known oxide-ion conductivities.[40] Previous vacancy-pair models, based on study of the average structure, inadequately described the local disorder; the local environments of Bi^{3+} are 5-coordinate like those of the α-polymorph, rather than the expected eight-coordinate geometry of the fluorite structure.[1,41] The study of a large configuration showed that each of

the distorted local environments of Bi^{3+} are randomly oriented to one another, such that the average long-range structure, determined through diffraction, is cubic.

In ferroelectric $Na_{0.5}Bi_{0.5}TiO_3$ perovskites, RMC revealed that the local environments of sodium and bismuth were dissimilar with different displacements, despite diffraction-based techniques placing them upon the same site.[42,43] This proved critical to understanding their properties, and is applicable to our current study, as both pyrochlores contain alkali metals and bismuth cations on the same crystallographic position.

A study performed by Shoemaker *et al.*,[44] displayed the extent of disorder on the A_2O' network in the $Bi_2Ti_2O_7$ pyrochlore. Probability densities produced from RMC simulations showed that bismuth atoms form hollow rings around the ideal site, and the O' atoms are distributed in a tetrapod-like shape centred on the ideal position. These distributions resulted from the preferential "zig-zag" arrangements of neighbouring bismuth atoms along the A_2O' chains. When compared to the structure of $Bi_2Ru_2O_7$, similar displacements were found, but of much smaller magnitude, resulting in ellipsoids around the A site.[45] No relationship was found between neighbouring bismuth atoms in $Bi_2Ru_2O_7$, with the displacements driven solely by steric requirements of the $6s^2$ electron lone pair.

3.1.1 Scope of this chapter

This chapter reports the synthesis of two new metastable pyrochlore phases, by using mild hydrothermal chemistry. Detailed study of these new materials is described using traditional diffraction, as well as total scattering techniques that provide insight into the local structure. The thermal and magnetic properties of the pyrochlores were also explored.

The time-averaged structures were solved using simultaneous Rietveld analysis of both X-ray and time-of-flight neutron diffraction data, and are supported by data from several complementary techniques.

The short-range structures of these pyrochlores were examined through total scattering techniques, probing the local disorder present in these systems. RMC analysis is used in order to accurately model this short-range disorder.

An investigation into the magnetic properties of these pyrochlores is presented in order to examine the effects that the metal-mixing and disorder have on the spin interactions.

3.2 Synthesis

The hydrothermal synthesis of Bi-Fe-Mn pyrochlores were performed in Teflon®-lined stainless-steel autoclaves with internal volumes of approximately 20 ml. Sodium bismuthate(V) dihydrate (0.5000 g, 85% Acros Organics), iron(III) nitrate nonahydrate (0.3306 g, 98% ACS reagent grade), and manganese(II) chloride tetrahydrate (0.0313 g, 99% Alfa Aesar) were dissolved into 8 ml of ultra-pure water in molar ratios of 1:0.5:0.1, respectively. This molar ratio was optimised after performing several syntheses, which will be discussed further into this chapter. The level of hydration of the starting materials was verified using TGA prior to synthesis. Pellets of sodium (1.28 g) or potassium (1.79 g) hydroxide (analytical grade) of sufficient quantity to give concentrations of 4.0 M were added to the solutions, before stirring for 15 minutes. The reactions were then sealed inside the autoclaves and placed inside preheated forced-air ovens (Genlab MINO/40) at 200 °C for a period of 6 hours, before being removed and allowed to cool naturally to room temperature. The brown polycrystalline powders were collected via suction filtration after being washed several times with deionised water, and dried at 75 °C in air for characterisation.
Typical product masses were $\sim$ 0.42 g, which corresponds to a 92% yield.

3.2.1 Synthesis of XANES Reference Materials

Several oxide materials containing bismuth or iron of known oxidation state were synthesised as reference materials for XANES measurements.

Bismuth ferrite ($BiFeO_3$), used as a reference for both Bi^{3+} and Fe^{3+}, was synthesised hydrothermally following the reported method of Chen *et al.*[9] Bismuth(III) nitrate pentahydrate (0.5000 g, 98%+ A.C.S. reagent grade) and iron(III) nitrate nonahydrate (0.4168 g, 98%+ A.C.S. reagent grade) were dissolved into a 4.0 M solution of potassium hydroxide (1.3347 g in 6 ml water). The slurry was stirred for 15 minutes before being sealed in a Teflon®-lined stainless-steel autoclave and heated to 200 °C for 6 hours. The only difference between the synthesis here and that reported by Chen *et al.*, is that stirring was used rather than ultrasonic dispersion, before the solutions were heated in the autoclave.

The Bi_2O_4 bismuth oxide was used as a mixed valence Bi^{3+}/Bi^{5+} reference material, and was synthesised following the reported hydrothermal method of Kumada et al.[46] The dissolution of an equimolar ratio of sodium bismuthate(V)

dihydrate (1.0000 g, 85% Acros Organics) and sodium nitrate (0.3027 g, minimum 99% Sigma) into deionised water, and heating to 140 °C inside an autoclave for a period of 4 days resulted in the formation of Bi_2O_4. The material is slightly impure with the high-temperature phase of δ-Bi_2O_3 as a secondary phase, consistent with the synthesis of Kumada *et al.*[46] A multiphase Reitveld refinement of PXRD data, shown in Figure 3.2, was used to determine accurately the ratio of the two phases, and therefore the average oxidation state of the mixture. The amount of product produced ($\sim$ 0.7 g) corresponds to a percentage yield of 81%.

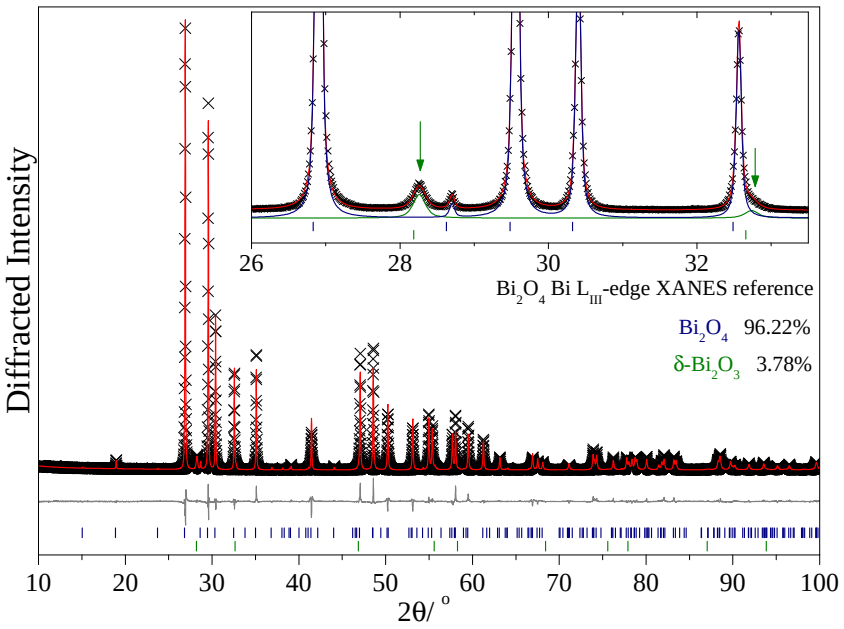

Figure 3.2: Multiphase Rietveld refinement against PXRD data of the Bi_2O_4 reference material. The inset shows the δ-Bi_2O_3 secondary phase in greater detail. Observed (black crosses), calculated (red line), and difference (grey line) patterns are shown, whilst contributions from Bi_2O_4 and δ-Bi_2O_3 are shown separately by blue and green lines or tick marks, respectively.

The refinement showed that the mixed powder consists of approximately 96% Bi_2O_4 and 4% of δ-Bi_2O_3, giving an average bismuth oxidation state in the powder of +3.96. The analysis of Bi L_{III}-edge XANES data discussed later in this chapter is based upon this value.

3.3 Results and Discussion

A successful hydrothermal method has been developed for the production of some new cubic pyrochlore oxides that contain bismuth, iron, and manganese. These

combinations of metals in the pyrochlore structure have not previously been reported in the literature.

The syntheses were optimised such that the single-phase pyrochlores formed in solutions of 4.0 M hydroxide concentration, that were heated to 200 °C for durations of 6 hours. Variations from these optimal conditions resulted in the production of secondary phases as impurities. For the pyrochlore made in NaOH, Figure 3.3 shows that solution concentrations and reaction temperatures above or below 4.0 M and 200 °C, respectively, as well as synthesis durations longer than 6 hours lead to the formation of $BiFeO_3$ and $Bi_{12}MnO_{20}$/$Bi_{25}FeO_{40}$ (sillenite) as impurity phases.

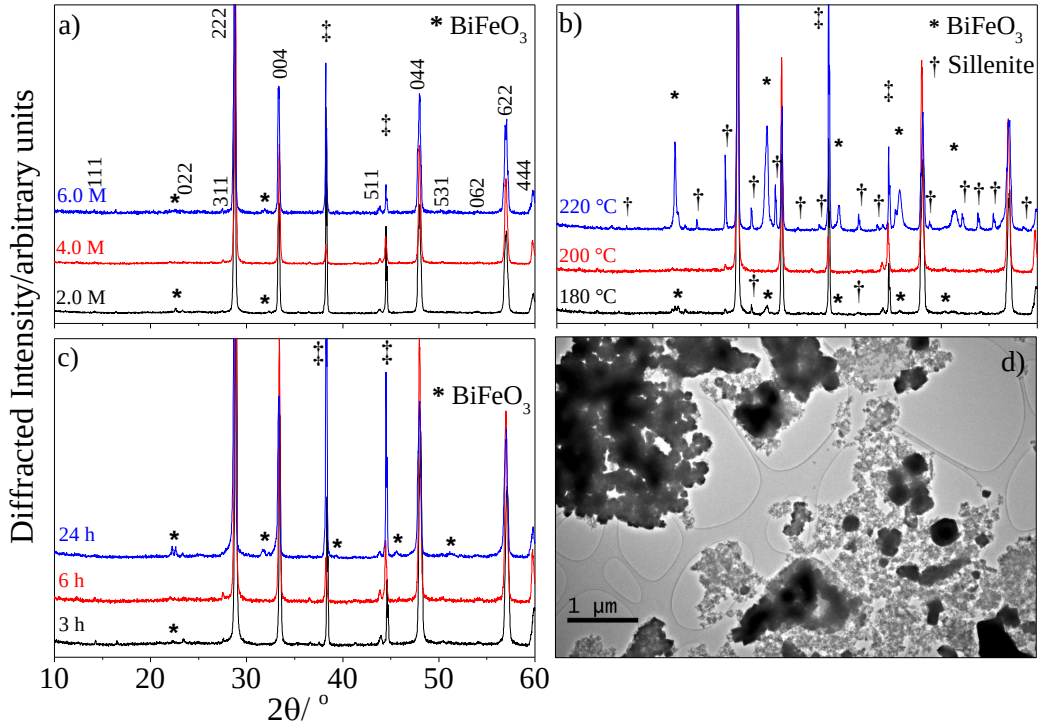

Figure 3.3: Effect of various reaction conditions on final product of pyrochlore phase made in NaOH solution. Influence of mineraliser solution concentration at 200 °C for 6 hours is shown in a), the variation in temperature in 4 M solutions for 6 hours is shown in b), whilst c) displays different synthesis durations of 4 M solutions at 200 °C. The ‡ symbol indicates aluminium reflections from the sample holder. A TEM image d) of the crystallites formed under optimum conditions.

Also shown in Figure 3.3 is a TEM image of the particles formed under such conditions. The dense octahedral shaped particles correspond to the pyrochlore phase, whilst it is always accompanied by a secondary phase shown as the

amorphous flaky phase around the bottom-right of the image. It was found that this secondary phase, not observed by XRD and only under the electron microscope, could be removed if the molar ratio of Bi:Fe:Mn was altered from the original 1:0.5:0.5. Thus, reduction of the manganese content in the synthesis, giving 1:0.5:0.1 minimised the production of this secondary amorphous phase. When using the original molar ratio, it was also noted that the post-reaction filtrate was always intense green in colour, suggesting that excess manganese remains in the solution as the MnO_4^{2-} manganate(VI) ion. The reduction in manganese content lead to the post-reaction filtrate being colourless, indicating that the manganese reagent was engaged in the reaction. The above observations suggest that there is a limit to the concentration of manganese in these pyrochlores.

During the synthesis optimisation of these pyrochlore phases, it was possible to produce the same pyrochlore phases by using different reagents. Potassium permanganate(VII) can be used as the oxidising agent alongside bismuth(III) nitrate pentahydrate, however, using sodium bismuthate(V) results in "cleaner" products with regards to the flaky amorphous phase observed by electron microscopy.

3.3.1 General Characterisation

3.3.1.1 Powder X-ray and Neutron Diffraction

It is possible to produce two different pyrochlore phases depending upon the alkali metal hydroxide used as the mineraliser in the synthesis. A slight shift is observed between the peak positions of pyrochlores produced in NaOH and KOH, with peaks being shifted to slightly lower 2θ values for the latter, as can be seen in Figure 3.4 a). Through refinement, a larger lattice parameter is therefore observed for the pyrochlore made in KOH of $a = 10.70849(12)$ Å, compared to the phase made in NaOH with $a = 10.6947(3)$ Å. The only difference between the synthesis of two phases are the hydroxide solutions, indicating that the alkali metals may actually be present in the structure of the pyrochlore and influencing the size of the unit cell. The observed change in lattice parameter is consistent with the presence of the larger K^+ ion in the structure, with K^+ and Na^+ having dramatically different ionic radii of 1.51 and 1.18 Å, respectively, expected for the eight-coordinate environment of the A site.[47] These results imply that the alkali metals may actually be necessary to the synthesis and are required for each pyrochlore phase to form. In order to test this hypothesis, syntheses were performed in water as well as another basic

solution that didn't contain alkali metal cations, such as ammonium hydroxide. No crystalline products were observed from the reactions performed in water, whilst the results of the synthesis in ammonia are shown in Figure 3.4 b). A mixture of several phases was produced, and no pyrochlores form under such conditions. The observed reflections can be identified as unreacted $NaBiO_3$, $Bi(OH)_3$, and the dominating phase has reflections that match those of Bi_8RuO_{14}, which has a monoclinic unit cell. This suggests the formation of Bi_8MO_{14} where M = Fe or Mn (more likely Mn^{4+}), which is a phase that has not previously been reported. Following these observations, both pyrochlores are henceforth referred to regarding the alkali metal that they contain, so 'Na-pyrochlore' and 'K-pyrochlore'.

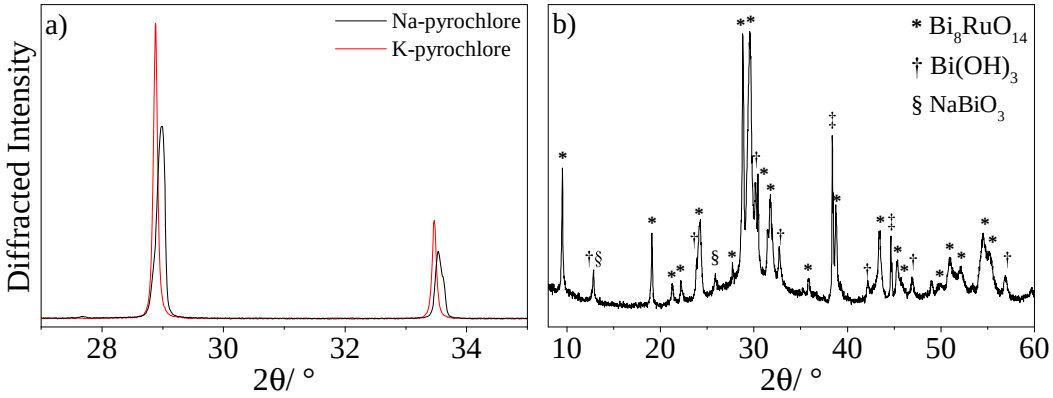

Figure 3.4: a) Observed peak shift between the Na- and K-pyrochlores. Panel b) shows the phases formed under identical conditions in a solution of NH_4OH.

The presence of the alkali metals in each pyrochlore was confirmed through elemental analysis. The results of ICP-OES and XRF analysis, including relative amounts of other metals, are given in Table 3.1. The values obtained through both techniques are very similar, the only discrepancy being that of sodium in the Na-pyrochlore, for which XRF gives a much lower value. This is not unexpected as sodium fluorescence is on the lower limit of the detectable energy range of the instrument. However, although the XRF value for sodium is not quantitative, it certainly confirms the presence of the metal in the structure. Again, these results show that the alkali metals are necessary for the synthesis and allow the pyrochlore phase to form.

Table 3.1: Elemental analysis for all metals present in the pyrochlore materials from ICP-OES and XRF measurements.

Element/at. %	Bi	*M* (Na or K)	Fe	Mn
Na-pyrochlore				
ICP-OES	53.87	12.51	27.99	5.63
XRF	56.59	5.82	31.15	6.44
K-pyrochlore				
ICP-OES	60.62	4.89	30.41	4.06
XRF	60.62	5.75	30.74	3.88

The ratios of metals obtained from elemental analysis were used to guide starting compositions for preliminary refinement of the structure against PXRD data. The initial refinements showed that the average long-range order represented by diffraction is described by the cubic space group $Fd\overline{3}m$. As the alkali metals are much larger with respect to the other metals present, the only realistic site that they could occupy is the eight-coordinate A site. Some of the bismuth on the A site was therefore replaced by the alkali metal, however satisfactory refinement of the model against the data was only achieved when the bismuth taken off the A site was incorporated onto the octahedral B site. With bismuth excluded from the B site, the intensities for all of the odd *hkl* reflections were inaccurately modelled. The bismuth that is on the B site must be of the higher oxidation state Bi^{5+}, for reasons of both charge balance and size. The presence of the monovalent alkali metal on the A site requires balancing, and the B site is at the centre of an octahedral coordination environment, much smaller than that of the eight-coordinate A site, so the cation must be smaller. Bi^{5+} also does not carry the electron lone pair, so is able to occupy a smaller symmetric octahedral environment. This is an example of the site mixing observed in many other pyrochlores, and was previously observed in other bismuth-containing pyrochlore oxides.[28–30]

Figure 3.5 shows the final refinements made against PXRD data, which were performed simultaneously alongside refinement against time-of-flight neutron data, which will be discussed below.

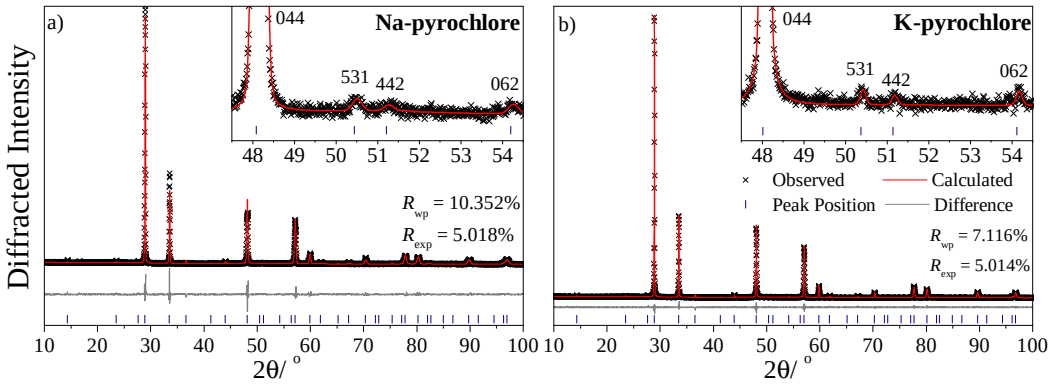

Figure 3.5: Results from Rietveld refinements for the a) Na-pyrochlore and b) K-pyrochlore against high-resolution PXRD data, carried out simultaneously against neutron data. The inset in each highlights the small intensity of the 442 reflection that is characteristic of A site disorder.

Closer inspection of the PXRD data reveals the appearance of a weak diffraction feature in the position expected for the 442 crystallographic reflection, highlighted in the insets of Figure 3.5. Although this is an allowed reflection for space group $Fd\bar{3}m$, for cubic pyrochlores in which the A site cation is on the ideal 16*d* site, this reflection has negligible or zero intensity.[48] This reflection violates the special conditions of three of the four unique sites encountered in the ideal pyrochlore structure (16*d*, 16*c*, 8*b*), suggesting that some of the atoms are displaced onto lower symmetry positions.[49] The appearance of this peak has been explained previously by the displacement of the Bi^{3+} cation toward the surrounding oxygen ions, away from the ideal site onto a lower symmetry position such as the 96*h*.[50] With the known stereochemically-active lone pair of Bi^{3+}, these observations are not wholly unexpected.

In order to study any possible atomic displacements in these phases, the inclusion of neutron diffraction data in this study is advantageous for the reasons described in Chapter 2. The Z^2 dependence of X-ray scattering cross-sections, which often leads to diffraction patterns being dominated by heavy elements, bismuth in this case, can be circumvented by the neutron scattering lengths of each element. This allows the oxygen positions to be better defined, important as any disorder induced from the Bi^{3+} on the A site will likely result in disorder in the surrounding oxygen sublattice. Disorder of this kind is often exhibited in pyrochlore materials that contain lone-pair active ions, such as Sn^{2+} and Bi^{3+}.[51] As the O′ anions do not form any part of the BO_6 octahedral network, and only bridge distances between adjacent A cations, any disorder introduced onto the A

site will consequently generate disorder on the neighbouring O′ sites as well.

A combined refinement of PXRD and time-of-flight neutron data from GEM yields compositions of $(Na_{0.60}Bi_{1.40})(Fe_{1.06}Mn_{0.17}Bi_{0.77})O_{6.87}$ and $(K_{0.24}Bi_{1.51})(Fe_{1.07}Mn_{0.15}Bi_{0.78})O_{6.86}$ for the Na- and K-pyrochlores, respectively. The refinements against neutron data make use of data from Banks 3, 4, and 5 of GEM (mean scattering angles of 35.14°, 62.39°, and 92.83°, respectively), and are shown in Figure 3.6.

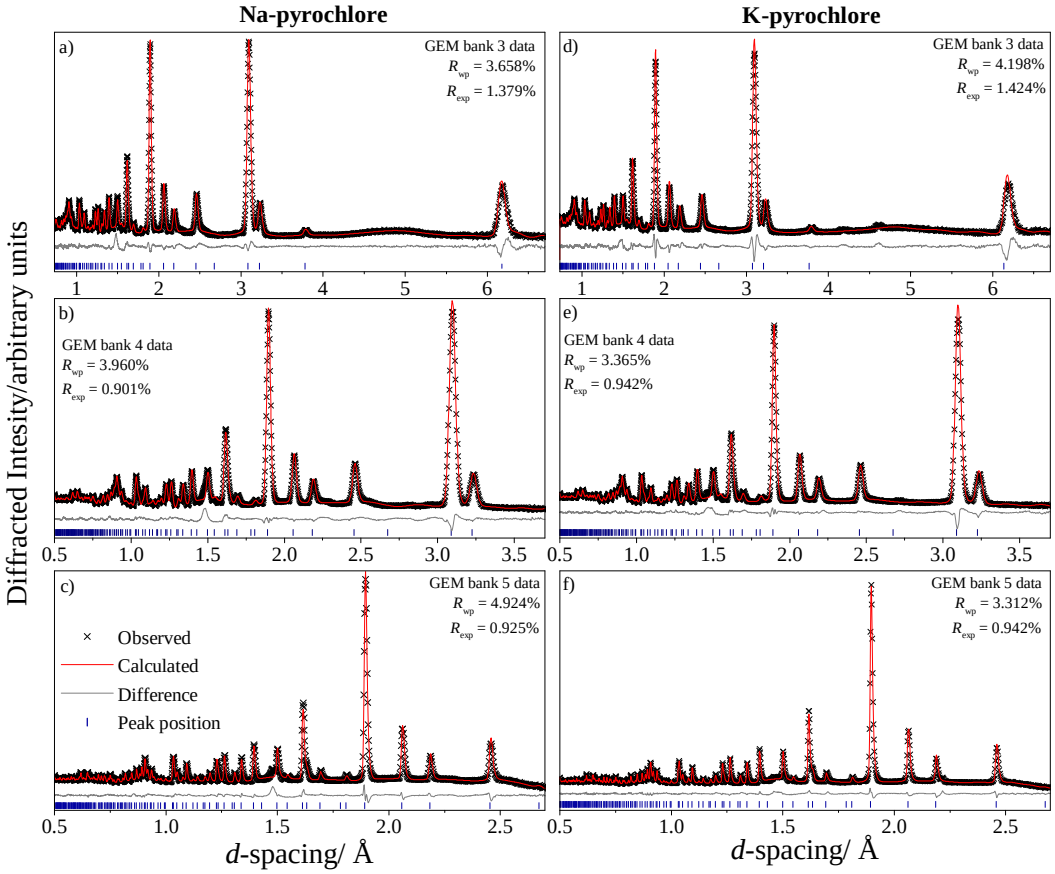

Figure 3.6: Results from final Rietveld refinements against time-of-flight neutron data from detector banks 3, 4, and 5 of GEM. Data for Na-pyrochlore are shown in a), b), and c), whilst data for K-pyrochlore are given in d), e), and f).

The highly symmetrical ideal $A_2B_2O_6O'$ pyrochlore structure has only one positional parameter that can be refined, the x coordinate of the 48f oxygen.[52] Refinements made against the X-ray and neutron data using this ideal model resulted in large anisotropic thermal parameters for the A site cations and isotropic thermal factors of a similar magnitude for the 8b O′ site. Any disorder on

the ideal positions will likely manifest itself in large thermal displacement parameters for the A and O′ sites, the magnitude of which can be amplified further by the presence of vacancies on these sites. The resulting thermal parameters from this refinement for both the A and O′ sites are shown in Figure 3.7 a), which displays the A_4O' tetrahedron.

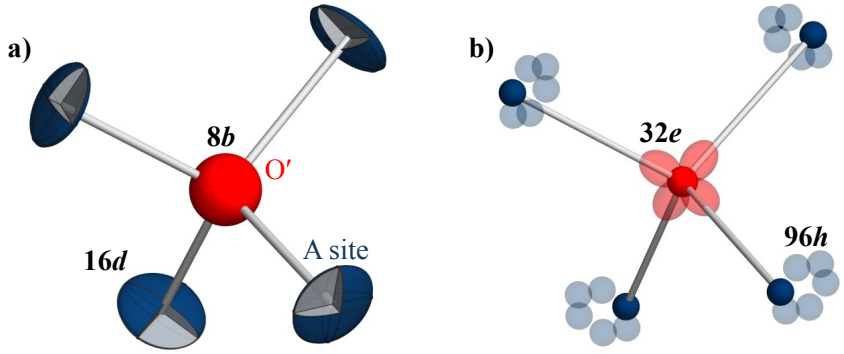

Figure 3.7: Structural representation of A_4O' tetrahedra produced from Rietveld refinements using a) ideal 16d site for the A cation, and b) the six-fold 96h position for the A cation, and 32e position for the O′ site.

A more accurate way to model the average structure of pyrochlores such as these is to allow the Bi^{3+} cation to be displaced off-centre, onto the 96h site, resulting in the formation of a ring around the ideal site with six-fold symmetry. The 96g site is a similar possibility, but one which produces a ring that is canted 30° to that of the 96h. For the 96h position, the A site moves towards the hexagon of surrounding O (48f) anions, and so is therefore often the more favourable choice over the 96g position. The 96h position has been used to model both stoichiometric pyrochlores,[2,48,53] as well as nonstoichiometric systems that contain multiple metals on a single site, or metals mixed across both the A and B sites.[32,38,54]

It is clear from Figure 3.7 that the anisotropic displacement parameters (ADPs) for the A site result in thermal ellipsoids that are flattened in the same plane of the 96h position. Given that the observed 442 reflection in the PXRD data supports the notion of cation off-centring in these systems, refinements were made where the A site metals were displaced from the ideal positions onto the 96h sites. These refinements resulted in R_{wp} values of 4.826% and 3.890% for the Na- and K-pyrochlores, respectively, compared with R_{wp} = 5.071% and 4.014% when the metals are confined to the ideal 16d site. As one would expect, the shift of the A site cations off-centre dramatically reduces their ADPs; however, the isotropic

thermal parameters for the 8*b* O′ site still remain larger than expected. Allowing some of the O′ atoms to displace away from the 8*b* position by refining the occupancy and position of the tetrahedral 32*e* site improves the fit further, giving $R_{\mathrm{wp}} = 4.688\%$ for the Na-pyrochlore and $R_{\mathrm{wp}} = 3.799\%$ for the K-pyrochlore. This results in a 5-fold reduction in the magnitude of the thermal parameter for the 8*b* site, whilst the ADPs for the 32*e* site result in slightly elongated thermal ellipsoids directed toward the coordinating A site atom, as seen in Figure 3.7 b). The question now arising from this improved model is whether all of the O′ atoms are displaced onto the 32*e* site, or whether they are distributed over both the 32*e* and 8*b* sites. Comparison of these two models shows insignificant differences between the refinement statistics and thermal parameters obtained. As the A site is partially occupied with the alkali metal, which unlike Bi^{3+} has no lone pair to drive static displacements, the mixed O′ 8*b*/32*e* model is perhaps the more realistic solution as the coordination environments of Bi^{3+} and Na^{+}/K^{+} are not alike. The resulting displacements in both the Na-pyrochlore and the K-pyrochlore are rather similar. The displacement of the A site cation away from the ideal 16*d* position is 0.3296(5) Å for the Na-pyrochlore, and 0.3280(6) Å for the K-pyrochlore, whilst the 32*e* O′ site is displaced from the 8*b* position toward the coordinating A site atoms by 0.3446(8) and 0.3314(8) Å for the Na- and K-pyrochlores, respectively.

The *x* positions of the 48*f* oxygen remain as 0.32770(7) and 0.32704(6) for the Na- and K-pyrochlores, respectively, regardless of the different positions used to describe the A and O′ sites. This is to be expected as the 48*f* oxide ions only partake in bonding with the BO_6 octahedral network, and would be negligibly affected by disorder present on the A site. These values show that the B site metals reside in nearly perfect octahedra, whilst the A site has a more distorted eight-coordinate environment, as described in Chapter 1. The results from Rietveld refinement of both pyrochlores are listed in Table 3.2, along with statistical measures of the fit quality.

Table 3.2: Structural details obtained from Rietveld refinement against X-ray and neutron data for the pyrochlores $(Na_{0.60}Bi_{1.40})(Fe_{1.06}Mn_{0.17}Bi_{0.77})O_{6.87}$ and $(K_{0.24}Bi_{1.51})(Fe_{1.07}Mn_{0.15}Bi_{0.78})O_{6.86}$.

Atom	Site	x	y	z	occupancy
Na-pyrochlore, $Fd\bar{3}m$, a = 10.6947(3) Å, $\alpha = \beta = \gamma$=90°					
R_{wp} = 4.688%, GOF = 3.194, density = 7.0183(5) g cm^{-3}					
Bi	96h	1/2	0.52179(9)	0.47821(9)	0.1169(4)
Na	96h	1/2	0.52179(9)	0.47821(9)	0.0497(4)
Fe	16c	0	0	0	0.534(2)
Mn	16c	0	0	0	0.086(5)
Bi	16c	0	0	0	0.384(2)
O	48f	0.32770(7)	1/8	1/8	1.0000
O′	8b	3/8	3/8	3/8	0.140(5)
O′	32e	0.3936(3)	0.3936(3)	0.3936(3)	0.1830(14)
K-pyrochlore, $Fd\bar{3}m$, a = 10.70849(12) Å, $\alpha = \beta = \gamma$=90°					
R_{wp} = 3.799%, GOF = 2.506, density = 7.2007(8) g cm^{-3}					
Bi	96h	1/2	0.52329(7)	0.47671(7)	0.1261(3)
K	96h	1/2	0.52329(7)	0.47671(7)	0.0200(8)
Fe	16c	0	0	0	0.535(2)
Mn	16c	0	0	0	0.075(4)
Bi	16c	0	0	0	0.392(2)
O	48f	0.32704(6)	1/8	1/8	1.0000
O′	8b	3/8	3/8	3/8	0.134(4)
O′	32e	0.3914(3)	0.3914(3)	0.3914(3)	0.1838(13)

The thermal behaviour of each site, described using anisotropic displacement parameters, are listed in Table 3.3.

Table 3.3: Anisotropic thermal displacement parameters for each site in the Na- and K-pyrochlore structures.

Atom	Site	ADPs/Å^2
Na-pyrochlore		
A	96h	$U11$=0.0084(15), $U22$=$U33$=0.0145(10), $U12$=$U13$=0.0021(6), $U23$=–0.0019(10)
B	16c	$U11 = U22 = U33$ = 0.0040(2), $U12 = U13 = U23$ = 0.0003(2)
O	48f	$U11$ = 0.0151(7), $U22 = U33$ = 0.0148(5), $U23$ = 0.0062(7)
O′	8b	$U11 = U22 = U33$ = 0.013(4)
O′	32e	$U11 = U22 = U33$ = 0.025(4), $U12 = U13 = U23$ = –0.0021(6)
K-pyrochlore		
A	96h	$U11$ = 0.0014(7), $U22 = U33$ = 0.0120(6), $U12 = U13$ = 0.0007(5), $U23$ = –0.0012(8)
B	16c	$U11 = U22 = U33$ = 0.0037(2), $U12 = U13 = U23$ = –0.0003(2)
O	48f	$U11$ = 0.0160(5), $U22 = U33$ = 0.0134(3), $U23$ = 0.0098(4)
O′	8b	$U11 = U22 = U33$ = 0.011(3)
O′	32e	$U11 = U22 = U33$ = 0.048(4), $U12 = U13 = U23$ = –0.0028(3)

Table 3.2 shows that the A site is slightly deficient for the K-pyrochlore, and the refined potassium content is much lower than compared to the sodium content of the Na-pyrochlore. The values observed from bulk elemental analysis were used to guide the initial refinements, which once refined, agree very well with variation of only 1-2%, shown in Figure 3.4. This shows that the structural models are good descriptions of these complex mixed-metal systems.

Table 3.4: Comparison of results from elemental anlysis against those obtained from simultaneous Rietveld refinement against PXRD and neutron data.

Element/at. %	Bi	*M* (Na or K)	Fe	Mn
Na-pyrochlore				
ICP-OES	53.87	12.51	27.99	5.63
XRF	56.59	5.82	31.15	6.44
Rietveld	54.18	14.89	26.66	4.27
K-pyrochlore				
ICP-OES	60.62	4.89	30.41	4.06
XRF	60.62	5.75	30.74	3.88
Rietveld	61.15	6.38	28.49	3.97

Vacancies on the A site of the pyrochlore structure can be accommodated, and partial occupation is common for many systems.[52,55] Although the Bi^{3+} cation would not reside in a symmetrical coordination environment, its tabulated ionic radius is 1.17 Å, almost identical to that of Na^+ (1.18 Å). It is likely that the introduction of the much larger K^+ (1.51 Å) causes the expansion of the lattice. Where the ionic radii of Bi^{3+} and Na^+ seem well matched, there is a much greater difference between the ionic radii of Bi^{3+} and K^+, and it could be that cation size variance effects produce a solubility limit for potassium on the A site of the structure. The lattice parameter is affected by the K^+ content, and is slightly larger even with the reduced amount of potassium compared to sodium. So it could be both size variance effects and the expansion of the lattice that limits the solubility of K^+ within the structure.

It is worth noting that the refined occupancy of the A site for the K-pyrochlore, equal to 0.8766, is almost the same as the occupancy of the neighbouring O′ site (0.8688), once multiplicity is taken into account. The deficiencies of these two sites are likely to be related as both form part of the A_2O' network; however this effect is not observed for the Na-pyrochlore which has a fully occupied A site and slightly vacant O′ site.

The densities measured from the Na- and K-pyrochlores are very similar and agree

with the densities calculated from the refined crystal structures, providing more evidence that the refined models give a good description of their structures. For the Na-pyrochlore, the values are almost identical with a crystallographic density of 7.018 g cm^{-3} and experimentally-determined value of 7.064 g cm^{-3}, while for the potassium analogue the calculated and experimental values are 7.201 and 7.094 g cm^{-3}, respectively. The powders were heated prior to measurement to drive off any residual moisture, but these small discrepancies could be due to the presence of some surface water that results in slight inaccuracies in the pycnometry results.

3.3.1.2 XANES Measurements

X-ray absorption near-edge structure spectroscopy was used to determine the oxidation states of the metals in the two pyrochlores. The near-edge region of the spectra are also compared against those of the reference materials, providing an estimation of the local coordination of each metal. Data were recorded over energy ranges that include the edge energies of the Mn K-edge (6.539 keV), the Fe K-edge (7.112 keV), and the Bi L_{III}-edge (13.418 keV).

From comparison with reference materials, the edge positions of the pyrochlore samples in the Mn K-edge spectra are similar to that of rutile-structure MnO_2, suggesting the presence of octahedral Mn^{4+}, shown in Figure 3.8. This is consistent with our Rietveld model that places the manganese on the B site of the pyrochlore structure, and shows that Jahn-Teller distortions of the octahedra should not be expected for this $3d^3$ ion.

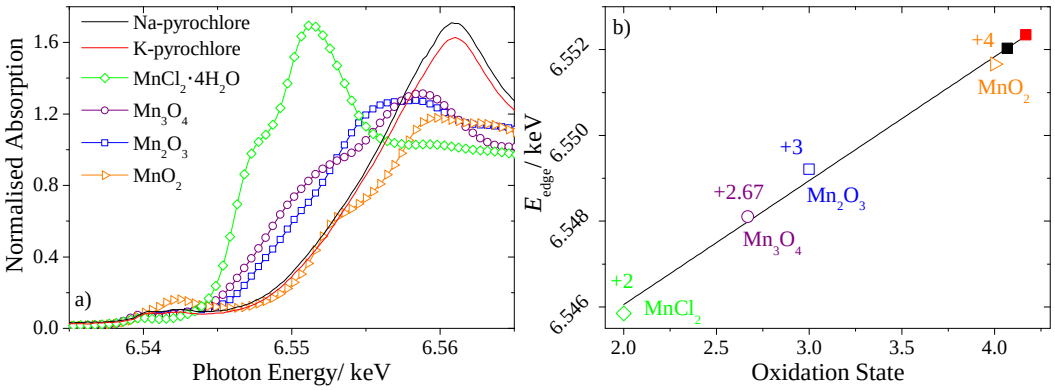

Figure 3.8: Mn K-edge XANES spectra of the pyrohclores compared to those of reference materials. Na- (black) and K-pyrochlores (red) are represented as lines, and references are shown as datapoint lines. Panel b) shows a plot of edge shift against oxidation state, with the pyrochlores marked using filled squares.

The Fe K-edge spectra have edge positions for both pyrochlores that are shifted to slightly higher energies than the Fe^{3+} references, shown in Figure 3.9. It should be borne in mind that XANES analyses performed at the K-edges can be sensitive to the local coordination environment of the target metal as well as its oxidation state. This slight increase would be consistent with the expected difference in local coordination environments between the pyrochlores and those of both α-Fe_2O_3 and $BiFeO_3$. However, the post-edge region of the data look very similar for both the pyrochlore and $BiFeO_3$ spectra, which one could say is expected, as the Fe^{3+} in $BiFeO_3$ is octahedrally coordinated and also has the stereochemically active Bi^{3+} lone pair cation on the A site, much like the pyrochlores.

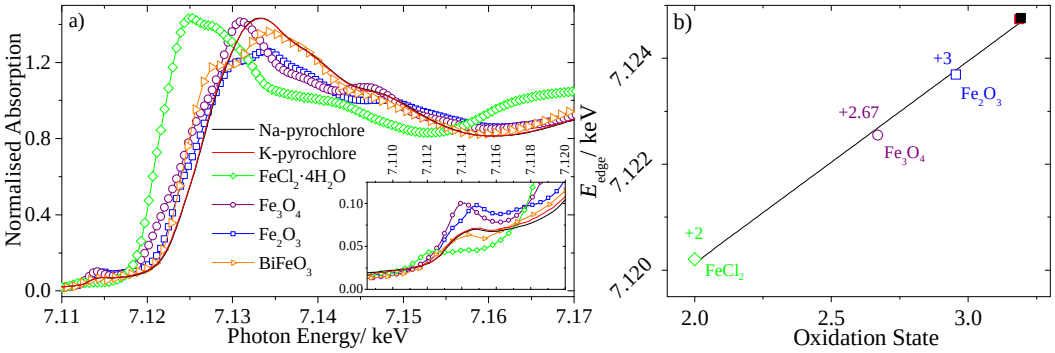

Figure 3.9: Fe K-edge XANES spectra shown over an extended range to show the similarity between the data of the pyrochlores and that of $BiFeO_3$. A plot of edge shift against oxidation state b), shows the observed shifts to high energies for the pyrochlores (filled squares), likely a result of local coordination.

A pre-edge feature that is observed at *ca* 7.114 keV in the Fe K-edge spectrum is due to the $1s$-$3d$ transition, characteristic of local environments with reduced symmetry, or non-octahedral, as seen in the spectrum for Fe_3O_4 which adopts a spinel-type structure with some Fe^{3+} coordinated in a tetrahedral environment. The absence of any such features in the Mn and Fe K-edge spectra confirms that the transition metals have octahedral coordination environments, agreeing with the X-ray and neutron data, showing that the incorporation of the transition metals on the B site is correct.

Perhaps another explanation that accounts for the difference between the pyrochlores and reference materials in the Fe K-edge spectra, is that a small amount of iron could be present on the A site of the structure, a common trait of disordered pyrochlores that contain multiple transition metals.[37,38,56]

Rietveld refinements of models that contain small amounts of iron on the A site

resulted in no improvement nor reduction to the quality of the fits, and therefore did not present a clear conclusion on the possibility of A site iron. Using the same off-centred sites to describe the A and O′ sites, the inclusion of iron on the A site gave R_{wp} values of = 4.717% and 3.893% for the Na- and K-pyrochlores, respectively, comparable to the refinements when iron was only on the B site (R_{wp} = 4.688% for the Na-pyrochlore and 3.799% for the K-pyrochlore). The presence of iron on the A site causes only very slight changes in the ADP values for all sites, and these refinements result in compositions of $(Na_{0.45}Bi_{1.33}Fe_{0.18})(Fe_{1.07}Mn_{0.17}Bi_{0.76})O_{6.87}$ and $(K_{0.17}Bi_{1.43}Fe_{0.16})(Fe_{1.05}Mn_{0.15}Bi_{0.81})O_{6.86}$. It is interesting to note that even with the iron present, the vacancy still remains on the A site of the K-pyrochlore, and that for both pyrochlores the relative occupancies of the three metals on the B site do not change. Because of this, when comparing these compositions against the elemental ratios provided by ICP, there are greater discrepancies than when compared to the models without A site iron.

It is possible to obtain further information on the local coordination of the Fe^{3+} environment through Mössbauer spectrometry. Transmission ^{57}Fe Mössbauer spectra were recorded at 300 and 77 K for both pyrochlores and both display symmetrical quadrupolar doublets with broadened lines, shown in Figure 3.10. The observed data have relatively low statistics due to the high content of absorbing bismuth in these pyrochlores, however, the spectra for each pyrochlore are almost identical, with quadrupolar isomer shifts δ that are consistent with the presence of Fe^{3+} in an octahedral environment, and also in high-spin configuration. The data provide no evidence for the presence of other iron species in different coordination environments.

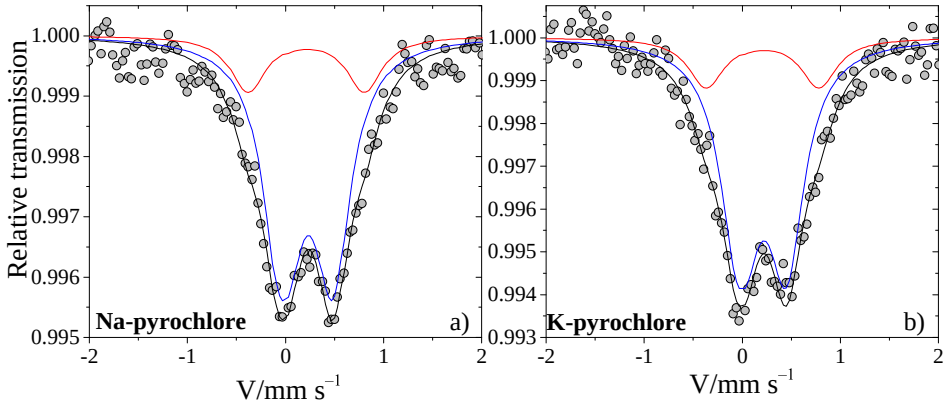

Figure 3.10: Transmission ^{57}Fe Mössbauer spectra of the a) Na- and b) K-pyrochlores recorded at 300 K, showing a two-component fit (black, blue, and red lines) to the data (grey points).

It is not possible to fit the spectra using a single doublet component, however, using two quadrupolar components accurately reproduces the line profile. The hyperfine structural details are given in Table 3.5, and show that the two components observed in each spectrum have very different quadrupolar splittings, though they are very similar for each of the pyrochlores.

Table 3.5: Results from fitting of ^{57}Fe Mössbauer Spectra recorded at 300 K for both the Na- and K-pyrochlores.

	Isomer Shift (δ) /mm s^{-1}	Linewidth (Γ) /mm s^{-1}	Quadrupolar Splitting (δ) /mm s^{-1}	Contribution /%
Na-pyrochlore				
Component 1	0.33(1)	0.44(2)	1.12(2)	19(2)
Component 2	0.33(1)	0.44(2)	0.45(2)	81(2)
K-pyrochlore				
Component 1	0.34(1)	0.44(2)	1.16(2)	19(2)
Component 2	0.34(1)	0.44(2)	0.50(2)	81(2)

Similar findings have been reported previously for other iron-containing pyrochlores, such as $(Bi_{1.8}Fe_{0.2})(FeSb)O_7$ and $Bi_2BB'O_7$ (where B = Cr or Fe, and B′ = Nb, Ta, and Sb).[57,58] The authors of these studies concluded that the two observed components were due to small amounts of iron that were located on the A site, with the majority on the B site. However, in this study, the two component fit could be equally due to the presence of chemical disorder in the crystal structure, not only from the A site Bi^{3+}, but also the static disorder present on the B site which is a result of three cations of different oxidation state and radius occupying the same position (ionic radii of high-spin Fe^{3+}, Mn^{4+}, and Bi^{5+} are 0.645, 0.53, and 0.76 Å, respectively[47]). This static disorder in the environments local to the B site also explains the rather large line widths that are observed for both pyrochlores.

The XANES data recorded at the Bi L_{III}-edge, when compared with reference samples, show that the pyrochlores do contain a mixture of both Bi^{3+} and Bi^{5+}, akin to other mixed-valence bismuth-containing pyrochlores.[28–30] The data, shown in Figure 3.11, display a shape in both the near edge regions and also the immediate post edge regions that is very similar to that of Bi_2O_4, in which Bi^{5+} occupies a regular octahedral environment, whilst Bi^{3+} is in an irregular cubic, eight-coordinate environment, comparable to the structure of the pyrochlores. The incorporation of both Bi^{3+} and Bi^{5+} within the β-Sb_2O_4-type structure of Bi_2O_4 means that the edge energy observed by XANES would correspond to an average oxidation state of +4.

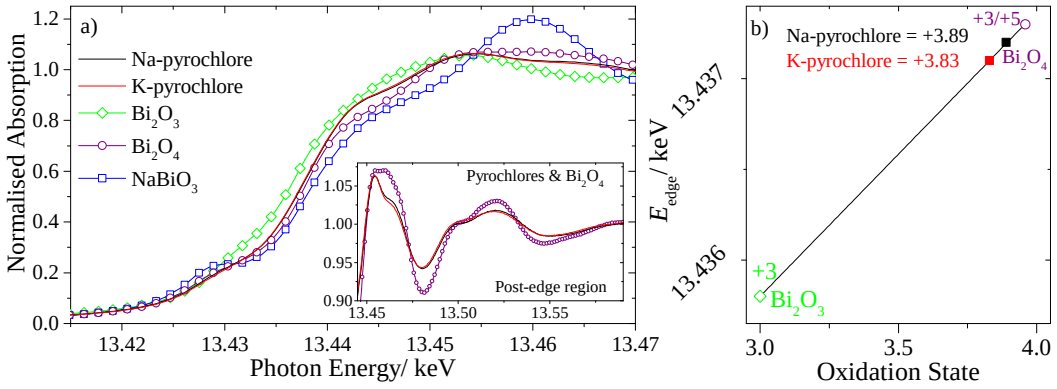

Figure 3.11: Bi L_{III}-edge XANES data for the pyrochlores and reference materials. The inset in a) shows the similarity in the immediate post-edge region between the pyrochlores and Bi_2O_4, discussed in the text. Plot of edge energy against oxidation state b) confirms a mixture of Bi^{3+} and Bi^{5+}.

As is described in the synthesis section of this chapter, the Bi_2O_4 reference was synthesised hydrothermally following the method of Kumada *et al.*,[46] and the powder produced was not entirely phase-pure, containing a small amount (3.35%) of Bi_2O_3, giving the reference material an average oxidation state of +3.96. The average oxidation states of bismuth determined from XANES were +3.89 and +3.83 for the Na-pyrochlore and K-pyrochlore, respectively, agreeing well with the results of structure refinement by showing the slight dominance of Bi^{3+} over Bi^{5+}. The slightly lower oxidation state observed for the K-pyrochlore is also consistent with the refined composition.

3.3.1.3 Thermal Behaviour of the Pyrochlores

The thermal behaviours of the two pyrochlore phases were examined through several techniques, testing their thermal stability, and the likelihood of them containing structural water.

Both of the pyrochlores are metastable and break down at comparable decomposition temperatures through similar intermediates, to give almost identical products. The decomposition mechanisms for both pyrochlores are examined through *in situ* X-ray diffraction, alongside TGA-DSC data in Figure 3.12.

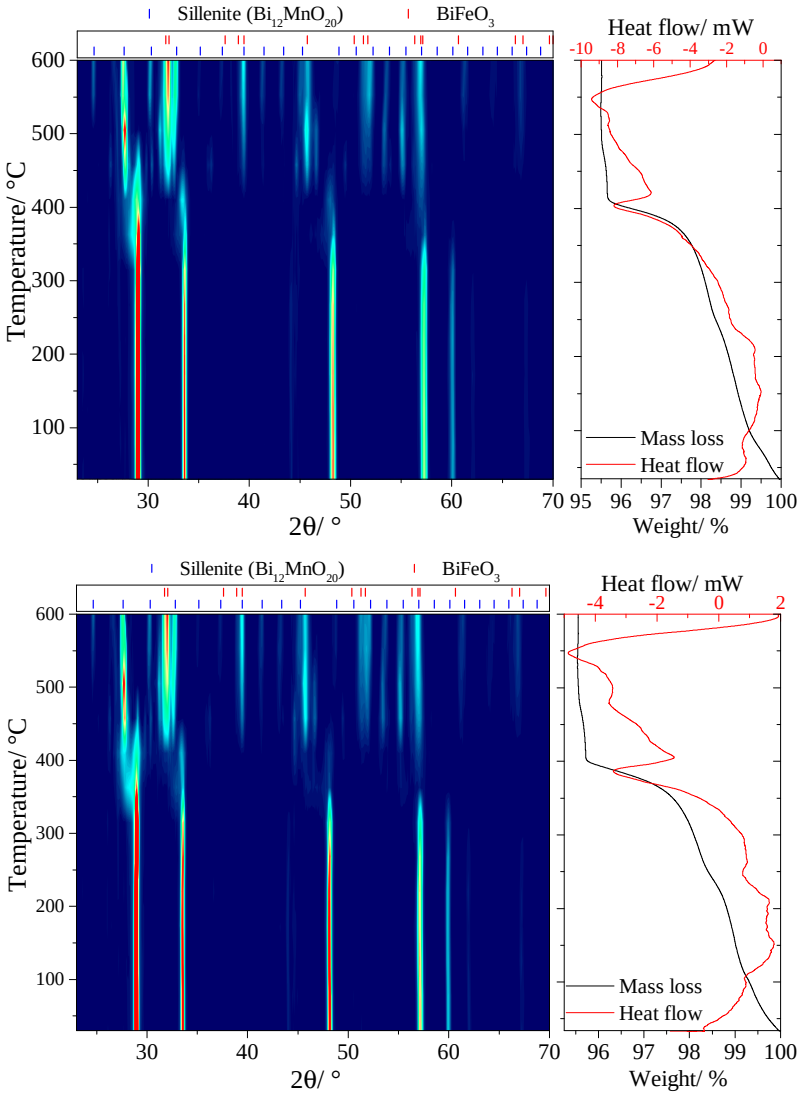

Figure 3.12: Thermal behaviour of both the Na- (top) and K-pyrochlores (bottom) from room temperature up to 600 °C. A contour plot of powder XRD data shows the decomposition mechanism discussed in the text, with tick marks provided for the products. The TGA plots on the right show the corresponding mass loss, and DSC traces provide accurate endothermic decomposition temperatures for each.

The endothermic peaks observed in the DSC curve provide accurate values for the decomposition temperatures; 403 °C and 387 °C for the Na- and K-pyrochlores, respectively. The decompositions of each are similar and pass through several intermediate steps before reaching the final thermodynamic products, which are indexed in Figure 3.12. As they begin to break down, the *in situ* powder XRD shows the development of weak shoulders on the higher *d*-spacing sides of the 222, 004, 044, 622 pyrochlore reflections. The positions of these shoulders match those

of the cubic fluorite δ-Bi_2O_3, a phase which is usually only stable above 730 °C,[4] but can be stabilised at considerably lower temperatures when doped with another metal.[1,59] These observed shoulders have very low intensity and overlap considerably with those of the pyrochlore reflections, so it is not possible to assign them to this fluorite-type phase with complete certainty. With increasing temperature, the pyrochlore continues to decompose with the simultaneous formation of sillenite (a mixture of both $Bi_{12}MnO_{20}$ and $Bi_{25}FeO_{40}$) and bismuth ferrite ($BiFeO_3$) over the range of 400-450 °C. Above this temperature, at $\sim$ 500 °C the $Bi_{25}FeO_{40}$ disappears as $BiFeO_3$ crystallises further, suggesting that the iron analogue of the sillenite structure is a kinetic intermediate and bismuth ferrite is the thermodynamic product from the decomposition. The remaining reflections that correspond to a sillenite phase agree with those of $Bi_{12}MnO_{20}$.[60]

With regards to the possibility of structurally-coordinated water, an excess of oxygen is observed from Rietveld refinement on the 8*b* O′ site when considering the balance of charge from the four different metals. This excess could be due to the presence of structural water or even hydroxide ions, as seen in other pyrochlores.[61] In terms of modelling structural water, the oxygen can be placed on the 8*b* site, with the hydrogen atoms being located approximately 1 Å away on the 32*e* site, as shown for Na-Ca-Ir pyrochlores.[62]

TGA data, also shown in Figure 3.12, clearly show a gradual loss of water up to the temperature at which each pyrochlore decomposes. The mass loss from 80 °C, the temperature at which the samples were heated prior to measurement in the neutron beam, up to the decomposition temperature of around 395 °C corresponds to an equivalent number of water molecules to the excess oxygen on the O′ site. For example, the O′ site in the Na-pyrochlore is over-occupied (from charge balancing) by 0.61, and by the mass loss from 80 °C up to the decomposition temperature corresponds to 0.63 mol of H_2O. Attempts were made to introduce crystal water into structural refinements, however, these proved unsuccessful; following previous reports by placing hydrogen or deuterium on the 32*e* site resulted in no improvement of the fit to the data, and the occupancy of hydrogen and deuterium always refined down to negligible amounts.

The presence of water is, however, observed through IR spectroscopy, as shown in the inset of Figure 3.13. The broad band in the region of *ca* 3300 cm^{-1} corresponds to the O–H stretching mode, and is typical of water or hydroxide species being present in the powders. A sharp vibrational mode is also observed at *ca* 1637 cm^{-1}, corresponding to the H–O–H bending motion of water, and is

consistent with the spectra recorded from several other hydrated pyrochlores.[63,64] The pyrochlore powders were heated to 80 °C before further investigation by IR spectroscopy. After this drying, these observed modes were diminished in both pyrochlores, suggesting that they are associated mainly to moisture that is coordinated on the surface of the powders, and not within the crystal structure.

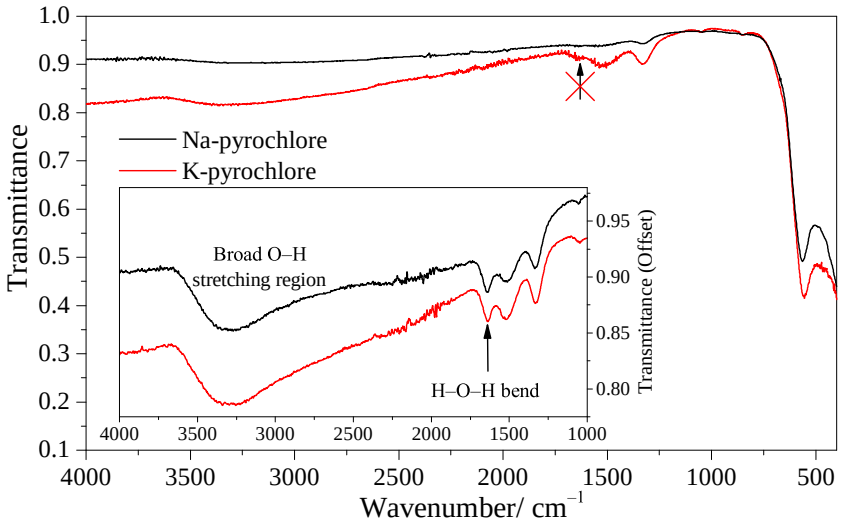

Figure 3.13: IR spectra recorded from both the Na- (black) and K-pyrochlore (red), after heating to 80 °C. The inset shows data recorded prior to heating, showing the stretching and bending vibrational modes assigned to O–H and water.

3.3.1.4 Electron Microscopy

Observation of the crystallites from both pyrochlore powders under an electron microscope shows octahedral crystallites with a fairly wide size distribution. Figure 3.14 shows a mixture of TEM and SEM micrographs recorded from both the Na- and K-pyrochlore. The dark dense crystals observed in the TEM images correspond to particles of the pyrochlore phase, however, it is possible to also see small amounts of the amorphous flaky material that forms as a secondary phase in these hydrothermal reactions. Minimisation of this phase was achieved by altering the manganese content of the synthesis, described in the synthesis section above, however, it is clear that small amounts of this amorphous by-product remain.

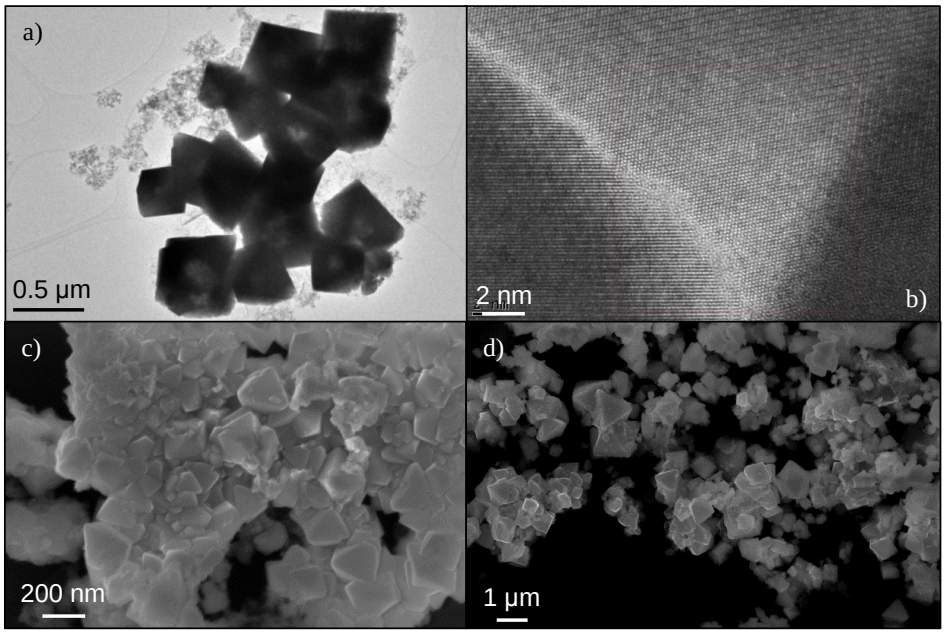

Figure 3.14: TEM image a) of agglomerated crystallites of the Na-pyrochlore phase with octahedral morphologies, and b) high-resolution image of a single crystallite focused on a vertex and edges of the octahedral shaped crystal. SEM c) and d) reveals the crystallised nature of the particles of both the Na- and K-pyrochlores, respectively.

The TEM image in Figure 3.14 a) shows how the octahedral crystals agglomerate together, however, it is demonstrated more distinctly by the SEM images from both the Na- and K-pyrochlores in panels c) and d), respectively, that the crystallites are not merely agglomerated, but actually appear to crystallise and grow from one another.

3.3.2 Characterisation using Total Neutron Scattering

The Rietveld models of the two pyrochlores show their average structures to be complex, involving partial occupancies of certain sites and also the displacement of several atoms away from their ideal positions. Other techniques, such as XANES spectroscopy and Mössbauer spectrometry, have confirmed the presence of disorder, hence the use of total scattering methods in order to study this deviation away from the average structure is important to further understand the materials.

3.3.2.1 Pair Distribution Function Analysis

Total neutron scattering data were recorded for both pyrochlores. The normalised distinct scattering functions for each pyrochlore are shown in Figure 3.15, and

illustrate the selection of the value of Q_{max} for each.

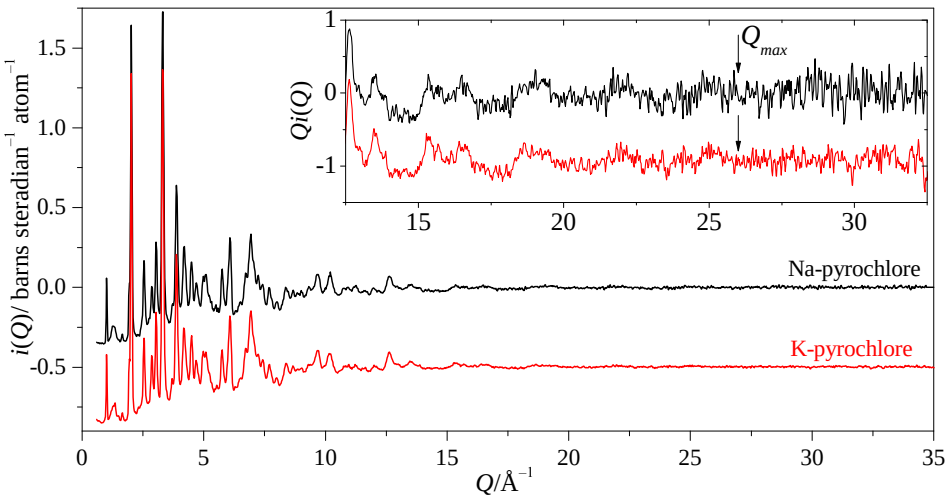

Figure 3.15: Distinct scattering data for Na-pyrochlore (upper) and K-pyrochlore (lower), as a function of Q. The inset displays $Qi(Q)$ data and illustrates the chosen values of Q_{max}.

The value of 26 Å^{-1} was selected as the value of Q_{max} for both pyrochlores; this is the point at which observable oscillations of the data about zero disappear, and excludes the increasingly noisy data at higher Q values, shown by the $Qi(Q)$ data plotted in the inset of Figure 3.15.

The use of this Q_{max} value with the step modification function in the Fourier transform of the $i(Q)$ results in the pair distribution functions displayed in Figure 3.16. The PDFs plotted out to a range of 10 Å show correlation distances between various atoms in the very short-range structure of the pyrochlores. From closer inspection, unphysical features in the region of the PDF below $\sim$ 2 Å can be assigned as noise resulting from the termination ripples induced from the Fourier transform, and the larger features are likely due to underlying curvature in the background that was not fully corrected.

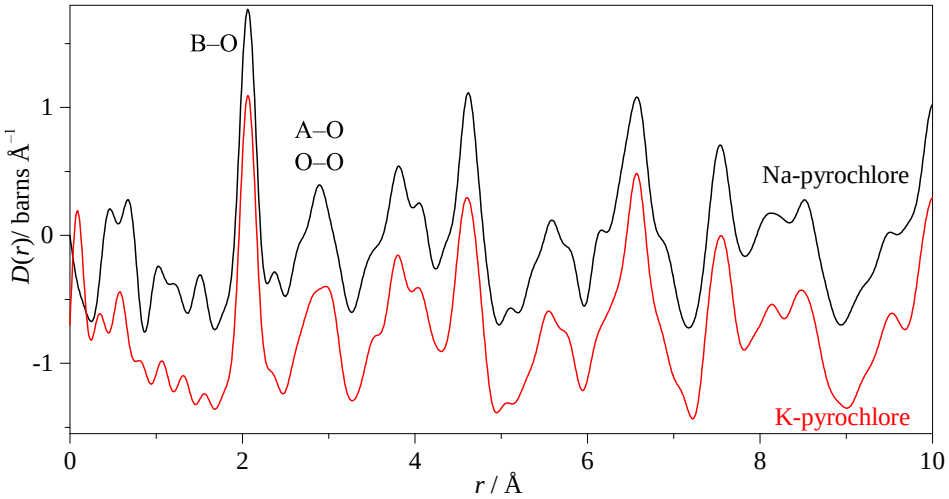

Figure 3.16: PDFs for the Na-pyrochlore (upper) and K-pyrochlore (lower) following the Fourier transformation of $i(Q)$ data using step function and Q_{max} of 26 Å^{-1}.

The PDFs for both pyrochlores are very similar, as expected from the measurements made from every other analysis technique used. The shortest observed correlation in both pyrochlores is assigned to the B–O distances between the octahedral B site and coordinating 48f oxygen, with no contributions from any other atom pair. This peak at $\sim$ 2 Å in the PDF agrees well with the refined Rietveld model which produces an average bond length of 2.06 Å. The second, much broader, peak consists of both A site metal-oxygen (A–O) and oxygen-oxygen (O–O) correlations, and is therefore more difficult to assign accurate values for each distance. For an ideal pyrochlore the A site metals should be coordinated by oxide ions that are 2.33-2.4 Å away, however, with the displacement of the A site onto the 96h position, in reality the range of possible A–O bond lengths is expected to be much greater, with potential distances up to $\sim$ 2.9 Å.

It is possible to fit the PDFs with slight refinement of the crystallographic-based models produced from Rietveld analysis. The fits for each pyrochlore are given in Figure 3.17, showing reasonable agreement between the data and the model. Above $\sim$ 12 Å, the agreement shows that the Rietveld model provides a good description of the long-range structure over length scales larger than the unit cell. However, for the region $r < 12$ Å, the fit is rather poor implying that even when using the displaced 96h and 32e sites, the average model does not account for the local structure present in these pyrochlores.

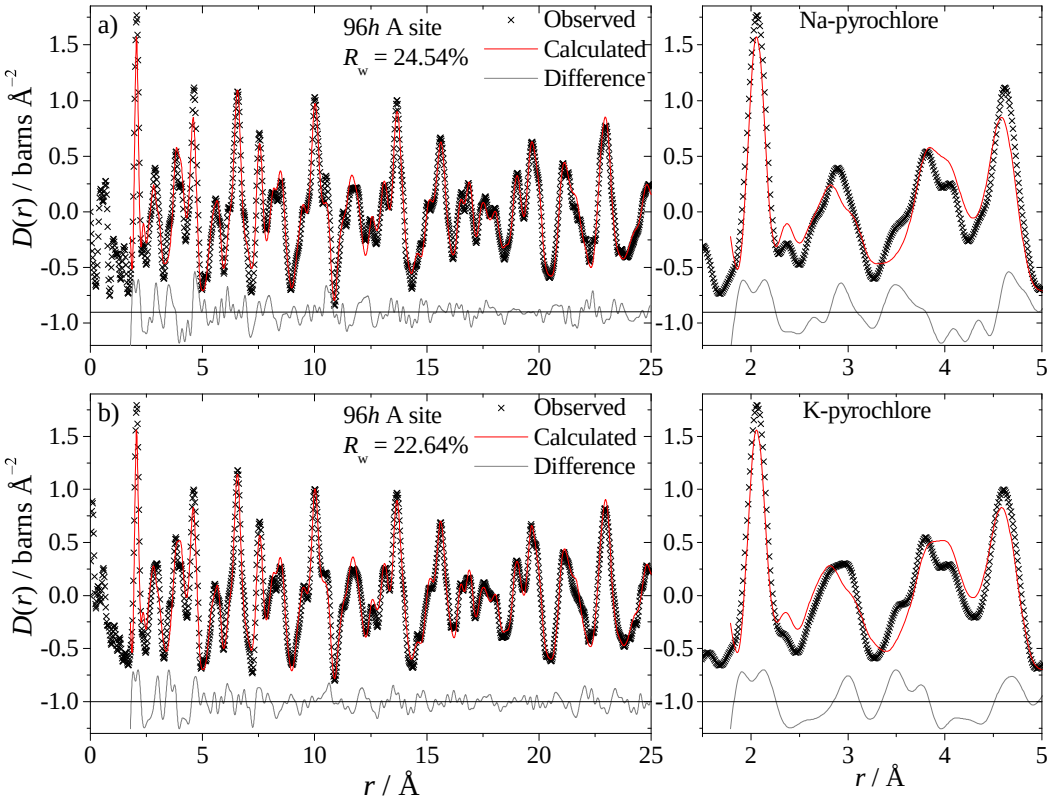

Figure 3.17: Fits of the Rietveld models against the PDF data up to r = 25 Å (left), and magnified region of the fit from 2 to 5 Å (right), for both a) Na- and b) K-pyrochlores.

It is clear to see from the magnified low r regions in Figure 3.17, that the main discrepancies between the data and model arise from the second and third atomic correlations located at r = 2.9 and 3.75 Å, respectively. Although the areas of the first and fourth correlations are not accurately reproduced, the positions of the simulated peaks agree with the observed data indicating that the bond distances responsible for those correlations are modelled well. It is encouraging that the main discrepancies are observed only with correlations that involve the A site cations, whose local coordination environments are known to be disordered.

There is scope for the fit to the low r region of the PDF to be improved by exploring the coordination environment of the A site more closely. Certainly, when confining the A site cations onto the ideal 16d site and the O′ site onto the 8b position, the fit is of poorer quality compared to the 96h and 32e positions, respectively, shown in Figure 3.18 a) and b). It is worth noting that when fitting only the low r region of the PDF, the areas of the first and fourth correlations are more accurately modelled, compared to when fitting out to 25 Å, further

highlighting the inconsistencies present between the long-range and short-range structure.

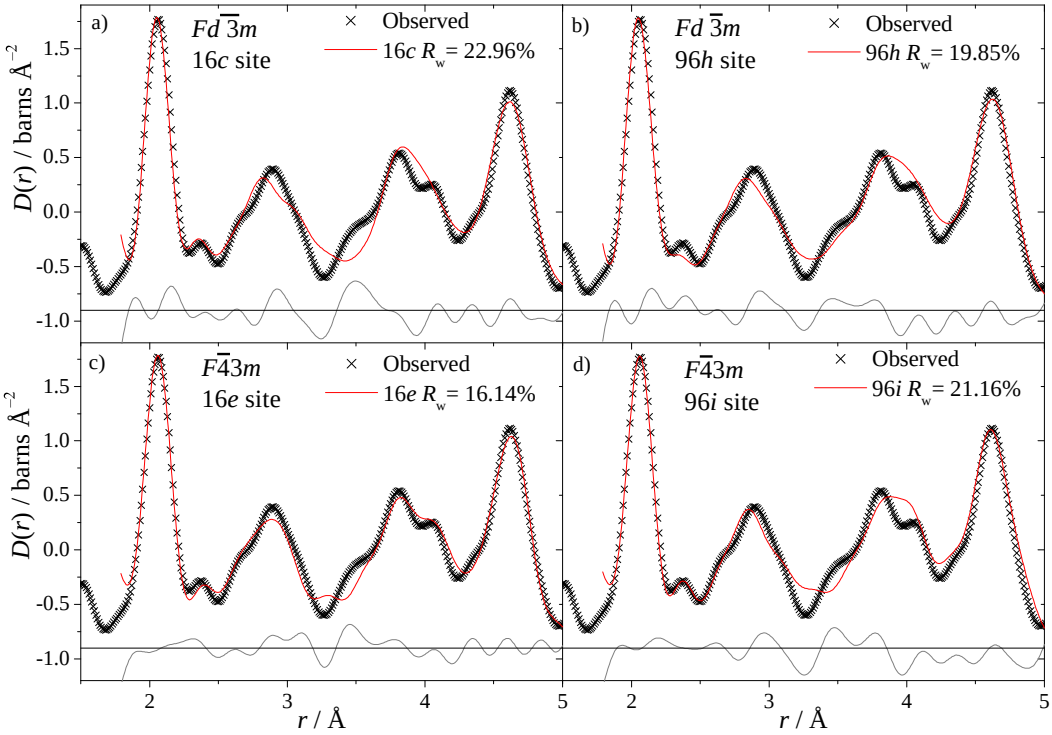

Figure 3.18: Results of fitting various models to the low r region of the PDF data of the Na-pyrochlore. These models are a) ideal 16d A and 8b O′ sites, b) six-fold 96h A and 32e O′ sites, whilst c) and d) use the lower symmetry space group $F\bar{4}3m$ with the 16e and 96i positions to describe the A site, respectively.

The idea of relaxing the symmetry around these sites was then tested, since this may result in a more accurate model of the local structure, whilst maintaining the overall long-range order. This can be achieved by using a lower symmetry space group; $F\bar{4}3m$, for example is a non-centrosymmetric subgroup of the higher symmetry $Fd\bar{3}m$ space group, and has been used to model successfully the short-range disorder in several disordered metal oxides that have average long-range structures based upon $Fd\bar{3}m$ symmetry,[65,66] including pyrochlores such as $Ce_2Zr_2O_{7.5}$,[67] $Pb_2Ru_2O_{6.5}$,[68], Y-doped $Bi_2Sn_2O_7$,[69] and more recently $(Na_{0.33}Ce_{0.53}Ti_{0.14})_2Ti_2O_7$.[70] The 16$e$ site of this space group allows for the positions of the A and B site metals to be refined, rather than confining them to a special position, whilst the 48f and 8b positions each split into the 24g and 4a sites, respectively, providing further positional degrees of freedom.

The fit is enhanced further by using the lower symmetry space group $F\bar{4}3m$; the

16e model certainly describes the shape of the second and third correlations more accurately than any of the others, shown in Figure 3.18 c). The A site anisotropic thermal parameters for the 16e model are rather large, like those of the ideal 16d site when using the $Fd\bar{3}m$ model. When visualised, the thermal ellipsoids are displaced towards the neighbouring 24g oxide ions, seen in Figure 3.19 c), so allowing the displacement of the A site onto the 96i position, equivalent to the 96h site in the $Fd\bar{3}m$ model, would appear to be a sensible approach. This attempt at introducing further degrees of freedom to the model, however, resulted in a reduction in fit quality to the low r data, shown in Figure 3.18 d).

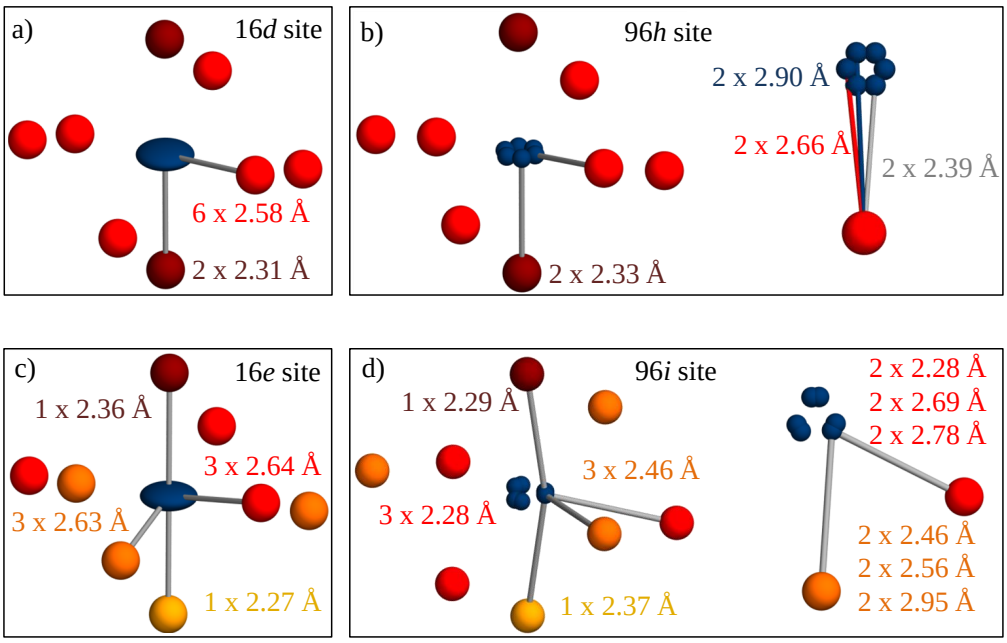

Figure 3.19: Different A site coordinations used to model the low r region of the pyrochlore PDF data. The 16d and 96h positions of the $Fd\bar{3}m$ space group are shown in a) and b), respectively, whilst c) and d) show the equivalent positions in the $F\bar{4}3m$ space group, the 16e and 96i sites, respectively.

These results show that it is not possible to achieve a *true* model of the short-range disorder present in these systems, when constrained by the symmetry operators put in place by crystallography. It is possible to manually fit the first peak of each PDF using the separate contributions from the three metals on the B site, through the bond valence approach. The Rietveld model constrains the three metals to the same position, giving Mn^{4+}, Fe^{3+}, and Bi^{5+} identical distances to their neighbouring oxygen atoms, 2.0651 Å for the Na-pyrochlore, and 2.0635 Å the K-pyrochlore. However, in reality each metal has a different ionic radius and

so therefore would not share the same distance with neighbouring oxide ions. The ideal distances that each metal would possess based on octahedral geometry were determined through bond valence. For example, Bi^{5+} being the larger of the three cations would have the longest distance to its nearest neighbour. It is possible to model accurately the first correlation in the PDF based upon the contributions of each metal from the distances provided by bond valence, as shown in Figure 3.20. The widths of each partial function correspond to the thermal parameters of the atom pair. For B–O correlations these were fitted to the data and consequently fixed at 0.0687 $Å^2$.

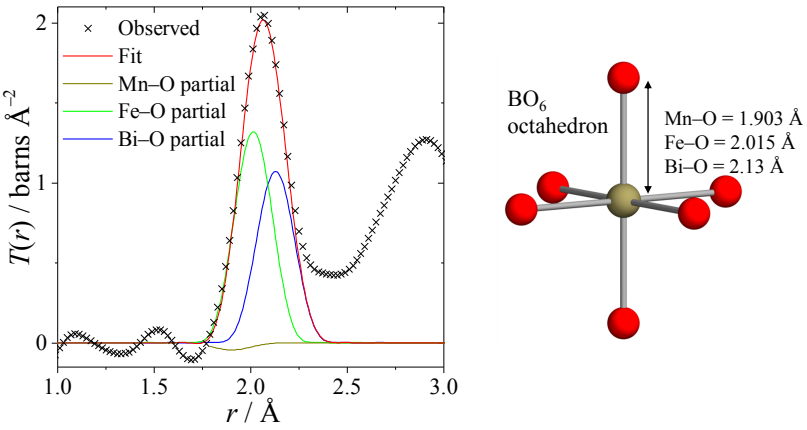

Figure 3.20: Manual fitting of first correlation in the PDF of the Na-pyrochlore (left) using contributions from the three different B site metals, and a BO_6 octahedron (right) listing three different distances based on bond valence. The partial contributions of Mn^{4+}, Fe^{3+}, and Bi^{5+} are shown by brown, green, and blue lines, respectively.

Modelling the second correlation in the PDF is more difficult due to the contributions of several atom pairs. However, it is worth noting that if there are separate B–O distances for the three metals, this would alter the volume of each type of BO_6 octahedra, and the distances between the oxide ions on each vertex would vary also. Refinement of the Rietveld model, based on diffraction data, would result in an average of the three different environments; a possible explanation of why the refined x positional parameter for the 48f oxygen in both pyrochlores has a value above 0.3125 (the value of regular symmetric BO_6 octahedra). Using the B–O distances from bond valence and assuming that each metal has a perfectly regular octahedral environment, with O–B–O angles of 90°, then it is possible to determine three separate O–O distances for each B site metal; more realistic than constraining them to the same site. This improves the fit to the second peak in the PDF, illustrated in Figure 3.21 b). The contributions of

each are normalised by the occupancy of each metal present on the B site. As the refined thermal displacement parameters of oxygen sites were larger than those of the B sites, the partial widths for O–O correlations were fixed at 0.1 Å^2.

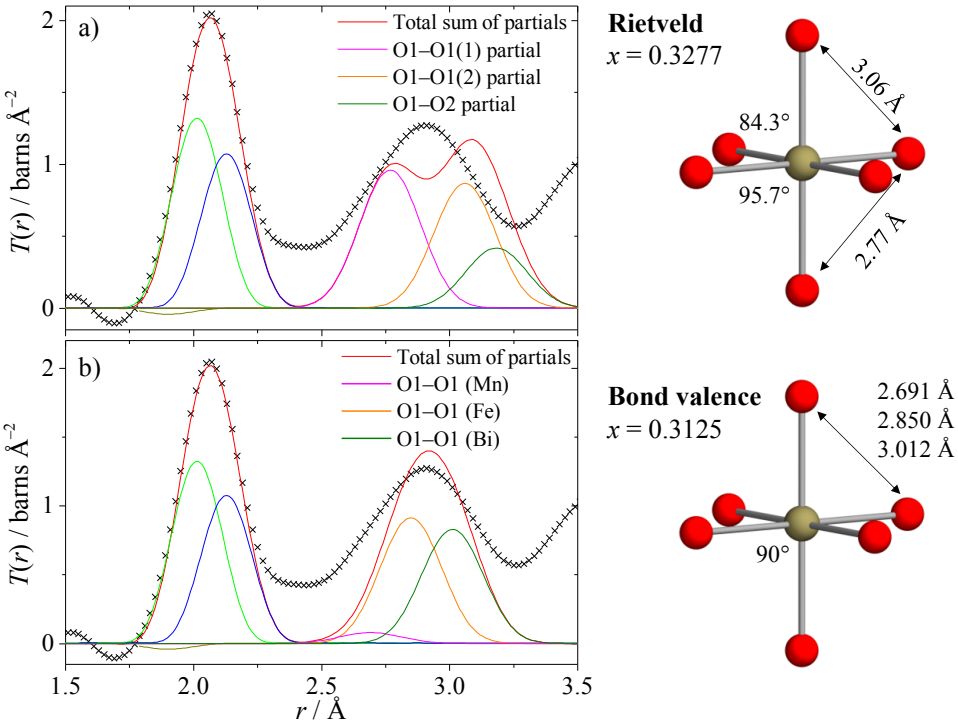

Figure 3.21: Manual fitting of O–O contributions to the second peak in the PDF. Partial contributions from the a) Rietveld model and from b) bond valence are shown.

These distances determined through bond valence are listed in Table 3.6 for both pyrochlores, and are compared against those obtained from Rietveld refinement.

Table 3.6: Comparison of bond lengths from Rietveld and bond valence approaches of various metals on the B site of each pyrochlore.

			Rietveld	Bond Valence	
B-site cation	Ionic radius/Å	B–O/Å	O–O/Å	B–O/Å	O–O/Å
Na-pyrochlore					
Mn^{4+}	0.53	2.0651	3×2.7679, 3×3.0659	1.903	2.691
Fe^{3+}	0.645(High-spin)	2.0651	3×2.7679, 3×3.0659	2.015	2.850
Bi^{5+}	0.76	2.0651	3×2.7679, 3×3.0659	2.13	3.012
K-pyrochlore					
Mn^{4+}	0.53	2.0635	3×2.7739, 3×3.0597	1.903	2.691
Fe^{3+}	0.645(High-spin)	2.0635	3×2.7739, 3×3.0597	2.015	2.850
Bi^{5+}	0.76	2.0635	3×2.7739, 3×3.0597	2.13	3.012

Whilst this rigid octahedra approach produces results in the correct position for the second correlation, the peak remains unsatisfactorily modelled due to there also being contribution from A–O pairs. With its preference for asymmetric coordination, the bond valence parameters for Bi^{3+} are not accurate and therefore cannot be used to model the partial contributions of the A–O correlations, which, in reality probably lie within the range of 2.35 to 2.95 Å. It is therefore sensible to allow a large configuration of atoms, built from the Rietveld model, to be released from the restraints of symmetry and be adjusted through the Reverse Monte Carlo (RMC) method, such that the low r region is satisfactorily modelled.

A 6×6×6 configuration was built for each pyrochlore from their Rietveld model, resulting in a supercell that contained a total of 216 unit cells and approximately 19000 atoms. The oxygen vacancies for each pyrochlore were distributed randomly throughout the configuration, as were the vacant positions on the A site of the K-pyrochlore. An atom-swap procedure was used to randomise the configuration such that initial bias is minimised in the fitting. Bond valence constraints and cut-off distances were defined for each element present in the configuration. The weightings that these constraints held over the configuration were varied for each atom such that the A site atoms, known to contain the majority of the disorder in the material, were constrained less compared to those of the B site.

In order to ensure the resulting configurations agree with both the short-range and long-range structure of the material, fits were made simultaneously against both the real-space $D(r)$, and also the reciprocal-space Bragg data from bank 3 of GEM. The results of fitting these datasets for both pyrochlores are shown in Figure 3.22, after approximately eight million random atom moves were generated and tested, and no further improvements were observed.

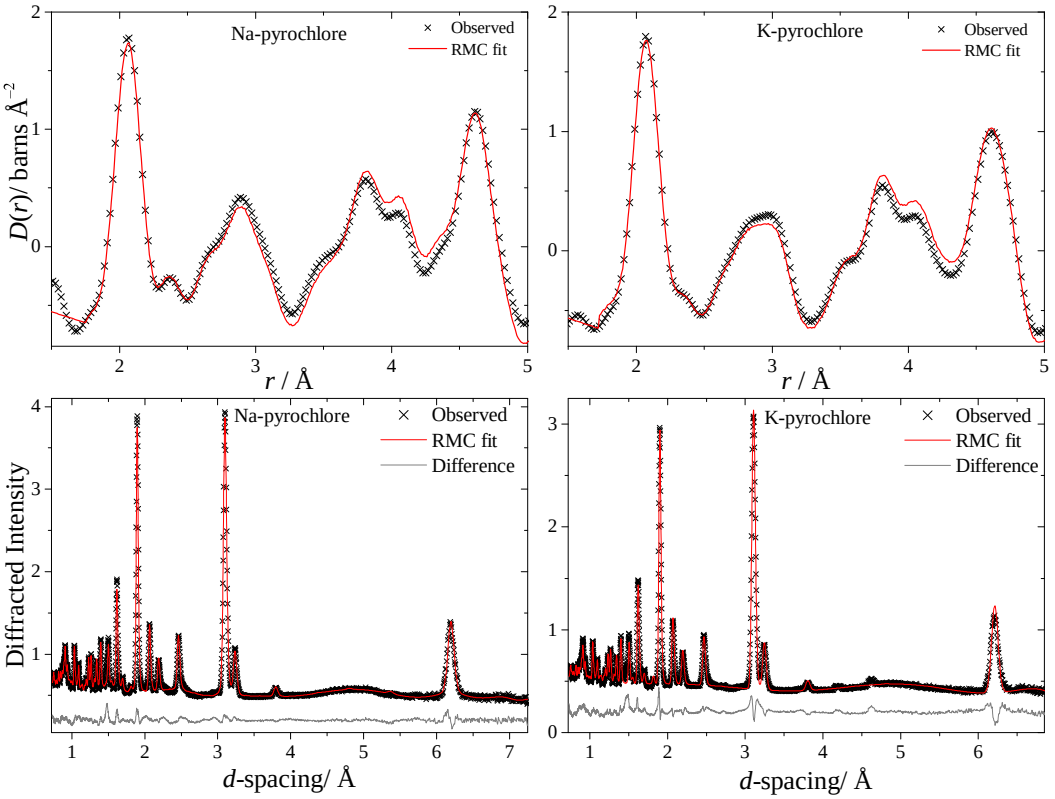

Figure 3.22: Final RMC fits to the $T(r)$ and Bragg data of the a) and c) Na-pyrochlore, and b) and d) K-pyrochlore, respectively. These results are from 48 hour long simulations.

It is evident through Figure 3.22, that it is possible through RMC to improve the fit to the short-range structure of the PDFs for both the Na- and K-pyrochlores, compared to when fitting the data using crystallographic constraints. The corresponding fits to the Bragg data for each pyrochlore are excellent with all intensities correctly modelled, and are comparable to the fits obtained through Rietveld refinement. This suggests that in order to model accurately the disorder described by the PDF data, the atoms do need to be displaced slightly away from the crystallographic sites, but not so much that the fit to the average structure is degraded. Extreme disorder can lead to the incorrect modelling of the 111 reflection (d-spacing of $\sim$ 6.2 Å) as the material becomes more fluorite-like, however, this is not observed for these pyrochlore systems.

The bond valence sums for each metal in the refined configuration are examined in Table 3.7, and are compared against those from Rietveld. The values obtained from the average model are erroneous for these materials due to the symmetry of the structure placing multiple metals on the same crystallographic site, resulting in the same distance for each metal to its neighbouring oxide ion. It is reassuring

that the valence values obtained from the refined RMC configurations are much closer to those observed from XANES analysis of the metals present.

Table 3.7: Comparison of bond valence sums from Rietveld to those refined from RMC configurations for both pyrochlores.

Element	Rietveld	RMC [6×6×6] box	RMC without BV
Na-pyrochlore			
Bi^{3+}	2.61	2.833	2.345
Na^{+}	1.19	1.004	1.157
Fe^{3+}	2.62	2.935	2.714
Mn^{4+}	2.58	3.790	2.627
Bi^{5+}	5.93	5.101	6.102
O	1.74	1.720	1.699
O′	1.82	2.225	2.078
K-pyrochlore			
Bi^{3+}	2.44	2.846	2.385
K^{+}	2.88	1.027	2.657
Fe^{3+}	2.63	2.911	2.631
Mn^{4+}	2.58	3.850	2.811
Bi^{5+}	5.94	5.083	5.972
O	1.87	1.705	1.681
O′	1.89	2.294	2.388

Removing the constraints of crystallography and accurately modelling the low r region of the PDF data clearly results in more realistic bond valence sums for the three metals mixed across the B site, as well as the Bi^{3+} and alkali metals on the A site. The distributions of bond valence values for each element in the RMC configuration of the Na-pyrochlore are shown in Figure 3.23, and compares them against those from Rietveld.

Also shown in Table 3.7 are values of final bond valence for configurations that did not use BV constraints. Although the fits to both the PDF and Bragg data are of high quality, the valence values that these result in are spurious for some of the elements, and ultimately show that the BV constraints are required in order to guide the simulation towards an accurate end model. These much broader distributions of bond valence are shown also in Figure 3.23.

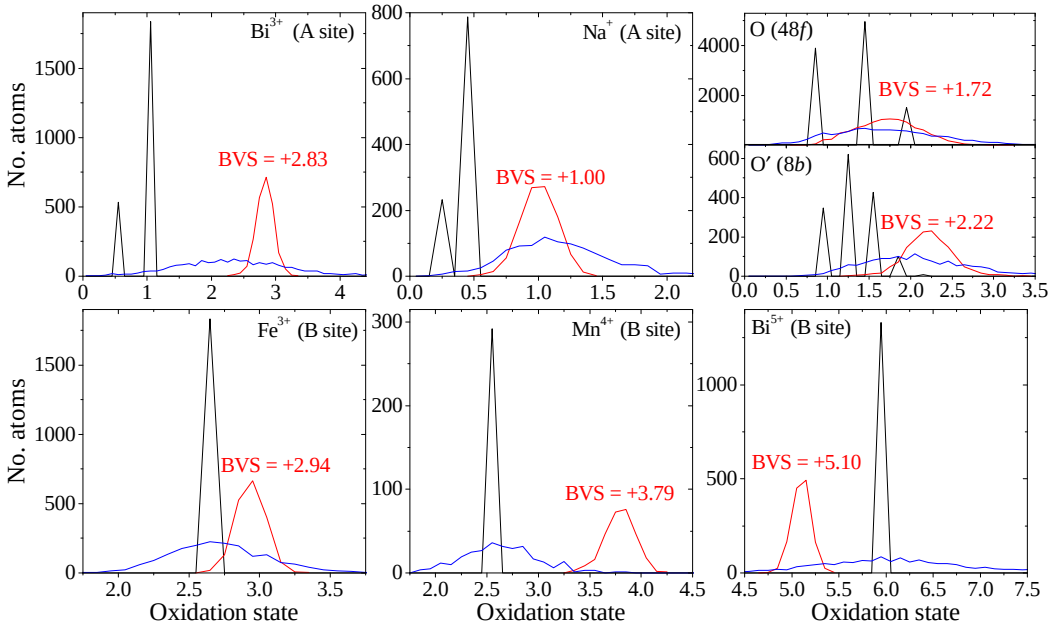

Figure 3.23: Bond valence distributions from RMC modelling for each atom in the Na-pyrochlore, shown in red. Initial (Rietveld) values are given as comparison, shown in black. Distributions from configurations without BV constraints are shown in blue.

Analysis of the configuration can also be carried out by visualising the box of atoms, after all 216 unit cells have been collapsed back into the original unit cell. This then results in "clouds" of atoms that describe the distribution of atoms around the average crystallographic positions. As seen through Figure 3.24 the atom distributions in the RMC configurations for both pyrochlores agree well with the thermal parameters observed through Rietveld refinement. When viewed down the [010] direction, the Rietveld models of both pyrochlores appear very similar, so for the purposes of Figure 3.24, the Rietveld structure of the Na-pyrochlore is used to compare against the RMC configurations for both pyrochlores.

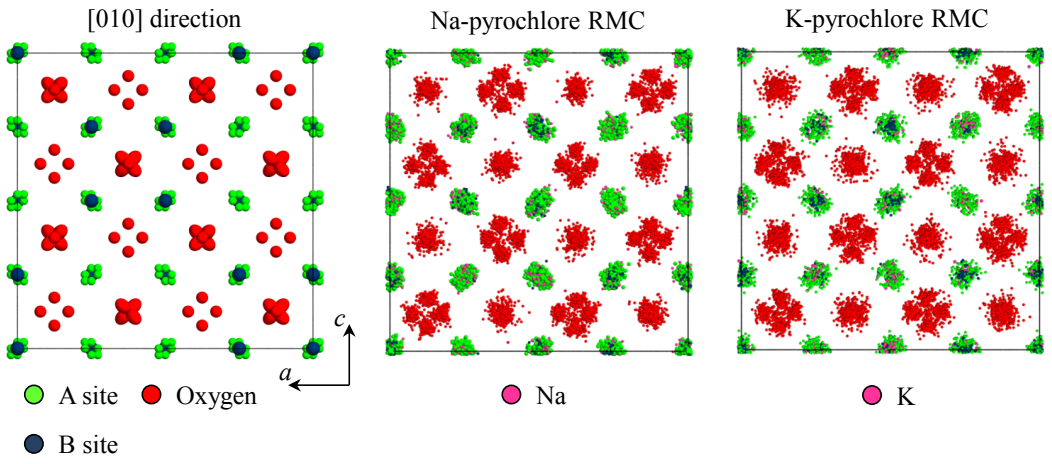

Figure 3.24: Final atomic arrangements from RMC for both Na- and K-pyrochlores, viewed along [010] direction. The Rietveld structure is compared on the left.

Inspection of the atom clouds shows very similar findings to the thermal displacement parameters from Rietveld analysis, which were largest for the O′ sites. The B site clouds are quite compact, indicating that despite the presence of three different metals, not much disorder is present. In contrast, the clouds that correspond to the A sites and O′ 8*b* sites are much more diffuse, confirming, that the majority of the disorder intrinsic in these pyrochlores resides on the A_2O' network.

On closer inspection, it is clear that the A site clouds have anisotropic shape, and are elongated towards the neighbouring 48*f* oxygen atoms, shown in Figure 3.25. When viewing the A site of the RMC configuration from a *top-down* view, along the O′–Bi–O′ distances, then the extent of the A site disorder becomes clear. The A site atoms have been displaced sufficiently from their ideal position towards the 48*f* oxygen, such that the clouds form ring shapes, very similar to the model obtained from Rietveld refinement. It is noted that the diffuse clusters of O′ atoms are most dense at the ideal 8*b* position, unlike the A site clusters, where the density is focused around the edges of the ring shapes, and not in the centre, where there is very little or no density of atoms.

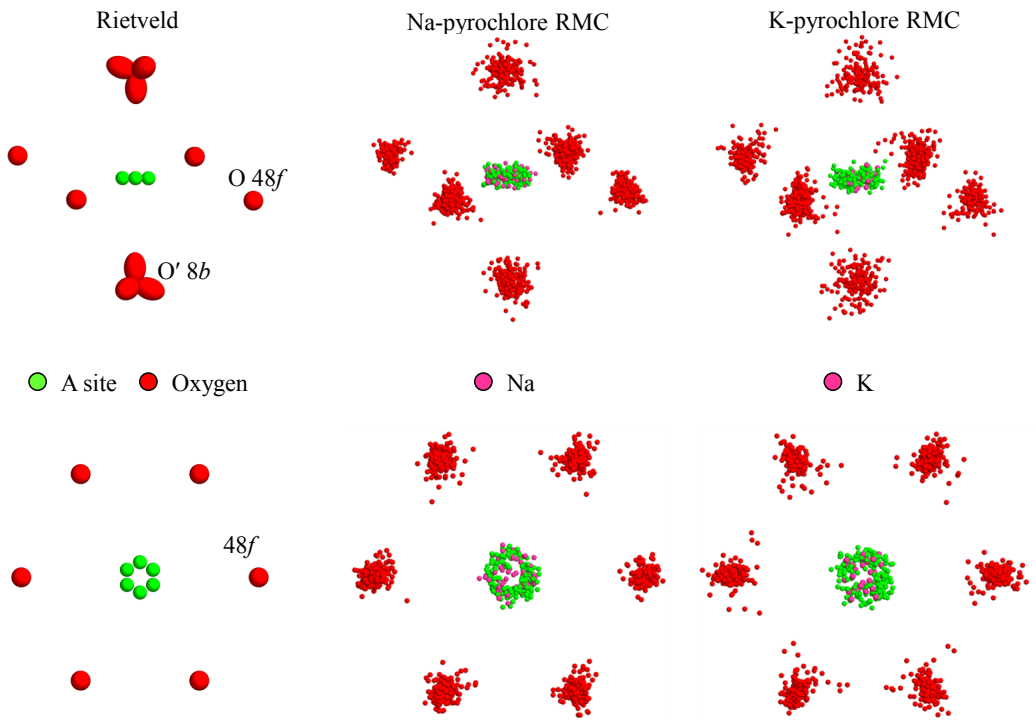

Figure 3.25: The A site coordinations of both Na- and K-pyrochlores compared against the Rietveld model (left). The full A site coordination environments are shown along the top, whilst along the bottom are *top-down* views (with 8*b* sites removed) of the A sites, highlighting the ring-shaped atom clouds.

3.3.3 Physical Properties

3.3.3.1 Magnetic Properties

Both Fe^{3+} and Mn^{4+} carry a magnetic moment, with electron configurations of $3d^5$ and $3d^3$, respectively, and it was confirmed by Mössbauer spectromety that Fe^{3+} is present in high-spin configuration. The observed molar magnetic susceptibilities for each pyrochlore, measured as a function of temperature in an applied field of 50 Oe, are shown in Figure 3.26. The figure includes data that were measured in the following order: zero field-cooled warming (ZFCW), field-cooled cooling (FCC), and remanent magnetisation (RM) curves.

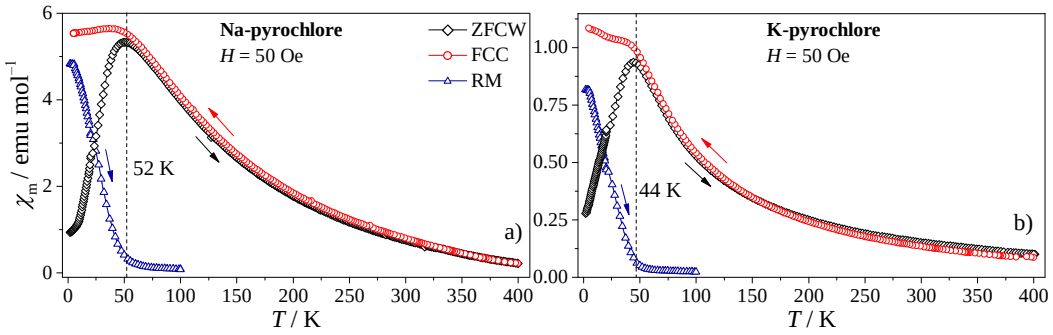

Figure 3.26: Molar magnetic susceptibility data vs temperature, measured in an applied field of 50 Oe for both the a) Na- and b) K-pyrochlores. ZFCW curves are shown by black diamonds, FCC curves by red circles, and RM data shown by blue triangles. The irreversibility temperature, discussed in the text, is marked by the vertical dashed line.

For both pyrochlores, a deviation between the ZFCW and FCC data is observed at low temperature: 52 K for the Na-pyrochlore and 44 K for the K-pyrochlore. This point of deviation has previously been labelled as the irreversibility temperature, and is a characteristic feature of materials that exhibit spin-glass type magnetic behaviour.[38,71] Another characteristic of spin-glass materials is the existence of remanent magnetisation in the material once the external field has been removed. The RM data shown in Figure 3.26 were collected on warming once the applied field was turned off, after the FCC data were measured. Under these conditions the magnitude of the measured susceptibility rapidly decreases to zero at the same temperatures as the ZFCW and FCC divergence. This supports the notion of the irreversibility temperature associated with frustrated systems, and indicates the presence of magnetic interactions occurring below this temperature.

The inverse susceptibility data, displayed in Figure 3.27, show that linear Curie-Weiss behaviour, usually characteristic of paramagnetism, is not observed. Instead the data tend towards high values at room temperature, likely a result of diamagnetic contributions. Equation 3.1 shows how diamagnetic terms from both the material (χ_0) and sample holder (χ_{SH}) can contribute to the observed susceptibility.

$$\chi = \frac{C}{T - \theta} + \chi_0 + \chi_{SH} \tag{3.1}$$

As a result of the large amount of bismuth present in these materials, which possesses a significant diamagnetic constant, the diamagnetic contributions from the sample are of a similar order of magnitude as the measured data at high temperature. This minimises the observed susceptibility in this region, and the effects of this become amplified in the inverse susceptibility data.

Although the data are dominated by diamagnetic contributions at high temperature, it is clear that interactions occur only at low temperature, supporting the observations from the susceptibility data in Figure 3.26.

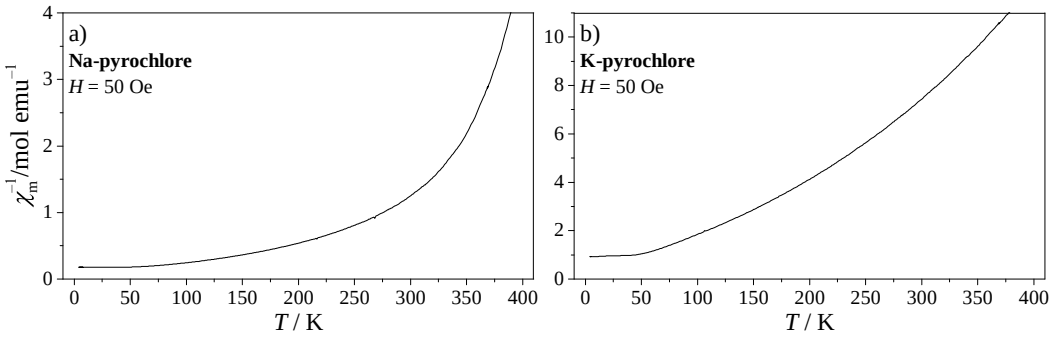

Figure 3.27: Inverse susceptibility curves as a function of temperature for the a) Na- and b) K-pyrochlores.

Heat capacity measurements were performed on the Na-pyrochlore in both zero field and in an applied field of 90 kOe, shown in Figure 3.28, and are consistent with the susceptibility data in showing that these materials lack any long-range magnetic order. There are no observable features in the data that may be associated with the magnetic entropy that would result from a spin-ordering transition, even when the material is saturated in an applied field of 90 kOe. This absence of any features also suggests that no other magnetic species are present as impurities in the sample. The presence of paramagnetic impurities can also be eliminated, as they would dominate the susceptibility data at low temperatures.

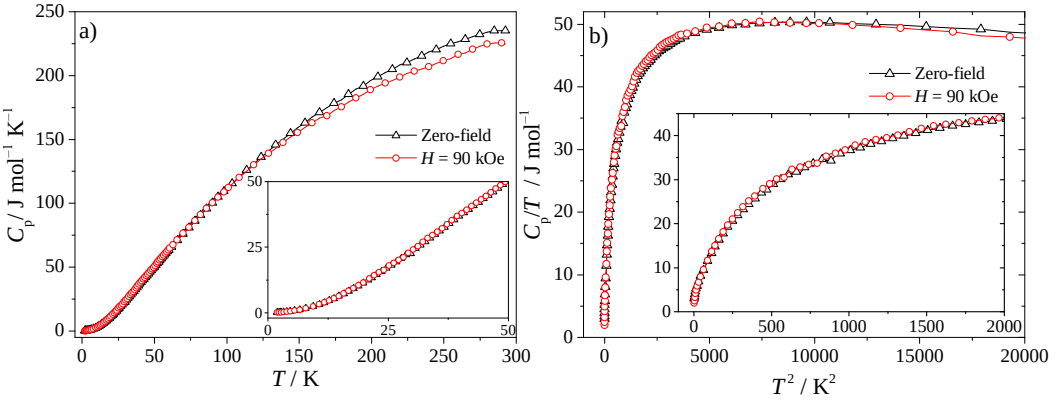

Figure 3.28: Specific heat data for the Na-pyrochlore in zero-field (black triangles) and an applied field of 90 kOe (red circles). The insets show that there are no observable features in the data even at low temperatures.

The irreversibility temperature, which is also referred to as the freezing temperature in spin-glass materials, has been associated with competing interactions between magnetically-ordered clusters or spins, and it is this which results in the spin-glass-like state.[38] For both pyrochlores, the interactions that occur below this transition point will depend strongly upon the number of next nearest neighbour metals that carry magnetic moments, especially as it has been shown that 40% of the B site is also shared by nonmagnetic Bi^{5+}. It was shown in similar complex pyrochlores like $(Bi_{1.89}Fe_{0.11})(Fe_{1.05}Nb_{0.95})O_7$ and $(Bi_{1.88}Fe_{0.12})(Fe_{1.42}Te_{0.58})O_7$, that this irreversibility temperature, characteristic of a spin-freezing transition, is dependent upon the magnitude of the applied external magnetic field.[38,50] It was shown for those materials that the irreversibility temperature decreases as a greater magnetic field is applied to the sample. This observation is characteristic of materials that exhibit spin-glass-like behaviour; a larger magnetic field will cause a saturation of the magnetic spins in the glassy state at lower temperatures. For materials which exhibit long-range macroscopic magnetic behaviour, ordering occurs below a specific temperature where the exchange interaction energy dominates over the thermal energy.

The effect of increasing the magnitude of the applied magnetic field on the irreversibility temperature in both pyrochlores is observed in Figure 3.29, and shows that the temperatures at which the ZFCW and FCC curves converge, decrease as the applied field increases. This further supports the conclusion that the pyrochlores exhibit spin-glass behaviour rather than long-range magnetic ordering. When the applied field is sufficiently large ($H > 10$ kOe) the convergence of the ZFCW and FCC curves is no longer observed due to the saturation of the spin-glass state.

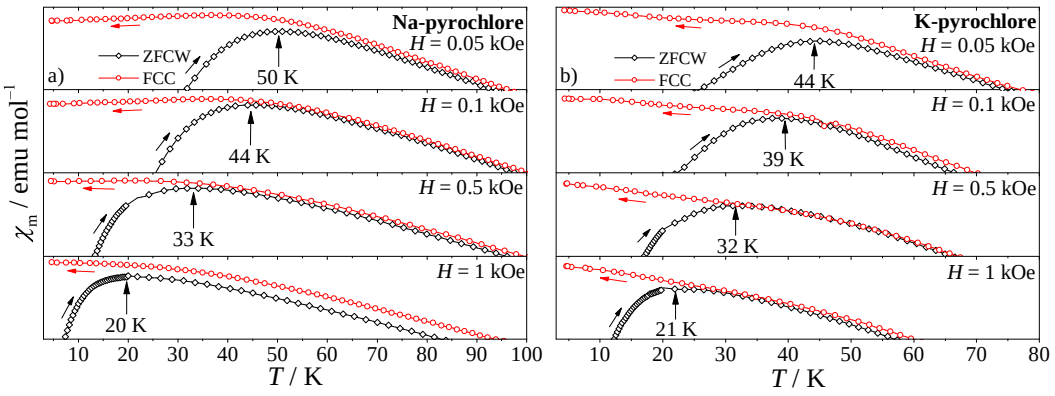

Figure 3.29: Variation in irreversibility temperature, defined as the point at which ZFCW and FCC data converge, in increasing magnetic fields for both pyrochlores.

Such frustrated behaviour, as all of the above observations suggest, is a feature common to pyrochlore oxides that contain magnetic ions and is a property inherent to the cation sublattice due to the tetrahedral nature of the metal positions. It is likely that the disorder present in our materials, resulting from multiple metals occupying the same crystallographic sites as well as stereochemically active lone pair cations, further contributes to the observed frustrated magnetic behaviour.

Magnetisation measurements recorded as a function of applied field below these irreversibility temperatures at 10 K, highlight a very weak hysteresis in both pyrochlores, shown in Figure 3.30. Each have a coercive field of *ca* 250 Oe signifying that they are relatively soft magnetic materials, whilst the remanent magnetisation for the Na-pyrochlore is approximately double that of the K-pyrochlore. The data measured above this irreversibility temperature at 100 K are shown in Figure 3.30 b), displaying typical paramaqnetic behaviour with no observed hysteresis, and that the highest magnetisation achieved at maximum field is lowered also.

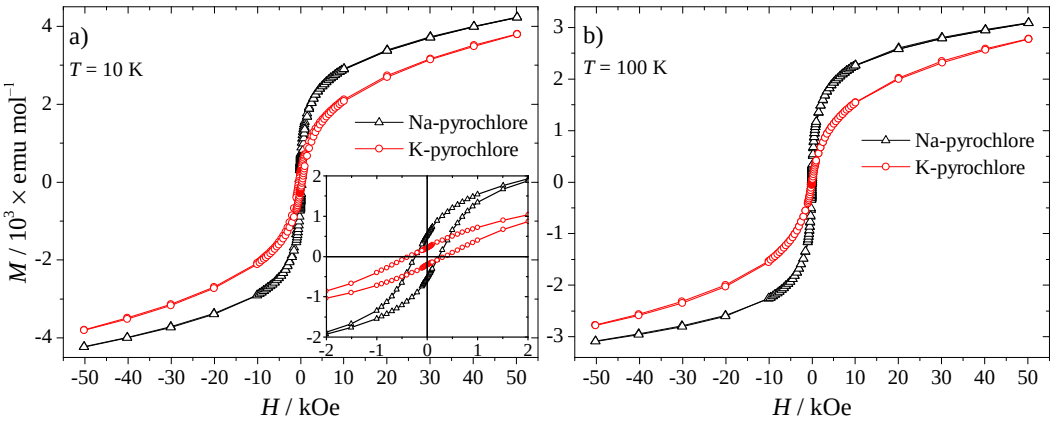

Figure 3.30: Variation in magnetisation for both pyrochlores as a function of applied field up to 50 kOe at a) 10 K and b) 100 K. The inset in a) highlights the weak hysteresis observed in both systems below the irreversibility temperature.

Also of note from the 10 K data is that saturation of the spins in the K-pyrochlore occurs at an applied field approximately twice as strong than what was observed for the Na-pyrochlore. A similar distinction between the two pyrochlores was observed in the shift of irreversibility temperature in Figure 3.29, where identical fields were used for each pyrochlore, but the temperature shift observed for the Na-pyrochlore is larger than that for the K-pyrochlore.

3.4 Conclusions

The direct hydrothermal synthesis of two new complex pyrochlore oxides has been explored. The optimum synthesis conditions for phase formation were shown to be 200 °C for periods of 6 hours, with the reactants dissolved in 4.0 M aqueous solutions of either NaOH or KOH. Using *in situ* diffraction methods, these pyrochlores were shown to be metastable, decomposing at *ca* 395 °C, making them inaccessible via conventional solid state synthetic routes.

The two pyrochlores differ through the presence of alkali metals in their structures, which originate from the hydroxides used in the synthesis. Preliminary analysis of powder XRD data showed that the average structure of the two phases could be described using a cubic unit cell with symmetry $Fd\bar{3}m$, and satisfactory refinements of these models were achieved only when some of the bismuth on the A site was replaced by the alkali metal, and consequently moved onto the B site of the structure.

A more in-depth analysis of the average structure included simultaneous refinements using both high-resolution XRD and neutron diffraction data. The best agreement between the model and the data was attained when the A site and O′ atoms were displaced away from their ideal sites, onto lower symmetry positions. These off-centrings were not unexpected given the known stereochemical activity of the Bi^{3+} cation, and are similar to the structures of many other reported pyrochlores described in the literature, which contain disorder within the A_2O' network.

The Rietveld analysis of these pyrochlores was supported by measurements from several other techniques, including ICP, XRF and TGA. XANES analysis revealed that the iron and manganese are present in oxidation states of +3 and +4, respectively, whilst data recorded at the Bi L_{III}-edge confirmed the mixing of bismuth across both the A and B sites of the structure, by showing a mix of both Bi^{3+} and Bi^{5+}. Mössbauer spectrometry indicated a level of static disorder was present also upon the B site of these materials, caused by the presence of three different metals.

Investigations were performed using total scattering data to study how, on a very local scale the structure deviates away from average as a result of the disorder present. Methods were used in an attempt to fit the local structure of the PDF using lower symmetry variations of the average Rietveld structure, however, a true description of the local disorder present in these materials required that the

symmetry constraints of crystallography be lifted. It was possible to model accurately the short-range structure of these pyrochlores using an RMC approach, revealing further information about the local coordination of metals within these structures which was not observed through the analysis of Bragg data alone. The results show that the three different metals on the B site produce disorder in the neighbouring oxygen positions; information which is lost in increased thermal parameters through Rietveld refinement. The probability densities of the A sites showed the formation of hollow rings in the plane of surrounding $48f$ oxygen ions. Diffuse clouds represented the $8b$ O′ sites, showing that the majority of the disorder in these systems resides on the A_2O' network. These models for the short-range disorder agree also with the average long-range structure, through simultaneous fitting of Bragg data, which resulted in more accurate values of bond valence for each metal incorporated within the structure.

The magnetic properties of these materials were investigated, and suggest that spin-glass behaviour is exhibited rather than a long-range magnetic configuration of the unpaired electron spins. Although such effects are common characteristics of many geometrically frustrated pyrochlores, it is likely that the high degree of structural disorder present in these systems also plays a large role in determining their properties. The magnetic moments undergo a spin-freezing, and increasing the magnitude of the external field results in saturation of these spins at lower temperatures.

References

[1] S. Hull, S. T. Norberg, M. G. Tucker, S. G. Eriksson, C. E. Mohn and S. Stølen, *Dalton Trans.*, 2009, 8737.

[2] A. L. Hector and S. B. Wiggin, *J. Solid State Chem.*, 2004, **177**, 139.

[3] I. Abrahams, X. Liu, S. Hull, S. T. Norberg, F. Krok, A. Kozanecka-Szmigiel, M. S. Islam and S. J. Stokes, *Chem. Mater.*, 2010, **22**, 4435.

[4] N. M. Sammes, G. A. Tompsett, H. Naäfe and F. Aldinger, *J. Eur. Ceram. Soc.*, 1999, **19**, 1801.

[5] A. Laarif and F. Theobald, *Solid State Ionics*, 1986, **21**, 183.

[6] I. Sosnowska, W. Schäfer, W. Kockelmann, K. H. Andersen and I. O. Troyanchuk, *Appl. Phys. A: Mater. Sci. Process.*, 2002, **74**, S1040.

[7] H. Jiang, Y. Morozumi, N. Kumada, Y. Yonesaki, T. Takei and N. Kinomura, *J. Ceram. Soc. Jpn.*, 2008, **116**, 837.

[8] A. A. Belik, K. Kodama, N. Igawa, S.-I. Shamoto, K. Kosuda and E. Takayama-Muromachi, *J. Am. Chem. Soc.*, 2010, **132**, 8137.

[9] C. Chen, J. Cheng, S. Yu, L. Che and Z. Meng, *J. Cryst. Growth*, 2006, **291**, 135.

[10] M. M. Kumar, V. R. Palkar, K. Srinivas and S. V. Suryanarayana, *Appl. Phys. Lett.*, 2000, **76**, 2764.

[11] B. Liu, B. Hu and Z. Du, *Chem. Commun.*, 2011, **47**, 8166.

[12] C. Chen, G. Zhan, X. He, H. Yang and H. Wu, *Cryst. Res. Technol.*, 2011, **46**, 309.

[13] X.-Z. Chen, Z.-C. Qiu, J.-P. Zhou, G. Zhu, X.-B. Bian and P. Liu, *Mater. Chem. Phys.*, 2011, **126**, 560.

[14] T. Atou, H. Chiba, K. Ohoyama, Y. Yamaguchi and Y. Syono, *J. Solid State Chem.*, 1999, **145**, 639.

[15] V. R. Palkar, D. C. Kundaliya and S. K. Malik, *J. Appl. Phys.*, 2003, **93**, 4337.

[16] I. O. Troyanchuk, A. N. Chobot, O. S. Mantytskaya and N. V. Tereshko, *Inorg. Mater.*, 2010, **46**, 424.

[17] S. K. Singh, H. Ishihwara and K. Maruyama, *Appl. Phys. Lett.*, 2006, **88**, 262908.

[18] A. Ianculescu, F. P. Gheorghiu, P. Postolache, O. Oprea and L. Mitoseriu, *J. Alloys Compd.*, 2010, **504**, 420.

[19] J. R. Sahu, C. R. Serrao, N. Ray, U. V. Waghmare and C. N. R. Rao, *J. Mater. Chem.*, 2007, **17**, 42.

[20] M. Kumar and K. L. Yadav, *Appl. Phys. Lett.*, 2007, **91**, 242901.

[21] M. Azuma, H. kanda, A. A. Belik, Y. Shimakawa and M. Takano, *J. Magn. Magn. Mater.*, 2007, **310**, 1177.

[22] A. A. Belik, A. M. Abakumov, A. A. Tsirlin, J. Hadermann, J. Kim, G. Van Tendeloo and E. Takayama-Muromachi, *Chem. Mater.*, 2011, **23**, 4504.

[23] Q. Dong, H. Jiang, N. Kumada, Y. Yonesaki, T. Takei and N. Kinomura, *J. Solid State Chem.*, 2011, **184**, 1899.

[24] Y. Mao, G. Li, W. Xu and S. Feng, *J. Mater. Chem.*, 2000, **10**, 479.

[25] J. Wu, F. Huang, X. Lü, P. Chen, D. Wan and F. Xu, *J. Mater. Chem.*, 2011, **21**, 3872.

[26] K. Sardar and R. I. Walton, *J. Solid State Chem.*, 2012, **189**, 32.

[27] K. Sardar, S. C. Ball, J. D. B. Sharman, D. Thompsett, J. Fisher, R. A. P. Smith, P. K. Biswas, M. R. Lees, R. J. Kashtiban, J. Sloan and R. I. Walton, *Chem. Mater.*, 2012, **24**, 4192.

[28] J. Trehoux, F. Abraham and D. Thomas, *J. Solid State Chem.*, 1977, **21**, 203.

[29] N. Kinomura, M. Hosoda, N. Kumada and H. Kojima, *J. Ceram. Soc. Jpn.*, 1993, **101**, 966.

[30] N. Kumada, M. Hosoda and N. Kinomura, *J. Solid State Chem.*, 1993, **106**, 476.
[31] O. Smirnova, M. Azuma, N. Kumada, Y. Kusano, M. Matsuda, Y. Shimakawa, T. Takei, Y. Yonesaki and N. Kinomura, *J. Am. Chem. Soc.*, 2009, **131**, 8313.
[32] Q. Zhou, B. J. Kennedy, V. Ting and R. L. Withers, *J. Solid State Chem.*, 2005, **178**, 1575.
[33] L. L. Garza-Tovar, L. M. Torres-Martínez, D. B. Rodríguez, R. Gómez and G. del Angel, *J. Mol. Catal. A: Chem.*, 2006, **247**, 283.
[34] M. W. Lufaso, T. A. Vanderah, I. M. Pazos, I. Levin, R. S. Roth, J. C. Nino, V. Provenzano and P. K. Schenck, *J. Solid State Chem.*, 2006, **179**, 3900.
[35] M. Bencina, M. Valant, M. W. Pitcher and M. Fanetti, *Nanoscale*, 2014, **6**, 745.
[36] W. Wu, K. Fumoto, Y. Oishi, M. Okuyama and Y. Hamakawa, *Jpn. J. Appl. Phys.*, 1996, **35**, 1560.
[37] G. S. Babu, S. Bedanta and M. Valant, *Solid State Commun.*, 2013, **158**, 51.
[38] W. Miiller, L. Causeret and C. D. Ling, *J. Phys.: Condens. Matter*, 2010, **22**, 486004.
[39] H. Y. Playford, L. R. Owen, I. Levin and M. G. Tucker, *Annu. Rev. Mater. Res.*, 2014, **44**, 429.
[40] S. T. Norberg, S. G. Eriksson and S. Hull, *Solid State Ionics*, 2011, **192**, 409.
[41] C. E. Mohn, S. Stølen, S. T. Norberg and S. Hull, *Phys. Rev. B*, 2009, **80**, 024205.
[42] D. S. Keeble, E. R. Barney, D. A. Keen, M. G. Tucker, J. Kreisel and P. A. Thomas, *Adv. Funct. Mater.*, 2013, **23**, 185.
[43] I. Jeong, C. Y. Park, D. J. Kim, S.-H. Kim, B. K. Moon, I. W. Kim and C. W. Ahn, *Z. Kristallogr.*, 2011, **226**, 150.
[44] D. P. Shoemaker, R. Seshadri, A. L. Hector, A. Llobet, T. Proffen and C. J. Fennie, *Phys. Rev. B*, 2010, **81**, 144113.
[45] D. P. Shoemaker, R. Seshadri, M. Tachibana and A. L. Hector, *Phys. Rev. B*, 2011, **84**, 064117.
[46] N. Kumada and N. Kinomura, *J. Solid State Chem.*, 1995, **116**, 281.
[47] R. D. Shannon, *Acta Cryst. A*, 1976, **32**, 751.
[48] S. J. Henderson, O. Shebanova, A. L. Hector, P. F. McMillan and M. T. Weller, *Chem. Mater.*, 2007, **19**, 1712.
[49] I. Levin, T. G. Amos, J. C. Nino, T. A. Vanderah, C. A. Randall and M. T. Lanagan, *J. Solid State Chem.*, 2002, **168**, 69.
[50] G. S. Babu, M. Valant, K. Page, A. Llobet, T. Kolodiazhnyi and A.-K. Axelsson, *Chem. Mater.*, 2011, **23**, 2619.
[51] M. T. Weller, R. W. Hughes, J. Rooke, C. S. Knee and J. Reading, *Dalton Trans.*, 2004, **19**, 3032.
[52] M. A. Subramanian, G. Aravamudan and G. V. Subba Rao, *Prog. Solid St. Chem.*, 1983, **15**, 55.
[53] R. Jones and K. S. Knight, *Dalton Trans.*, 1997, 2551.
[54] T. A. Vanderah, T. Siegrist, M. W. Lufaso, M. C. Yeager, R. S. Roth, J. C. Nino and S. Yates, *Eur. J. Inorg. Chem.*, 2006, **2006**, 4908.
[55] D. R. Modeshia and R. I. Walton, *Chem. Soc. Rev.*, 2010, **39**, 4303.
[56] Q. Zhou, P. E. R. Blanchard, B. J. Kennedy, C. D. Ling, S. Liu, M. Avdeev, J. B. Aitken, A. Tadich and H. E. A. Brand, *J. Alloys Compd.*, 2014, **589**, 425.
[57] A. V. Egorysheva, O. G. Ellert, Y. V. Maksimov, V. D. Volodin, N. N. Efimov and V. M. Novotortsev, *J. Alloys Compd.*, 2013, **579**, 311.
[58] M. C. Blanco, D. G. Franco, Y. Jalit, E. V. P. Miner, G. Brerndt, A. Paresano Jr, G. Nieva and R. E. Carbonio, *Physica B*, 2012, **407**, 3078.
[59] J. Xie, X. Lü, M. Chen, G. Zhao, Y. Song and S. Lu, *Dyes Pigm.*, 2008, **77**, 43.
[60] U. Delicat, S. F. Radaev and M. Trömel, *J. Solid State Chem.*, 1994, **110**, 66.

[61] P. G. Dickens and M. T. Weller, *Solid State Commun.*, 1986, **59**, 569.
[62] K. Sardar, J. Fisher, D. Thompsett, M. R. Lees, G. J. Clarkson, J. Sloan, R. J. Kashtiban and R. I. Walton, *Chem. Sci.*, 2011, **2**, 1573.
[63] C. A. Perottoni, J. Haines and J. A. H. da Jornada, *J. Solid State Chem.*, 1998, **141**, 537.
[64] G. K. L. Goh, S. M. Haile, C. G. Levi and L. F. F., *J. Mater. Res.*, 2002, **17**, 3168.
[65] H. Y. Playford, A. C. Hannon, E. R. Barney and R. I. Walton, *Chem. Eur. J.*, 2013, **19**, 2803.
[66] H. Y. Playford, A. C. Hannon, M. G. Tucker, M. R. Lees and R. I. Walton, *J. Phys.: Condens. Matter*, 2013, **25**, 454212.
[67] T. Sasaki, Y. Ukyo, K. Kuroda, S. Arai, S. Muto and H. Saka, *J. Ceram. Soc. Jpn.*, 2004, **112**, 440.
[68] R. A. Beyerlein, H. S. Horowitz, J. M. Longo and M. E. Leonowicz, *J. Solid State Chem.*, 1984, **51**, 253.
[69] Ismunandar, B. J. Kennedy, B. A. Hunter and T. Vogt, *J. Solid State Chem.*, 1997, **131**, 317.
[70] H. Y. Playford, D. R. Modeshia, E. R. Barney, A. C. Hannon, C. S. Wright, J. M. Fisher, A. Amieiro-Fonseca, D. Thompsett, L. A. O'Dell, G. J. Rees, M. E. Smith, J. V. Hanna and R. I. Walton, *Chem. Mater.*, 2011, **23**, 5464.
[71] G. Filoti, M. Rosenberg, V. Kuncser, B. Seling, A. Fries, T. Spies and S. Kemmler-Sack, *J. Alloys Compd.*, 1998, **268**, 16.

Chapter 4

Characterisation of $La_xSm_{1-x}CrO_3$ Perovskite Solid Solutions

4.1 Background

Rare-earth orthochromites, or $R\mathrm{CrO_3}$, adopt a distorted perovskite structure based upon an orthorhombic unit cell with *Pnma* (or the alternative setting *Pbnm*) symmetry that contains four formula units ($Z = 4$). The entire range of $R\mathrm{CrO_3}$ have been synthesised from R = La to Lu, including Y,[1] as well as the high-pressure syntheses of In and even Sc.[2] The distortion in these particular systems is driven by the size mismatch of the A and B cations which results in the tilting of octahedra in the BO_6 network. The tolerance factors (based on nine-coordinate radii of R^{3+}) for the series range from 0.92 for $LaCrO_3$ down to 0.85 for $LuCrO_3$, following lanthanide contraction across the period. As the size of the cation occupying the A site decreases, the distances to the coordinating oxide ions become shortened as the rigid octahedra undergo rotations about the smaller A site, leading to a monotonic reduction in unit cell volume from La^{3+} to Lu^{3+}.[1]

The unit cell of $LaCrO_3$ is shown in Figure 4.1, and has dimensions of $a = 5.524$ Å, $b = 7.767$ Å, and $c = 5.484$ Å.[3] With its smaller ionic radius (1.216 Å and 1.132 Å for La^{3+} and Sm^{3+}, respectively[4]), $SmCrO_3$ has reduced unit cell dimensions of $a = 5.488$ Å, $b = 7.626$ Å, and $c = 5.354$ Å.[1] The Goldschmidt tolerance factor gives an indication of the expected distortion in the structures, and decreases from 0.92 for $LaCrO_3$ to 0.89 for $SmCrO_3$, showing that greater distortion is observed in the latter.

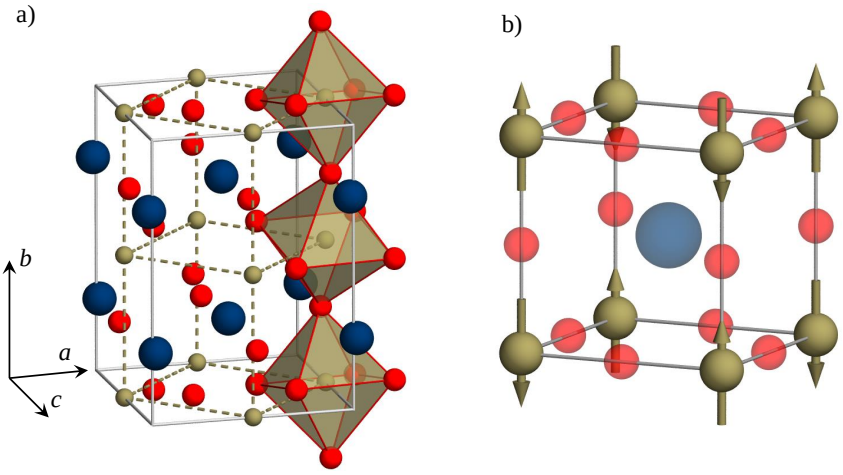

Figure 4.1: a) Orthorhombic (*Pnma*) unit cell of $LaCrO_3$ showing the four formula units contained within ($Z = 4$). Blue corresponds to lanthanum, beige to chromium, and red to oxygen ions. Dashed lines show how the primitive cubic unit cell fits within this structure. Example of b) G-type antiferromagnetic ordered structure.

Figure 4.1 a) also illustrates how the orthorhombic unit cell relates to the primitive cubic structure. The primitive parameters are used to compare the orthorhombic unit cell (*Pnma* setting) to its cubic counterpart and are related through the following equations:

$$a_\mathrm{p} = \frac{a}{\sqrt{2}}; \quad b_\mathrm{p} = \frac{b}{2}; \quad c_\mathrm{p} = \frac{c}{\sqrt{2}} \tag{4.1}$$

a relationship that results in the volume of the cubic unit cell being a quarter of the orthorhombic volume.

$LaCrO_3$ undergoes a phase transition into the lower symmetry rhombohedral $R\bar{3}c$ structure (tilt system $a^-a^-a^-$) at the relatively low temperature of ~ 270 °C.[5] The lattice parameters, determined at room temperature, show that $LaCrO_3$ lies very close to this orthorhombic-to-rhombohedral transition, due to the fact that $c > a$, whereas for all other $RCrO_3$, it is the other way round. The ratio of c/a for $LaCrO_3$ is almost equal to unity, which also highlights its proximity to the higher symmetry rhombohedral structure.

The magnetic ordering of the Cr^{3+} moments in $RCrO_3$ occurs below the Néel temperature (T_N), and is based upon a G-type antiferromagnetic structure, illustrated in Figure 4.1 b), where each ion has six antiparallel nearest-neighbours.[6] The degree of structural distortion influences the temperature at which this magnetic ordering occurs. The subtle increase in

structural distortions across the series leads to an ordering temperature that is *ca* 170 °C lower for $LuCrO_3$ than for $LaCrO_3$. Weak ferromagnetism is also observed below T_N alongside the antiferromagnetic ordering, and is a result of the slight canting of the Cr^{3+} spins away from the antiferromagnetic axis.[7]

For the majority of RCrO$_3$, the rare-earth cation is also magnetic and the increasing number of valence electrons in the $4f$ orbital across the period lead to interesting differences in their magnetic properties. $SmCrO_3$ has been shown to undergo a second-order spin reorientation at *ca* 33 K, much lower than T_N. It has been shown that this spin reorientation is driven by coupling effects between the Sm^{3+} on the A site and the Cr^{3+} on the B site, through anisotropic exchange interactions between the rare-earth and the weak ferromagnetic component of the Cr^{3+} sublattice.[8,9]

Rare-earth orthochromites are widely known for the plethora of useful properties that they possess. They are reported to be p-type semiconductors and therefore show sensitivity toward particular organics such as methanol and ethanol as well as humidity, making them possible candidates for sensor applications.[10,11] Some exhibit increased catalytic activity toward the decomposition of N_2O gas into N_2 and O_2, as well as the oxidation of CO.[12,13] Replacing small amounts of the A site rare-earth with strontium gives rise to increased oxidative behaviour towards hydrocarbons.[14] Doping calcium and other divalent alkaline-earth metals into the structure of RCrO$_3$ is the most common method of improving the p-type semiconductive behaviour, such that the solid solution becomes useful for applications as interconnect materials in solid oxide fuel cells (SOFCs).[15,16] The high temperature chemical stability of $LaCrO_3$ in both oxidising and reducing conditions makes it suited to such applications, whilst the doping of divalent ions act as electron acceptors and subsequently enhance the p-type semiconductivity sufficiently enough to be considered as an interconnect material.[17]

Of most interest, however, and most applicable to this project, are the potential magnetoelectric properties exhibited by many of the rare-earth orthochromites. Theoretical predictions based upon symmetry analysis reveal that an electric polarisation, either spontaneous or one induced by a magnetic field, can exist whilst the RCrO$_3$ are in the antiferromagnetically ordered state.[18] These postulations are supported by the experimental observations of both canted antiferromagnetism and ferroelectricity below the magnetic ordering temperatures of several RCrO$_3$.[19] Electric polarisation is observed in $SmCrO_3$ at T_N as well as the spin reorientation T_{SR}.[20] The observation of such polarisation at temperatures

relating to magnetic transitions leads to the proposal that the electric polar order is induced due to the interactions between the magnetic Sm^{3+} ions and the weak ferromagnetic component of the ordered Cr^{3+} sublattice breaking the inversion centre of the centrosymmetric space group *Pnma*.[20] The presence of spin-phonon coupling observed at the Néel temperature of $SmCrO_3$, and other $RCrO_3$ that contain magnetic rare-earths,[21] confirms that the antiferromagnetic ordering of the Cr^{3+} moments, and the subsequent effect that this has on the Sm^{3+} sublattice, alters the characteristics of the structure below this temperature, and could allude to the origin of these induced polarisations.[22] No such effects are observed for orthochromites that contain a non-magnetic A site such as $R = Y^{3+}$, La^{3+}, and Lu^{3+}.

With the materials possessing such an assortment of functional properties, this has resulted in many different synthesis routes for $RCrO_3$ and their doped counterparts. The hydrazine method uses basic $(N_2H_4)\cdot 2H_2O$ to crystallise $LaCrO_4$, which is then decomposed into $LaCrO_3$.[23] Microwave-assisted techniques follow a similar reaction pathway, starting from an amorphous phase formed after 10 minutes of microwave irradiation.[1] The spray pyrolysis technique involves the atomisation and spraying of a solution containing lanthanum and chromium nitrates onto heated yttria-stabilised zirconia electrolyte substrates.[24] Procedures such as the calcination of co-precipitated precursors and sol-gel prepared citrate gels are used to enhance the chemical homogeneity of the precursors prior to annealing.[25,26] Metathesis reactions of metal chloride salts use Li_2O to drive the reaction forward through the formation of lithium chloride.[27] Self-propagating high temperature synthesis makes use of strong oxidising agents mixed with the reagents to maintain the reaction once ignited by an electric filament.[28] Finally, many rare-earth orthochromites have been produced through traditional solid state synthesis.[29] It is noted that for all of the methods listed above, an extra high-temperature annealing step typically above 900 °C, is required post-treatment in order to achieve highly crystalline products.[30]

Some of the reported hydrothermal syntheses of orthochromites also required high-temperature sintering steps after the material had been heated in an autoclave, consequently removing the *soft chemical* aspect.[31,32] The few reports of hydrothermal routes focus only on $LaCrO_3$ and Ca-doped analogues,[33,34] whilst it was shown that crystallisation of $LaCrO_3$ can occur at temperatures as low as 260 °C if high potassium hydroxide concentrations were used in week-long reactions.[3]

A single-step hydrothermal synthesis of the complete range of $RCrO_3$ (where $R =$

La to Lu) is possible, but only at temperatures elevated above those usually used in the laboratory. The powders were crystallised at 370 °C for 48 hours from co-precipitated hydroxide precursors.[5]

4.1.1 Scope of this chapter

This chapter covers the high-temperature hydrothermal synthesis of a new mixed rare-earth chromium $La_xSm_{1-x}CrO_3$ perovskite solid solution. In-depth characterisation of these new materials was completed through the use of powder XRD, Raman spectroscopy, and electron microscopy.

The analysis of Raman spectra throughout the series, supported by shell model calculations, provided clarification on the phonon mode behaviour within the complex low-wavenumber region that was highlighted in previous work by Weber *et al.*[35] The presence of mode mixing in this region was confirmed and the contributions of specific atomic motions to various observed phonon modes were explored.

Electron microscopy is used to observe particle morphologies of these materials, whilst STEM provides atomic resolution imaging that can be compared directly to the crystal structures obtained from Rietveld refinement.

The evolution of the magnetic behaviour of each solid solution as a function of x was studied, and is presented alongside an investigation into any potential magnetoelectric effects that can be induced by the anisotropic exchange interactions between the separate samarium and chromium magnetic sublattices. Pyroelectric measurements and low-temperature dielectric measurements were used to examine the possibility of polar ordering in these materials. Temperature-dependent Raman scattering was used to support these measurements.

4.2 Synthesis and Preparation

The hydrothermal synthesis of the rare-earth orthochromite series $La_xSm_{1-x}CrO_3$ requires temperatures higher than 240 °C, which is typically the maximum temperature that a conventional Teflon®-lined autoclave can be taken to. This method therefore makes use of the high-temperature and high-pressure hydrothermal apparatus described in Chapter 2.

The amorphous hydroxide precursor of $La_{0.5}Sm_{0.5}CrO_3$ was produced by dissolving 1.0832 grams of lanthanum(III) nitrate hexahydrate (99.999% Aldrich),

1.1115 grams of samarium(III) nitrate hexahydrate (99.9% Aldrich), and 2.0006 grams of chromium(III) nitrate nonahydrate (99% Aldrich) into 100 ml of deionised water before adding 25 ml of 2.0 M KOH solution, resulting in the precipitation of the mixed-metal hydroxide gel. The gel was stirred for 15 minutes to ensure adequate mixing, before being separated from solution by suction filtration and washed several times with deionised water. Excess moisture was removed by heating the gel to 75 °C for 24 hours, before the green precipitate was ground into a fine powder. Typically 5 mmol of $Cr(NO_3)_3{\cdot}9H_2O$ was dissolved whilst $La(NO_3)_3{\cdot}6H_2O$ and $Sm(NO_3)_3{\cdot}6H_2O$ were used in appropriate amounts to give solid solutions of the desired compositions.

Typically, reaction yields were of the order of 85-90%, with precipitate masses being $\sim$ 1.4 grams.

Approximately 400 mg of the powdered precursor was placed inside an Inconnel high-pressure vessel along with 20 ml of deionised water. With regards to Figure 2.2, this fill fraction produced high autogenous pressures that were maintained at *ca* 200 bar. Although it was possible to form the orthochromites using a lower fill fraction and therefore lower pressure, these particular powders often contained small amounts of $La(OH)_3$, and were not as crystalline as those formed under pressures of 200+ bar.

The duration of hydrothermal treatment was just 6 hours, an improvement on the previously reported method of Sardar *et al.* whom used an identical technique, but maintained the reaction temperature for 48 hours.[5]

The outcome of the reaction was found to depend on the temperature much more than the pressure. It is possible to produce $LaCrO_3$ at 375 °C, and whilst there was no definite correlation through the series, it seemed that the optimum conditions were *ca* 390 °C for the slightly more distorted $SmCrO_3$. The controlled temperature of the external heating block was varied between 450 to 550 °C, approached at a rate of 20 °C/minute, to give solution temperatures within the vessels of 370 to 390 °C and pressures of $\sim$ 210 bar. Solutions that were held under these conditions for 6 hours produced highly crystalline bright green rare-earth orthochromite powders which were collected and washed under suction filtration, before being dried at 75 °C in air for characterisation.

4.3 Results and Discussion

The formation of the never-before-reported series of rare-earth chromites $La_xSm_{1-x}CrO_3$ requires a minimum reaction temperature of 370 °C. It was possible to produce the perovskite phase at temperatures lower than this, however, the end product always contained small amounts of the $Sm(OH)_3$ impurity, as shown by Figure 4.2. Although the X-ray patterns of $R(OH)_3$ are very similar, the impurity is thought to be $Sm(OH)_3$ because the main perovskite phase shows a slight shift to lower 2θ, indicating that perhaps more of the larger La^{3+} is in the structure.

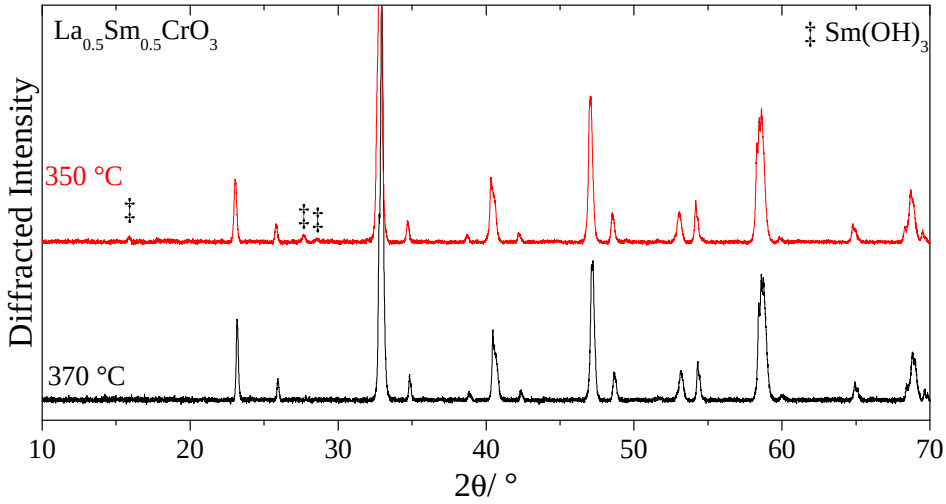

Figure 4.2: XRD patterns of $La_{0.5}Sm_{0.5}CrO_3$ hydrothermally synthesised at temperatures of 370 °C (black) and 350 °C (red). The ‡ symbol highlights the $Sm(OH)_3$ impurity present in the latter.

The hydrothermal treatment of the amorphous precursor using a conventional Teflon®-lined autoclave at 240 °C for varying durations is summarised in Figure 4.3. The amorphous precursor was placed inside the Teflon® liner along with deionised water before being sealed and heated. Reaction durations of 48 hours resulted in the formation of small amounts of $LaCO_3OH$ and the perovskite phase $La_{0.5}Sm_{0.5}CrO_3$, and increasing the length of reaction to 5 days caused both phases to crystallise further. Attempts were also made to replicate the synthesis method of Zheng *et al.* which uses very concentrated potassium hydroxide solution as the mineraliser in week-long reactions.[3] The nitrates were dissolved into 8.0 M KOH solution and heated inside the autoclaves to 240 °C for 7 days. Akin to the above reactions, this did form the perovskite phase, however, also contained $La(OH)_3$ as the impurity phase, shown in Figure 4.3 d).

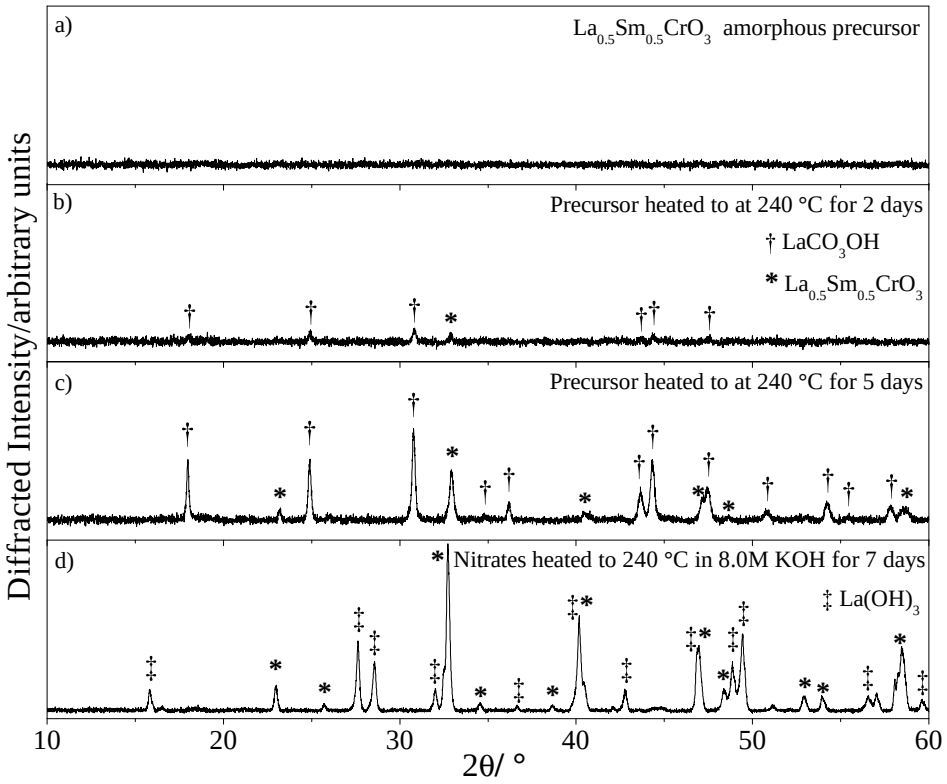

Figure 4.3: XRD patterns of a) amorphous hydroxide precursor, and attempted syntheses of $La_{0.5}Sm_{0.5}CrO_3$ in water at 240 °C for b) 2 days, c) 5 days, and d) shows a reaction in concentrated base for 7 days (following the report of Zheng *et al.*[3]). The symbols of *, †, and ‡ label reflections of $La_{0.5}Sm_{0.5}CrO_3$, $LaCO_3OH$, and $La(OH)_3$ respectively.

The coprecipitation of mixed nitrate salts works well for conventional solid state synthesis also, as previously reported for several $RCrO_3$.[25,36,37] Figure 4.4 shows XRD patterns of the $La_{0.5}Sm_{0.5}CrO_3$ solid solution prepared through different methods; one which was hydrothermally treated and one through solid state synthesis. Both routes started from the amorphous hydroxide precursor described above. For the conventional solid state technique, the powdered precursor was fired at 1200 °C for 12 hours, resulting in the formation of the perovskite phase. The reflections in the pattern of the sample produced through hydrothermal synthesis are slightly more resolved, indicating that it could be the more crystalline of the two.

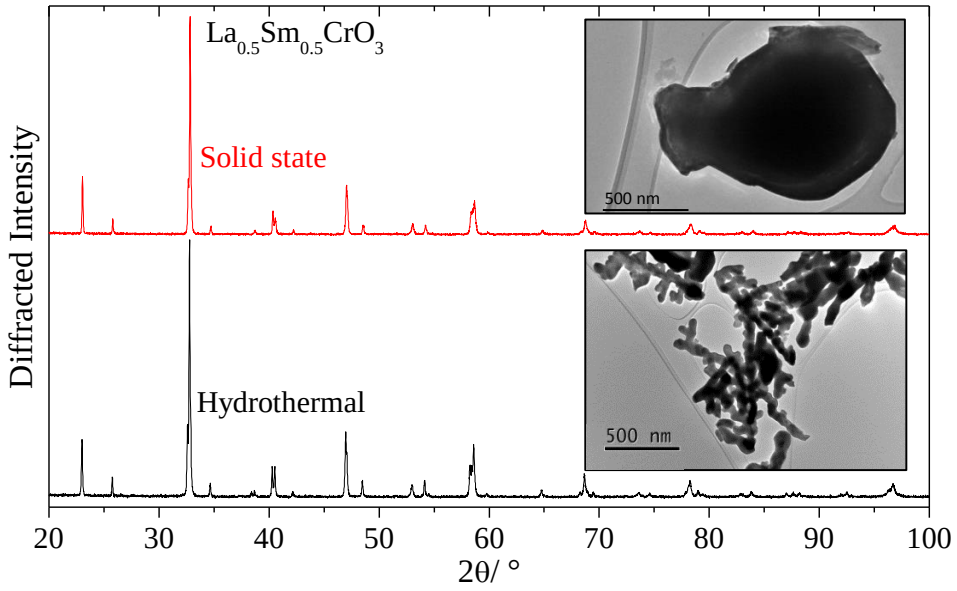

Figure 4.4: Comparison of XRD patterns along with TEM images of $La_{0.5}Sm_{0.5}CrO_3$ from hydrothermal (lower) and solid state (upper) synthesis.

TEM images from each are also included in Figure 4.4, and show a stark difference in particle morphology and size. The single solid state crystallite shown is not representative of the bulk sample, however, as there is a much greater variation in particle size for the solid state material, ranging from ~ 10 μm down to ~ 0.1 μm. The particle sizes observed from the hydrothermally prepared materials are much more homogeneous.

4.3.1 Characterisation

4.3.1.1 Powder X-ray Diffraction

Solid solutions of $La_xSm_{1-x}CrO_3$ with $x = 0.0$, 0.25, 0.50, 0.625, 0.75, 0.875, and 1.0 were prepared from hydrothermal treatment of amorphous precursor at 370 °C for periods of 6 hours. High-resolution XRD patterns, given in Figure 4.5, of the green polycrystalline powders confirm they are phase pure. The increasing amount of samarium in the structure causes the intensity of some reflections to alter, as well as the observed peak shifts for all reflections. This peak shift is due to the changing dimensions of the unit cell as the larger La^{3+} is substituted for the smaller Sm^{3+} cation.

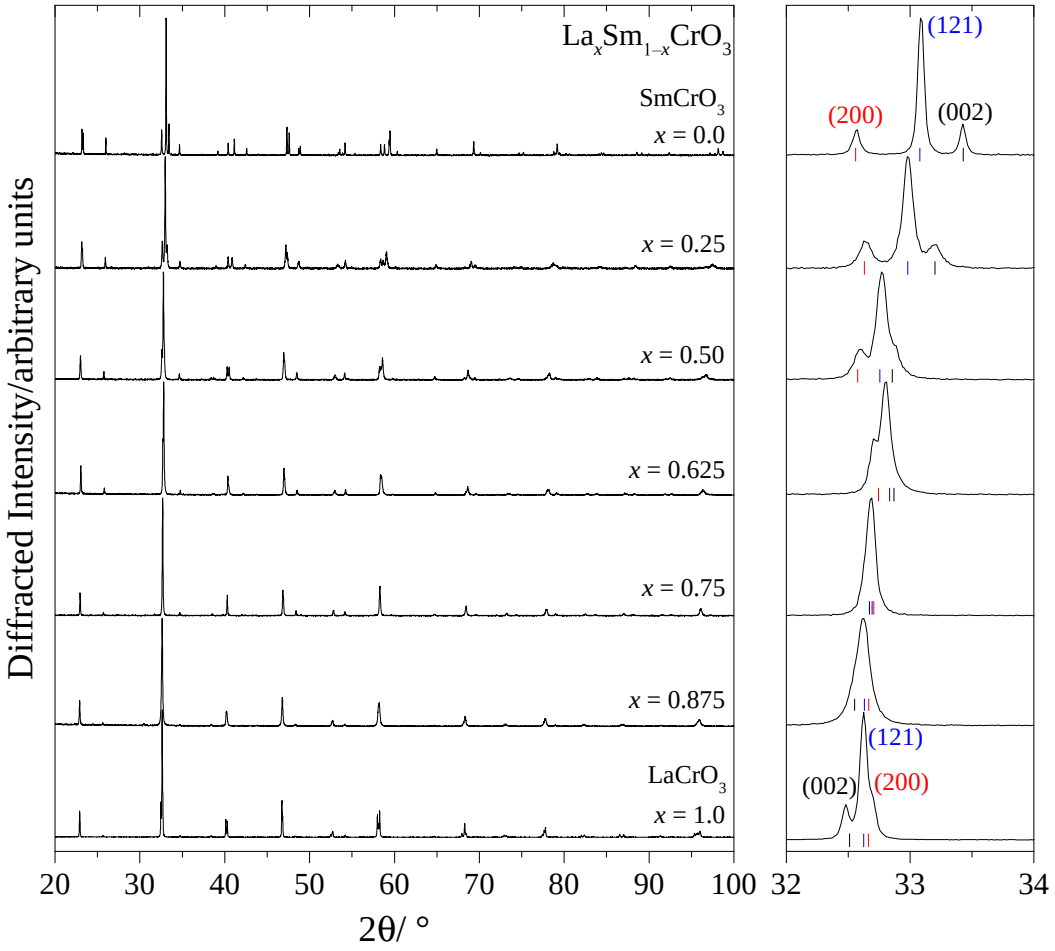

Figure 4.5: Powder XRD patterns of $La_xSm_{1-x}CrO_3$ solid solutions. The right-hand panel enlarges the region including the (002), (121), and (200) reflections.

This observed shift and the more subtle effects that this has on the separate lattice parameters (a, b, c) are highlighted in the right-hand panel of Figure 4.5, which focuses on the (002), (121), and (200) group of reflections. The (121) reflection exhibits a dependency on all three lattice parameters, and moves to a lower 2θ value with increasing Sm^{3+}, and relative to the other two reflections remains in the same position. The (002) and (200) reflections, however, switch positions relative to each other as the unit cell shrinks from $LaCrO_3$ to $SmCrO_3$. This shows how the $c > a$ relationship, discussed for $LaCrO_3$ in the introduction to this chapter, changes throughout the series. It seems that the c/a ratio approaches unity in the solid solution of $x = 0.75$, more so than in $LaCrO_3$.

Rietveld refinements against the high-resolution PXRD data show that all of the solid solutions in the $La_xSm_{1-x}CrO_3$ series crystallise with a distorted perovskite

structure that can be described by the space group *Pnma* (no. 62). The lattice parameters obtained from the end members, $LaCrO_3$ and $SmCrO_3$, agree well with those reported in the literature, which were synthesised through a mixture of hydrothermal and other techniques, and can be seen in Table 4.1.

Table 4.1: Comparison of lattice parameters for end members $LaCrO_3$ and $SmCrO_3$, obtained from Rietveld refinement against PXRD data, against values previously reported in the literature.

RCrO$_3$	Synthesis technique	a/Å	b/Å	c/Å	V/Å^3
$LaCrO_3$	Hydrothermal (this study)	5.48848	7.77796	5.51879	235.322
	Flux-method[29]	5.477	7.755	5.514	234.202
	Solid-state[38]	5.4786	7.7573	5.5146	234.366
	Solid-state[39]	5.48588	7.76824	5.52467	235.437
	Solid-state[40]	5.4803	7.7597	5.5165	234.592
	Solid-state[41]	5.478	7.757	5.514	234.306
	Hydrothermal[5]	5.49365	7.7766	5.51975	235.814
	Microwave-assisted solid-state[1]	5.4790	7.7616	5.5164	234.589
$SmCrO_3$	Hydrothermal (this study)	5.50385	7.64364	5.36567	225.731
	Flux-method[29]	5.502	7.650	5.372	226.109
	Hydrothermal[5]	5.52357	7.63654	5.36563	226.328
	Microwave-assisted solid-state[1]	5.48848	7.62627	5.35381	224.092

The variation in the primitive unit cell dimensions (a_p) and primitive unit cell volume (V_p) are shown in Figure 4.6. Cell length a increases slightly, whilst both b and c decrease, with increasing Sm^{3+} substitution. Overall, this results in a monotonic decrease in unit cell volume, shown in Figure 4.6 b), and is attributed to the smaller ionic radius of Sm^{3+}. This linear shrinking has been observed for several other mixed rare-earth chromite perovskites, $La_xR_{1-x}CrO_3$ where R = Pr, Nd, and Gd,[40–42] and across the entire series of RCrO$_3$ (from La^{3+} to Lu^{3+}).[1,5]

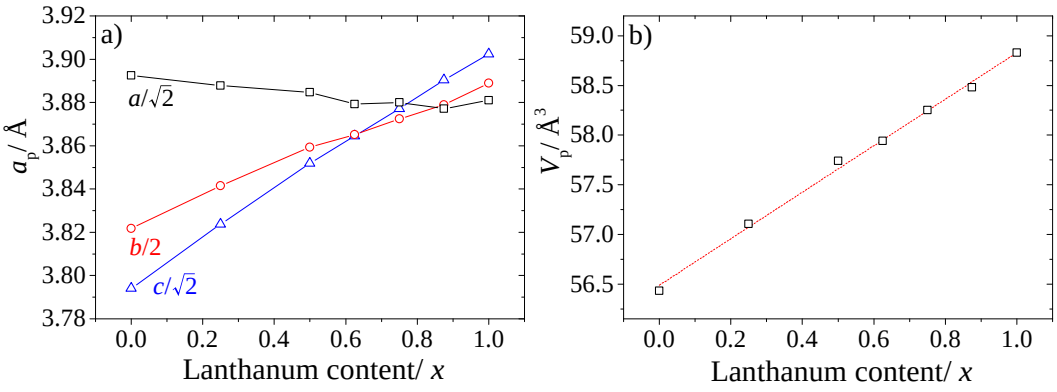

Figure 4.6: Variation of primitive unit cell a) parameters (a_p) and b) volume (V_p) against lanthanum content (x), determined from Rietveld refinement against PXRD data for the $La_xSm_{1-x}CrO_3$ perovskites. Errors bars are smaller than the datapoints.

The lattice parameters obtained from Rietveld refinement, as well as unit cell volumes for each solid solution, are provided in Table 4.2.

Table 4.2: Unit cell parameters and volumes of each solid solution in the $La_xSm_{1-x}CrO_3$ series, based on the orthorhombic *Pnma* space group.

x	a/Å	b/Å	c/Å	V/Å^3
1.0	5.48848(4)	7.77796(6)	5.51879(4)	235.322(3)
0.875	5.48231(17)	7.7561(2)	5.50088(16)	233.929(14)
0.75	5.4868(2)	7.7449(2)	5.4831(2)	233.009(15)
0.625	5.48598(14)	7.7299(2)	5.46514(18)	231.757(12)
0.50	5.49294(11)	7.71860(17)	5.44731(12)	230.954(9)
0.25	5.49810(19)	7.6831(3)	5.40771(18)	228.435(14)
0.0	5.50385(6)	7.64364(8)	5.36567(5)	225.731(4)

Atomic positions were also extracted from Rietveld refinement. For space group *Pnma*, some of the sites have fractional coordinates that are not refineable, for example, the B site Cr^{3+} has a special position of $(0,0,\frac{1}{2})$. The x and z positions, however, are refineable for both the A and O(1) atoms, and it is possible to refine the x, y, and z positions for the O(2) position. The Rietveld refinement made against the PXRD data of $La_{0.5}Sm_{0.5}CrO_3$ is shown in Figure 4.7, and the refinements for each solid solution produced fits of a similar quality. Once individual parameters had stabilised, all of the parameters were refined simultaneously, giving fourteen structural degrees of freedom, including isotropic thermal parameters.

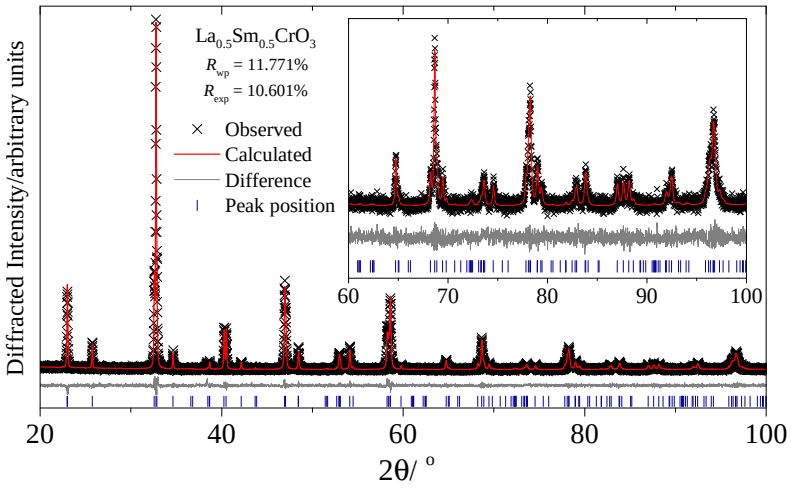

Figure 4.7: Rietveld refinement performed against PXRD data (λ = 1.5406 Å) of $La_{0.5}Sm_{0.5}CrO_3$. Observed (black crosses), calculated (red line), and difference (grey line) patterns are shown. Blue tick marks represent allowed peak positions.

As powder diffraction provides a very limited insight into disorder that takes place

on length scales equivalent to the unit cell, and also because it would be impossible to distinguish between them using X-rays, both the La^{3+} and Sm^{3+} in the mixed solid solutions were modelled using the same $4c$ crystallogrpahic site. In reality, one would imagine that in the solid solutions, the smaller Sm^{3+} cation would have a more distorted local environment than that of La^{3+} when considering only the nearest-neighbour oxide ions. The occupancies for each rare-earth site were fixed during the refinements, however when they were allowed to refine, they remained close to the initial values.

Isotropic temperature factors (U_{iso}), used to described the thermal behaviour of each site, were refined, starting with the heavier atoms. Some of the values for the oxide ions became unphysical, likely due to the weak scattering power of oxygen compared to the much heavier lanthanides, and so is not unexpected.

The refined structural parameters, and fit statistics, for each solid solution in the $La_xSm_{1-x}CrO_3$ series are provided in Table 4.3.

Table 4.3: Structural details obtained from Rietveld refinements against PXRD data for the $La_xSm_{1-x}CrO_3$ solid solutions, including R_{wp} and R_{exp} values for each.

Atom	Site	x	y	z	$U_{iso}/Å^2$
$x = 1.0$				$R_{wp} = 11.987\%$, $R_{exp} = 10.354\%$	
$a = 5.48848(4)$ Å, $b = 7.77796(6)$ Å, $c = 5.51879(4)$ Å					
La	4*c*	0.0188(2)	0.25	-0.0042(3)	0.0056(3)
Cr	4*b*	0	0	0.5	0.0015(4)
O(1)	4*c*	0.494(2)	0.25	0.064(2)	0.003(3)
O(2)	8*d*	0.272(2)	0.035(1)	0.728(2)	0.008(2)
$x = 0.875$				$R_{wp} = 13.717\%$, $R_{exp} = 12.547\%$	
$a = 5.48490(6)$ Å, $b = 7.75658(10)$ Å, $c = 5.50170(7)$ Å					
La/Sm	4*c*	0.0225(3)	0.25	-0.0041(8)	0.0075(6)
Cr	4*b*	0	0	0.5	0.0013(8)
O(1)	4*c*	0.492(2)	0.25	0.061(5)	0.005(5)
O(2)	8*d*	0.284(4)	0.034(2)	0.719(3)	0.005(4)
$x = 0.75$				$R_{wp} = 11.876\%$, $R_{exp} = 10.527\%$	
$a = 5.48687(22)$ Å, $b = 7.74497(22)$ Å, $c = 5.48311(23)$ Å					
La/Sm	4*c*	0.0302(3)	0.25	-0.0067(9)	0.0036(9)
Cr	4*b*	0	0	0.5	0.0093(12)
O(1)	4*c*	0.490(2)	0.25	0.065(5)	0.006(4)
O(2)	8*d*	0.289(5)	0.038(3)	0.718(12)	–0.013(6)
$x = 0.625$				$R_{wp} = 14.265\%$, $R_{exp} = 11.777\%$	
$a = 5.48598(14)$ Å, $b = 7.72994(22)$ Å, $c = 5.46514(18)$ Å					
La/Sm	4*c*	0.0342(3)	0.25	-0.0077(7)	0.0069(8)
Cr	4*b*	0	0	0.5	0.0038(11)
O(1)	4*c*	0.493(3)	0.25	0.073(5)	–0.029(6)
O(2)	8*d*	0.296(3)	0.025(3)	0.707(3)	0.033(6)
$x = 0.50$				$R_{wp} = 11.771\%$, $R_{exp} = 10.601\%$	
$a = 5.49294(11)$ Å, $b = 7.71860(17)$ Å, $c = 5.44731(12)$ Å					
La/Sm	4*c*	0.0382(2)	0.25	-0.0086(6)	0.0016(5)
Cr	4*b*	0	0	0.5	0.0052(9)
O(1)	4*c*	0.486(2)	0.25	0.077(3)	–0.033(5)
O(2)	8*d*	0.292(3)	0.037(2)	0.715(3)	0.005(4)
$x = 0.25$				$R_{wp} = 13.820\%$, $R_{exp} = 13.185\%$	
$a = 5.49810(19)$ Å, $b = 7.68309(27)$ Å, $c = 5.40771(18)$ Å					
La/Sm	4*c*	0.0449(3)	0.25	-0.0094(8)	0.0059(10)
Cr	4*b*	0	0	0.5	0.0034(15)
O(1)	4*c*	0.485(3)	0.25	0.085(4)	–0.004(5)
O(2)	8*d*	0.299(3)	0.046(2)	0.716(3)	0.002(2)
$x = 0.0$				$R_{wp} = 10.200\%$, $R_{exp} = 9.664\%$	
$a = 5.50385(6)$ Å, $b = 7.64364(8)$ Å, $c = 5.36567(5)$ Å					
Sm	4*c*	0.0508(3)	0.25	-0.0106(6)	0.0047(11)
Cr	4*b*	0	0	0.5	0.0005(3)
O(1)	4*c*	0.472(2)	0.25	0.097(2)	–0.008(5)
O(2)	8*d*	0.295(3)	0.049(2)	0.707(3)	0.005(4)

Owing to the decrease in size of the A site cation from $LaCrO_3$ to $SmCrO_3$, there is a corresponding increase in distortion of the structure as it minimises the tension placed upon the A–O distances by increasing the octahedral tilt angles. This is observed in Figure 4.8 a) through decreasing Cr–O–Cr bond angles, which become less linear toward $SmCrO_3$.

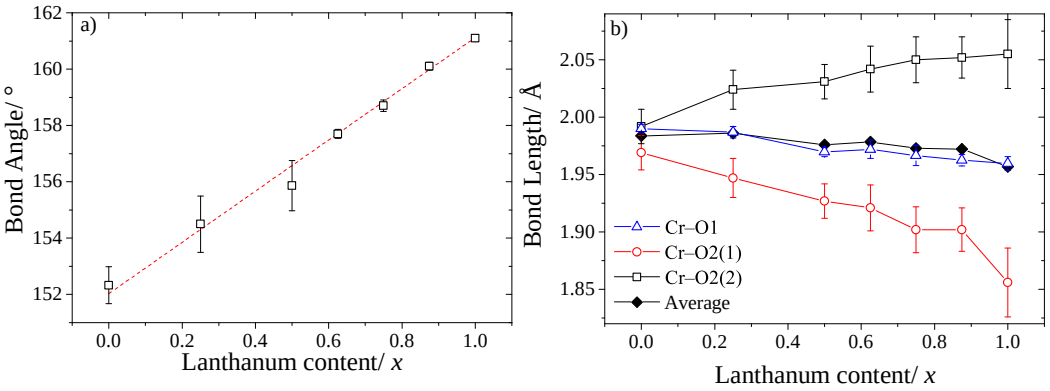

Figure 4.8: Variation of a) Cr–O–Cr bond angles and b) Cr–O bond lengths against lanthanum content, determined from Rietveld refinement. The Cr–O1 bond is oriented along the *b* direction, while both the Cr–O2(1) and Cr–O2(2) bonds lie in the *ac* plane.

The Cr–O bond lengths also vary with increasing Sm^{3+} content, shown in Figure 4.8 b). The Cr–O1 bond lies along the *b* direction of the unit cell, and both the Cr–O2(1) and Cr–O2(2) bonds are oriented in the *ac* plane. As more Sm^{3+} is added into the structure, the Cr–O1 and Cr–O2(1) bonds both increase in length, whilst the Cr–O2(2) bond gets shorter, with the average distance increasing toward $SmCrO_3$. As described above, the decreasing size of the A site (with increasing Sm^{3+} content) places tension on the A–O distances which shorten as the octahedra undergo further rotation. The octahedra themselves are rather rigid, and as the stress upon them is minimised through this rotation, the Cr–O distances increase. The average bond lengths for the end members $LaCrO_3$ and $SmCrO_3$ are 1.9569 Å and 1.9836 Å, respectively, and agree well with those reported previously.[1,29,39] The Cr–O distances and Cr–O–Cr angles for all solid solutions are provided in Table 4.4.

Table 4.4: Cr–O distances and Cr–O–Cr angles from Rietveld refinement of the $La_xSm_{1-x}CrO_3$ solid solutions. Bond lengths Cr–O2(1) and Cr–O2(2) lie in the *ac* plane, while Cr–O1 is oriented along the *b* direction.

x	Cr–O1/ Å	Cr–O2(1)/ Å	Cr–O2(2)/ Å	Average Cr–O bond length/Å	Cr–O–Cr bond angle/°
1.0	1.960(6)	1.86(3)	2.06(3)	1.95(2)	161.10(12)
0.875	1.963(5)	1.902(19)	2.052(18)	1.972(14)	160.30(14)
0.75	1.967(9)	1.90(2)	2.05(2)	1.973(16)	158.7(2)
0.625	1.972(8)	1.92(2)	2.04(2)	1.978(16)	157.10(16)
0.50	1.969(4)	1.927(15)	2.031(15)	1.976(11)	155.9(9)
0.25	1.987(5)	1.947(17)	2.024(17)	1.986(13)	154.0(10)
0.0	1.990(4)	1.969(16)	1.992(15)	1.984(11)	151.9(8)

The Cr–O bond length splitting, where the lengths of the three different bonds diverge from each other, is characteristic of the local structural distortions intrinsic to orthorhombic perovskites, and is observed to increase towards $LaCrO_3$ in Figure 4.8 b). This is contradictory to the results reported by Zhou *et al.*,[43] who found that the maximum value in the bond length splitting was observed at an A site radius of 1.11 Å in both $R CrO_3$ and $R FeO_3$.[44] This corresponds to the ionic radius of Eu^{3+}, and so does not agree with our current findings. It is noted that the study of Zhou *et al.* includes the refinement of neutron data, except for a few absorbing rare-earths (Sm, Eu, and Gd), which would result in more accurate positions for the oxide anions. It is also worth noting that the presence of two rare-earths on the A site, each with a different coordination preference, could perhaps affect the bond length splitting. The observation of increasing bond lengths towards $SmCrO_3$ is supported by several other studies that include $La_xNd_{1-x}CrO_3$ solid solutions.[38,41] It was reported that the decrease in average ionic radius on the A site from La^{3+} to Nd^{3+} causes a similar expansion of the Cr–O distances.

Table 4.5 shows the change in tolerance factor across the $La_xSm_{1-x}CrO_3$ series, and also lists the tilt angles of the CrO_6 octahedra, calculated from the atomic positions. As described in Chapter 1, the tilts ϕ and θ describe the rotation of the octahedra about the [010] and [101] axes, respectively, and were calculated using Equations 1.3 and 1.4.

Table 4.5: Variation of the average ionic radius of the A-site cation and tolerance factor (t) throughout the $La_xSm_{1-x}CrO_3$ series. Octahedral tilt angles, ϕ and θ, are calculated using the atomic positions determined from Rietveld refinement.

x	Mean R^{3+} ionic radius/Å	Tolerance factor t	$\phi_{[010]}/°$	$\theta_{[101]}/°$
1.0	1.216	0.9201	5.18	9.38
0.875	1.206	0.9164	7.41	9.90
0.75	1.195	0.9127	8.12	10.76
0.625	1.185	0.9090	9.01	11.72
0.50	1.174	0.9052	8.80	12.46
0.25	1.153	0.8978	9.60	13.44
0.0	1.132	0.8904	9.99	15.82

The magnitudes of ϕ and θ for the end members agree well with the few values that are reported in the literature,[1,35] whilst a linear trend in θ is observed across the series, shown in Figure 4.9 a). The trend for ϕ is approximately linear with a slightly more erroneous spread of the data, shown in Figure 4.9 b).

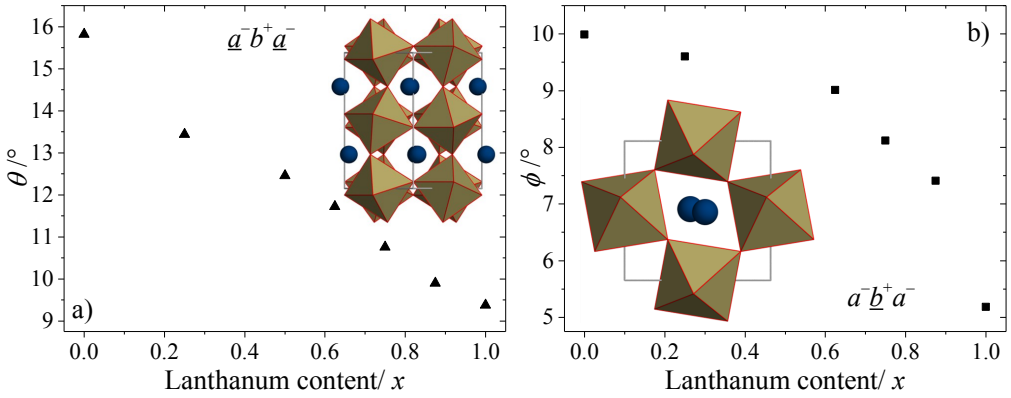

Figure 4.9: Variation in octahedral tilt angles a) θ and b) ϕ, which describe rotations about the [101] and [010] axes respectively, with composition.

4.3.1.2 Raman Scattering

Raman scattering is a technique used ubiquitously in the study of crystalline materials, and is useful to use alongside diffraction in this case, due to its sensitivity to local structural distortions in orthorhombic systems. The frequencies of specific lattice vibrational modes are directly related to the degree of distortion in the structure. It is widely recognised that a complex relationship exists between the lattice distortions of perovskite systems and any magnetic, dielectric, or transport properties that they possess, making understanding of the interplay between the two increasingly important. In RMnO$_3$, for example, the strong mixing and spectral weight transfer that occurs between the A_g antistretching and

bending modes, observed in the high-wavenumber region, correlates with the drastic changes in the magnetic structure from A-type antiferromagnetic for R = La to Eu, to an incommensurate antiferromagnetic structure with sine-wave ordering along the a axis for R = Gd to Ho.[45]

The orthorhombic *Pnma* structure ($a^-b^+a^-$) is one of the most common tilt systems found in perovskites, along with the rhombohedral $R\bar{3}c$ structure ($a^-a^-a^-$). Raman scattering in the ideal cubic perovskite ($Pm\bar{3}m$) is formally forbidden due to symmetry, where all the atoms occupy centrosymmetric sites with fixed coordinates. For the *Pnma* structure, it is the antiphase tilts of adjacent BO_6 octahedra about the [101] and [010] axes that break the cubic symmetry, and give rise to Raman-active vibration modes. Only the B site remains an inversion centre, and of the twelve atomic coordinates for the four non-equivalent sites (A, B, O1, and O2), only five are fixed (A(y), B(x, y, z), and O1(y)), whilst the other seven can be considered as degrees of freedom, resulting in lattice distortions.

It was predicted using group theory,[46] that for the orthorhombic *Pnma* system, there are a total of sixty possible irreducible representations, with twenty-four being Raman-active vibration modes as a result of the structural distortions, and are shown in Equation 4.2.

$$\Gamma = 7\,A_g + 5\,B_{1g} + 7\,B_{2g} + 5\,B_{3g} \tag{4.2}$$

Twenty-five of the remaining representations are IR-active, eight are silent modes, and three are acoustic phonons.

Raman spectra recorded at –150 °C are shown in Figure 4.10 for each solid solution in the $La_xSm_{1-x}CrO_3$ series. The number of observed phonon modes is at most fourteen, with any others being either too weak in intensity or observed at energies below the experimental cut-off of the instrument. The spectra confirm the synthesis of genuine solid solutions of $La_xSm_{1-x}CrO_3$, rather than mixtures of the separate end members, $LaCrO_3$ and $SmCrO_3$. The observation of much broader modes for the solid solutions also supports this as it demonstrates that both La^{3+} and Sm^{3+} are present on the A site. This increased broadening is due to the static chemical disorder, or variance, introduced into the structure from two different rare-earth ions occupying the same crystallographic site.

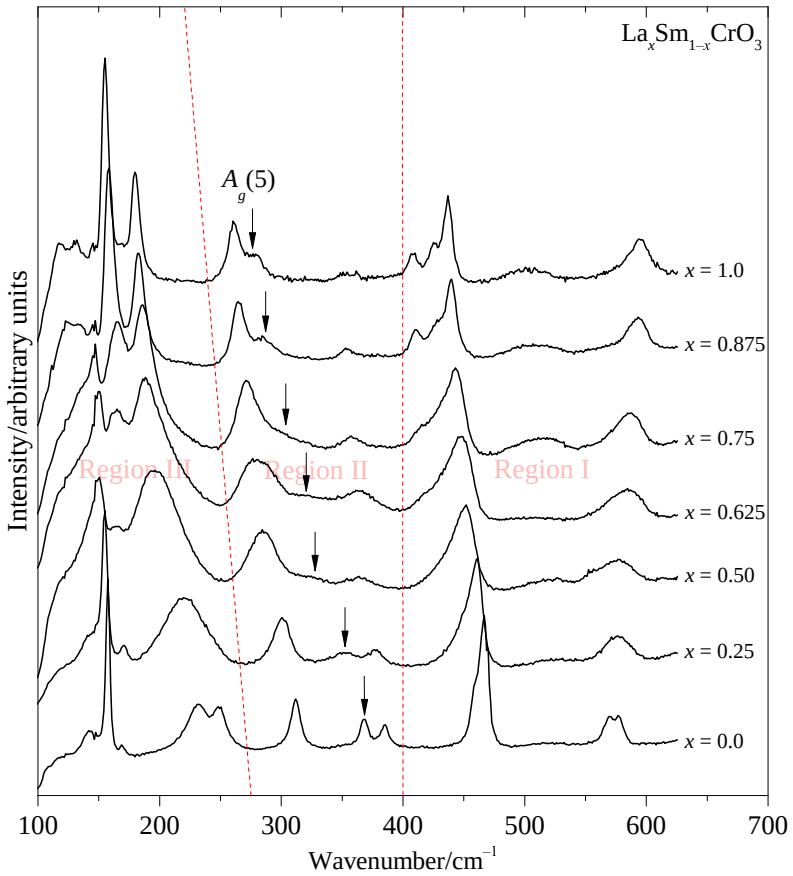

Figure 4.10: Raman spectra of the $La_xSm_{1-x}CrO_3$ solid solutions recorded at –150 °C using a 632.8 nm He-Ne laser line. Arrows show how specific modes, $A_g(5)$ in this case, move through the series. Dashed lines represent regions I, II, and III, of the spectra, that are separated to describe the behaviour of each mode throughout the series.

As a result of this static disorder, the phonon line-widths scale with variance, as demonstrated by the $A_g(4)$ and $B_{3g}(3)$ phonon modes in Figure 4.11. The broadening effects that result from the thermal motion of atoms within the lattice were negated by the spectra being recorded at –150 °C, allowing for the line-widths from static disorder to be solely studied.

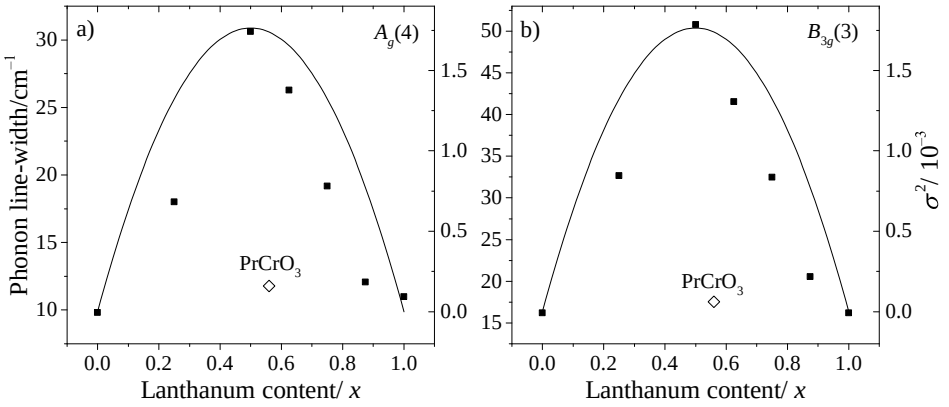

Figure 4.11: Variation in line-widths (datapoints) for the $A_g(4)$ and $B_{3g}(3)$ phonon modes as a function of lanthanum content in the $La_xSm_{1-x}CrO_3$ perovskites. Line-widths for $PrCrO_3$ are included, which would correspond to an A site radius equivalent to a solid solution of $x = 0.56$. The black line shows the A site variance throughout the series, corresponding to the right-hand axes of each plot.

This static disorder is also evident when comparing the spectra of $La_{0.5}Sm_{0.5}CrO_3$ and $PrCrO_3$, in Figure 4.12. The single rare-earth ion on the A site of $RCrO_3$, gives zero variance, resulting in much narrower line-widths for all $RCrO_3$. The distortion in both structures is comparable due to the ionic radius of Pr^{3+} being similar to the mean of both La^{3+} and Sm^{3+} ($r_{Pr^{3+}} = 1.179$ Å, mean of $r_{La^{3+}}$ and $r_{Sm^{3+}} = 1.174$ Å)[4], giving $PrCrO_3$ a tolerance factor of $t = 0.9070$, almost identical to $La_{0.5}Sm_{0.5}CrO_3$ ($t = 0.9052$). This results in very similar Raman spectra for both, but with much broader modes observed for $La_{0.5}Sm_{0.5}CrO_3$.

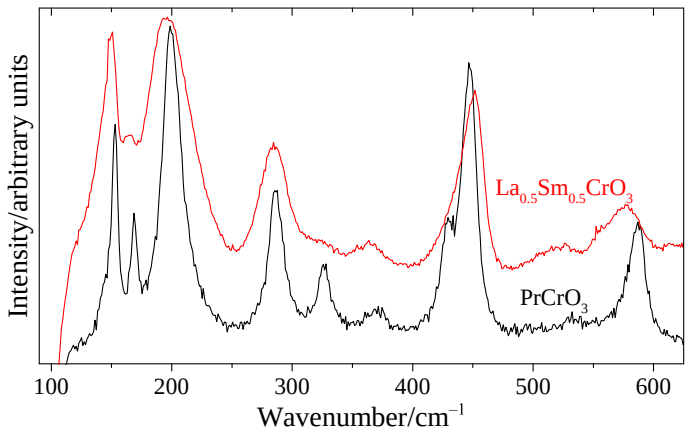

Figure 4.12: Raman spectra of $PrCrO_3$ (black) and $La_{0.5}Sm_{0.5}CrO_3$ (red) recorded at –150 °C, highlighting the increased line-width as a result of static disorder.

It is evident from Figure 4.10 that the majority of the observed phonon modes decrease in wavenumber, or rather, undergo a *mode softening*, towards $LaCrO_3$. The observed phonon modes were assigned to specific vibrational symmetries using data from a previous systematic study of $RCrO_3$ that included the end members $LaCrO_3$ and $SmCrO_3$.[35] This study describes the observation of mode softening for numerous bands throughout the $RCrO_3$ series towards $LaCrO_3$, and ultimately through the assignment of each mode, how they exhibit a close relationship to the level of structural distortion. The prior knowledge of mode assignments for the end members, and the continuous change between the spectra of each solid solution aid the assignment of observed bands for the previously un-reported $La_xSm_{1-x}CrO_3$ series.

The phonon positions and line-widths were determined through profile fitting, as shown in Figure 4.13 for the $La_{0.5}Sm_{0.5}CrO_3$ solid solution. Each spectrum was modelled with 15 or 16 separate modes.

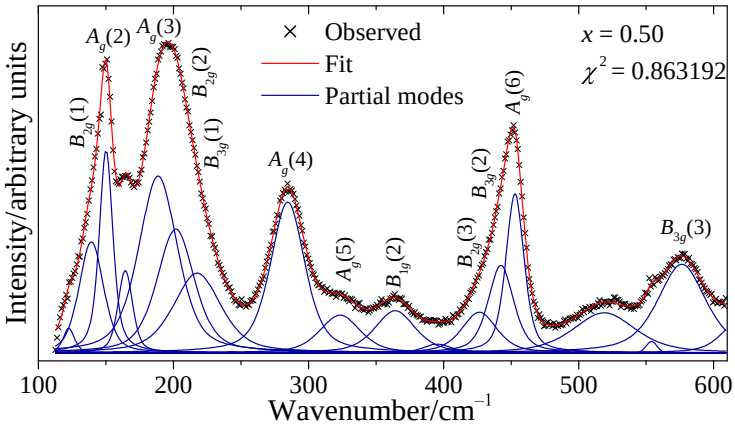

Figure 4.13: Fitted Raman spectrum of $La_{0.5}Sm_{0.5}CrO_3$. Observed data (black crosses), partial phonon modes (blue lines), and overall fit (red line) are shown.

All of the assigned phonon modes and their positions are listed in Table 4.6. For most of the solid solutions, it is possible to assign at least twelve modes with their corresponding vibrational symmetries, and modes such as the $B_{3g}(0)$ become apparent in only a few of the materials (144.6 cm^{-1} for $x = 1$, and 147.8 cm^{-1} for $x = 0.25$). In some of the spectra there are one or two observed modes that remain un-assigned and are not previously reported. It is not clear whether these modes result from a slight impurity or some other artefact present in the powders.

Table 4.6: Assigned symmetries of the observed phonon modes and their band positions (in cm^{-1}) for each solid solution in the $La_xSm_{1-x}CrO_3$ series.

			A_g			B_{1g}		B_{2g}			B_{3g}	
x	(2)	(3)	(4)	(5)	(6)	(2)	(1)	(2)	(3)	(1)	(2)	(3)
1.0	179.7	118.3	260.3	278.0	436.9	357.9	156.4	131.4	407.9	-	425.4	594.0
0.875	182.9	136.0	264.5	286.4	439.9	356.5	156.1	147.2	410.4	202.2	427.8	592.1
0.75	170.6	157.3	271.1	302.9	443.1	360.0	149.4	178.4	417.3	208.0	434.4	586.1
0.625	165.1	180.6	279.8	318.0	448.4	365.0	148.3	193.9	427.0	209.5	444.2	583.7
0.50	155.3	189.7	284.4	331.2	451.8	365.2	148.6	208.6	432.8	218.2	446.6	577.9
0.25	149.6	206.3	300.7	352.9	460.2	377.5	155.2	235.0	456.7	210.1	447.4	576.7
0.0	141.8	231.7	311.7	368.1	466.7	385.2	157.5	250.5	470.0	216.4	460.0	569.3

The low wavenumber modes, particularly the $A_g(3)$ and $B_{2g}(2)$ bands, are estimated from the spectra that display data down to ~ 110 cm^{-1}, however, given the complexity of this region, and also the proximity of these modes to the lower spectral limit of the instrument, their values could be slightly erroneous. Because of this, and the reported existence of modes below this experimental cut-off, predicted from Shell-model calculations,[47] this low wavenumber region was investigated further using an instrument which has a lower spectral cut-off, based at the CRP Gabriel Lippmann in Luxembourg. These low wavenumber Raman data, collected by Mads Weber, are shown in Figure 4.14 and are compared against the current data. The data clearly show the presence of the expected low-wavenumber $A_g(1)$ mode, whilst also displaying the complex region involving the $A_g(3)$ and $B_{2g}(2)$ bands mentioned above. The offset between the datasets is likely due to slightly different instrumental filters used.

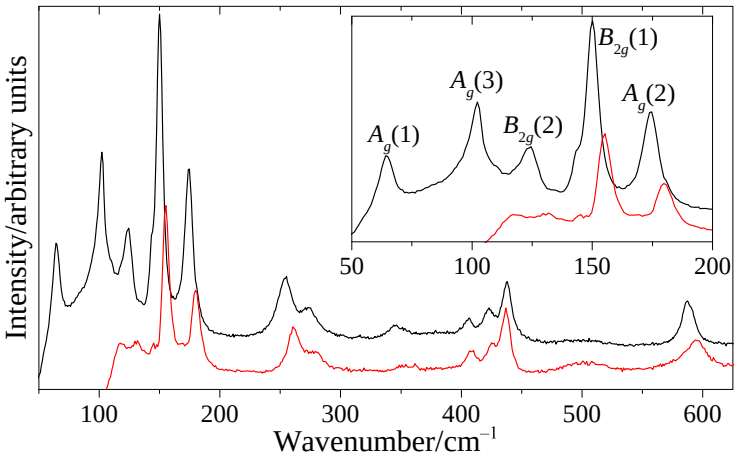

Figure 4.14: Raman data of $LaCrO_3$ measured by Mads Weber using an instrument with lower spectral cut-off (black), based in Luxembourg. The data show the presence of the predicted low wavenumber $A_g(1)$ mode, and provides improved resolution on the $A_g(3)$ and $B_{2g}(2)$ modes that lie close to the spectral cut-off of the instrument based in Warwick (red).

As noted above, the majority of the observed modes decrease in wavenumber undergoing a mode softening as the La^{3+} content increases, consistent with observations from various other orthorhombic rare-earth perovskites, such as RFeO$_3$, RCrO$_3$, and RMnO$_3$.[35,45,48] This is consistent with the less distorted structure of LaCrO$_3$, observed through XRD, and is related to the increasing unit cell volume. The variations in assigned mode positions against La^{3+} content are illustrated in Figure 4.15, which highlights the overall softening. The figure also draws attention to the low wavenumber region, enclosed in the dashed line, which contains several observed modes that exhibit mode mixing behaviour, a phenomenon discussed in more detail further into this chapter.

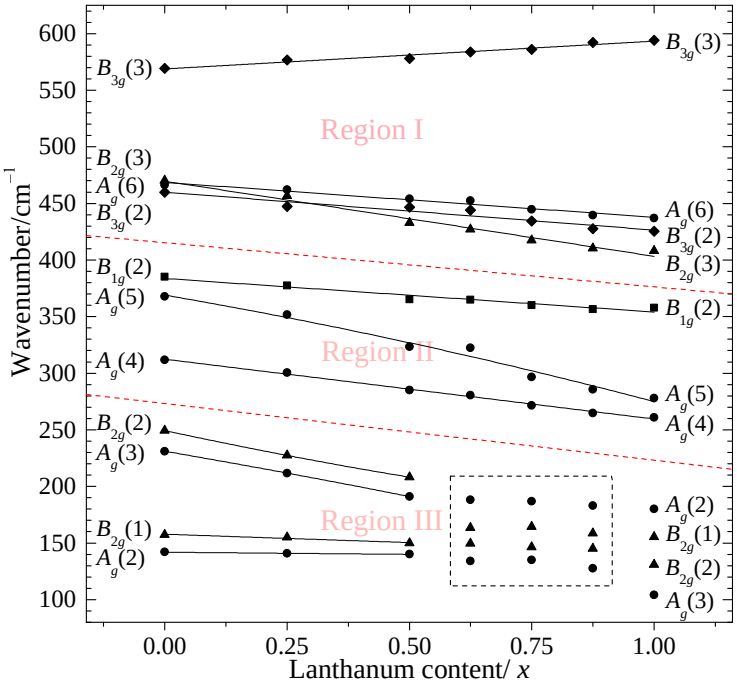

Figure 4.15: Wavenumber shifts in phonon modes for the $La_xSm_{1-x}CrO_3$ series as a function of lanthanum content. The fitted lines act as guides to the eye only. The dashed box signifies the complex low wavenumber region in which several modes transfer vibrational character, and the red lines represent the separate regions discussed in the text.

The specific distortions of the individual observed modes are summarised in Table 4.7, and the main atomic motions involved with those vibrations are described also. These are taken from the previous Raman study of the entire series of RCrO$_3$ by Weber *et al.*,[35] that, crucially, included the end members LaCrO$_3$ and SmCrO$_3$.

Table 4.7: Activating distortions and atomic motions for the assigned vibrations observed in the $La_xSm_{1-x}CrO_3$ series. Mode positions are from $SmCrO_3$ ($x = 0.0$).

Symmetry	Position/ cm^{-1}	Activating distortion	Main atomic motion
$A_g(2)$	141.8	rot[101]	A(z) out-of-plane
$A_g(3)$	231.7	rot[010], JT	BO_6 in-phase y rotations
$A_g(4)$	311.7	A shift	$O_1(x)$, $A(-x)$
$A_g(5)$	368.1	rot[101]	BO_6 out-of-phase x rotations
$A_g(6)$	466.7	rot[101]	BO_6 bendings
$B_{1g}(2)$	385.2	A shift	A(z), $O_1(-z)$
$B_{2g}(1)$	157.5	rot[101]	A(x)
$B_{2g}(2)$	250.5	A shift	A(z), $O_1(z)$
$B_{2g}(3)$	470.0	rot[101]	BO_6 out-of-phase bendings
$B_{3g}(1)$	216.4	rot[101]	A(y)
$B_{3g}(2)$	460.0	rot[101]	out-of-phase O_2 scissors-like
$B_{3g}(3)$	569.3	rot[101]	O_2,O_1 anti-stretching

In order to describe the behaviour of individual modes, the spectra are divided into separate regions as shown in Figures 4.10 and 4.15. Starting with the high wavenumber region, Region I (above 400 cm^{-1}) contains four observed modes, Region II (275 to 400 cm^{-1}) is characterised by three modes, and Region III includes the phonon modes that undergo a complex mode mixing in the range of 100 to 275 cm^{-1}.

4.3.1.2.1 Region I ($>$ 400 cm^{-1})

Region I at first glance appears to be quite sparse with regards to the number of bands, containing just two features observed at approximately 470 and 570 cm^{-1}, with respect to the spectrum of $SmCrO_3$. There are however multiple underlying modes beneath these observed bands, and this becomes more clear when following the continuous change in the spectra across the series.

The broadness of the observed band at $\sim$ 570 cm^{-1} hints that there are multiple modes contributing to this feature; consistent with studies involving polarised Raman scattering from single crystals.[49,50] A mode of $B_{3g}(3)$ symmetry, associated with the stretching vibrations in CrO_6 octahedra, was assigned to this feature. Figure 4.15 shows that this is one of the few modes that doesn't soften in wavenumber towards $LaCrO_3$, and instead, increases by approximately 25 cm^{-1} from $SmCrO_3$ to $LaCrO_3$. The $B_{3g}(3)$ mode involves only stretching vibrations of the CrO_6 octahedra, and not rotational motion, meaning it is insensitive to the degree of structural distortion. The increase is likely related to the change in the average Cr–O distances, which decrease towards $LaCrO_3$. The shorter Cr–O bonds of $LaCrO_3$, with higher force constant k, would vibrate at a higher energy. Though the spread of the data is rather large, this relationship is shown by Figure 4.16, and similar behaviour for the $B_{3g}(3)$ mode is observed in $R$$MnO_3$.[45]

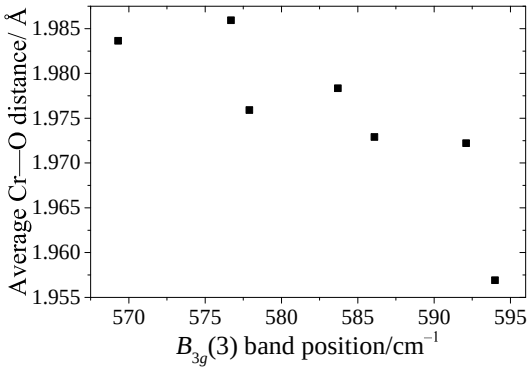

Figure 4.16: Variation of average Cr–O bond length and band position of the $B_{3g}(3)$ mode, associated with stretching vibrations of the CrO_6 octahedra.

The other feature in Region I, observed at approximately 470 cm^{-1}, also has multiple underlying modes which are of three different symmetries: $B_{2g}(3)$, $A_g(6)$, and $B_{3g}(2)$. These modes all decrease in wavenumber towards $LaCrO_3$ and become more resolved in the process, shown in Figure 4.17. The different symmetries of these modes allows them to cross and have almost identical energies, forming a single intense band in $SmCrO_3$. The close proximity of the three bands means that assignment of each becomes difficult for the powder samples, however it is possible with reference to polarised Raman scattering data recorded from single crystals of various $RCrO_3$ in the literature.[47,49] Both the $A_g(6)$ and $B_{3g}(2)$ modes undergo a similar shift throughout the series and do not cross, instead it is the $B_{2g}(3)$ mode that exhibits the most significant shift where it crosses from the high wavenumber side of the group in $SmCrO_3$ to the low wavenumber side in $LaCrO_3$, as shown in Figure 4.17 b).

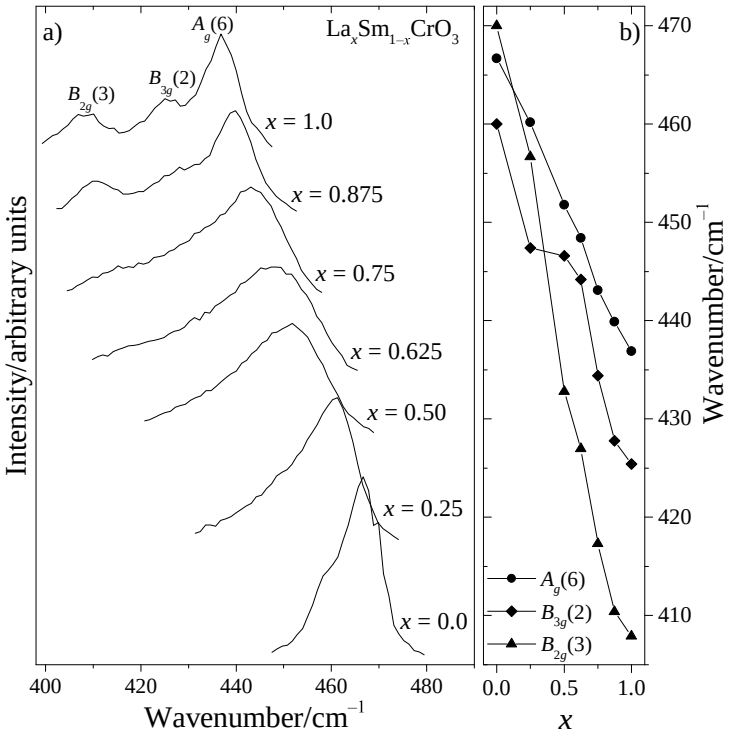

Figure 4.17: Evolution of band positions in Region I (> 400 cm^{-1}). Panel b) shows how the $B_{2g}(3)$ mode undergoes the most significant shift throughout the series.

4.3.1.2.2 Region II (275 to 400 cm^{-1})

Region II contains just three observed bands, assigned as the $A_g(4)$ mode at $\sim$ 311 cm^{-1}, the $A_g(5)$ mode at $\sim$ 368 cm^{-1}, and the $B_{1g}(2)$ mode at $\sim$ 385 cm^{-1}.

The $A_g(5)$ mode shows the most significant shift from one end member to the other, due to its association with a vibration involving the tilting of CrO_6 octahedra, and is assigned as one of the *octahedral soft modes*. These modes exhibit greater dependence upon the octahedral tilt angle compared to other modes. In particular, the $A_g(5)$ mode is associated to the out-of-phase rotation of the CrO_6 octahedra along the [101] direction.

Both the $A_g(4)$ and $B_{1g}(2)$ modes soften towards $LaCrO_3$ and so have some relation to the orthorhombicity of the structure, but much less so than the $A_g(5)$ mode. In $LaCrO_3$, the $A_g(4)$ and $A_g(5)$ modes have very similar wavenumbers, shown by Figure 4.18. In such close proximity, it is possible for same-symmetry modes to mix and transfer a degree of vibrational character to each other, however, since the intensities of the two remain fairly constant throughout the series, this doesn't seem to be the case.

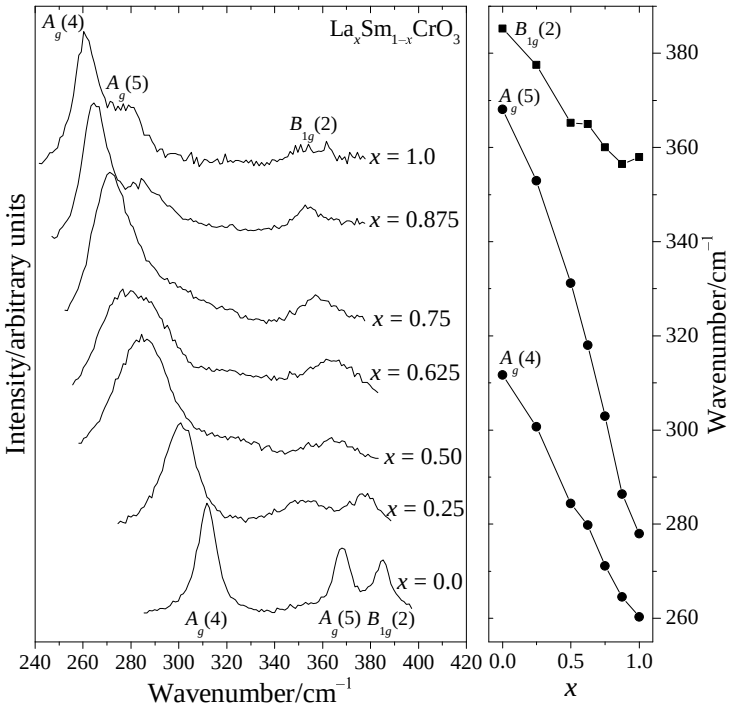

Figure 4.18: Evolution of the band positions in Region II (275 to 400 cm^{-1}), showing the pronounced shift of the $A_g(5)$ mode.

The $A_g(5)$ mode shifts sufficiently enough such that in $SmCrO_3$ it neighbours the $B_{1g}(2)$ band. Different symmetries allow for these modes to cross without interaction, and this would be the case if the size of the A site cation were to decrease further than Sm^{3+}, as the mode crossing occurs in $GdCrO_3$.[35]

4.3.1.2.3 Region III (100 to 275 cm^{-1})

Region III contains at least four distinguishable modes of $A_g(2)$, $A_g(3)$, $B_{2g}(1)$, and $B_{2g}(2)$ symmetry, with other bands such as the $B_{3g}(1)$ mode becoming apparent in only a few of the solid solutions.

It has been shown by Weber *et al.*[35] that two of these low wavenumber modes are only slightly affected by the degree of structural distortion, and instead, are more dependent on the mass of the A site cation. The frequency increase observed for the $A_g(2)$ band towards $LaCrO_3$ is appreciated when considering the approximation of a harmonic oscillator:

$$\omega = \sqrt{\frac{k}{\mu}} \tag{4.3}$$

where ω is the vibration frequency, k the force constant, and μ the reduced mass.

Equation 4.3 shows that lighter atoms should display modes at higher frequencies than heavier ones, and the observed increase is consistent with the decreasing average mass of the A site cation (m_{Sm} = 150.36 and m_{La} = 138.91 g mol^{-1}). The relationship between the average A site cation mass to the $A_g(2)$ band position is shown in Figure 4.19.

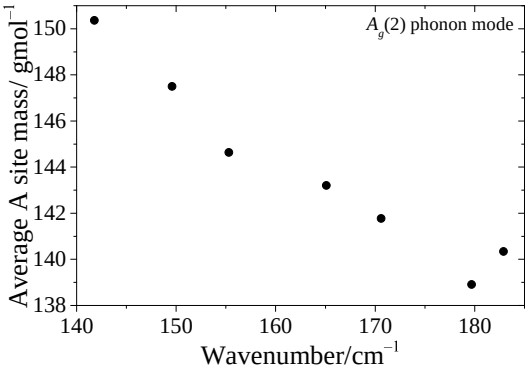

Figure 4.19: Dependence of the $A_g(2)$ mode on A site cation mass for the $La_xSm_{1-x}CrO_3$ series.

Where the $A_g(2)$ and $B_{2g}(1)$ modes increase in wavenumber due to their cation mass dependence, the other two bands in Region III, the $A_g(3)$ and $B_{2g}(2)$ modes, are more dependent on orthorhombic distortion, with the $A_g(3)$ mode being the other octahedral soft mode, associated with the in-phase tilting of the CrO_6 octahedra along the [010] direction. Like the majority of the other observed modes, these soften in wavenumber towards $LaCrO_3$, making Region III particularly complex due to the convergence of two band pairs, each containing a A_g and B_{2g} mode. It is forbidden for modes of the same symmetry to cross, so when they are in close proximity to each other, they display a mode mixing behaviour, where a degree of both vibrational character and intensity is transferred. Such behaviour was observed in the previous study by Weber *et al.*,[35] however, the evolution of each band proved difficult to trace as the investigation involved only end members $RCrO_3$ where $R = La^{3+}$, Pr^{3+}, and Sm^{3+}. The study of $La_xSm_{1-x}CrO_3$ solid solutions provided more clarity regarding this region, allowing for closer inspection of the mixing interactions.

Figure 4.20 shows that with increasing La^{3+} content, the $A_g(2)$ and $A_g(3)$ modes approach each other ultimately leading to a crossover which is accompanied, or rather evidenced by, an exchange of their intensity. Such changes also occur for the two B_{2g} modes: in $LaCrO_3$ the $B_{2g}(2)$ mode is weak but is reasonably intense in $SmCrO_3$, whilst the $B_{2g}(1)$ mode is very intense in $LaCrO_3$, then becomes weaker

throughout the series before sharpening again in $SmCrO_3$. The observed intensity changes and close approach, but not crossing, of the modes are strong indications of this mode mixing.

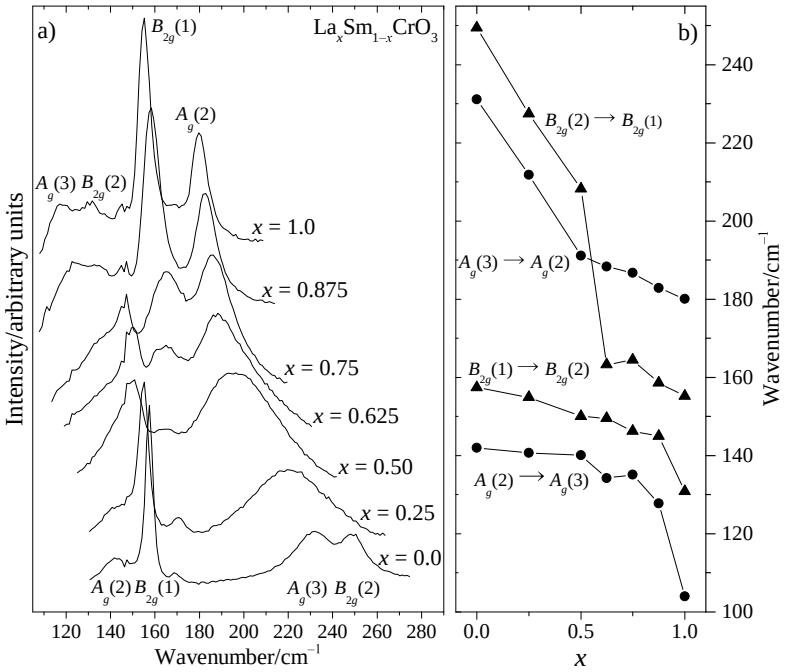

Figure 4.20: Band evolution in Region III (100 to 275 cm^{-1}), with b) showing the mode repulsion in more detail, discussed in the text.

Ultimate proof of this mode mixing is confirmed by the use of Shell-model calculations, which provide an idea of the mixing involved for each individual mode. These lattice dynamical calculations make use of the model developed for $LaCrO_3$ by Iliev *et al.*,[47] and this was used as an initial configuration for the $La_xSm_{1-x}CrO_3$ series. Described in Chapter 2, these calculations were performed using the program GULP,[51] which represents the A and B site cations as point charges, and the oxide ions as a charged core surrounded by a charged massless shell linked through spring constant k. The program makes use of a Buckingham interatomic potential, and the variables used by Iliev *et al.*[47] to model $LaCrO_3$ formed our starting parameters. These were then fitted to the refined structural parameters of the current solid solutions, and the final values for these are summarised in Table 4.8. The calculated structure was found to agree well with the experimental data, with the deviation in lattice parameters for each solid solution being lower than 1%.

Table 4.8: Short range potentials and shell-model parameters used in the lattice dynamical calculations for the solid solutions in the $La_xSm_{1-x}CrO_3$ series. Z and Y are the core and shell charges of an ion, respectively, and k is the spring constant which links the core and shell. A and ρ are constants specific to each ion pair, and C is a constant. Shell-model calculations were performed by Dr Mael Guennou.

Ion	Z/ |e|	Y/ |e|	k/ eV Å^{-2}	ion-pair	A/ eV	ρ/ Å	C/ eV Å^6
La^{3+}	2.85	-	-	La–O	1284.6	0.3628	-
Sm^{3+}	2.85	-	-	Sm–O	1331.3	0.3488	-
Cr^{3+}	2.85	-	-	Cr–O	1717.1	0.2947	-
O^{2-}	0.80	–2.7	74.92	O–O	22764.0	0.1490	20.37

Phonon frequencies were calculated from these parameters and are within the common accuracy of 10 %. In order to visualise the phenomenon of mode mixing, eigenvectors and the contributions of the atoms to each vibration involved in the mode mixing were calculated. The evolution of the atomic contributions towards the two A_g and B_{2g} modes throughout the $La_xSm_{1-x}CrO_3$ series are shown in Figure 4.21. It is clear that a crossover is observed for both the A_g and B_{2g} phonon pairs and the contributions of each vary throughout the series. The most pronounced crossover is observed between the $B_{2g}(2)$ and $B_{2g}(1)$ modes. The $B_{2g}(2)$ mode in $SmCrO_3$ involves only vibrations associated with oxygen ions, i.e. the octahedra, whereas it becomes more dominated by the A cation motion through the series towards $LaCrO_3$, and vice versa for the $B_{2g}(1)$ mode. A similar behaviour is exhibited again between the $A_g(2)$ and $A_g(3)$ modes, where the former is associated mostly with A cation vibrations, and the latter is dependent upon the degree of orthorhombicity in the structure, however it is very clear from Figure 4.21 that these contributions change with composition.

The more pronounced crossover and drastic change in intensity between the two B_{2g} modes compared to the A_g modes is perhaps supported by the closer approach of the two B_{2g} modes observed in Figure 4.20 b). It is likely that this close-approach allows for a greater transfer of vibrational character between the two bands.

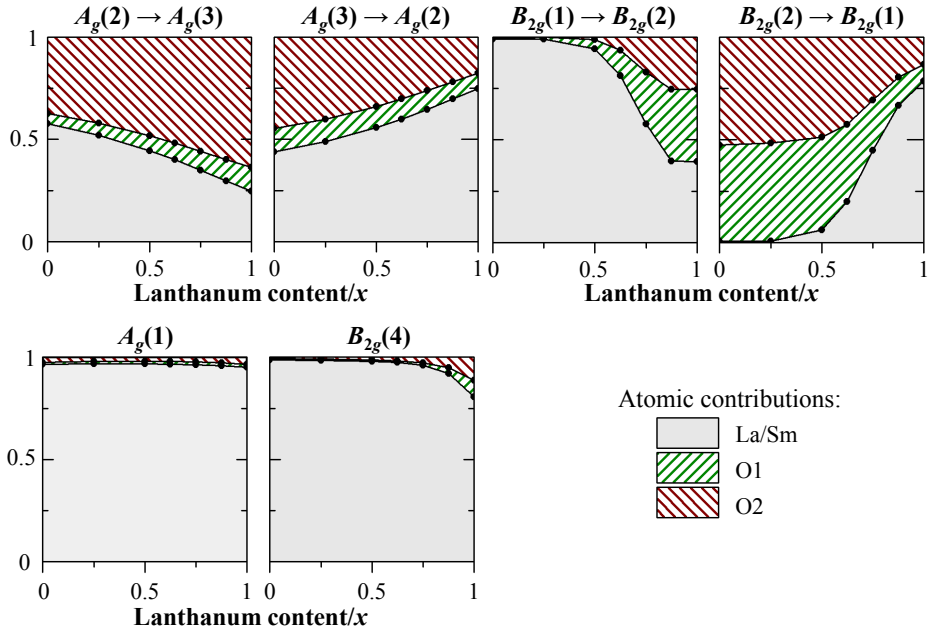

Figure 4.21: Atomic contributions to the two A_g and two B_{2g} phonon modes involved in the mode mixing phenomenon observed in Region III, calculated from the Shell-model. The atomic contributions to the $A_g(1)$ and $B_{2g}(4)$ modes remain dominated by A cation motion across the series, and are provided for comparison. The Shell-model calculations were performed by Dr Mael Guennou.

It is mentioned above that the two *octahedral soft* modes exhibit a much greater dependence on the rotation of the octahedra within the perovskite structure. It has been shown by studies of $R\mathrm{MnO_3}$,[45] and also temperature-dependent Raman studies of $R\mathrm{AlO_3}$ and $\mathrm{SrTiO_3}$ across their noncubic-to-cubic phase transitions,[52,53] that these soft modes typically scale with the octahedral tilt angle, and so can be used as a direct means of estimating the level of structural distortion. In the rhombohedral structures of $\mathrm{LaAlO_3}$ and $\mathrm{LaNiO_3}$, the A_{1g} mode shows a linear dependence upon the octahedral tilt angle, with slopes of 23.5 and 23 $\mathrm{cm^{-1}/^\circ}$, respectively.[54–56] In these rhombohedral structures, the rotation of the $\mathrm{BO_6}$ octahedra are about the $[111]_p$ psuedocubic diagonal of the unit cell. Incidentally, an almost identical relationship is observed between the wavenumber shift of octahedral soft modes and tilt angles of the octahedra in orthorhombic *Pnma* perovskites such as orthomanganites,[45] orthoscandates,[57] and orthochromites,[35] with slopes of ~ 22 $\mathrm{cm^{-1}/^\circ}$. It is expected that the wavenumber of the soft modes would decrease to zero should the tilt angle go to zero.

The relationships between the observed wavenumber shift of the two A_g soft modes and the octahedral tilt angles $\phi_{[010]}$ and $\theta_{[101]}$ are shown in Figure 4.22. The

relationship between parameters such as ionic radius, tolerance factor, tilt angle, and composition is close to linear, so any one of them can be used to characterise the variation in phonon positions.

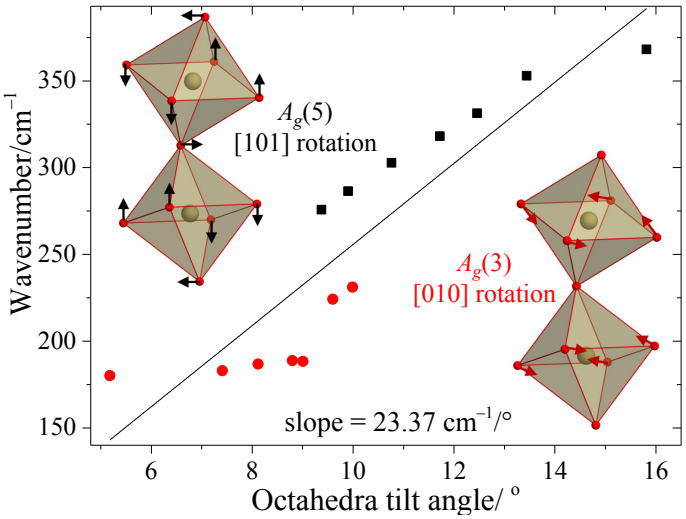

Figure 4.22: Phonon band positions of the two A_g octahedral soft modes as a function of octahedral tilt angle, $\phi_{[010]}$ and $\theta_{[101]}$, calculated from results of Rietveld refinement. The black line is a linear fit to the data points.

The observed slope between the two is equal to 23.37 cm^{-1}/°, and it is noted that the data points for the $A_g(3)$ mode are rather erroneous compared to the linear fit. Due to the involvement of the $A_g(3)$ band in the mode repulsion interactions described above, the accurate determination of the band positions becomes tricky and therefore produces a large deviation of data. Despite this, the slope does agree well with the value of 24.3 cm^{-1}/° reported by Weber *et al.*,[35] even using the limited range in ionic radii provided by La^{3+} to Sm^{3+}, compared to the entire range of $RCrO_3$ used previously.

4.3.1.3 Electron Microscopy

Transmission electron microscopy performed on the $La_xSm_{1-x}CrO_3$ series shows the homogeneous formation of $\sim$ 1 μm crystals which have dendritic-type morphologies for the hydrothermally-prepared materials. A TEM image of $La_{0.5}Sm_{0.5}CrO_3$ crystallites, along with an indexed selected area electron diffraction (SAED) pattern of a crystallite aligned along the [101] zone axis are shown in Figure 4.23.

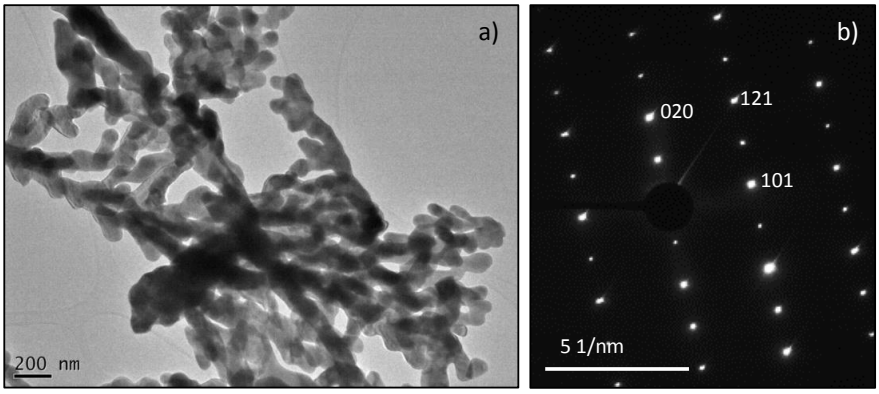

Figure 4.23: TEM image of hydrothermally synthesised $La_{0.5}Sm_{0.5}CrO_3$, with an indexed SAED pattern taken from a crystallite aligned along the [101] zone axis shown in b).

TEM images for the other solid solutions in the $La_xSm_{1-x}CrO_3$ series are shown in Figure 4.24. It can be seen that this dendritic-type morphology is characteristic of each material, and there are no obvious changes to the size and shape of the observed crystallites as a function of x.

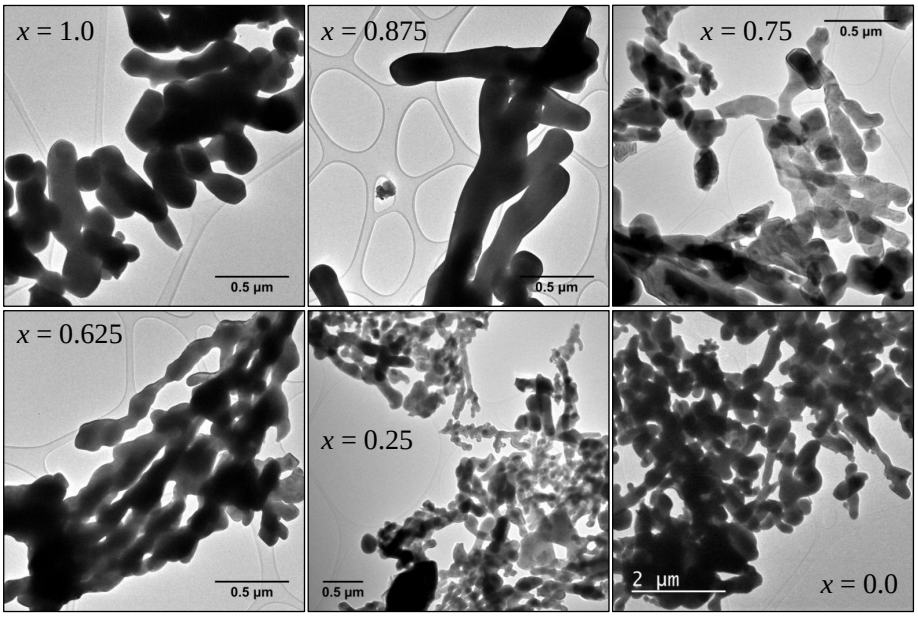

Figure 4.24: TEM images showing crystallite size and morphology for all solid solutions, except $x = 0.5$, in the $La_xSm_{1-x}CrO_3$ series.

As mentioned briefly above, the crystal morphology differs between samples prepared through the hydrothermal technique, compared with those from the solid state method, and it is often the case that the use of hydrothermal synthesis leads

to novel and unique crystal morphologies.[58]

In a previous study based on the hydrothermal synthesis of RCrO$_3$,[5] under the same conditions, the materials were shown to form agglomerated particles rather than the dendritic-type shapes observed here. Only when surfactants or additives, such as sodium dodecyl sulfate (SDS), were added to the hydrothermal reaction medium were the above dendritic-like morphologies observed. In the present case, however, it is clear that the end members form similar morphologies to the mixed solid solutions. It therefore can't be concluded that it is the doping of a second rare-earth cation onto the A site that influences the crystal morphology, such that these dendritic-like crystallites become the preference for growth. However, these types of crystals were observed in Ca- and Bi- doped $LaCrO_3$, produced through high-temperature hydrothermal synthesis,[59] and citrate-nitrate combustion method,[60] respectively.

The high degree of crystallinity of the $La_xSm_{1-x}CrO_3$ materials is shown by high angle annular dark field scanning transmission electron microscopy (HAADF-STEM), through which it was possible to obtain atomic resolution images, shown in Figure 4.25. This figure shows a crystallite that is aligned along the [101] zone axis, providing large separation between neighbouring rare-earth and chromium atomic columns, which appear as brighter, less intense areas, respectively. The crystal structure is compared against the enlarged region in b), and confirms the assignment of rare-earth and chromium columns. The faint smearing of the signal observed between the rare-earth columns corresponds to the small contribution of electron density from the oxide anions, as seen through comparison with the crystal structure in c).

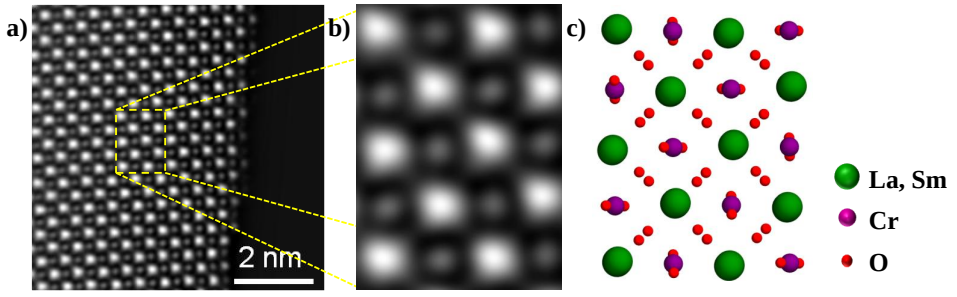

Figure 4.25: HAADF-STEM image of a) $La_{0.5}Sm_{0.5}CrO_3$ crystallite aligned along the [101] zone axis, with clear atomic columns of R^{3+} (brighter intensities) and Cr^{3+} (less intense) cations. Enlarged region b) highlights the observed oxygen contrast between R^{3+} atomic columns, and is compared with the crystal structure in c).

It is possible to discern the distortion present within the crystal lattice in the images, through the angles between each rare-earth column. Figure 4.26 a) shows alternating tilt patterns between the rare-earth columns throughout the structure of $La_{0.5}Sm_{0.5}CrO_3$. Regions of higher magnification; with b) being a dark-field image, and c) the corresponding bright-field image, are overlaid with the crystal structure. In dark-field images, heavily scattering elements appear brighter and with greater intensities, however, for bright-field images the brighter intensities correspond to lighter atoms with fewer electrons. The observed periodic bright spots in Figure 4.26 c) are actually the electron scatter from the oxide ions that are barely visible in the dark-field images.

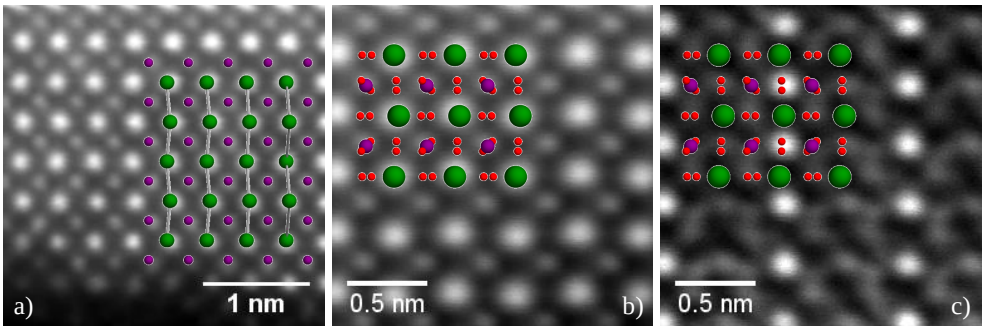

Figure 4.26: Both a) and b) show HAADF-STEM images of $La_{0.5}Sm_{0.5}CrO_3$ at different magnifications, whilst c) shows the corresponding bright-field image. The alternating tilting pattern is shown in a) through comparison with the structure.

4.3.2 Physical Properties

4.3.2.1 Magnetic Properties

This section describes a systematic study into the magnetic properties of the $La_xSm_{1-x}CrO_3$ solid solutions, and how subtle changes in structure, as well as increasing amounts of magnetic Sm^{3+}, affect their evolution throughout the series. In oxidation states of +3, both chromium ($3d^3$) and samarium ($4f^5$) are magnetic, with spin-only moments of $S = 3/2$ and $S = 5/2$, respectively. In contrast, La^{3+} has an empty $4f$ shell, and so is a nonmagnetic ion.

As described above in the introductory section of this chapter, it was previously shown that the magnetic moments of Cr^{3+} in all $RCrO_3$ undergo an antiferromagnetic ordering below their Néel temperatures (T_N), resulting in a G-type antiferromagnetic structure.[61] However, many studies have reported the observation of a weak ferromagnetism due to the slight canting of magnetic moments away from the antiferromagnetic axis,[7] which when paired with magnetic

rare-earth ions on the A site, can lead to unusual and interesting low temperature behaviour.[43]

The variations in the molar magnetic susceptibilities (χ_m) for each solid solution are shown in Figure 4.27, measured as a function of temperature on cooling. The data were recorded whilst an external field of 100 Oe was applied across the sample, and have subsequently been grouped together for comparison according to their magnitudes below the ordering temperature T_N.

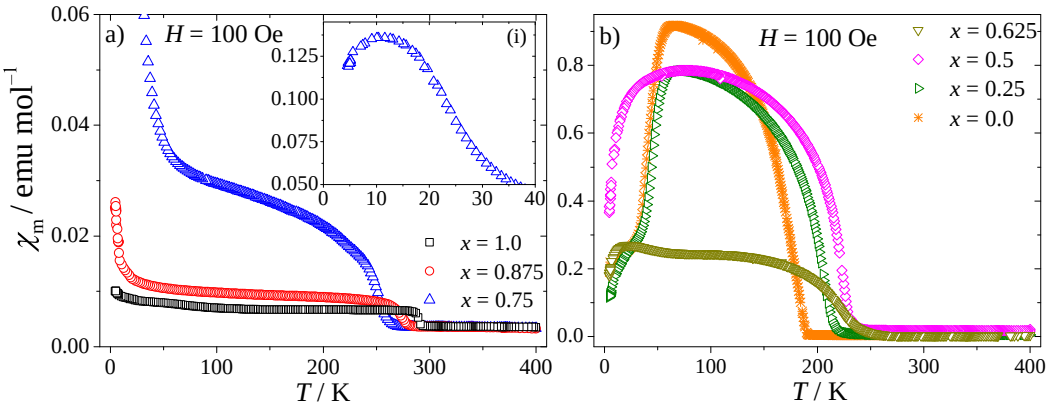

Figure 4.27: Temperature dependence of molar magnetic susceptibilities (χ_m) for the $La_xSm_{1-x}CrO_3$ series, measured in an applied field of 100 Oe. FCC curves for solid solutions of $x = 1.0$ to 0.75 are shown in a), with inset (i) showing the downturn in the data at ~ 11 K for $La_{0.75}Sm_{0.25}CrO_3$, which is described in the text. FCC data for the remaining solid solutions of $x = 0.625$ to 0.0 are shown in b).

Adjacent Cr^{3+} spins interact through the superexchange mechanism, which is the strongest form of magnetic interaction in the structure, leading to distinct features in the data that signify this onset of antiferromagnetic ordering. Above this Néel temperature, the Cr^{3+} and Sm^{3+} magnetic moments are paramagnetic, and therefore result in no net magnetic field in the material. Below T_N, the magnetic structure can be described by the configuration $\Gamma_4(G_x, A_y, F_z)$ (it is worth noting that this configuration applies to the crystallographic axes in the *Pbnm* setting), which shows that the G-type antiferromagnetic order is aligned along the a axis of the unit cell, with a small antiferromagnetic component along the b axis, and small ferromagnetic component along the c axis, both of which are a result of the slight canting of the Cr^{3+} spins away from the antiferromagnetic a axis.[8]

The data show that T_N varies with composition, however, this is perhaps appreciated more so in the differential molar magnetic susceptibility, which is displayed for each solid solution, as a function of temperature, in Figure 4.28.

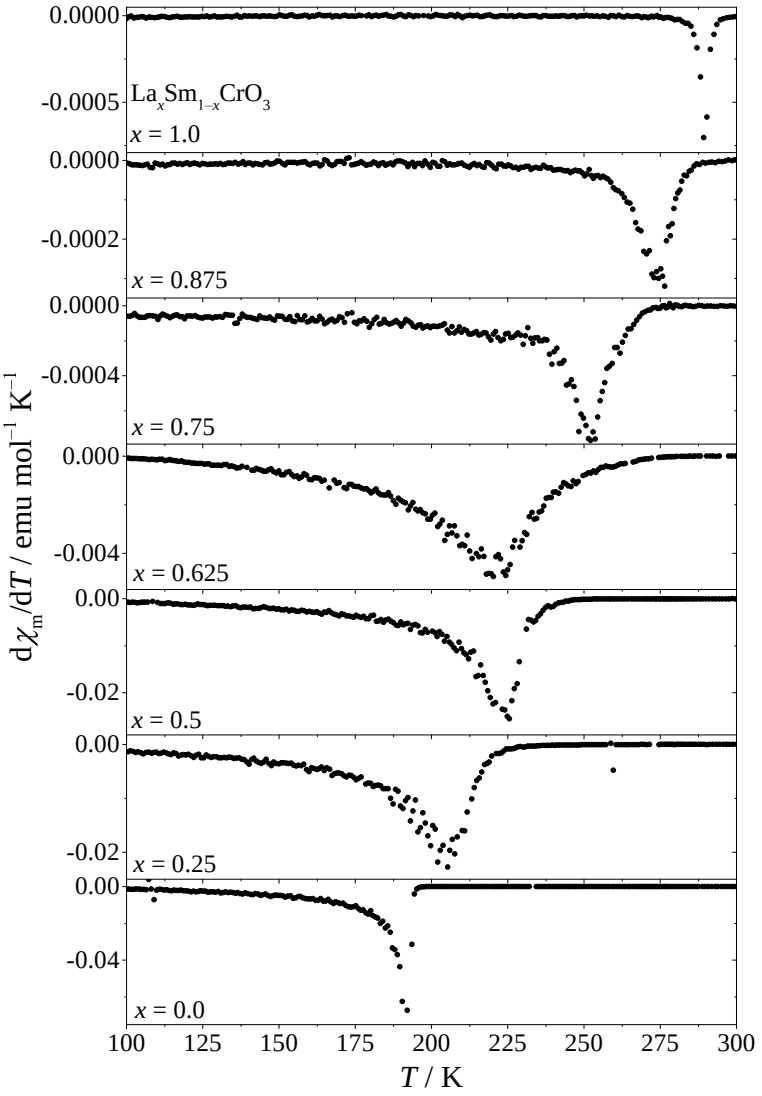

Figure 4.28: Differential molar magnetic susceptibilities as a function of temperature for each solid solution in the $La_xSm_{1-x}CrO_3$ series.

The negative features observed in the first derivatives of the susceptibility data correspond to T_N for each material,which clearly decreases with the increasing content of Sm^{3+}. A monotonic relationship is observed between T_N and the composition, displayed in Figure 4.29. As was shown in the characterisation section of this chapter, the composition is directly related to the level of distortion in the structure, so by extension, the Néel temperature also shows a dependence upon the structural distortion.

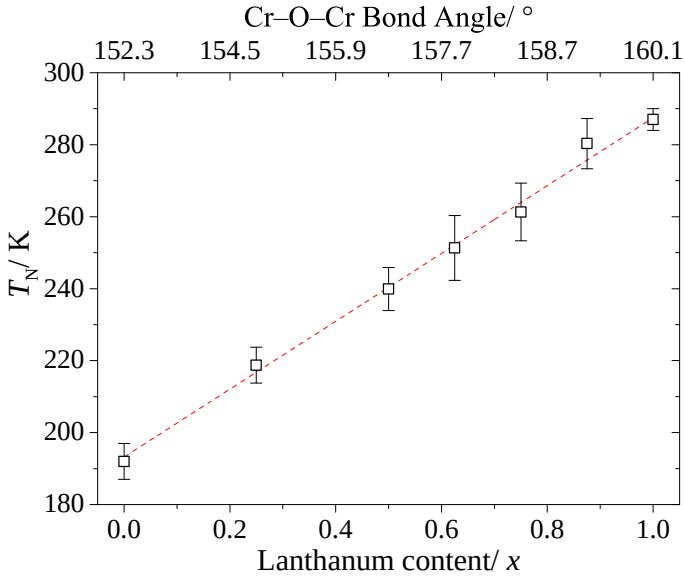

Figure 4.29: Variation of T_N as a function of composition. The illustrations on the right give an idea of how T_N is affected by the overlap between chromium d and oxygen p orbitals, which changes with octahedral tilting.

The decrease in Néel temperature with ionic radius of the A site cation has been observed across the entire series of RCrO$_3$ (with R = La^{3+} to Lu^{3+}),[5,43], in mixed rare-earth chromites La$_x R_{1-x}$CrO$_3$ (where R = Pr^{3+}, Nd^{3+}, and Gd^{3+}),[40–42] as well as the series of RMnO$_3$,[62] and RFeO$_3$.[44] As the value of T_N decreases monotonically across the series it is clear that any coupling between the A site R^{3+} and B site Cr^{3+} has a negligible effect on the ordering of the the Cr^{3+} moments. The linear decrease has been generally explained through the mechanism of superexchange for RFeO$_3$, where less overlap between the d orbitals of chromium and p orbitals of oxygen, which ultimately govern the superexchange pathways, leads to a reduced ordering temperature for the Cr^{3+} moments. The degree of overlap between the orbitals is affected by the level of structural distortion; orbital overlap is minimised when octahedral tilt angles are large, so a more distorted structure will have a lower ordering temperature, explaining why the observed T_N for SmCrO$_3$ is lower than LaCrO$_3$. The observed values of T_N, as well as previously reported values for the end members, are compared against the octahedral tilt angles in Table 4.9.

Table 4.9: Observed and reported Néel temperatures compared against the octahedral tilt angles calculated from Rietveld.

x	T_N/K		Cr–O–Cr bond angle/°	$\phi_{[010]}$/°	$\theta_{[101]}$/°
	This study	Literature			
1.0	289	288 [1,42], 287 [5], 295 [61], 282 [63]	161.10(12)	5.18	9.38
0.875	279	-	160.30(14)	7.41	9.90
0.75	261	-	158.70(20)	8.12	10.76
0.625	251	-	157.10(16)	9.01	11.72
0.50	240	-	155.86(89)	8.80	12.46
0.25	219	-	154.00(100)	9.60	13.44
0.0	192	197 [1], 192 [5,64], 193 [7], 190 [9]	151.95(79)	9.99	15.82

However, it was shown recently that superexchange orbital overlap alone cannot account for the decreasing T_N in $RCrO_3$, and that the variation in Néel temperature is also strongly dependent on t_{2g}-e_g orbital hybridisation.[43] The overall change in the Cr–O–Cr bond angle in $RCrO_3$ is very similar to that of $RFeO_3$, however, the change in T_N from each end member is much larger for the chromites, such that it is estimated that the superexchange angle dependence contributes to only 30% of this change. The dependence of T_N on t_{2g}-e_g orbital hybridisation is introduced from distortions that are intrinsic to orthorhombic perovskites, causing overlap of the π and σ bonds between adjacent Cr^{3+} ($t_{2g}^3 e_g^0$) ions. For the $RFeO_3$ the superexchange interactions over the half-filled π bond t_{2g}^3-O-t_{2g}^3 and the half-filled σ bond e_g^2-O-e_g^2 are all antiferromagnetic. The t_{2g}-e_g hybridisation does not produce any new component to the overall superexchange mechanism. In comparison, only the t_{2g} orbitals are half-filled for $RCrO_3$, whilst the e_g orbitals are empty. The t_{2g}-e_g hybridisation results in a virtual charge transfer to the empty e_g orbital, giving t_{2g}^3-O-e_g^0 which results in a ferromagnetic contribution that is comparable to the antiferromagnetic coupling from t^3-O-t^3. Thus it is these effects which mostly govern the large observed shift in T_N across the $La_xSm_{1-x}CrO_3$ series.

Rather large differences in the magnetic response just below T_N are observed for each solid solution, and these become larger with increasing Sm^{3+} content. This was explained by the increasing amount of magnetic Sm^{3+} species, however, the moments of Sm^{3+} remain paramagnetic unless very low temperatures are achieved, and so therefore should not contribute to the observed susceptibility. The isotropic superexchange interactions between neighbouring Sm^{3+} spins form the weakest interaction in the structure, so the second Néel temperature T_{N2} which corresponds to the ordering of the Sm^{3+} sublattice is typically well below 5 K. The observed enhancement of magnetisation as a result of Sm^{3+} doping indicates that

coupling interactions exist between the A site Sm^{3+} and B site Cr^{3+}. Only the Cr^{3+} moments are ordered at this temperature, however, it has been shown that the weak ferromagnetic component, arising from the antiferromagnetic lattice due to spin-canting, generates a polarisation of the paramagnetic Sm^{3+} moments.[8] The Sm^{3+} moments are not ordered with respect to each other, but are instead aligned along the direction of the weak ferromagnetic component originating from the Cr^{3+} sublattice, resulting in the increased susceptibility observed in the data.

For solid solutions with low x (x = 1.0 to 0.75), the small amount of Sm^{3+} acts as a paramagnetic impurity and therefore dominates the susceptibility curve at low temperature, shown in Figure 4.27 a). It is only when adequate isotropic distribution of the Sm^{3+} ions is achieved in solid solutions of x = 0.625 to 0.0, that exchange pathways can begin to form between neighbouring Sm^{3+} cations, and an immediate response is observed in the magnetisation below T_N due to this polarisation.

The polarisation of the Sm^{3+} moments is also evident from magnetisation data recorded as a function of applied field, where the hysteric behaviour increases with increasing Sm^{3+} content. Figure 4.30 shows such data below T_N at 150 K. The remanent magnetisation and coercive field reach their maxima in solid solutions of x = 0.5 and 0.0, respectively, with saturation of the slight ferromagnetic component occurring at fields above 40 kOe.

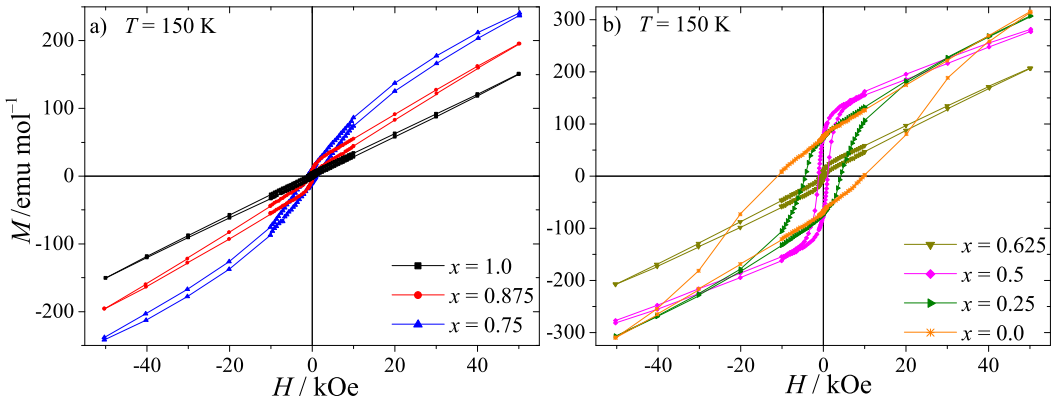

Figure 4.30: Magnetisation data recorded as a function of applied field up to 50 kOe for all solid solutions in the $La_xSm_{1-x}CrO_3$ series.

For solid solutions that contain magnetic Sm^{3+} ions, a second transition is observed at low temperatures. This is not an ordering transition, but instead, corresponds to a *spin reorientation* of the ordered Cr^{3+} moments.[65] It is a second-order continuous reorientation, driven by free energy which becomes

available to the system as it moves into a lower energy state. The anisotropic interactions between the ordered Cr^{3+} sublattice and the magnetic Sm^{3+} ions result in this unusual low-temperature behaviour. The anisotropic exchange interactions produce different effective fields for the neighbouring Cr^{3+} spins that are aligned antiparallel. These effective fields are perpendicular to the antiparallel spins, opposing one another, therefore, a reorientation of the Cr^{3+} spins is favoured.[8] As the temperature decreases, the magnitudes of these effective fields increase due to the increasing rare-earth magnetisation, and when the interaction energy of the Cr^{3+} spins with these effective fields exceeds the anisotropic exchange energy, the spin reorientation occurs.

As mentioned above, the following configurations and description of this reorientation are written with the crystallographic axes in the *Pbnm* setting. Below T_N the Cr^{3+} moments are ordered in the configuration $\Gamma_4(G_x, A_y, F_z)$, however, below the spin reorientation temperature T_{SR}, this configuration becomes $\Gamma_2(F_x, C_y, G_z)$, where the G-type antiferromagnetic ordering is now aligned along the c axis of the unit cell, with the small ferromagnetic component aligned along the a axis.[8] C_y corresponds to a small hidden canting contribution along the b axis. So this reorientation involves the antiferromagnetic axis rotating from the a axis, to the c axis on cooling through T_{SR},[9] whilst the weak ferromagnetic contribution undergoes the opposite rotation from the c to the a axis.[64] The Sm^{3+} moments also rotate through the reorientation, but below T_{SR}, become polarised antiparallel to the weak ferromagnetic component of the Cr^{3+} sublattice, causing the rapid downturn in magnetic susceptibility, observed in the data in Figure 4.27. Even in solid solutions that contain small amounts of magnetic Sm^{3+}, this downturn is visible, where a maximum is observed at ~ 11 K for $x = 0.75$. The data for end member $SmCrO_3$ show the spin reorientation to occur at $T_{SR} \sim 33$ K, which is in good agreement with the second-order reorientation that has been reported previously.[9] The temperature of this spin reorientation rises with Sm-content, as the statistical probability of neighbouring Sm^{3+} ions increases, resulting in the growth of a superexchange pathway between adjacent ions, that strengthens as the concentration of Sm^{3+} increases.[8]

With these observed spin reorientations being driven by the anisotropic interactions between the ordered Cr^{3+} sublattice and magnetic Sm^{3+} ions, it is clear that no spin reorientation is observed from solid solutions with high x ($x = 0.875$), or indeed for $LaCrO_3$, with nonmagnetic La^{3+}. This is also observed for other $RCrO_3$ where the rare-earth ion is nonmagnetic, such as Y^{3+} and Lu^{3+}.[5]

The spin configuration for $LaCrO_3$ remains as $\Gamma_4(G_x, A_y, F_z)$ for the entire temperature range below T_N, as no anisotropy energy is exceeded.

At high temperatures above T_N in the paramagnetic region, all solid solutions of the $La_xSm_{1-x}CrO_3$ series exhibit typical Curie-Weiss behaviour, shown by the inverse susceptibility data in Figure 4.31.

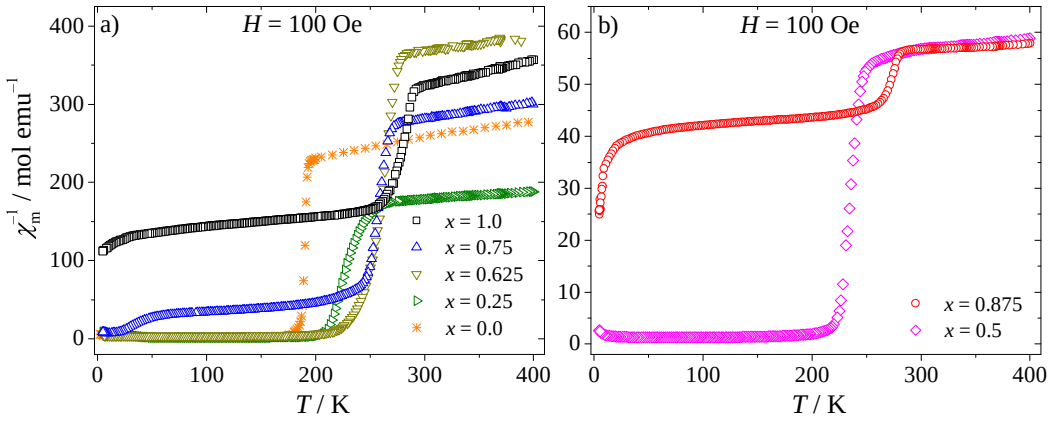

Figure 4.31: Temperature dependence of the inverse molar magnetic susceptibility χ_m^{-1} for each solid solution. The data were collected under FCC conditions in an applied field of 100 Oe, and are grouped accordingly to their magnitude.

Using adequate ranges of data points (larger than 100 K) between T_N and the maximum measurement temperature of 400 K, the paramagentic regions of the data are fitted using Equation 4.4:

$$\chi_m(T) = \frac{C}{T - \theta} + \chi_0 \tag{4.4}$$

and this allows the determination of the Curie constant C, and the Weiss temperature θ. Knowledge of such values allows for the calculation of individual effective moments μ_{eff} of the Sm^{3+} and Cr^{3+} ions. The effective magnetic moment per formula unit is calculated through Equation 4.5.

$$\mu_{eff}^2 = \frac{3k_B C}{N_A \mu_B^2} \tag{4.5}$$

where k_B is the Boltzmann constant, N_A is Avogadro's number, and μ_B the Bohr magneton. The value of μ_{eff} can then be used to determine the separate moment on the Sm^{3+} site through Equation 4.6.

$$\mu_{eff} = \sqrt{[(\mu_{Sm^{3+}})^2 + (\mu_{Cr^{3+}})^2]} \tag{4.6}$$

The values of the above mentioned parameters for each solid solution are summarised in Table 4.10.

Table 4.10: Magnetic parameters for each solid solution, determined by fitting the Curie-Weiss paramagnetic region of inverse susceptibility data. The value of $\mu_{Cr^{3+}}$ from $LaCrO_3$ is applied to all, and values of $\mu_{Sm^{3+}}$ are determined from Equation 4.6.

x	$\lvert\theta\rvert$/K	C/μ_B	μ_{eff}/μ_B	$\mu_{Sm^{3+}}/\mu_B$	$\mu_{Cr^{3+}}/\mu_B$
1.0	633.8	2.985	4.887	0	4.887
0.875	2962.8	23.53	13.72	-	-
0.75	843.1	4.085	5.717	2.967	4.887
0.625	1243.8	4.204	5.799	3.122	4.887
0.50	834.4	4.872	6.243	3.885	4.887
0.25	1091.2	7.299	7.641	5.874	4.887
0.0	613.4	7.432	7.711	5.964	4.887

The measured moment of $LaCrO_3$ indicates that chromium is present in the oxidation state of +3, giving an effective moment slightly higher than the expected value of 3.87 μ_B, which is determined through $2\sqrt{[S(S+1)]}$ ($S = 3/2$). The effective moment clearly increases as more nonmagnetic La^{3+} is substituted for magnetic Sm^{3+}.

The theoretical value of $\mu_{Sm^{3+}}$ can be calculated through $g\sqrt{[J(J+1)]}$, where g is the Landé g-factor given by $g = 1 + [J(J+1) + S(S+1) - L(L+1)/2J(J+1)]$, where J and L are the total angular momentum and orbital angular momentum, respectively. The experimentally determined values are much higher than the theoretical value of 0.84 μ_B, however, reported values for samarium can often be high due to low lying excited states being thermally accessible.

The Weiss temperatures θ for these materials are very high compared to their observed antiferromagnetic Néel temperatures. The value for $LaCrO_3$ is calculated to be 633 K, slightly reduced from the reported values of 750 and 800 K.[5,7] Such discrepancies between these values could be due to the possibility of these materials containing certain amounts of frustration, as postulated previously.[5]

4.3.2.2 Electric Properties

There have been several recent studies that use pyroelectric measurement to explore the magnetoelectric properties observed in $RCrO_3$,[20,66] and others that report the observation of spin-phonon coupling in Raman scattering data for chromites that contain magnetic rare-earth ions.[21,22] From these observations, it was proposed that the interactions between the magnetic rare-earth ions and the weak ferromagnetic component of the Cr^{3+} sublattice break the centrosymmetric

symmetry of the unit cell contents, and induce a spontaneous polarisation. Such effects have also been observed in other perovskites such as RMnO$_3$,[67] as well as RFeO$_3$.[68] These phenomena were not observed in YCrO$_3$ and LuCrO$_3$ due to the presence of nonmagnetic A site ions. This section focusses on an investigation of such properties in $La_{0.25}Sm_{0.75}CrO_3$ through polarisation measurements, and their relationship to magnetic data, as well as structural effects seen through temperature-dependent Raman scattering. The interplay between the observed polarisation and the magnetic ordering in these systems could be mediated through a coupling between the ordered magnetic spins and the crystal lattice, and probing the local structure using Raman scattering could provide insight into the mechanisms behind these observations.

The results of pyroelectric measurements made on $La_{0.25}Sm_{0.75}CrO_3$ are compared against molar magnetic susceptibility data in Figure 4.32. The data were measured on warming after the material was poled in electric fields of ± 1.89 kV cm^{-1}. A switchable polarisation of ± 0.006 μC cm^{-2} was observed at approximately $\sim$ 46 K in the vicinity of the low-temperature spin reorientation transition that is observed in the magnetic data at approximately 40 K. This is associated with the change in the magnetic structure from Γ_4 to Γ_2 configuration below which the polarised Sm^{3+} spins are aligned anti-parallel to the weak ferromagnetic component of the Cr^{3+} sublattice. The observed polarisation is much smaller than that previously observed for end member SmCrO$_3$,[20] however, it is noted that the material studied here contains nonmagnetic La^{3+}, and the value does not take account of the polarisation that may also arise from interactions around T_N.

Unfortunately, it was not possible to obtain quality data over a suitable temperature range including T_N; high levels of noise are present in the data above $\sim$ 100 K, shown in the figure. It is likely that above this temperature, the conductivity of the material increases sufficiently enough for it to act as a short, so the remaining current from the initial pole field is able to flow around the circuit. Whilst this was not observed for end member SmCrO$_3$,[20] this could arise from the lanthanum doped in to the material, where it is known that undoped LaCrO$_3$ exhibits p-type semiconductive behaviour due to the electron holes present in the 3d conduction band of the chromium ions.[69]

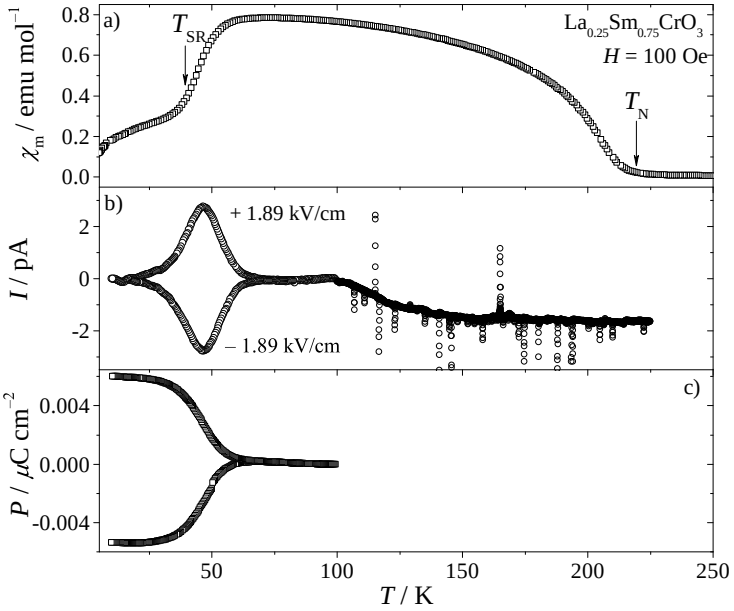

Figure 4.32: Variation of a) FCC magnetic susceptibility, b) pyroelectric current, and c) electric polarisation as a function of temperature for $La_{0.25}Sm_{0.75}CrO_3$.

The Raman spectrum of $La_{0.25}Sm_{0.75}CrO_3$, recorded at 123 K, is shown along with mode assignments in Figure 4.33. Several bands which do not overlap with other modes are suitable to study. The extraction of positions for several bands is difficult due to their close proximity with other modes, such as the two broad bands at $\sim$ 225 cm^{-1} and $\sim$ 450 cm^{-1}, which each consist of at least three overlapping modes. The five remaining bands that are suitable for study are the $B_{2g}(1)$, $A_g(4)$, $A_g(5)$, $B_{1g}(2)$, and $B_{3g}(3)$ modes.

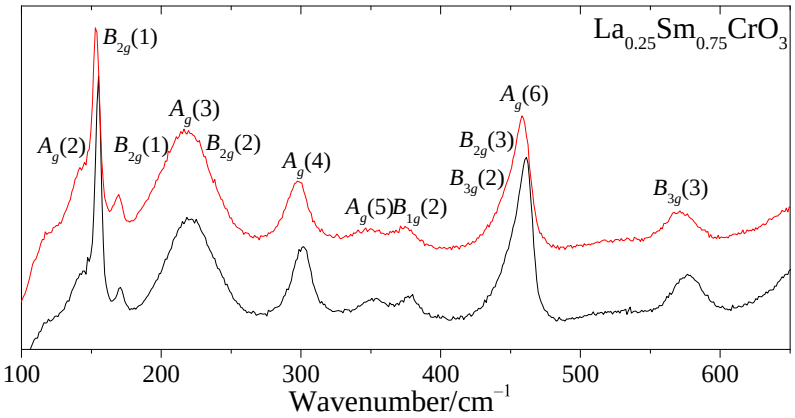

Figure 4.33: Raman spectra of $La_{0.25}Sm_{0.75}CrO_3$ solid solution measured at 123 K (lower) and room temperature (upper).

The number of phonon modes in Figure 4.33 remain unchanged between room temperature and 123 K, indicating that no structural transitions, that would otherwise hinder this investigation, take place within this temperature range.

The temperature dependence of phonon frequency is based upon several factors; the frequency shift that corresponds to the change in lattice volume, an intrinsic anharmonic contribution, and also other potential effects such as spin-phonon or electron-phonon coupling. An increase in phonon frequency as the temperature decreases is typically observed due to the anharmonic effect.[22,70,71]

The temperature dependencies of the $A_g(5)$ and $B_{1g}(2)$ bands are shown in Figure 4.34. Anomalies are observed in the thermal behaviour of both modes as the material passes through the antiferromagnetic ordering temperature at $T_N = 219$ K. The $A_g(5)$ corresponds to a tilting motion of the CrO_6 octahedra, and the $B_{1g}(2)$ mode to the displacement of A site and O(1) ions along the z direction. The anomaly observed in the $A_g(5)$ mode is interesting, as this atomic motion is directly linked to the BO_6 octahedral framework that makes up the unit cell, and therefore the lattice. During this vibration, as the octahedra rotate further, the distance between adjacent Cr^{3+} ions is altered; the observed anomaly suggests that the antiferromagnetic ordering of the spins influences these rotations, likely resulting in a magnetostrictive effect on the entire lattice.[21] The large anomaly observed for the $B_{1g}(2)$ mode clearly shows that the magnetic ordering has a substantial effect on the A cation displacement also.

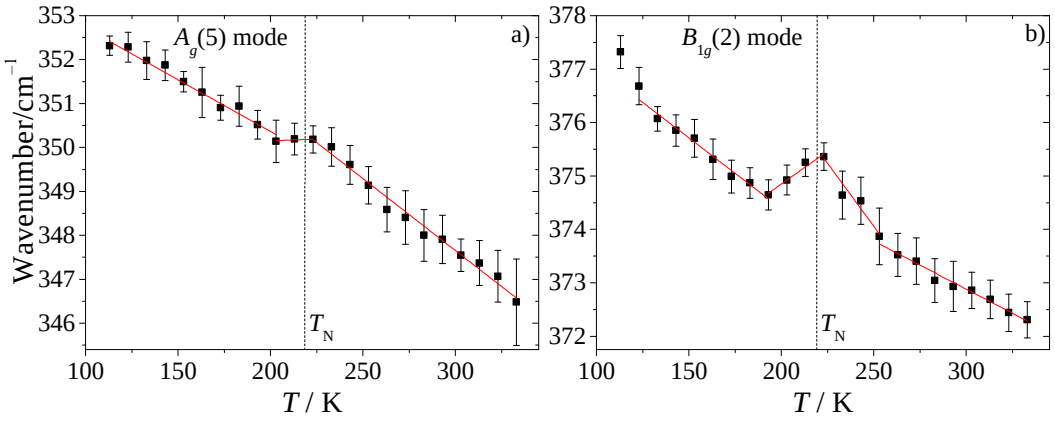

Figure 4.34: Temperature dependence of the frequencies for both the a) $A_g(5)$ and b) $B_{1g}(2)$ modes in $La_{0.25}Sm_{0.75}CrO_3$.

The widths of Raman lines are related to phonon lifetimes and are not affected by subtle changes in the lattice due to effects such as magnetostriction. The lifetime

of a phonon can be affected by several factors including thermal energy,[70] and disorder, as well as spin-phonon coupling processes, so the analysis of phonon line-widths is useful to confirm the presence of spin-phonon coupling.[21,72] Due to the weak intensity of the $A_g(5)$ and $B_{1g}(2)$ bands, it was not possible to extract reliable line-widths for these modes. However, for the other modes under study, line-widths were successfully determined, and the temperature dependence of these are shown in Figure 4.35. These include the $B_{2g}(1)$, $A_g(4)$ modes, both of which involve displacements of the A site cations in the x direction, and the $B_{3g}(3)$ band which exhibits a strong dependence on the Cr–O distances and is insensitive to the structural distortion. The $B_{2g}(1)$ and $A_g(4)$ modes exhibit similar behaviour to $B_{1g}(2)$, which also displays a dependence upon the A site cation. These modes undergo a hardening as they pass through T_N, before continuing to soften in wavenumber above T_N where the material is no longer magnetically ordered. The expected increase in their line-widths is observed, along with slight variations that occur around, or more specifically, either side of T_N.

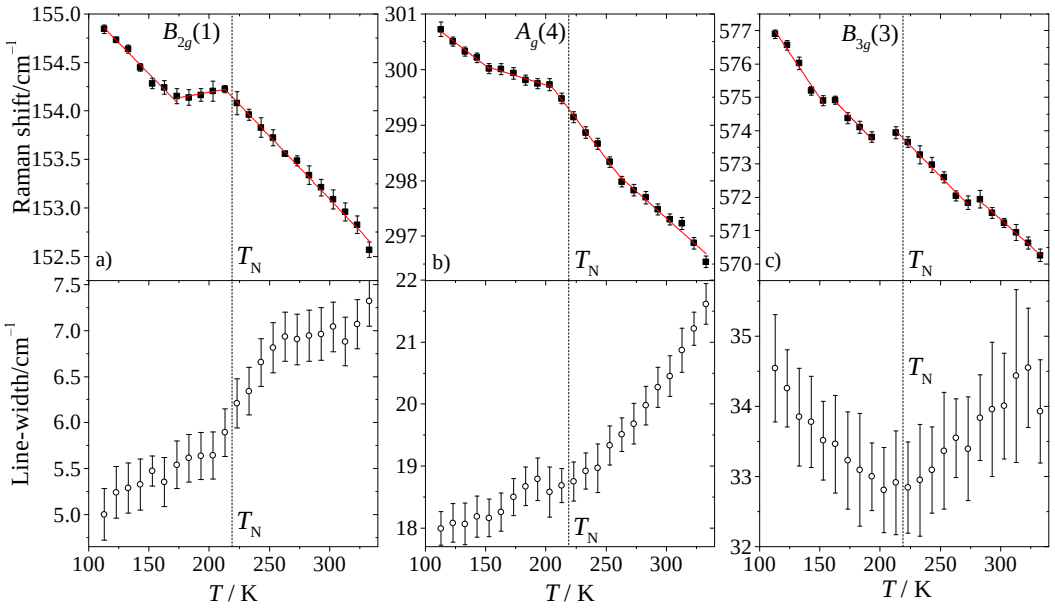

Figure 4.35: Temperature dependence of mode frequencies (upper) and phonon line-widths (lower) for a) $B_{2g}(1)$, b) $A_g(4)$, and c) $B_{3g}(3)$ modes.

Anomalies are also observed in the frequency dependence of the $B_{3g}(3)$ band, which reveals a considerable step in the mode softening occurring at T_N. Interesting behaviour is also observed from the line-width of this mode, which broadens as the temperature both increases or decreases away from T_N, indicating

that the band is sharpest as the Cr^{3+} spins magnetically order. As this mode is associated with the antistretching vibrations of the CrO_6 octahedra, which affects the covalency of the Cr–O bonds, it could be that the magnetic interactions that occur around T_N influence the motion of these atoms.

Ultimately, the changes in phonon behaviour that are observed as the material passes through T_N show that the modes display a dependence on the magnetic interactions between the Cr^{3+} spins. These anomalies suggest that the spin-phonon coupling leads to slight alterations in the local structure, potentially breaking the inversion symmetry as several other studies have reported previously.[21,22,72] Although it was not possible to support these observations by performing pyroelectric measurements through T_N, it is likely that these interactions between both magnetic and crystal lattice lead to an induced spontaneous polarisation within $La_{0.25}Sm_{0.75}CrO_3$, observed at temperatures that correspond to changes in the magnetic structure, such as that observed at T_{SR}. Likewise, it was not possible to study the effects that the observed low temperature polarisation has on the structure, however, this could be achieved through measurement of Raman scattering data at low temperatures across this transition.

4.4 Conclusions

The high-temperature high-pressure hydrothermal synthesis of a new series of mixed rare-earth orthochromites has been studied in detail. The materials contain both lanthanum and samarium on the A site of an distorted perovskite, and all of the collected data confirm the formation of homogeneous solid solutions of $La_xSm_{1-x}CrO_3$ with x = 1.0, 0.875, 0.75, 0.625, 0.5, 0.25, and 0.0. It has been shown that a minimum synthesis temperature of 370 °C is required to eliminate hydroxide impurities from the product, and that the quality of the prepared samples is comparable, if not greater, than the same materials that were also produced through conventional solid state synthesis.

In-depth analysis of powder X-ray diffraction data shows that the orthochromites crystallise with the orthorhombic space group *Pnma*, and that the distortion increases with samarium doping. The structural distortion is quantified by lattice parameters and octahedral tilt angles calculated from Rietveld analysis, and it is shown to increase towards $SmCrO_3$ due to the smaller ionic radius of Sm^{3+} compared to that of La^{3+}.

Phonon Raman scattering proved to be a very useful technique in order to perform a more in-depth analysis of the distortions present in the structure. The observed bands were assigned based upon the complex shift of modes throughout the series, as well as Shell-model calculations, and the mode assignments from earlier work that involved single rare-earth chromites, $R\mathrm{CrO}_3$.[35] It is clear that most bands undergo a *mode softening* as the series approaches LaCrO_3, supporting the lesser degree of structural distortion in the end member observed by XRD. Our study of individual bands provides a clear and concise analysis of the local structural distortions and the observed modes in the $La_xSm_{1-x}CrO_3$ series. With the aid of shell model calculations, the mode assignment and coupling phenomena between two A_g and two B_{2g} modes in the complicated low-wavenumber region below 250 cm^{-1}, have been resolved and described.

The use of electron microscopy revealed the formation of dendritic-type crystallites from hydrothermal synthesis, whilst STEM imaging highlighted the high degree of crystallinity of these particles, able to resolve rare-earth and chromium atomic columns, as well as observing electron density from bridging oxide ions.

Through measurement of magnetic data, a close relationship was shown between the structure of the material and its magnetic properties. The subtle distortions of the structure that accompany slight changes in samarium content have a significant effect on the magnetic behaviour. It has been described how coupling effects resulting from anisotropic exchange interactions between the magnetic A and B site metals generate unusual low-temperature magnetic behaviour.

The possibility of magnetoelectric effects has been explored through the measurement of pyroelectric data and temperature-dependent Raman scattering. The observation of a spontaneous switchable polarisation at T_{SR}, and changes in the local structure observed through a spin-phonon coupling suggests that these materials are characteristic of type II multiferroics, where the ferroelectric properties are induced by the pre-existing magnetic behaviour.

References

[1] J. Prado-Gonjal, R. Schmidt, J.-J. Romero, D. Ávila, U. Amador and E. Morán, *Inorg. Chem.*, 2013, **52**, 313.

[2] A. A. Belik, Y. Matsushita, M. Tanaka and E. Takayama-Muromachi, *Chem. Mater.*, 2012, **24**, 2197.

[3] W. Zheng, W. Pang, G. Meng and P. D., *J. Mater. Chem.*, 1999, **9**, 2833.

[4] R. D. Shannon, *Acta Cryst. A*, 1976, **32**, 751.

[5] K. Sardar, M. R. Lees, R. J. Kashtiban, J. Sloan and R. I. Walton, *Chem. Mater.*, 2011, **23**, 48.

[6] W. C. Koehler and E. O. Wollan, *J. Phys. Chem. Solids*, 1957, **2**, 100.

[7] E. F. Bertaut, G. Bassi, G. Buisson, P. Burlet, J. Chappert, A. Delapalme, J. Mareschal, G. Roult, R. Aleonard, R. Pauthenet and J. P. Rebouillat, *J. Appl. Phys.*, 1966, **37**, 1038.

[8] T. Yamaguchi, *J. Phys. Chem. Solids*, 1974, **35**, 479.

[9] G. Gorodetsky, R. M. Hornreich, S. Shaft, B. Sharon, A. Shaulov and B. M. Wanklyn, *Phys. Rev. B*, 1977, **16**, 515.

[10] M. Siemons and U. Simon, *Sens. Actuators, B*, 2007, **126**, 181.

[11] D. Lakshmi and R. Sundaram, *Sens. Transducers J.*, 2008, **97**, 74.

[12] N. Russo, D. Mescia, D. Fino, G. Saracco and V. Specchia, *Ind. Eng. Chem. Res.*, 2007, **46**, 4226.

[13] G. A. Tompsett and N. M. Sammes, *J. Power Sources*, 2004, **130**, 1.

[14] J. Beckers and G. Rothenberg, *ChemPhysChem*, 2005, **6**, 223.

[15] Z. Liu, D. Dong, X. Huang, Z. Lü, Y. Sui, X. Wang, J. Miao, Z. X. Shen and W. Su, *Electrochem. Solid-State Lett.*, 2005, **8**, A250.

[16] Y. Shen, M. Liu, T. He and S. P. Jiand, *J. Power Sources*, 2010, **195**, 977.

[17] J. W. Fergus, *Solid State Ionics*, 2004, **171**, 1.

[18] A. K. Zvezdin and A. A. Mukhin, *JETP Lett.*, 2008, **88**, 505.

[19] J. R. Sahu, C. R. Serrao, N. Ray, U. V. Waghmare and C. N. R. Rao, *J. Mater. Chem.*, 2007, **17**, 42.

[20] B. Rajeswaran, D. I. Khomskii, A. K. Zvezdin, C. N. R. Rao and A. Sudaresan, *Phys. Rev. B*, 2012, **86**, 214409.

[21] V. S. Bhadram, B. Rajeswaran, A. Sundaresan and C. Narayana, *EPL*, 2013, **101**, 17008.

[22] M. El Amrani, M. Zaghrioui, V. Ta Phuoc, F. Gervais and N. E. Massa, *J. Magn. Magn. Mater.*, 2014, **361**, 1.

[23] T. Kikkawa, M. Yoshinaka, K. Hirota and O. Yamaguchi, *J. Mater. Sci. Lett.*, 1995, **14**, 1071.

[24] Y. Jiang, J. Gao, M. Liu and G. Wang, Y. Meng, *Mater. Lett.*, 2007, **61**, 1908.

[25] M. Inagaki, O. Yamamoto and M. Hirohara, *J. Ceram. Soc. Jpn.*, 1990, **98**, 675.

[26] P. S. Devi, *J. Mater. Chem.*, 1993, **3**, 373.

[27] I. P. Parkin, A. V. Komarov and Q. Fang, *Polyhedron*, 1995, **15**, 3117.

[28] M. V. Kuznetsov and I. P. Parkin, *Polyhedron*, 1998, **17**, 4443.

[29] S. Geller, *Acta Crystallogr.*, 1957, **10**, 243.

[30] L. M. Daniels, M. C. Weber, M. R. Lees, M. Guennou, R. J. Kashtiban, J. Sloan, J. Kreisel and R. I. Walton, *Inorg. Chem.*, 2013, **52**, 12161.

[31] J. Ovenstone, K. C. Chan and C. B. Ponton, *J. Mater. Sci.*, 2002, **37**, 3315.

[32] L. P. Rivas-Vázquez, J. C. Rendón-Angeles, J. L. Rodríguez-Galicia, K. Zhu and K. Yanagisawa, *Solid State Ionics*, 2004, **172**, 389.

[33] M. Yoshimura, S. T. Song and S. Sōmiya, *Yogyo Kyokai Shi*, 1982, **90**, 91.

[34] S. T. Song, H. Y. Pan, Z. Wang and B. Yang, *Ceram. Int.*, 1984, **10**, 143.

[35] M. C. Weber, J. Kreisel, P. A. Thomas, M. Newton, K. Sardar and R. I. Walton, *Phys. Rev. B*, 2012, **85**, 054303.
[36] P. Gupta, R. Bhargava, R. Das and P. Poddar, *RSC Adv.*, 2013, **3**, 26427.
[37] A. Durán, A. M. Arévalo-López, E. Castillo-Martínez, M. Garcíia-Guaderrama, E. Morán, M. P. Cruz, F. Fernández and M. A. Alario-Franco, *J. Solid State Chem.*, 2010, **183**, 1863.
[38] H. Taguchi and M. Nagao, *J. Solid State Chem.*, 1995, **114**, 236.
[39] K. Oikawa, T. Kamiyama, T. Hashimoto, S. Y. and Y. Morii, *J. Solid State Chem.*, 2000, **154**, 524.
[40] K. Yoshii, A. Nakamura, Y. Ishii and Y. Morii, *J. Solid State Chem.*, 2001, **162**, 84.
[41] Y. Du, Z. X. Cheng, X.-L. Wang and S. X. Dou, *J. Appl. Phys.*, 2010, **108**, 093914.
[42] N. Sharma, B. K. Srivastava, A. Krishnamurthy and A. K. Nigam, *Solid State Sci.*, 2010, **12**, 1464.
[43] J.-S. Zhou, J. A. Alonso, V. Pomjakushin, J. B. Goodenough, Y. Ren, J.-Q. Yan and J.-G. Cheng, *Phys. Rev. B*, 2010, **81**, 214115.
[44] J.-S. Zhou and J. B. Goodenough, *Phys. Rev. B*, 2008, **77**, 132104.
[45] M. N. Iliev, M. V. Abrashev, J. Lavèrdiere, S. Jandl, M. M. Gospodinov, Y.-Q. Wang and Y.-Y. Sun, *Phys. Rev. B*, 2006, **73**, 064302.
[46] M. N. Iliev, M. V. Abrashev, H.-G. Lee, V. N. Popov, Y.-Y. Sun, C. Thomsen, R. L. Meng and C. W. Chu, *Phys. Rev. B*, 1998, **57**, 2872.
[47] M. N. Iliev, A. P. Litvinchuk, V. G. Hadjiev, Y.-Q. Wang, J. Cmaidalka, R.-L. Meng, Y.-Y. Sun, N. Kolev and M. V. Abrashev, *Phys. Rev. B*, 2006, **74**, 214301.
[48] S. Venugopalan, M. Dutta, A. K. Ramdas and J. P. Remeika, *Phys. Rev. B*, 1985, **31**, 1490.
[49] N. D. Todorov, M. V. Abrashev, V. G. Ivanov, G. G. Tsutsumanova, V. Marinova, Y.-Q. Wang and M. N. Iliev, *Phys. Rev. B*, 2011, **83**, 224303.
[50] M. Udagawa, K. Kohn, N. Koshizuka, T. Tsushima and K. Tsushima, *Solid State Commun.*, 1975, **16**, 779.
[51] J. D. Gale and A. L. Rohl, *Molecular Simulation*, 2003, **29**, 291.
[52] J. F. Scott, *Phys. Rev. B*, 1969, **183**, 823.
[53] P. A. Fleury, J. F. Scott and J. M. Worlock, *Phys. Rev. Lett.*, 1968, **21**, 16.
[54] S. A. Hayward, F. D. Morrison, Refdern, S. A. T., E. K. H. Salje, J. F. Scott, K. S. Knight, S. Tarantino, A. M. Glazer, V. Shuvaeva, P. Daniel, M. Zhang and M. A. Carpenter, *Phys. Rev. B*, 2005, **72**, 054110.
[55] N. Chaban, M. C. Weber, S. Pignard and J. Kreisel, *Appl. Phys. Lett.*, 2010, **97**, 031915.
[56] G. Gou, I. Grinberg, A. M. Rappe and M. J. Rondinelli, *Phys. Rev. B*, 2011, **84**, 144101.
[57] O. Chaix-Pluchery and J. Kreisel, *Phase Transitions*, 2011, **84**, 542.
[58] D. R. Modeshia and R. I. Walton, *Chem. Soc. Rev.*, 2010, **39**, 4303.
[59] L. P. Rivas-Vázquez, J. C. Rendón-Angeles, J. L. Rodríguez-Galicia, C. A. Gutiérrez-Chavarria, K. J. Zhu and K. Yanagisawa, *J. Eur. Ceram. Soc.*, 2006, **26**, 81.
[60] J. I. L. Chen and Z.-G. Ye, *J. Mater. Sci.*, 2007, **42**, 3767.
[61] I. Weinberg and P. Larsen, *Nature*, 1961, **192**, 445.
[62] T. Kimura, S. Ishihara, H. Shintani, T. Arima, K. T. Takahashi, K. Ishizaka and Y. Tokura, *Phys. Rev. B*, 2003, **68**, 060403.
[63] J. D. Gordon, R. M. Hornreich, S. Shtrikman and B. M. Wanklyn, *Phys. Rev. B*, 1976, **13**, 3012.
[64] K. Tsushima, K. Aoyagi and S. Sugano, *J. Appl. Phys.*, 1970, **41**, 1238.
[65] X. Qian, L. Chen, S. Cao and J. Zhang, *Solid State Commun.*, 2014, **195**, 21.
[66] R. Saha, A. Sundaresan and C. N. R. Rao, *Mater. Horiz.*, 2014, **1**, 20.
[67] J. Laverdiére, S. Jandl, A. A. Mukhin, V. Y. Ivanov, V. G. Ivanov and M. N. Iliev, *Phys. Rev.*

B, 2006, **73**, 214301.

[68] J.-H. Lee, Y. K. Jeong, J. H. Park, M.-A. Oak, H. M. Jang, J. Y. Son and J. F. Scott, *Phys. Rev. Lett.*, 2011, **107**, 117201.

[69] J. Cheng and A. Navrotsky, *J. Solid State Chem.*, 2005, **178**, 234.

[70] M. Balkanski, R. F. Wallis and E. Haro, *Phys. Rev. B*, 1983, **28**, 1928.

[71] E. Granado, A. García, J. A. Sanjurjo, C. Rettori, I. Torriani, F. Prado, R. D. Sánchez, A. Caneiro and S. B. Oseroff, *Phys. Rev. B*, 1999, **60**, 11879.

[72] P. Mandal, V. S. Bhadram, Y. Sundarayya, C. Narayana, A. Sundaresan and C. N. R. Rao, *Phys. Rev. Lett.*, 2011, **107**, 137202.

Chapter 5

A-site Radius Variance Effects in Mixed Rare-Earth Orthochromites

5.1 Background

The presence of multiple metals of different ionic radii on the same crystallographic position in mixed-metal oxides can lead to random disorder and compositional inhomogeneity, which can be overlooked when studying the materials through the usual diffraction-based methods. The A site cation radius variance effect, proposed by Attfield,[1] was explained in Chapter 1, where the maximum variance is observed at $x = 0.5$ in mixed A site oxides of composition $A_xA'_{1-x}BO_3$. When the disparity in size is large enough, segregation between the cations occurs, resulting in layered materials such as $YBaMn_2O_5$ and $NaLaMgWO_6$.[2]

Attfield *et al.*[3] went on to show that radius variance effects display a strong influence over the local, incoherent lattice strains that govern the metal-insulator transition in manganese-based perovskites. The A site cation disorder generated random anion displacements away from their average positions, resulting in linear dependencies on the A site variance of the magnetic and electronic properties of both magnetoresistive manganites and superconducting cuprates.[1]

Ordered arrangements of A site cations in multi-element perovskites are uncommon compared to those on the B site,[2] and typically involve the substitution of a divalent ion for a trivalent ion, which can be accompanied by an

appropriate concentration of charge-compensating vacancies on the A site, or mixed-valence species on the B site.[4] Despite such occurrences being rare, the transitions between cation order and disorder can play a critical role in dictating the stability, crystal chemistry, and properties of many solid state systems. Variations in the degree of order can induce significant alterations in magnetic behaviour, electronic or ionic conductivity, magnetoresistive, and dielectric or ferroelectric properties.[5]

The incorporation of alkaline-earth metals into rare-earths orthochromite solid solutions has resulted in enhanced p-type semiconductive behaviour, properties useful for SOFC interconnect materials.[6] However, the synthesis and study of solid solutions that contain two rare-earth cations are rather more scarce. All of the previously reported solid solutions of $R_xR'_{1-x}CrO_3$, where two rare-earth cations have been incorporated simultaneously into the chromite structure, are summarised in Table 5.1, and are compared against those studied in the current work.

Table 5.1: Previously reported mixed rare-earth orthochromites based on general formula $R_xR'_{1-x}CrO_3$. Ionic radii are nine-coordinate values tabulated by Shannon.[7]

R (radius/Å)	R' (radius/Å)	range of x	$\overline{r}_A$ (Å) at $x = 0.5$	σ^2 (Å^2) at $x = 0.5$
Reported				
La^{3+} (1.216)	Ce^{3+} (1.196)	$0.0 \leq x \leq 1.0$ in steps of 0.1[8]	1.206	10^{-4}
La^{3+} (1.216)	Pr^{3+} (1.179)	$0.0 \leq x \leq 1.0$ in steps of 0.1[9]	1.198	3.42×10^{-4}
La^{3+} (1.216)	Nd^{3+} (1.163)	$0.0 \leq x \leq 1.0$ in steps of 0.2[10–12]	1.163	7.02×10^{-4}
La^{3+} (1.216)	Gd^{3+} (1.107)	0.1[13] and 0.5[14]	1.162	2.97×10^{-3}
This study				
Y^{3+} (1.075)	Ho^{3+} (1.072)	$0.0 \leq x \leq 1.0$ in steps of 0.5	1.0735	2.25×10^{-6}
La^{3+} (1.216)	Sm^{3+} (1.132)	$0.0 \leq x \leq 1.0$ in steps of 0.25	1.174	1.76×10^{-3}
La^{3+} (1.216)	Tb^{3+} (1.095)	$0.0 \leq x \leq 1.0$ in steps of 0.5	1.156	3.66×10^{-3}

Radius variance is determined through $\sigma^2(r_A) = \langle r_A^2 \rangle - \langle r_A \rangle^2$.

All of the materials described in the literature were produced through traditional solid state techniques, with the requirement of a two-step synthesis for $La_xCe_{1-x}CrO_3$. This involved a glycine combustion followed by annealing in evacuated quartz tubes, in order to avoid the oxidation of Ce^{3+}.[8]

This chapter covers the high-temperature hydrothermal synthesis of two new mixed rare-earth chromium perovskite solid solutions, namely $La_xTb_{1-x}CrO_3$ and $Y_xHo_{1-x}CrO_3$. These new materials were characterised using PXRD and Raman spectroscopy, and alongside the $La_xSm_{1-x}CrO_3$ materials discussed in Chapter 4,

were combined into a study of cation size variance within rare-earth orthochromite perovskites.

Atomic-resolution electron energy loss spectroscopy (EELS) is used to assess the homogeneity of rare-earth distribution in each material and ultimately investigate the effects that different cation sizes have on the structure and synthesis of orthochromite perovskites. The choice of these three particular solid solutions provides a range of cation size variance to be studied, as shown in Figure 5.1. The almost identical ionic radii of Y^{3+} and Ho^{3+} (1.075 Å and 1.072 Å, respectively[7]) result in negligible variance effects in $Y_xHo_{1-x}CrO_3$, whilst at the other extreme, the disparate sizes of La^{3+} and Tb^{3+} (1.216 Å and 1.095 Å, respectively[7]) provide increased variance as well as a greater separation of edge energies, useful for EELS. Although the difference between the ionic radii of La^{3+} and Tb^{3+} is only 30% greater than that between La^{3+} and Sm^{3+}, it provides a $\sim$ 50% increase in variance for the $La_{0.5}Tb_{0.5}CrO_3$ solid solution.

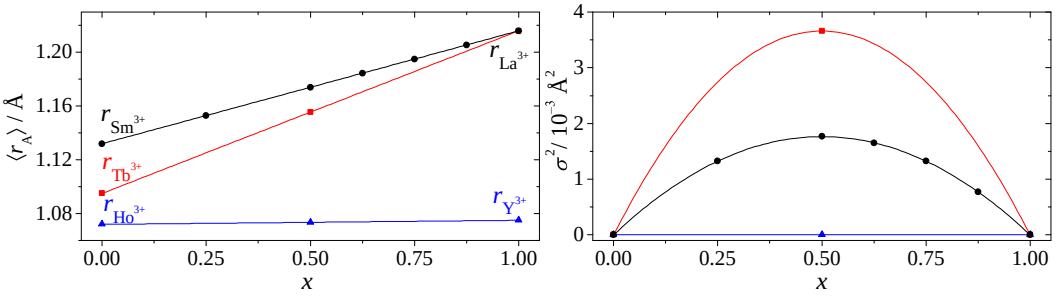

Figure 5.1: Variation in mean rare-earth A site cationic radii for the studied solid solutions. Blue corresponds to $Y_xHo_{1-x}CrO_3$, red to $La_xTb_{1-x}CrO_3$, and black to $La_xSm_{1-x}CrO_3$. Points along each line represent solid solutions that have been synthesised in the present study.

The same solid solutions were made via conventional solid state techniques to investigate the structure and properties of products from both synthesis methods.

The syntheses of solid solutions other than those described above are also explored, in order to add further structure to the study of both the effects of variance and tolerance factor in these materials.

The magnetic properties of these new solid solutions including those produced through different synthetic routes were investigated, and are presented alongside the EELS maps. By doing so, any potential effects of variance upon the magnetic properties of these materials were examined.

5.2 Synthesis

Solid solutions of $La_xTb_{1-x}CrO_3$ and $Y_xHo_{1-x}CrO_3$ are produced using the same route as the La-Sm materials described in Chapter 4, where a precipitated amorphous precursor was treated hydrothermally at high temperature and pressure.

The amorphous precursors were produced by dissolving either lanthanum(III) nitrate hexahydrate (0.9675 g, 99.999% Aldrich) and terbium(III) nitrate hexahydrate (0.9706 g, 99.9% Alfa Aesar), or yttrium(III) nitrate hexahydrate (0.8574 g, 99.8% Aldrich) and holmium(III) nitrate hexahydrate (0.9879 g, 99.9% Aldrich), along with chromium(III) nitrate nonahydrate (2.0000 g, 99% Aldrich) into 100 ml of deionised water in molar ratios to give desired compositions of $La_xTb_{1-x}CrO_3$ and $Y_xHo_{1-x}CrO_3$. Adding 25 ml of 2.0 M KOH solution caused the precipitation of a mixed-metal hydroxide gel, which was stirred for 15 minutes before being filtered and washed copiously with deionised water. Moisture was removed by drying at 75 °C for 24 hours, before being ground into a fine powder.

Reaction yields were of the order of 85-90%, with precipitate masses being $\sim$ 1.5 g.

The powdered precursors were placed inside an Inconel high-pressure vessel along with 20 ml of deionised water. The precursors of $Y_xHo_{1-x}CrO_3$, and end members $LaCrO_3$ and $TbCrO_3$ were heated to 380 °C for 6 hours, whilst it was found that pure samples of $La_{0.5}Tb_{0.5}CrO_3$ were formed under 12 hour reactions at 410 °C. Pressures of 200+ bar were achieved in the reactions. The bright green powders were then collected using filtration and dried at 75 °C in air.

Solid-state syntheses were also performed for both solid solutions; $Y_{0.5}Ho_{0.5}CrO_3$ was produced by a single firing of the amorphous precursor to 1200 °C for a period of 12 hours, whilst $La_xTb_{1-x}CrO_3$ was heated to 1400 °C for 12 hours, a total of four times with regrinding of the powder in between each firing, based on the reported solid state synthesis of $La_{0.5}Gd_{0.5}CrO_3$.[14]

5.3 Results

5.3.1 Characterisation

5.3.1.1 $La_xTb_{1-x}CrO_3$

All three polycrystalline materials were phase pure, shown by PXRD data in Figure 5.2. The observed peak splitting from $LaCrO_3$ to $TbCrO_3$ is evidence of

the decreasing unit cell volume and increasing structural distortion, discussed in Chapter 4. The reflections for the hydrothermal $La_{0.5}Tb_{0.5}CrO_3$ solid solution display peak splitting like the end members, showing that a well crystalline sample can be produced using the increased synthesis temperature and duration.

For comparison PXRD data are also provided for solid solutions of $La_{0.5}Tb_{0.5}CrO_3$ that were prepared through different methods. This involved annealing the hydrothermal sample at 1000 °C for 12 hours, and another sample produced through solid state synthesis at 1400 °C for 48 hours. Considerable differences are observed between the hydrothermal and solid state materials, where the latter produces broad diffraction peaks, and does not confirm the formation of a homogeneous solid solution. The pattern of the solid state phase resembles that of a distorted perovskite, however, it is clear that the firing does not produce the same material as hydrothermal treatment at 410 °C. Annealing the hydrothermally-prepared material to 1000 °C results in slight changes. Some of the reflections, marked by arrows in Figure 5.2 b), display a sharpening such that they appear more similar to those in the solid state sample, rather than the hydrothermal material.

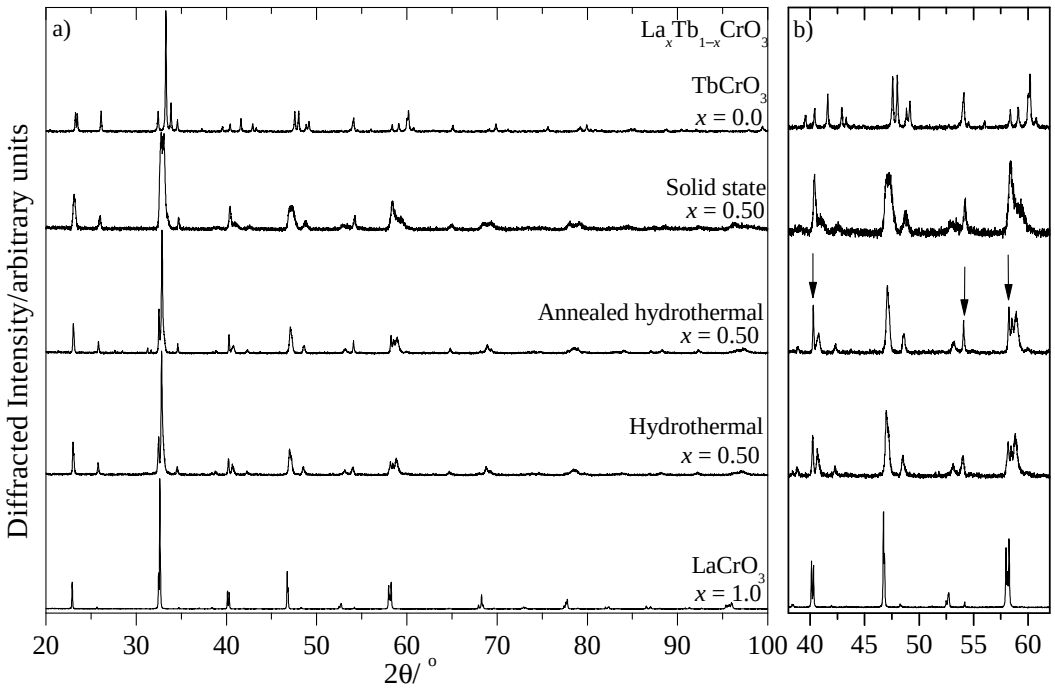

Figure 5.2: XRD patterns of end members and solid solutions of $La_xTb_{1-x}CrO_3$, including those prepared through hydrothermal, post-annealing, and solid state synthesis. Changes between materials prepared through different methods are highlighted by arrows in b).

Rietveld refinements made against the data using space group *Pnma* show the same linear dependence of the unit cell volume on mean A site cation radius, as is observed for the $La_xSm_{1-x}CrO_3$ materials in Chapter 4. The lattice parameters determined for $TbCrO_3$ agree well with those reported previously,[15] and the variation in both the primitive unit cell dimensions and volumes with increasing Tb^{3+} content are illustrated in Figure 5.3.

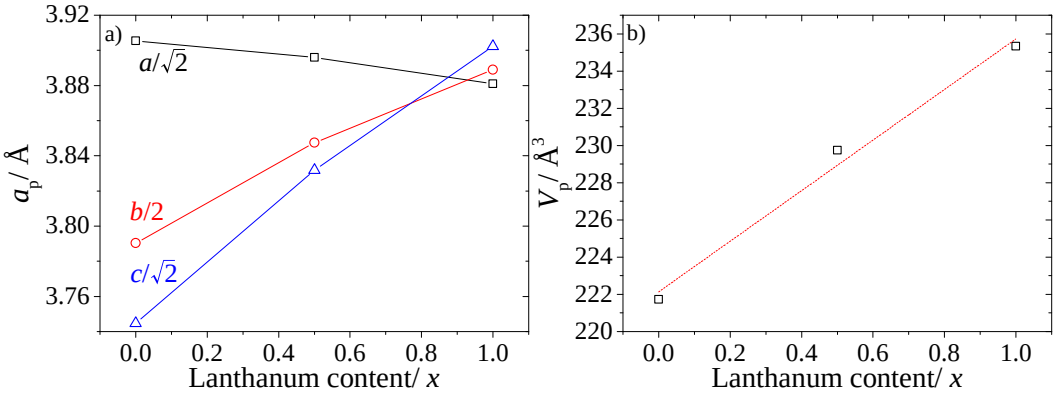

Figure 5.3: Variation of primitive a) unit cell parameters and b) unit cell volume with lanthanum content for $La_xTb_{1-x}CrO_3$ solid solutions, determined from Rietveld refinement. Error bars are smaller than the datapoints.

Results of Rietveld refinement for hydrothermal $La_{0.5}Tb_{0.5}CrO_3$ are shown in Figure 5.4. Both La^{3+} and Tb^{3+} cations are placed on the same crystallographic $4c$ site, despite the large difference in local coordination preference for each.

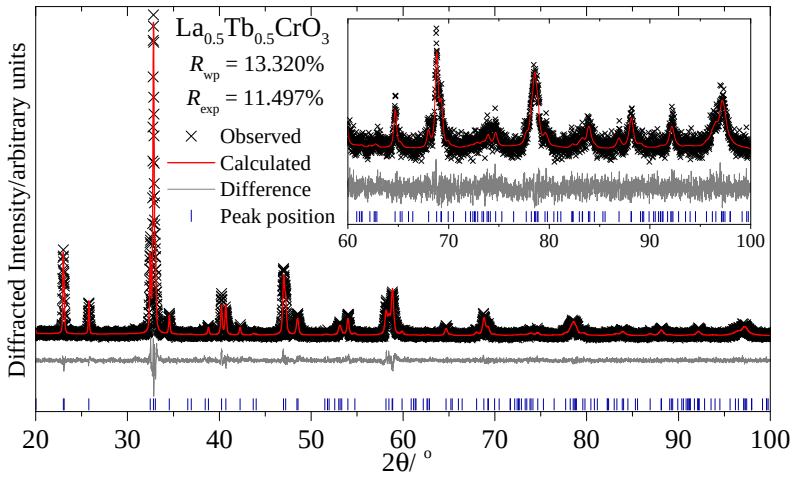

Figure 5.4: Rietveld refinement performed against PXRD data (λ = 1.54056 Å) of hydrothermal $La_{0.5}Tb_{0.5}CrO_3$. Observed (black crosses), calculated (red line), difference (grey line) patterns are shown, whilst blue tick marks represent allowed peak positions.

The results for each member of the $La_xTb_{1-x}CrO_3$ series, obtained from Rietveld refinement, are listed in Table 5.2. The structural parameters for $LaCrO_3$ were discussed in Chapter 4, whilst the parameters for end member $TbCrO_3$ agree almost identically with those previously reported by Prado-Gonjal *et al.*[15]

Table 5.2: Structural details obtained from Rietveld refinements against PXRD data for the $La_xTb_{1-x}CrO_3$ solid solutions, including R_{wp} and R_{exp} values for each.

Atom	Site	x	y	z	U_{iso}/Å^2
$x = 1.0$				$R_{wp} = 11.987\%$, $R_{exp} = 10.354\%$	
$a = 5.48848(4)$ Å, $b = 7.77796(6)$ Å, $c = 5.51879(4)$ Å					
La	4*c*	0.0188(2)	0.25	-0.0042(3)	0.0056(3)
Cr	4*b*	0	0	0.5	0.0015(4)
O(1)	4*c*	0.494(2)	0.25	0.064(2)	0.003(3)
O(2)	8*d*	0.272(2)	0.035(1)	0.728(2)	0.008(2)
$x = 0.50$				$R_{wp} = 13.320\%$, $R_{exp} = 11.497\%$	
$a = 5.5097(2)$ Å, $b = 7.6946(3)$ Å, $c = 5.4190(2)$ Å					
La/Tb	4*c*	0.0433(3)	0.25	-0.0107(9)	0.0057(9)
Cr	4*b*	0	0	0.5	0.0017(12)
O(1)	4*c*	0.485(3)	0.25	0.078(4)	0.0077(19)
O(2)	8*d*	0.289(4)	0.040(2)	0.714(5)	0.0007(19)
$x = 0.0$				$R_{wp} = 9.603\%$, $R_{exp} = 8.690\%$	
$a = 5.52310(13)$ Å, $b = 7.58067(15)$ Å, $c = 5.29589(11)$ Å					
Tb	4*c*	0.0605(3)	0.25	-0.0147(6)	0.0052(10)
Cr	4*b*	0	0	0.5	0.0037(14)
O(1)	4*c*	0.465(3)	0.25	0.096(3)	0.005(15)
O(2)	8*d*	0.296(3)	0.0545(7)	0.699(3)	0.0019(15)

The decreasing size of the A site cation, resulting in increased octahedral tilting, also places the Cr–O distances under tension, so on average, the bonds increase in length slightly as the composition approaches $TbCrO_3$. The increasing tilt angles are evident through the Cr–O–Cr bond angles, which deviate further from the ideal 180°, shown in Figure 5.5. The same divergence of the three distances, or bond length splitting is observed, as seen in the $La_xSm_{1-x}CrO_3$ solid solutions, where the CrO_6 octahedra become more regular and symmetrical as the structure becomes more distorted.

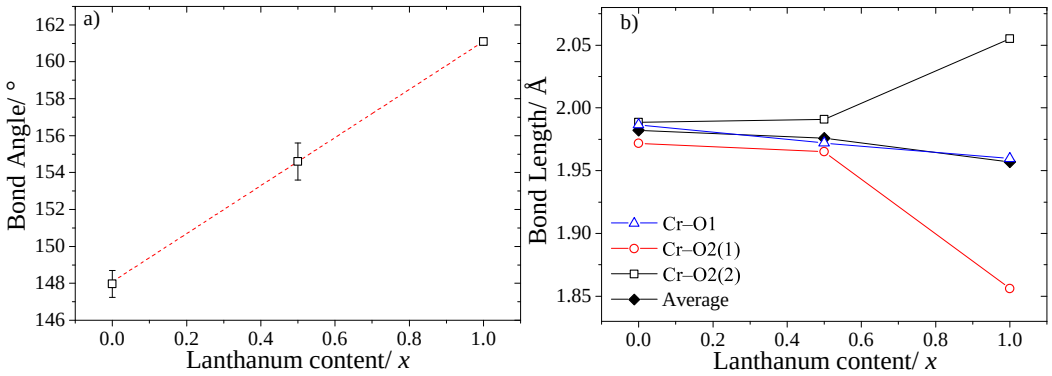

Figure 5.5: Variation of a) Cr–O–Cr bond angles and b) Cr–O bond lengths against lanthanum content, for the $La_xTb_{1-x}CrO_3$ perovskites. The Cr–O1 bond is oriented along the *b* direction, while both the Cr–O2(1) and Cr–O2(2) bonds both lie in the *ac* plane.

Tabulated values of Cr–O distances and Cr–O–Cr bond angles for the La-Tb materials are given in Table 5.3, along with octahedral ϕ and θ tilt angles, which describe rotations about the [010] and [101] axes, respectively.

Table 5.3: Cr–O distances and Cr–O–Cr angles from Rietveld refinement of the $La_xTb_{1-x}CrO_3$ solid solutions. Bond lengths Cr–O2(1) and Cr–O2(2) lie in the *ac* plane, while Cr–O1 is oriented along the *b* direction. The octahedral tilt angles, ϕ and θ, are calculated from atomic coordinates.

x	Cr–O1/ Å	Cr–O2(1)/ Å	Cr–O2(2)/ Å	Average Cr–O distance/Å	Cr–O–Cr angle/°	$\phi_{[010]}$/°	$\theta_{[101]}$/°
1.0	1.960(6)	1.86(3)	2.06(3)	1.95(2)	161.10(12)	5.18	9.38
0.5	1.972(4)	1.965(13)	1.991(10)	1.976(9)	154.60(10)	8.54	12.62
0.0	1.972(4)	1.986(8)	1.989(11)	1.982(8)	147.96(73)	10.97	16.01

Raman scattering, Figure 5.6, was used to confirm that the $La_{0.5}Tb_{0.5}CrO_3$ material is indeed a solid solution, and not merely a mixture of the separate end members. It is clear that the spectrum is not a sum of the two end members, with continuous shifts for the majority of the modes observed through the series. The increased broadness of the observed peaks, which arises as a result of the static disorder present, confirms the presence of two rare-earth cations of varied ionic radii on the same crystallographic position.

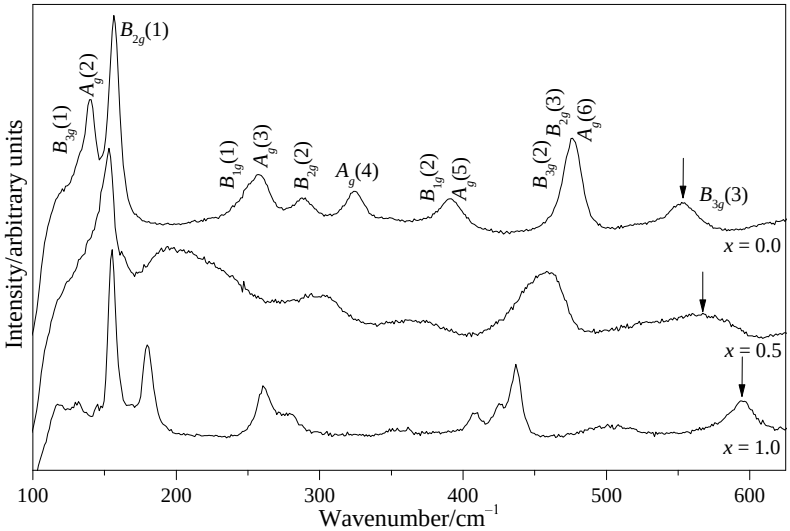

Figure 5.6: Raman spectra of $La_xTb_{1-x}CrO_3$ solid solutions recorded at –150 °C using a 632.8 nm He-Ne laser, along with mode assignments for $TbCrO_3$. Arrows show the progression of the $B_{3g}(3)$ mode through the series.

These Raman data were collected only to confirm the mixed La-Tb solid solution, and so an in-depth discussion of particular mode behaviours throughout the series, as performed for the La-Sm materials, was not undertaken. Such a study would require data from several further solid solutions with varying concentrations of x, such that mode interactions can be studied in detail. It is, however, possible to observe some relationships using the three spectra presented in Figure 5.6, and the previous mode assignments made for the end members.[15,16] For example, the $B_{3g}(3)$ mode labelled with arrows in Figure 5.6, is associated with the stretching vibrations of the CrO_6 octahedra and is therefore indirectly affected by structural distortion. The mode undergoes a clear softening in wavenumber towards $TbCrO_3$, which is due to the longer Cr–O bonds of $TbCrO_3$ exhibiting lower frequency vibrational modes, than those of $LaCrO_3$. Despite the effects of broadening, it is clear that the group consisting of the $B_{3g}(2)$, $B_{2g}(3)$, $A_g(6)$ bands in between 400-500 cm^{-1} converge to form the single intense peak in $TbCrO_3$. The broad mode at approximately 200 cm^{-1} in the spectrum for $La_{0.5}Tb_{0.5}CrO_3$ corresponds to the hardening of the $B_{2g}(2)$ and $A_g(3)$ modes, as they shift from the low wavenumber region in $LaCrO_3$ to their position in $TbCrO_3$. It is also clear that the two octahedral soft modes ($A_g(3)$ and $A_g(5)$), that exhibit an increased dependence on the tilting of the CrO_6 octahedra, undergo the largest shifts of any mode from one end member to the other.

5.3.1.2 $Y_xHo_{1-x}CrO_3$

As mentioned above, the almost identical ionic radii of Y^{3+} and Ho^{3+} (1.075 Å and 1.072 Å, respectively[7]) offer the possibility of producing solid solutions where the A site radius variance remains close to zero across the series. In addition to this, the degree of structural distortion would also remain constant as Y^{3+} is replaced for Ho^{3+}.

The three materials, including $Y_{0.5}Ho_{0.5}CrO_3$ and both end members, were prepared hydrothermally by heating the mixed-metal precursors to 380 °C for 6 hour durations. The PXRD patterns for each material, shown in Figure 5.7, appear to be very similar due to the almost identical distortions of each structure, with only very subtle changes in some peak intensities. Holmium has twenty-eight more electrons than yttrium, and as a result will more strongly scatter X-rays, influencing the intensities of certain Bragg reflections.

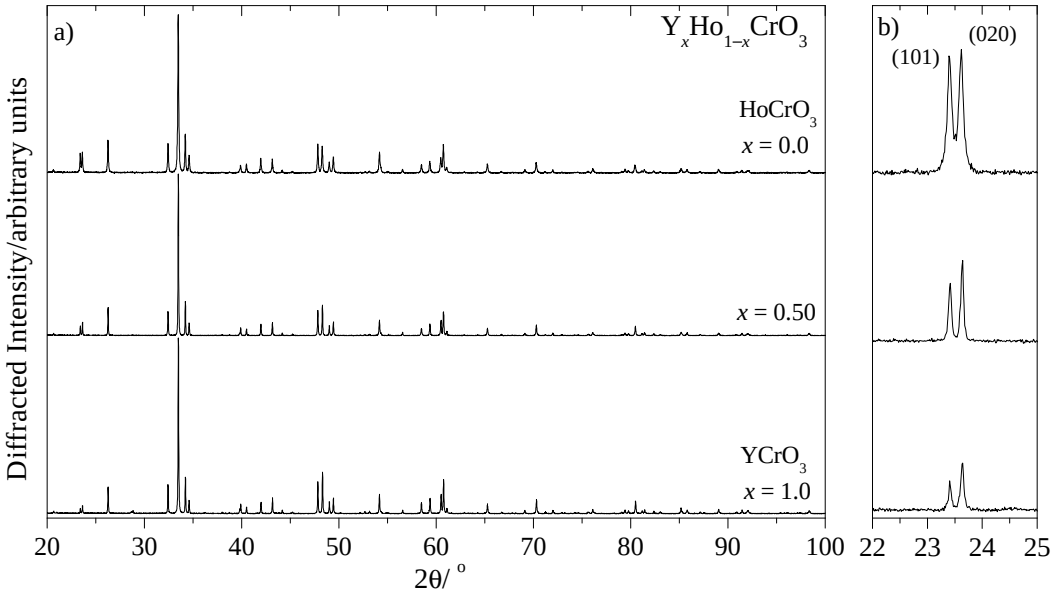

Figure 5.7: PXRD patterns of $Y_xHo_{1-x}CrO_3$ solid solutions, with b) highlighting the subtle changes in relative intensities as Ho^{3+} content increases.

The results of structural refinement against PXRD data of the $Y_{0.5}Ho_{0.5}CrO_3$ solid solution are shown in Figure 5.8. This involved the refinement of the same fourteen structural parameters that were refined against data of the La-Sm and La-Tb solid solutions, including lattice parameters, atomic coordinates, and isotropic temperature factors.

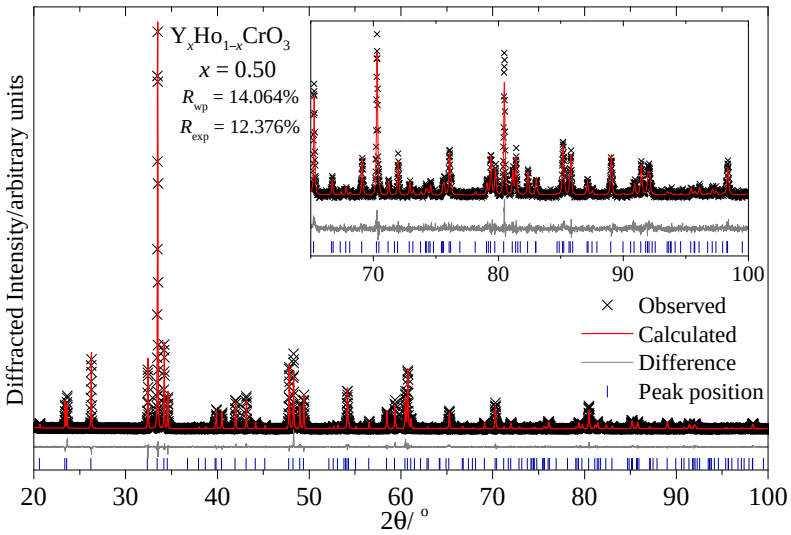

Figure 5.8: Rietveld refinement performed against PXRD data (λ = 1.54056 Å) of $Y_{0.5}Ho_{0.5}CrO_3$. Observed (black crosses), calculated (red line), difference (grey line) patterns are shown, whilst blue tick marks represent allowed peak positions.

The structures were modelled and refined using space group *Pnma*. As Y^{3+} and Ho^{3+} were the smallest rare-earth ions used in this study their chromite structures are the most distorted, and due to very comparable radii, the three materials are almost perfectly isostructural. The refined parameters are given in Table 5.4 and show just how comparable the structures are for each material with the largest deviations, though still very slight, observed in the oxygen positions. The only appreciable differences between each material are the increasing densities, observed as yttrium is substituted by heavier holmium.

Table 5.4: Structural details obtained from Rietveld refinements against PXRD data for the $Y_xHo_{1-x}CrO_3$ solid solutions, including R_{wp} and R_{exp} values for each.

Atom	Site	x	y	z	U_{iso}/Å^2
$x = 1.0$			a = 5.52539(5) Å, b = 7.53629(6) Å, c = 5.24390(5) Å		
Y	4c	0.0659(2)	0.25	-0.0169(3)	0.0045(6)
Cr	4b	0	0	0.5	0.0044(7)
O(1)	4c	0.4608(13)	0.25	0.1108(13)	0.005(2)
O(2)	8d	0.3017(9)	0.0542(6)	0.6942(9)	0.0103(18)
crystallographic density = 5.74601(8) g cm^{-3}, R_{wp} = 15.038%, R_{exp} = 11.191%					
$x = 0.50$			a = 5.52525(4) Å, b = 7.53808(5) Å, c = 5.24512(4) Å		
Y/Ho	4c	0.0665(2)	0.25	-0.0168(2)	0.0043(5)
Cr	4b	0	0	0.5	0.0015(7)
O(1)	4c	0.4641(15)	0.25	0.1157(19)	0.006(2)
O(2)	8d	0.2984(9)	0.0521(6)	0.6959(9)	0.0024(18)
crystallographic density = 6.89922(10) g cm^{-3}, R_{wp} = 14.064%, R_{exp} = 12.376%					
$x = 0.0$			a = 5.52372(7) Å, b = 7.54000(9) Å, c = 5.24524(7) Å		
Ho	4c	0.0660(2)	0.25	-0.0171(2)	0.0053(6)
Cr	4b	0	0	0.5	0.0008(2)
O(1)	4c	0.4638(13)	0.25	0.1091(13)	0.004(2)
O(2)	8d	0.2996(11)	0.0545(7)	0.6953(11)	0.0020(7)
crystallographic density = 8.05499(17) g cm^{-3}, R_{wp} = 12.600%, R_{exp} = 11.478%					

The lattice parameters, Cr–O distances, and Cr–O–Cr bond angles determined from Rietveld refinement of the three materials remain constant from one end member to the other. The Cr–O bond lengths are provided in Table 5.5 and agree within 0.01 Å of each other, and the octahedral rotations about the [010] and [101] axes are also very comparable.

Table 5.5: Cr–O distances and Cr–O–Cr angles from Rietveld refinement of the $Y_xHo_{1-x}CrO_3$ solid solutions. Bond lengths Cr–O2(1) and Cr–O2(2) lie in the ac plane, while Cr–O1 is oriented along the b direction. The octahedral tilt angles, ϕ and θ, are calculated from atomic coordinates.

x	Cr–O1/ Å	Cr–O2(1)/ Å	Cr–O2(2)/ Å	Average Cr–O distance/Å	Cr–O–Cr angle/°	$\phi_{[010]}$/°	$\theta_{[101]}$/°
1.0	1.983(2)	1.985(5)	1.996(5)	1.988(4)	143.6(4)	12.12	18.22
0.5	1.978(2)	1.981(3)	1.986(4)	1.982(3)	144.6(3)	11.57	18.71
0.0	1.980(2)	1.987(5)	1.989(3)	1.985(3)	144.3(4)	11.77	17.83

Because of the similar PXRD patterns that show the same average crystal structure, Raman scattering is perhaps most crucial when applied to $Y_xHo_{1-x}CrO_3$, compared to the other materials studied in this thesis. The majority of the observed phonon modes, highlighted in Figure 5.9, arise from the vibrational motion of octahedra, and therefore exhibit a dependence upon the level of structural distortion, which doesn't change. As a result, the most apparent

observation is that these modes do not change in wavenumber, and the only changes observed lie in the low wavenumber region.

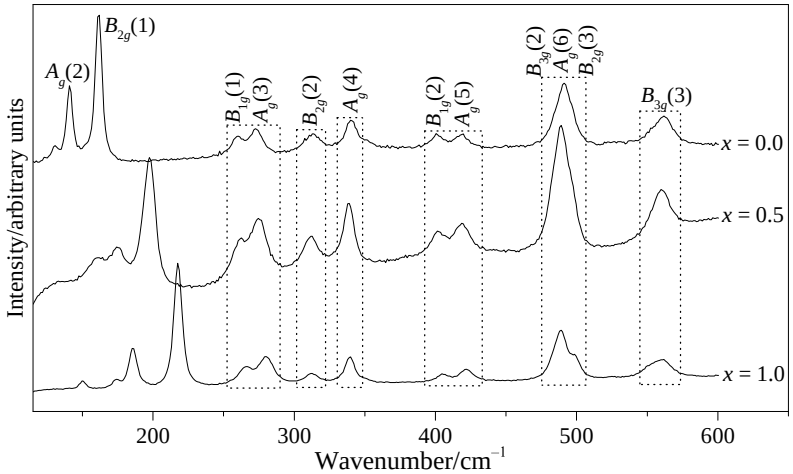

Figure 5.9: Raman spectra of the $Y_xHo_{1-x}CrO_3$ solid solutions recorded at –150 °C using a 632.8 nm He-Ne laser, along with mode assignments for $HoCrO_3$. The dashed regions highlight bands dependent upon orthorhombic distortion.

It is advantageous in this case to exploit the few modes that don't display a large dependence on structural distortion, through modes that are dominated by vibrations of the A site cations. The $A_g(2)$ and $B_{2g}(1)$ bands are assigned as two modes that depend upon A site cation vibrations and are insensitive to changes in orthorhombic distortion.

As described for the same two modes for the La-Sm materials in Chapter 4, under the approximation of a harmonic oscillator (Equation 4.3), heavier atoms exhibit vibrational modes with lower frequencies than those of lighter atoms. For the study of the La-Sm and La-Tb materials discussed above, the observed shifts of these bands throughout the series remained rather small as the mass difference between the two rare-earth cations is very small. This small shift, in fact, assisted in the assignment of these particular modes. However, for the $Y_xHo_{1-x}CrO_3$ solid solutions, the mass difference between the two A site cations is significantly larger, with holmium being almost twice the mass of yttrium (m_{Ho} = 164.93 and m_Y = 88.91 g mol^{-1}). This difference, therefore accounts for the large shift of $\sim$ 50 cm^{-1} for both the $A_g(2)$ and $B_{2g}(1)$ modes from $YCrO_3$ to $HoCrO_3$, which are shown in further detail by Figure 5.10.

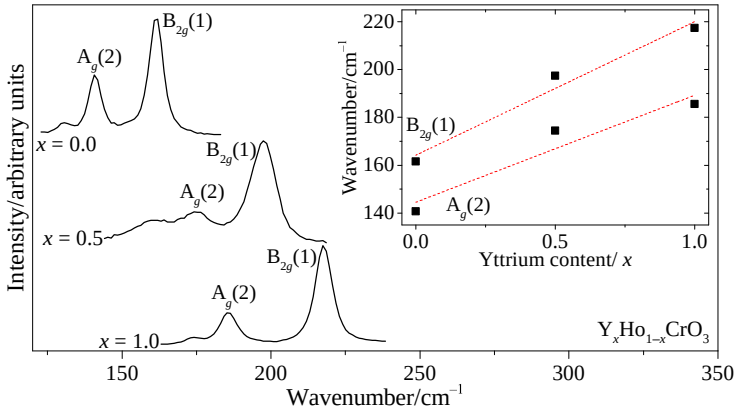

Figure 5.10: Variation in band positions for the $A_g(2)$ and $B_{2g}(1)$ modes throughout the $Y_xHo_{1-x}CrO_3$ series. Inset data shows a linear dependence on average A-site cation mass.

The two bands are slightly broader for the solid solution compared to the end members, consistent with the local disorder introduced onto the A site of the structure, as well as the large difference in mass for the two lanthanides. It is interesting to note that due to the similar levels of structural distortion, distinguishing between each material using XRD is problematic, however, it is possible to easily do so using Raman scattering.

5.3.2 Magnetic Properties

Figure 5.11 shows molar magnetic susceptibilities measured as a function of temperature for $La_xTb_{1-x}CrO_3$. Both Cr^{3+} and Tb^{3+} carry magnetic moments, with spin-only moments of $S = 3/2$ and $S = 8/2$, respectively, and La^{3+} being nonmagnetic, which explains the large differences observed between each material.

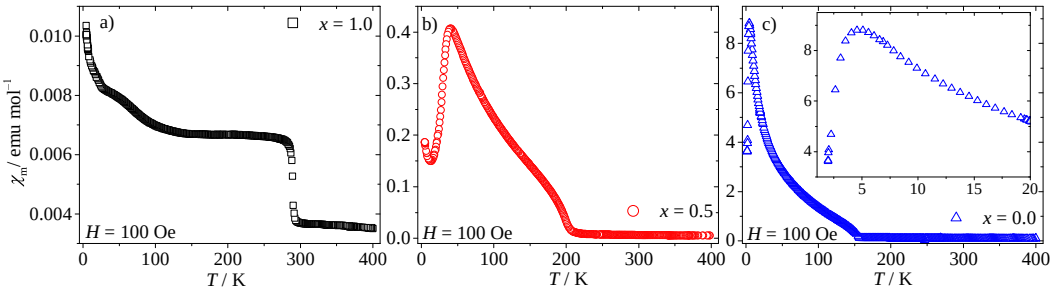

Figure 5.11: FCC curves for hydrothermal $La_xTb_{1-x}CrO_3$ materials, measured in applied fields of 100 Oe. Figures a), b), and c) show data for $x = 1.0$, 0.5, and 0.0, respectively. The inset in c) highlights the ordering of Tb^{3+} spins at ~ 5 K.

The superexchange interactions causing the antiferromagnetic ordering of adjacent Cr^{3+} spins are responsible for the observed magnetic responses below the Néel temperature of each material. Although the magnitude of the susceptibility in $LaCrO_3$ is small, T_N is clear for each material following a sharp increase in magnetic response. Below T_N, the magnetic structure of these materials is based upon a Γ_4 representation, with G-type antiferromagnetic order aligned along the c axis of the unit cell (crystallographic axes in the *Pbnm* setting).[17] There is a sharp downturn in the data of $TbCrO_3$ at very low temperature ($\sim$ 5 K) which is associated with the ordering of the Tb^{3+} moments, separate to the Cr^{3+} sublattice.[15] Although the Tb^{3+} spins are paramagnetic above this temperature, the moments contribute to the observed susceptibility through coupling interactions with the ordered Cr^{3+} sublattice; the isotropic superexchange interactions between neighbouring Tb^{3+} spins being so weak that they order only at very low temperatures. Above this, the spins of Tb^{3+} are polarised parallel to the weak ferromagnetic component of the Cr^{3+} sublattice, and below this temperature they decouple and order antiferromagnetically.[17]

The greater structural distortion of $TbCrO_3$ compared to $LaCrO_3$, and t_{2g}-e_g orbital hybridisation that this results in, are responsible for the much lower Néel temperature observed for the former.[18] A linear trend is observed for T_N as the composition changes from $LaCrO_3$ to $TbCrO_3$, shown in Figure 5.12 a).

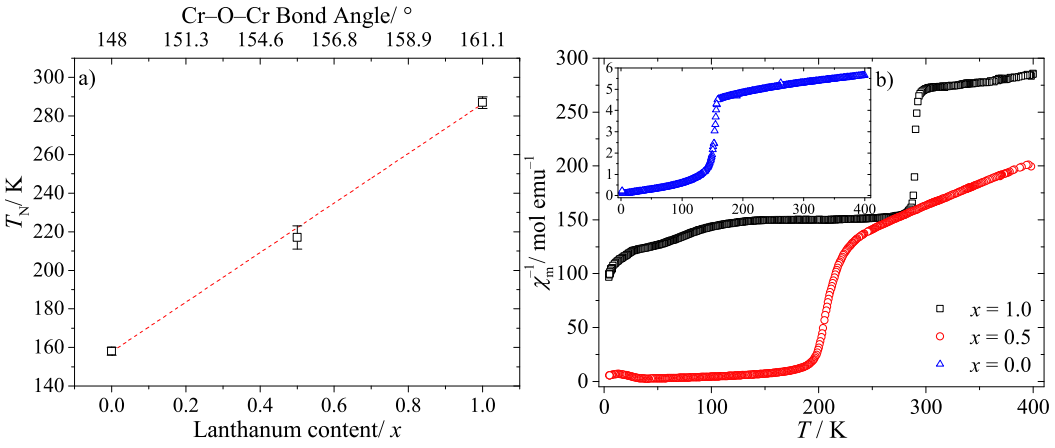

Figure 5.12: Variation of a) T_N as a function of composition and superexchange bond angle, and b) inverse molar magnetic susceptibility as a function of temperature. The data were collected under FCC conditions in an applied field of 100 Oe, and are grouped according to their magnitude.

Above T_N, each solid solution exhibits Curie-Weiss behaviour as shown by the inverse susceptibility data in Figure 5.12 b). The magnetic parameters determined

from fitting this region of the data are summarised in Table 5.6.

The value of $\mu_{Cr^{3+}}$ determined from $LaCrO_3$ is assumed for each member of the series, and is used to calculate the experimental moment of $\mu_{Tb^{3+}}$ through Equation 5.1.

$$\mu_{\text{eff}} = \sqrt{[(\mu_{Tb^{3+}})^2 + (\mu_{Cr^{3+}})^2]} \tag{5.1}$$

The theoretical effective moments were determined assuming a spin-only contribution from Cr^{3+} (3.87 μ_B), and a full J moment from the Tb^{3+} (9.72 μ_B) on the A site.

Table 5.6: Magnetic parameters determined from Curie-Weiss fitting of inverse susceptibility data for the $La_xTb_{1-x}CrO_3$ solid solutions. Parameters for the hydrothermal (hyd.), annealed (ann.) and solid state (s.s.) materials are given. Values of theoretical effective moments μ_{theo} are determined assuming full J and spin moments on both the A and B sites, respectively.

	T_N/K		$\lvert\theta\rvert$/	C/	μ_{eff}/	μ_{theo}/	$\mu_{Tb^{3+}}$/	$\mu_{Cr^{3+}}$/
x	This study	Literature	K	μ_B	μ_B	μ_B	μ_B	μ_B
1.0	287	288,[14,15] 287,[19] 295,[20] 282[17]	633.8	2.985	4.887	3.87	0	4.887
0.5 hyd.	217	-	79.4	9.11	6.97	6.21	4.970	4.887
0.5 ann.	-	-	28.9	7.60	6.37	6.21	4.085	4.887
0.5 s. s.	-	-	20.9	7.31	6.24	6.21	3.880	4.887
0.0	158	159[15,21]	190.9	41.08	12.82	10.46	11.852	4.887

Like with the La-Sm solid solutions, the effective moments indicate that Cr^{3+} is present in its +3 oxidation state with $S = 3/2$, and $\mu_{Tb^{3+}}$ increases as the nonmagnetic La^{3+} is substituted by Tb^{3+}.

The Weiss temperatures for $x = 0.5$ and 0.0 are less negative and much closer to the observed Néel temperatures, compared to $LaCrO_3$, and the parameters determined for $TbCrO_3$ agree well with those reported in the literature.[15]

When comparing the materials prepared through different synthesis methods, the hydrothermal sample provides a Weiss temperature closest to the Néel temperature. The different parameters support the observations from XRD, which shows that when the hydrothermal material is annealed to 1000 °C, it becomes more like the sample prepared through solid state synthesis, where the values for θ, C and μ_{eff} agree very well for both the annealed and solid state samples.

The stark differences in the magnetic properties of $La_{0.5}Tb_{0.5}CrO_3$ solid solutions prepared through the different methods are clear when comparing molar magnetic susceptibility data in Figure 5.13.

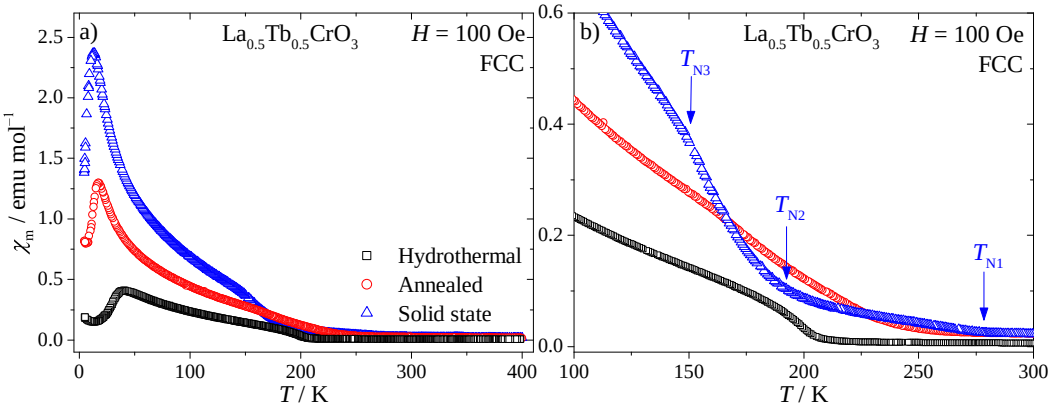

Figure 5.13: Comparison between FCC data of $La_{0.5}Tb_{0.5}CrO_3$ materials prepared through various synthesis methods. A magnified plot of the T_N region is shown in b) with labels corresponding to events described in the text.

As discussed above, the data from the hydrothermally prepared material display a T_N that agrees with the linear relationship between the end members, as well as exhibiting both interesting low temperature behaviour, and typical Curie-Weiss behaviour above T_N. In contrast, data recorded from the materials prepared through other methods differ greatly. The solid state sample shows several events near to the expected T_N, which are labelled as T_{N1}, T_{N2}, and T_{N3} in Figure 5.13 b). This observation suggests that each corresponds to the Néel temperatures of the three individual materials; $La_{0.5}Tb_{0.5}CrO_3$, and the two end members, $LaCrO_3$ and $TbCrO_3$. The first, very weak, upturn is observed at approximately 280 K, close to the ordering temperature of $LaCrO_3$.[19] T_{N2} corresponds to a broad upturn in the data occurring at a similar temperature to the T_N of the hydrothermal sample. Finally, the point labelled T_{N3} shows a small feature at a temperature similar to the ordering of $TbCrO_3$.[15,21]

The transitions around the ordering temperature of the annealed material are not as abrupt as those described above in the solid state material. Instead, a broad upturn in the data is observed at approximately 50 K higher than the hydrothermally-prepared sample. This temperature difference implies that the hydrothermal material has indeed changed during the annealing process, possibly becoming more like the solid state material.

The data at low temperature for both solid state and annealed materials are very similar to the end member $TbCrO_3$, where all three display the downturn that corresponds to the ordering of the Tb^{3+} spins. The observed downturn in the data for the hydrothermal material is at a much higher temperature than that observed

for the other two. The difference in low-temperature behaviour of the hydrothermal material is discussed below in reaction to the observations from EELS.

Similar results are obtained when measuring the magnetisation as a function of applied field. Figure 5.14 a) compares data recorded at 5 K from the hydrothermal material against the end members, which display increased loop-opening and saturation magnetisation with increasing Tb^{3+} content. Part b) compares data recorded at 100 K from the $La_{0.5}Tb_{0.5}CrO_3$ material made through different synthesis methods. The data of the annealed material are different from the hydrothermal sample, and display hysteric behaviour that is similar to that of the solid state material.

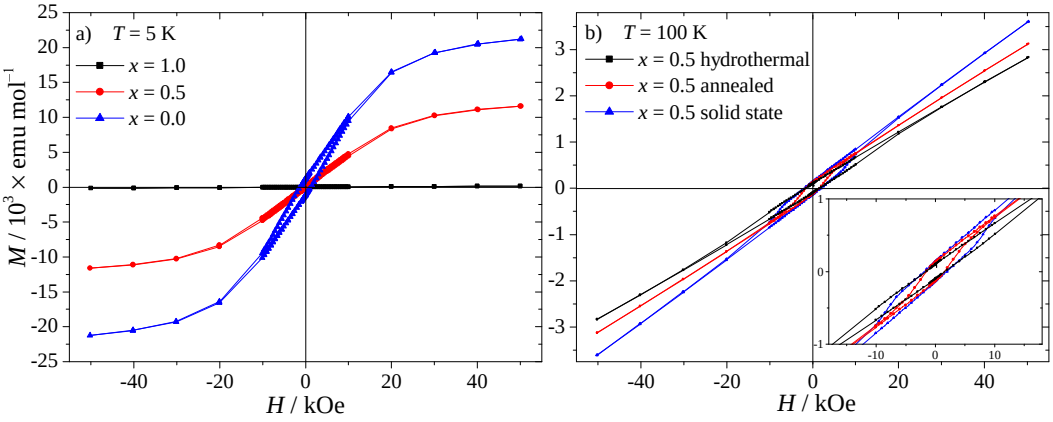

Figure 5.14: Magnetisation data recorded as a function of applied field for the a) $La_xTb_{1-x}CrO_3$ solid solutions ($0 \leq x \leq 1$) at 5 K, and the b) $La_{0.5}Tb_{0.5}CrO_3$ materials prepared through different synthesis methods at 100 K.

In contrast, the data for $La_{0.5}Sm_{0.5}CrO_3$ materials prepared by each synthesis method agree rather well, displaying similar values of T_N and similar low temperature behaviour, associated with the spin-reorientation of Cr^{3+} moments. This is consistent with the results of XRD and Raman spectroscopy, showing that both the hydrothermal and solid state methods produce very similar samples. A slightly lower susceptibility is observed for the solid state material, shown in Figure 5.15 a), supported by a weaker remanent magnetisation in data recorded as a function of applied field at 150 K. Similar observations are made when hydrothermal $La_{0.5}Sm_{0.5}CrO_3$ is annealed at 1000 °C for 12 hours, which appears to display a susceptibility in between the hydrothermal and solid state materials.

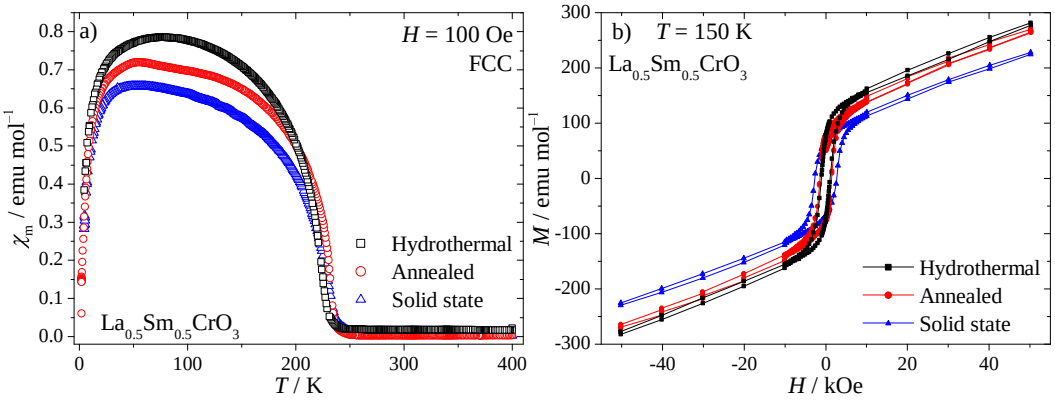

Figure 5.15: a) FCC data comparing $La_{0.5}Sm_{0.5}CrO_3$ materials prepared through hydrothermal, annealed and solid state syntheses. Magnetisation measured as a function of applied field at 150 K are shown in b).

The case of the $Y_xHo_{1-x}CrO_3$ solid solutions also includes the mixture of nonmagnetic (Y^{3+}) and magnetic (Ho^{3+}) rare-earth cations on the A site of the perovskite structure. Alongside the moment of Cr^{3+}, a spin-only moment of $S = 10/2$ is carried by Ho^{3+}, giving a total (**J**) theoretical moment of 10.6 μ_B.[22] Yttrium does not contribute to the magnetic properties of the materials, and so a significant increase in the molar magnetic susceptibility is observed below T_N where Y^{3+} is replaced by Ho^{3+}, shown in Figure 5.16 a).

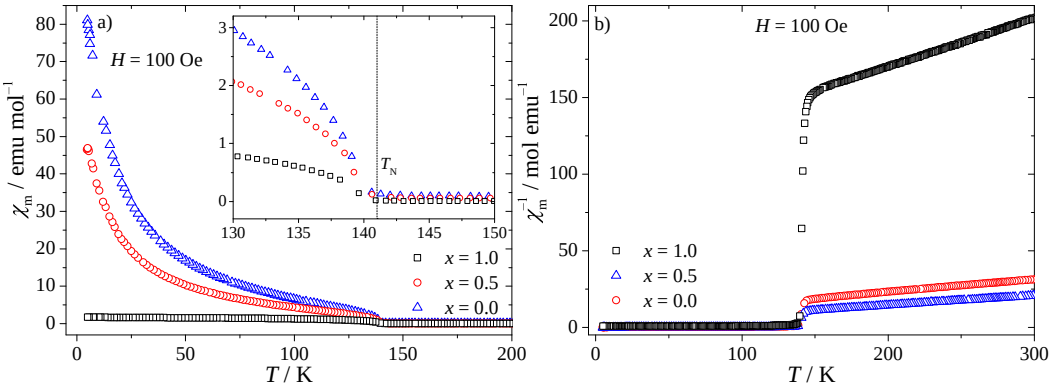

Figure 5.16: Temperature dependence of a) molar magnetic susceptibilities (FCC) of $Y_xHo_{1-x}CrO_3$ materials, measured in an applied field of 100 Oe. Inverse molar magnetic susceptibilities as a function of temperature are shown in b). The inset in a) draws attention to the very similar T_N for these materials.

The onset of antiferromagnetic ordering of the Cr^{3+} spins is clear from the molar magnetic susceptibility data. It is known that the onset temperature of this behaviour in $RCrO_3$ is governed by superexchange interactions along the Cr–O–Cr

pathways as well as the t_{2g}–e_g orbital hybridisation,[18] both of which are affected by the level of structural distortion. As was established through PXRD and Raman spectroscopy, the structures of these three materials are almost identical, and therefore it is not unexpected that the Cr^{3+} moments order at very similar temperatures, $\sim$ 141 K, shown by the data in Figures 5.16 a) and b).

Below T_N, the weak ferromagnetic component that results from the canted Cr^{3+} moments imposes a local field upon the paramagnetic Ho^{3+} moments which become polarised along the direction of the weak ferromagnetic field, increasing the magnitude of the observed susceptibility as the temperature decreases further. In comparison, the FCC curve of $YCrO_3$ shows saturation below T_N due to this weak ferromagnetic component of the Cr^{3+} ordering. The slight downturn in the data of $HoCrO_3$ at very low temperatures signifies the antiferromagnetic ordering of the Ho^{3+} spins, which was previously reported to occur at $\sim$ 12 K,[17,21] however, more recent studies showed this ordering to take place at 7.5 K.[23,24]

Curie-Weiss behaviour is shown above T_N by Figure 5.16 b), and effective moments are determined by fitting the region above this ordering, with values summarised in Table 5.7. The Weiss temperatures for each material are negative showing a predominance of antiferromagnetic interactions between the Cr^{3+} spins, and become less negative as more Ho^{3+} is introduced into the structure. The effective moment also increases significantly as the amount of Ho^{3+} increases, and is used to determine the separate contributions from both Ho^{3+} and Cr^{3+}. The value of 5.006 μ_B for $YCrO_3$ is considerably larger than the theoretical moment that should arise from Cr^{3+} (3.87 μ_B), and perhaps suggests the small ferromagnetic component of the ordered Cr^{3+} spins increases this value. For $HoCrO_3$, the calculated value of $\mu_{Ho^{3+}}$ agrees well with the theoretical full J value of 10.6 μ_B.

Table 5.7: Magnetic parameters determined by fitting the Curie-Weiss paramagnetic region of inverse susceptibility data for the $Y_xHo_{1-x}CrO_3$ solid solutions. Values of theoretical effective moments μ_{theo} are determined assuming full J and spin moments on both the A and B sites, respectively.

	T_N/K		$\lvert\theta\rvert$/	C/	μ_{eff}/	μ_{theo}/	$\mu_{Ho^{3+}}$/	$\mu_{Cr^{3+}}$/
x	This study	Literature	K	μ_B	μ_B	μ_B	μ_B	μ_B
1.0	141.5	141 [15,19,25]	332.7	3.13	5.01	3.87	0	5.01
0.50	141	-	90.8	12.62	8.20	6.56	6.49	5.01
0.0	140.5	142 [15,19,21,24]	26.4	15.79	11.24	11.28	10.06	5.01

The addition of Ho^{3+} to the $RCrO_3$ orthorhombic structure leads to the

observation of interesting magnetic effects, some of which are observed through magnetisation data that is recorded as a function of applied field. Such data recorded at 5 and 100 K are shown in Figure 5.17. The data recorded at 300 K, above room temperature, confirm that all three materials are paramagnetic at this temperature with no observed opening of the curves, though the magnetisation is observed to increase with Ho^{3+} content.

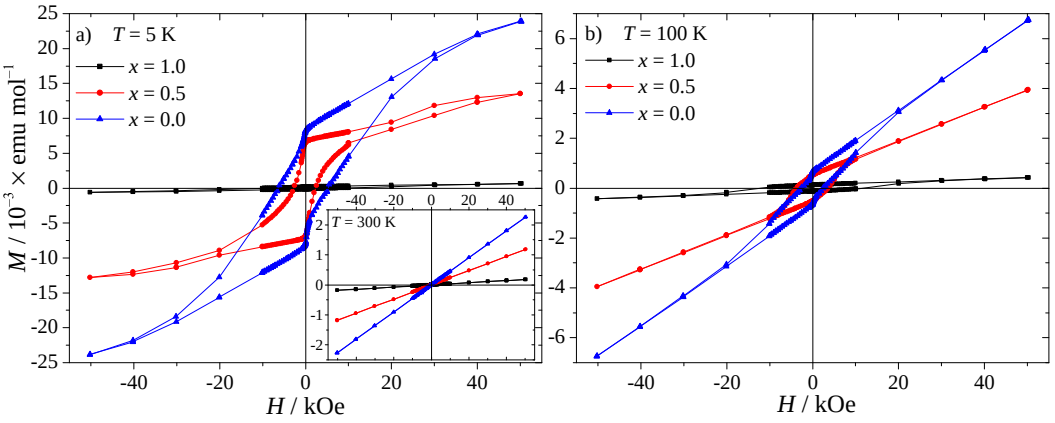

Figure 5.17: Magnetisation data recorded for the $Y_xHo_{1-x}CrO_3$ solid solutions as a function of applied field at a) 5 K (inset shows data measured at 300 K), and b) 100 K.

Data measured at 100 K, below T_N, shown in Figure 5.17 display increased hysteric behaviour which becomes more pronounced as Ho^{3+} content increases. The weak hysteresis observed in $YCrO_3$ is attributed to the weak ferromagnetic component resulting from the canted Cr^{3+} spins, and it is likely that this that leads to the unobserved saturation for each material.[24] Data measured at 5 K, shown in Figure 5.17 a), display increased hysteresis with no indication of saturation, even under an applied field of 50 kOe. It is worth noting that at this temperature, the Ho^{3+} spins have decoupled from the ordered Cr^{3+} arrangement, and are ordered antiferromagnetically. It is likely due to this antiferromagnetic exchange that saturation remains unobserved up to such large fields.[24]

5.3.3 EELS Study of Rare-earth Chromite Solid Solutions

So far, the effects of A site cation size variance have only been seen by the observed broadening of Raman modes between the solid solutions and end members. Direct study of any local ordering due to different coordination preferences for each lanthanide requires analysis performed on the atomic scale. Figure 5.18 shows a HR-TEM image of a $La_xSm_{1-x}CrO_3$ crystallite, aligned along

the [101] zone axis. Line profiles taken across several rare-earth atomic columns show intensity variations in each.

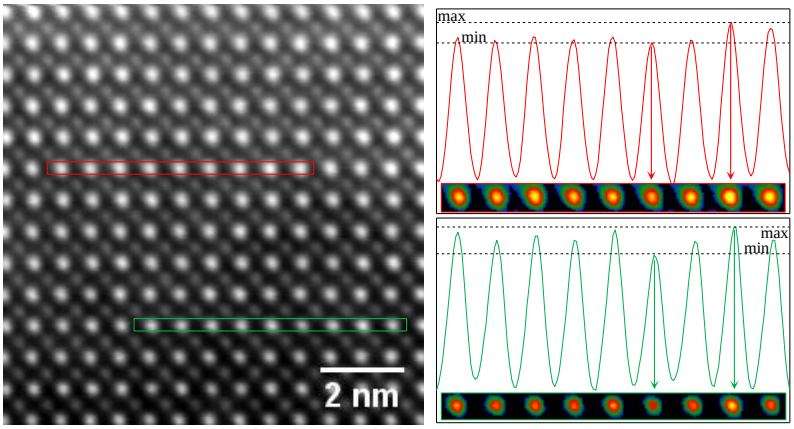

Figure 5.18: HAADF-STEM image (left) of $La_{0.5}Sm_{0.5}CrO_3$ crystallite aligned along [101] zone axis, and intensity profiles (right) of rare-earth columns only, normalised against the intensity of chromium columns, from selected areas labelled with corresponding colours.

The periodic structure of the B site sublattice, consisting only of ordered chromium columns, vary negligibly in intensity, but will be affected by sample thickness. Normalising the profiles from the rare-earth columns to the data from neighbouring chromium columns accounts for changes in crystal thickness, and allows for direct comparison between separate rare-earth columns. The profiles show that the intensities of each rare-earth column can vary by as much as 10-15%. As the incident beam is scattered by the electrons of the atom, scattering will be stronger if the target element has a greater number of electrons. Although this should not be unexpected given the limited number of atoms that were sampled, the observed variations in intensity do suggest that the distributions of both lanthanum and samarium within the atomic columns are not perfectly homogeneous, and that the columns of increased intensity could contain more samarium, due to its increased atomic number ($Z = 62$), compared to lanthanum ($Z = 57$). Reports using such techniques to study contrast ratios between heavy metal ions are rare, they are commonly used to study materials such as graphene doped with nitrogen,[26] for example, where the contrast between 6 and 7 electrons is much greater than that of 57 to 62. Atomic-resolution observations were made recently in complex $(La_{0.18}Sr_{0.82})(Al_{0.59}Ta_{0.41})O_3$ perovskites and were supported by atomic-resolution energy dispersive X-ray spectroscopy (EDX).[27] Again, the contrast ratios between the metals on both sites were much stronger, with La ($Z =$

57) and Sr ($Z = 38$) on the A site, and Al ($Z = 13$) and Ta ($Z = 73$) on the B site. HAADF-STEM was also recently used to directly image the octahedral distortions within complex molybdenum-vanadium oxides, and allowed information on the oxidation states of local metals to be obtained.[28]

To ascertain whether these observations from HAADF-STEM were genuine, and also to gain further information on the rare-earth distributions within each of the synthesised materials (La-Sm, La-Tb, and Y-Ho), an EELS study was undertaken. The technique provided atomically-resolved elemental maps, allowing for a direct study of the effects of variance.

The EELS maps confirm the existence of inhomogeneities in the distributions of lanthanum and samarium. Figure 5.19 shows both individual and combined EELS maps recorded from $La_{0.5}Sm_{0.5}CrO_3$. The individual maps show that there are variations for each element local to those atomic columns, and these become more obvious when combined into a single elemental map.

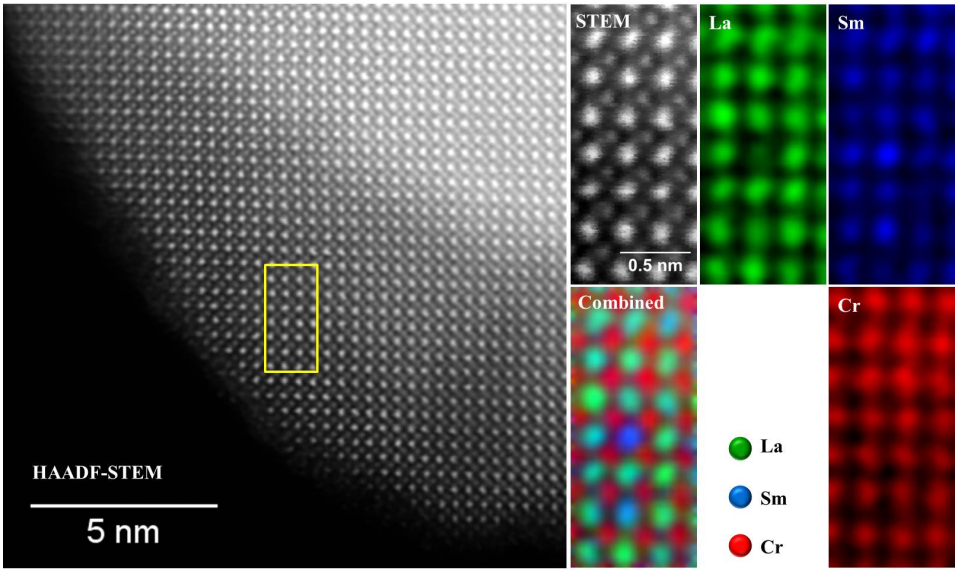

Figure 5.19: HAADF-STEM image (left) showing area selected for EELS. On the right are separate integrated EELS maps for chromium (red), lanthanum (green), and samarium (blue), along with all three combined into single map.

The individual map for chromium depends only upon sample thickness, displaying a drop-off in intensity towards the edge of the crystal, and no variations are observed between the atomic columns. In contrast, the maps for lanthanum and samarium show inhomogeneities within columns that complement each other when compared. For example, the column in the centre of the map that is

lanthanum-poor gives a strong signal in the corresponding samarium spectrum.

When comparing the EELS maps of La-Sm against those obtained from the other two materials, $La_{0.5}Tb_{0.5}CrO_3$ and $Y_{0.5}Ho_{0.5}CrO_3$, it is clear that the extent of local inhomogeneities are different in each. Example maps from each are compared in Figure 5.20; in the case of the Y-Ho solid solution, only maps integrated from the holmium spectra are used, as the K-edge of holmium dominates that of yttrium.

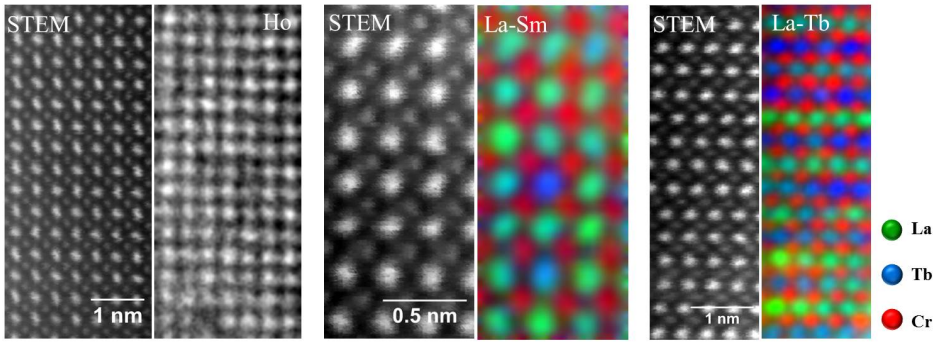

Figure 5.20: STEM images and corresponding EELS maps of $Y_{0.5}Ho_{0.5}CrO_3$ (left), $La_{0.5}Sm_{0.5}CrO_3$ (middle), and $La_{0.5}Tb_{0.5}CrO_3$ (right) crystallites along [101] zone axes.

To ensure that these observations were representative as much as possible to the bulk sample, EELS spectra were collected from approximately fifteen regions in each sample, recorded from several different crystallites. All of the recorded STEM images and EELS maps are included in Appendix A. It is clear, however, from the few given as examples in Figure 5.20, that the variation in rare-earth distribution is greatest in $La_{0.5}Tb_{0.5}CrO_3$, where lanthanum and terbium are observed to almost form separate layers. Further EELS spectra from several crystallites of $La_{0.5}Tb_{0.5}CrO_3$ showing such effects are provided in Figure 5.21.

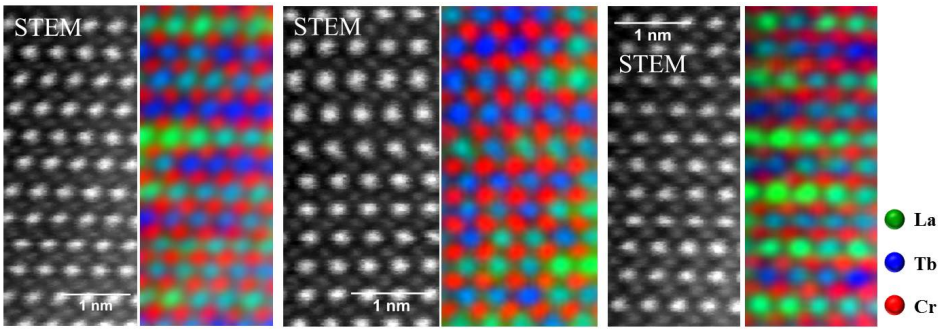

Figure 5.21: EELS maps of $La_{0.5}Tb_{0.5}CrO_3$ solid solution, measured from several different crystallites along the [101] zone axis.

The first conclusion to be drawn from these observations is that no structural evidence of these non-uniform distributions is presented by the other techniques used to study these materials. The short scale on which these inhomogeneities exist are below the observable limits of XRD and Raman scattering.

Analysis of the average structures of these materials through diffraction showed that the magnitude of octahedral tilting depends upon the amount of samarium or terbium present. Whilst this conclusion holds true, the observations of a non-uniform rare-earth distribution from EELS suggest that the octahedral tilts will also be inhomogeneous, and therefore it is inaccurate to describe the local structure using a single space group symmetry or tilt system. In reality, one would imagine that the local structural environments surrounding regions that are rich in the smaller samarium or terbium cations would be more distorted than areas that contain more lanthanum. It is likely that these effects are averaged out in $La_{0.5}Sm_{0.5}CrO_3$, whilst for $La_{0.5}Tb_{0.5}CrO_3$, it depends upon the length scales over which the layered-like structures are observed. A few tilt systems allow for the stabilisation of A site cation ordering by removing the equivalence of the A site positions. One such system, $a^+a^+a^+$, is commonly used to describe A site ordered $AA'_3B_4O_{12}$ perovskites.[2] The two A site cations are usually hugely different in size, however, with the A′ site typically accommodating a much smaller transition metal, for example, $CaCu_3Ti_4O_{12}$. Given that this results in an almost square planar coordination environment for three-fourths of the A site cations, this system would not be suitable to describe the layered-like structures observed in $La_{0.5}Tb_{0.5}CrO_3$.

As shown in Figure 5.1, the A site radius variance is approximately twice as much for La-Tb solid solutions of $x = 0.5$, than for La-Sm, and it is this that drives the increased separation observed in the former. The size difference between La^{3+} and

Tb^{3+} means that each cation has a different coordination preference, leading to size ordering effects; La^{3+} prefers to coordinate 9 oxygens in $LaCrO_3$, whilst Tb^{3+} prefers to bond to 8 in $TbCrO_3$. This is displayed clearly in Figure 5.22, showing the different coordination of the A sites in each structure, which represents the preferred coordination of each rare-earth, even in the $La_{0.5}Tb_{0.5}CrO_3$ solid solution.

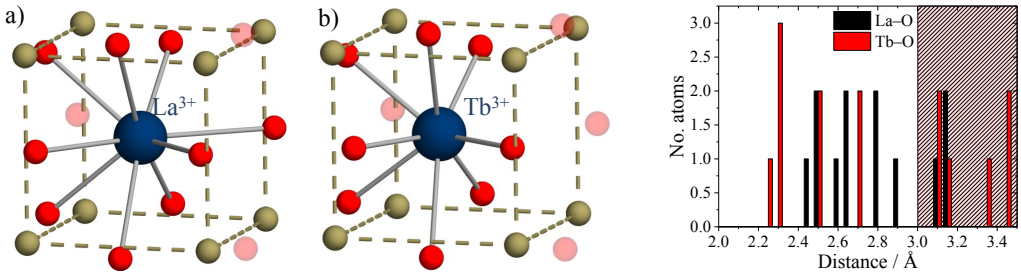

Figure 5.22: Different A site coordination environments in a) $LaCrO_3$ and b) $TbCrO_3$. Faded oxygen atoms are further away than the 3.0 Å cut-off limit, making La^{3+} nine-coordinate, and Tb^{3+} eight-coordinate. A histogram of the bond lengths of each is shown in c).

The tolerance factors of both $LaCrO_3$ and $TbCrO_3$ can be considered for the separate layers, which are 0.92 and 0.877, respectively. These will likely produce different degrees of octahedral tilting between the layers, resulting in competition and strain forces. These effects may even generate distortions to the CrO_6 octahedra themselves, causing them to deviate away from the ideal octahedron shape. It is possible to imagine that the separation of the rare-earths into regions, like the layered-like structures observed in this work, reduces strain on the structure, when compared to a *perfectly mixed* distribution (La-Tb-La-Tb), also referred to as rock salt,[2] where each La atom would have six Tb nearest neighbours, and vice versa. The observed grouping of more concentrated layered regions such as these must reduce the strain within the local structure.

Profile analyses in Figure 5.23 show a direct comparison between one of the EELS maps and its corresponding STEM image, both of which are normalised against the Cr signal. The variations in rare-earth distribution complement each other in both; the least intense column in the STEM image contains the highest concentration of lanthanum according to the EELS map, whilst the neighbouring column is terbium-rich, resulting in the most intense peak in the STEM image.

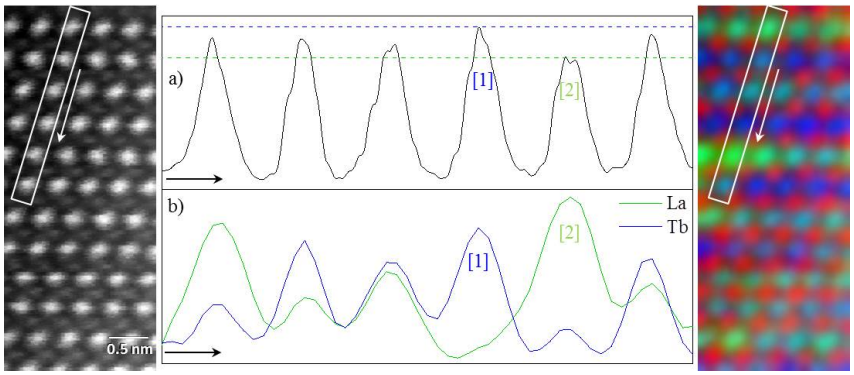

Figure 5.23: Line profiles for hydrothermal $La_{0.5}Tb_{0.5}CrO_3$ from the highlighted areas in a) STEM image (left), and b) corresponding EELS map (right), showing agreement between analysis of independent columns. The Tb-rich intense column is labelled as [1], and the La-rich less intense column is labelled as [2].

The almost identical ionic radii of Y^{3+} and Ho^{3+} means that the effects of variance are expected to be negligible in the $Y_{0.5}Ho_{0.5}CrO_3$ solid solution, therefore, the distribution of the two would be random. It is noted that a random distribution would still result in areas of non-uniformity, and in the most unlikely case, the possibility of atomic columns consisting solely of Y^{3+} or Ho^{3+}. It could be classed as a rock salt distribution if the two were distributed evenly in an alternating pattern throughout the structure, not a random one.[2] Since no variance effects exist to govern any form of distribution, it is the randomness that leads to the observed variations in the holmium EELS maps, shown in Figure 5.24.

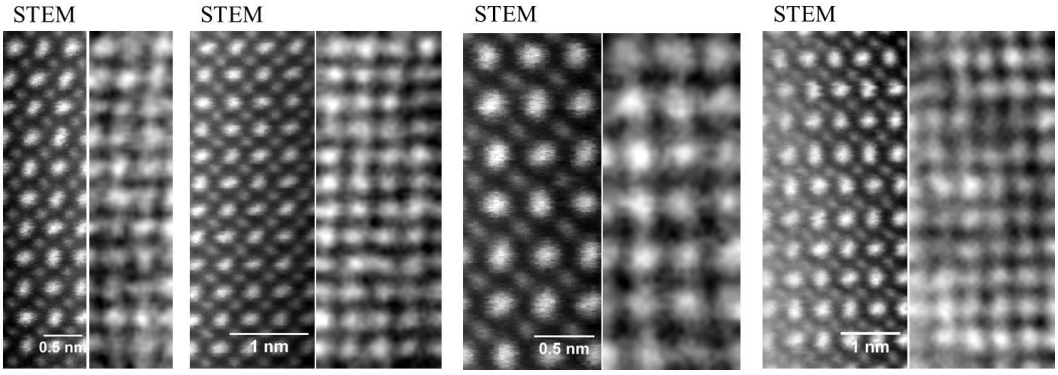

Figure 5.24: STEM images and corresponding EELS maps recorded from $Y_{0.5}Ho_{0.5}CrO_3$.

The effect of synthesis method on the rare-earth distribution was examined by comparison of materials produced through hydrothermal and solid state techniques. Solid state samples of each material were produced by firing the mixed metal amorphous precursors to 1200 °C in the case of $La_{0.5}Sm_{0.5}CrO_3$, and 1400

°C for $La_{0.5}Tb_{0.5}CrO_3$. The use of the same amorphous precursors ensured that the degree of mixing of both rare-earths prior to crystallisation was identical to those that underwent hydrothermal treatment. For the $La_{0.5}Sm_{0.5}CrO_3$ solid solutions, a comparison of the X-ray patterns and TEM images of the crystallites were made in Chapter 4. The XRD data are very similar for the materials produced from both methods, whilst the TEM images reveal a uniform size distribution of crystallites for the hydrothermal sample, but much greater variation in crystallite size for the solid state material.

The results from elemental mapping of both samples are consistent with XRD and Raman spectroscopy, where both of the materials appear to have similar distribution of the two rare-earths, lanthanum and samarium. The material prepared by solid state synthesis displays similar local inhomogeneities, resulting in La-rich and Sm-rich columns, much like those observed in the hydrothermal sample. A selected few EELS maps from each material are compared in Figure 5.25, and further EELS maps from each sample are provided in Appendix A.

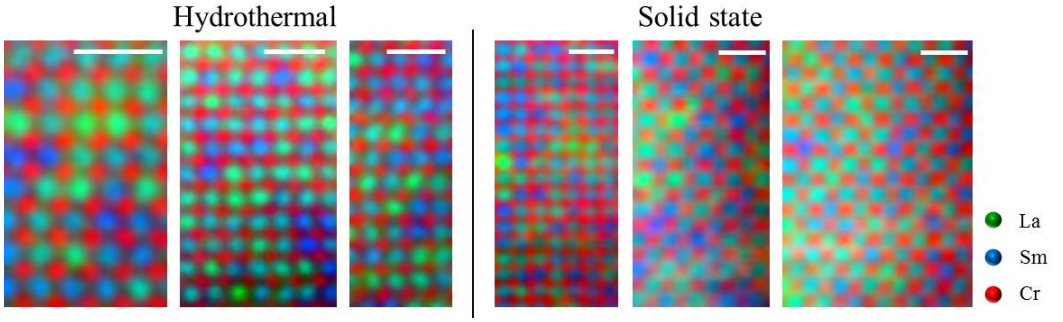

Figure 5.25: Selected EELS maps comparing the rare-earth distribution in $La_{0.5}Sm_{0.5}CrO_3$ materials made via hydrothermal (left) and solid state (right) synthesis. The white scale bars on each of the maps corresponds to 1 nm. Further maps are provided in Appendix A.

Unlike these relatively well-mixed distributions, comparison of the $La_{0.5}Tb_{0.5}CrO_3$ materials in Figure 5.26 shows much greater differences. There is no evidence that the layered-like distributions observed in the hydrothermal sample are present in the solid state material. Instead, the distribution varies more in the solid state sample resulting in much larger regions, over tens of nanometres in size, that are rich in lanthanum, separate to those that are rich in terbium. This is contrasted against the hydrothermal material which displays sub-nanometre regions where the rare-earths are constrained within layers.

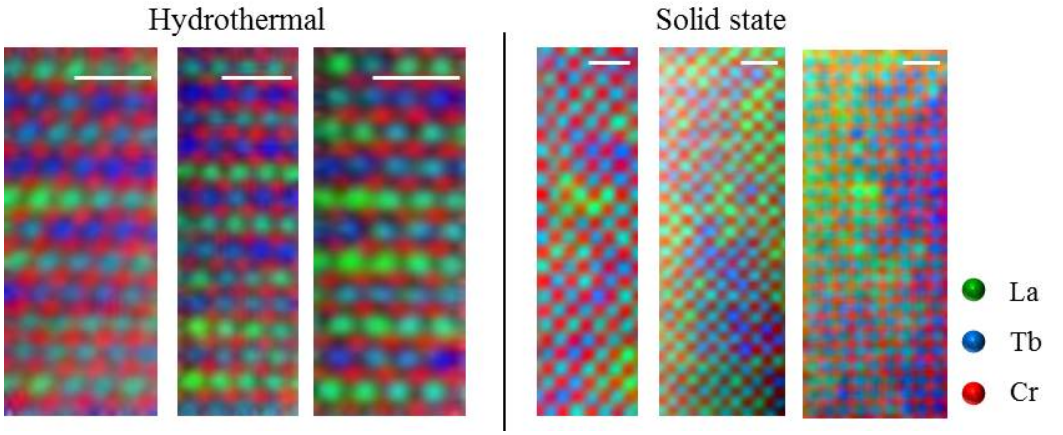

Figure 5.26: Selected EELS maps comparing rare-earth distributions in $La_{0.5}Tb_{0.5}CrO_3$ solid solutions made via hydrothermal (left) and solid state (right) synthesis. The white scale bar on each map corresponds to 1 nm. Further maps are provided in Appendix A.

Although it is not immediately obvious, these larger regions of varied distribution can be observed through careful analysis of the STEM images. Figure 5.27 a) shows a large scale EELS map along the edge of a crystallite which displays areas of phase separated $LaCrO_3$ shown in green, and $TbCrO_3$ shown in blue, with a higher magnification map of the boundary between them shown in b). Figure 5.27 c) and d) show HAADF-STEM images taken from regions separately rich in terbium and lanthanum, respectively. The structures of $TbCrO_3$ and $LaCrO_3$ are overlaid, and show the different degrees of distortion, resulting from octahedral tilting present in each region, where the rare-earth columns exhibit periodic horizontal displacements in the Tb-rich region, compared to the less distorted columns of the La-rich region, which resembles the less distorted structure of $LaCrO_3$.

Figures 5.27 e) and f) show HAADF-STEM and BF-STEM images, respectively, across the boundary between the two regions. Bright-field imaging is more sensitive to electron contributions from light atoms. The boundary is more clear in the BF image, where the array of atoms in the bottom left of the image is different to those in the top right corner, consistent with the different structures of $LaCrO_3$ and $TbCrO_3$, which would be more clearly observed through anion positions.

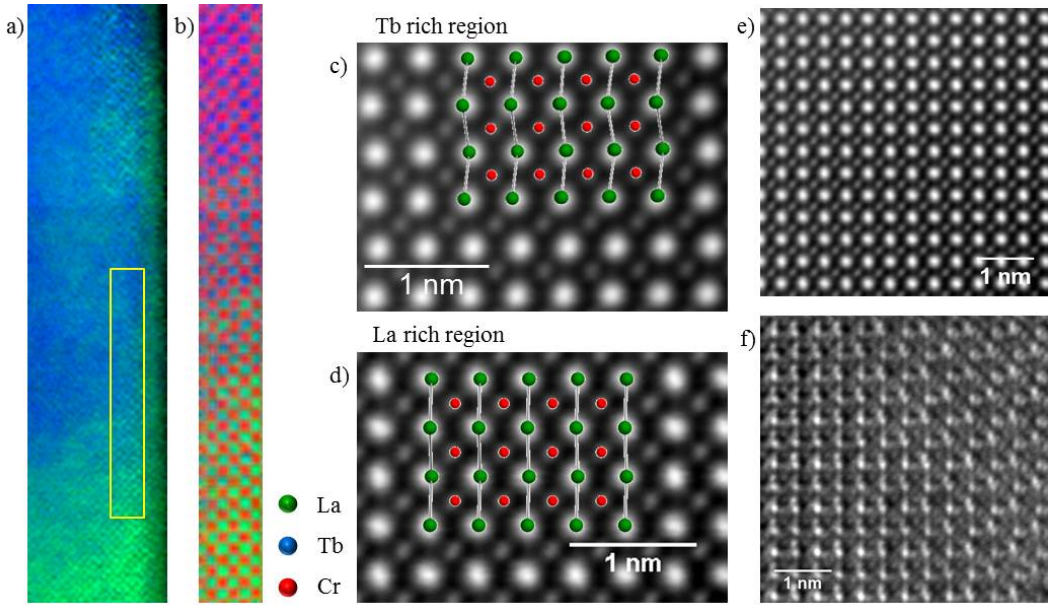

Figure 5.27: Large scale EELS maps a) and b) across boundary between La-rich and Tb-rich regions in $La_{0.5}Tb_{0.5}CrO_3$ made through solid state synthesis. HAADF-STEM images c) and d) are shown from each of these regions, whilst e) and f) display HAADF- and BF-STEM images, respectively, of the boundary area.

An attempt at increasing the A site radius variance further was made with the aim of synthesising a $La_{0.5}Ho_{0.5}CrO_3$ solid solution. However, a pure, crystalline sample was impossible to produce even when using higher synthesis temperatures than the $La_{0.5}Tb_{0.5}CrO_3$ material, shown in Figure 5.28. The difficulty of producing $La_{0.5}Tb_{0.5}CrO_3$ hydrothermally is highlighted in the section above, where the synthesis required increased temperature and duration relative to the end members; an observation also applicable to the solid state synthesis. The attempted synthesis of $La_{0.5}Ho_{0.5}CrO_3$ produced a perovskite phase with broad reflections, with small amounts of hydroxide impurity. The inclusion of holmium, smaller than terbium, into a solid solution with lanthanum was unsuccessful, likely due to the radius variance being too high. It is possible that the reaction resulted in a mixture of lower-variance solid solutions for example, $La_{0.25}Ho_{0.75}CrO_3$ and $La_{0.75}Ho_{0.25}CrO_3$, however, this information is lost to the broad peaks of the pattern. While holmium resides only a further two places along the period in the Periodic Table, the increase in radius variance is 40% over $La_{0.5}Tb_{0.5}CrO_3$. Certainly, it was found impossible to include rare-earths from opposite ends of the period, such as $La_{0.5}Yb_{0.5}CrO_3$, where a solid solution does not form, and instead, a powder mixture of the end members, $LaCrO_3$ and $YbCrO_3$, results, Figure 5.28.

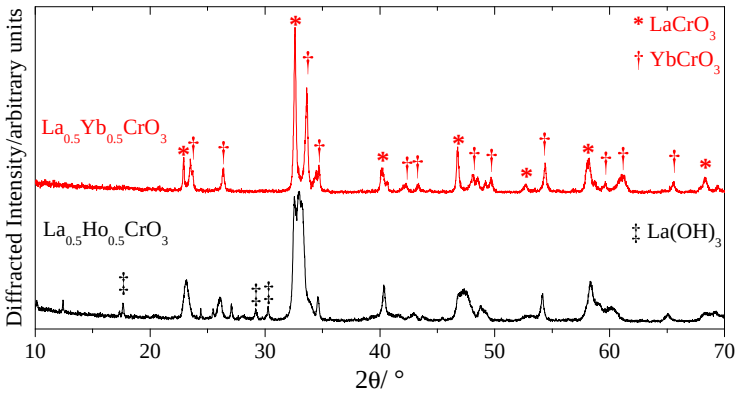

Figure 5.28: XRD patterns of phases produced from attempted hydrothermal syntheses of $La_{0.5}Yb_{0.5}CrO_3$ (top) and $La_{0.5}Ho_{0.5}CrO_3$ (bottom).

5.4 Discussion

Although there have been no previous reports involving the study of multiple rare-earth containing systems, EELS has been used previously to examine the order, and disorder, of various elements within many complex oxides. Examples of such include the study of boundaries between layered La-Sr manganite perovskites,[29,30] and distinct cation sites within the $Ba_{1.7}Ca_{2.4}Y_{0.9}Fe_5O_{13}$ material.[31] STEM and EELS were used in a complementary manner to inspect nano-chessboard arrangements of metals within Ca-stabilised $NdTiO_3$, showing almost layered-like structures as the Nd and Ca mostly occupied two different sites,[32] similar to the hydrothermal La-Tb materials of this study. These techniques were also used to atomically distinguish the fine structure of iron and cobalt species within Ca_2FeCoO_5 brownmillerite materials, which reside in octahedral and tetrahedral layers, respectively.[33]

Ordered cationic arrangements of A site metals are reported in several complex mixed-metal oxides. For example, cationic ordering exists in superconducting $Ba_2YCu_3O_{7-x}$, enhanced by the ordering of anion vacancies which reduces the coordination of some of the A site metals. This produces two different A site coordination geometries; 10 and 8, in this case, occupied by Ba^{2+} and Y^{3+} ions, respectively.[34] The presence of vacant A sites and the degree of their order promotes the mobility of Li^+ ions in ionic conducting rare-earth titanates ($R_{\frac{2}{3}-x}Li_{3x}TiO_3$).[35] An ordered structure was observed with rare-earth layers, separate to layers consisting of Li ions and vacancies. It was found that the ionic conductivity of the disordered structure, prepared from high-temperature quenching, was approximately an order of magnitude higher than that of the

ordered structure.[35,36] Cationic order plays a pivotal role in determining the electronic and magnetic properties of colossal magnetoresistive (CMR) materials, such as $La_{0.5}Ba_{0.5}MnO_3$, which can exist as either a cubic A site disordered polymorph or a tetragonal A site ordered polymorph, each with T_C of 270 and 335 K, respectively.[37]

The differences between the hydrothermal and solid state $La_{0.5}Tb_{0.5}CrO_3$ materials, observed through magnetic measurement, show the effect of homogeneous mixing on the magnetic properties. Not only does this result in different ordering transitions for the Cr^{3+} spins in each material, but also affects the mechanisms behind the Tb^{3+} ordering that occurs at very low temperatures. It was shown in Figure 5.13 that the ordering temperature of the Tb^{3+} moments decreases, not only with increasing Tb-content, but also from the hydrothermal, to the solid state material. This ordering occurs at $\sim$ 39 K in the layered hydrothermal material, $\sim$ 17 K in the annealed material, and $\sim$ 13 K in the solid state material, before decreasing further to 5 K in the end member $TbCrO_3$.

The increased ordering temperature of the hydrothermal material is likely due to the layered-like structure that was observed through EELS. These two-dimensional lanthanum-rich and terbium-rich layers along the [101] axis give rise to superexchange interactions between neighbouring Tb^{3+} spins within the layers, resulting in the higher ordering temperature, compared to a perfect rock salt-type ordering of the lanthanides. The exchange interactions between each terbium-rich layer are reduced by the intercalating layers of nonmagnetic lanthanum, and so overall, the observed magnetic response is smaller than when compared to a rock salt ordered material, as well as both the annealed and solid state materials. The observations of the solid state $La_{0.5}Tb_{0.5}CrO_3$ from EELS explain the reduced ordering temperature for the Tb^{3+} spins, where the magnetic behaviour from the large regions of phase-separated $TbCrO_3$ will dominate at low temperature over the smaller regions of mixed La-Tb structure.

The observed differences in magnetic behaviour between the hydrothermal, annealed, and solid state $La_{0.5}Tb_{0.5}CrO_3$ materials indicate that the structure changes upon annealing, and any ordered A site effects are diminished. There are some previous reports of the thermal randomisation of A site cationic order, which also suggest that the A site ordering is a metastable configuration. Nakajima *et al.* observed the high-temperature destabilisation of the ordering in $YBaMn_2O_6$.[38] The anti-site disordering between the Y^{3+} and Ba^{2+} ions occurs at around 1100 K, resulting in random A site distributions in $Y_{0.5}Ba_{0.5}MnO_3$. Direct hydrothermal

synthesis of mixed La-Ba perovskites produces the tetragonal layered structure $LaBaMn_2O_6$,[39] which is the metastable phase, since the ceramic synthesis results in the disordered cubic phase $La_{0.5}Ba_{0.5}MnO_3$. To produce the layered structure through solid state methods, it is necessary to first form the A site ordered oxygen-deficient $La_{0.5}Ba_{0.5}MnO_{2.5}$ material, before performing a controlled oxidation to $LaBaMn_2O_6$.[37] La^{3+} and Ba^{2+} are isoelectronic and there are similarities between the tetragonal and cubic unit cells, so distinguishing between the ordered and disordered structures of $LaBaMn_2O_6$ and $La_{0.5}Ba_{0.5}MnO_3$, respectively, required measurement of the magnetic properties. Such effects have also been observed in other mixed lanthanide-barium manganites,[40,41] where unique synthesis routes lead to the formation of both order and disordered A site distributions with dramatically different magnetic properties, relevant to the current study of $La_{0.5}Tb_{0.5}CrO_3$.[42]

The perovskite tolerance factor, used to gauge the level of structural distortion, as described in Chapter 1, can also be used to define the likelihood of the existence of a material. It is clear, however, from the current study of several mixed rare-earth chromite perovskites, that radius variance also needs to be considered. When the studied materials are plotted by their tolerance factor against variance in Figure 5.29, then a pattern begins to form with regards to the hydrothermal synthesis of these materials. The black data points in the figure correspond to rare-earth chromites that have been made hydrothermally, whilst those in red refer to unsuccessful syntheses through the hydrothermal method. All of the single rare-earth chromites $RCrO_3$, where $R = La^{3+}$ to Lu^{3+}, are shown and each has been made hydrothermally.[15,19] The solid solutions shown are from the present study, and the points for $InCrO_3$ and $ScCrO_3$ are also shown, as the high-temperature hydrothermal syntheses of these were attempted, but were unsuccessful. These two highly distorted materials have been previously made only through high-temperature, high-pressure solid state techniques.[43]

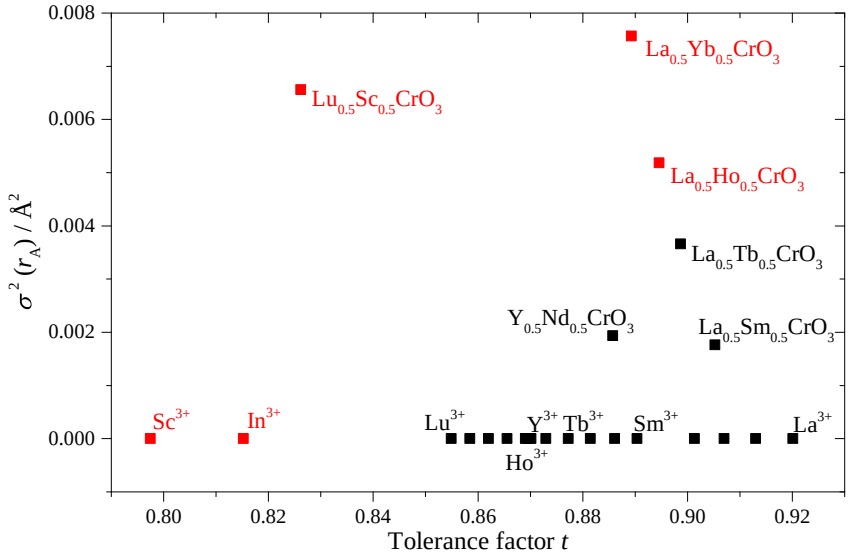

Figure 5.29: The materials studied in this work plotted as their variance as a function of their tolerance factor. Black symbols correspond to hydrothermally-synthesised materials, red symbols show unsuccessful syntheses.

Such a plot has been made previously when the hydrothermal syntheses of doped manganite perovskites were explored,[44] and are useful when considering the effects of tolerance factor and variance on the likelihood of successful synthesis. It is immediately clear that the region of materials that are in the lower-right corner of the plot, corresponding to t values close to 1 and low variance systems, are the easiest to produce hydrothermally at $\sim$ 370 °C. There appear to be limits to this region, however, where it is not possible to make chromite perovskites which have lower t, or higher σ.

The consideration of these limits is interesting because some of the low t, zero σ materials shown on the plot have been made through conventional solid state methods, such as $InCrO_3$ and $ScCrO_3$. It is therefore inferred that the lower limit of t, in this case is determined by the maximum achievable temperature of the high-temperature hydrothermal autoclaves used in the synthesis, which is approximately 600 °C as described in Chapter 2. This is not an unrealistic hypothesis, given that the theoretical formation energies of $RCrO_3$ become more exothermic as the ionic radius of the A site cation decreases.[45] In contrast, the limit to the highest achievable variance is a structure-limited parameter, which the synthesis temperature holds little-to-no influence over. It is observed that for two A site cations that are sufficiently different in size, instead of a solid solution, a mixture of the end member oxides will be produced.

5.5 Conclusions

The high temperature hydrothermal syntheses of two new mixed rare-earth orthochromite solid solutions, $Y_xHo_{1-x}CrO_3$ and $La_xTb_{1-x}CrO_3$, have been discussed in detail. It was concluded that the synthesis of the Y-Ho mixture was *easier*, compared to the synthesis of the La-Tb material, which required higher temperature and longer duration. This was despite the Y-Ho mixture having a much more distorted structure with lower tolerance factor. This suggests that the synthesis is also affected by the A site variance of the structure, generated by the different ionic radii of La^{3+} and Tb^{3+}.

Analysis of these distorted structures using XRD and Raman scattering indicate that their average structures are orthorhombically distorted and are described by the symmetry of *Pnma*, much like the $La_xSm_{1-x}CrO_3$ solid solutions covered in Chapter 4. The almost identical ionic radii of Y^{3+} and Ho^{3+} lead to a solid solution that is almost isostructural with each end member, whilst the structure of $La_xTb_{1-x}CrO_3$ depends greatly upon x, becoming more distorted towards $TbCrO_3$. The radius variance present on the A site of this material was suggested by the observation of increased Raman band line-widths.

Close inspection of the distributions of rare-earth cations within each material through EELS revealed inhomogeneous mixing of the two A site metals, and that the degree of inhomogeneity was influenced by the A site radius variance. Increased separation was observed in the La-Tb solid solution, where an almost layered structure was adopted in many regions of the sample. Although there would be strain between each layer, this effect may well reduce the strain within the structure when compared to a rock salt configuration, where the nearest neighbour rare-earths are different.

Solid solutions of the same compositions were prepared through solid state high-temperature synthesis, and were compared through EELS with the materials produced hydrothermally. Almost identical observations were made for the two $La_{0.5}Sm_{0.5}CrO_3$ solid solutions, whilst significant differences were observed between the two $La_{0.5}Tb_{0.5}CrO_3$ materials. The hydrothermally-prepared La-Tb material contained a homogeneous mixture of both rare-earths, where were incorporated into the structure, but showed almost layered-like ordering due to variance effects. In contrast, much larger regions of phase-separated structures were observed from the sample prepared through solid state synthesis. The lanthanum and terbium did not mix homogeneously during the solid state firing, despite the precursor for both hydrothermal and solid state materials being the

same mixed-metal amorphous gel. This inhomogeneous mixing of the two rare-earths was also evident in the measured magnetic data, which showed ordering transitions for both the end member materials and also the $La_{0.5}Tb_{0.5}CrO_3$ solid solution.

It was also observed that annealing the layered hydrothermal material to high temperatures influenced the magnetic properties. Unfortunately, it was not possible to study the effects of annealing through EELS, due to the crystallites agglomerating together, forming large clusters during the firing process. The amalgamation of many crystallites together meant that it was not possible to achieve atomic resolution images along suitable orientations. However, it was possible to study the effects of this annealing through magnetic measurement. The high-temperature firing resulted in the magnetic properties of the hydrothermal sample changing, such that they became more like that of the phase-separated solid state material.

Finally, the relationships between synthesis condition, tolerance factor and variance were explored. It was found that more distorted structures with lower tolerance factors require higher synthesis temperatures to form under hydrothermal conditions. Although slightly higher synthesis temperatures lead to the formation of the layered $La_{0.5}Tb_{0.5}CrO_3$ solid solution, it was determined that variance is predominantly a structure-limited parameter, where attempts to make $La_{0.5}Ho_{0.5}CrO_3$ and $La_{0.5}Yb_{0.5}CrO_3$ solid solutions resulted in poor samples or mixtures of end member oxides, respectively.

References

[1] J. P. Attfield, *Chem. Mater.*, 1998, **10**, 3239.

[2] G. King and P. M. Woodward, *J. Mater. Chem.*, 2010, **20**, 5785.

[3] L. M. Rodriguez-Martinez and J. P. Attfield, *Phys. Rev. B*, 1996, **54**, R15622.

[4] M. Karppinen, H. Okamoto, H. Fjellvåag, T. Motohashi and H. Yamauchi, *J. Solid State Chem.*, 2004, **177**, 2122.

[5] P. K. Davies, *Curr. Opin. Solid State Mater. Sci.*, 1999, **4**, 467.

[6] J. W. Fergus, *Solid State Ionics*, 2004, **171**, 1.

[7] R. D. Shannon, *Acta Cryst. A*, 1976, **32**, 751.

[8] R. Shukla, J. Manjanna, A. K. Bera, S. M. Yusuf and A. K. Tyagi, *Inorg. Chem.*, 2009, **48**, 11691.

[9] K. Yoshii, A. Nakamura, Y. Ishii and Y. Morii, *J. Solid State Chem.*, 2001, **162**, 84.

[10] H. Taguchi and M. Nagao, *J. Solid State Chem.*, 1995, **114**, 236.

[11] Y. Du, Z. X. Cheng, X.-L. Wang and S. X. Dou, *J. Appl. Phys.*, 2010, **108**, 093914.

[12] K. R. Chakraborty, A. Das, S. M. Yusuf, P. S. R. Krishna and A. K. Tyagi, *J. Magn. Magn. Mater.*, 2006, **301**, 74.

[13] N. Sharma, B. K. Srivastava, A. Krishnamurthy and A. K. Nigam, *J. Alloys Compd.*, 2012, **545**, 50.

[14] N. Sharma, B. K. Srivastava, A. Krishnamurthy and A. K. Nigam, *Solid State Sci.*, 2010, **12**, 1464.

[15] J. Prado-Gonjal, R. Schmidt, J.-J. Romero, D. Ávila, U. Amador and E. Morán, *Inorg. Chem.*, 2013, **52**, 313.

[16] M. C. Weber, J. Kreisel, P. A. Thomas, M. Newton, K. Sardar and R. I. Walton, *Phys. Rev. B*, 2012, **85**, 054303.

[17] J. D. Gordon, R. M. Hornreich, S. Shtrikman and B. M. Wanklyn, *Phys. Rev. B*, 1976, **13**, 3012.

[18] J.-S. Zhou, J. A. Alonso, V. Pomjakushin, J. B. Goodenough, Y. Ren, J.-Q. Yan and J.-G. Cheng, *Phys. Rev. B*, 2010, **81**, 214115.

[19] K. Sardar, M. R. Lees, R. J. Kashtiban, J. Sloan and R. I. Walton, *Chem. Mater.*, 2011, **23**, 48.

[20] I. Weinberg and P. Larsen, *Nature*, 1961, **192**, 445.

[21] E. F. Bertaut, G. Bassi, G. Buisson, P. Burlet, J. Chappert, A. Delapalme, J. Mareschal, G. Roult, R. Aleonard, R. Pauthenet and J. P. Rebouillat, *J. Appl. Phys.*, 1966, **37**, 1038.

[22] C. Kittel, *Introduction to Solid State Physics*, John Wiley & Sons Ltd, Hoboken, NJ, 8th Ed., 2005.

[23] Y. L. Su, J. C. Zhang, L. Li, J. Feng, B. Z. Li, Y. Zhou and S. X. Cao, *Ferroelectrics*, 2011, **410**, 102.

[24] B. Tiwari, M. K. Surendra and M. S. R. Rao, *J. Phys.: Condens. Matter*, 2013, **25**, 216004.

[25] K. Tsushima, K. Aoyagi and S. Sugano, *J. Appl. Phys.*, 1970, **41**, 1238.

[26] R. J. Nicholls, A. T. Murdock, J. Tsang, J. Britton, T. J. Pennycook, A. Koós, P. D. Nellist, N. Grobert and J. R. Yates, *ACS Nano*, 2013, **7**, 7145.

[27] X. Sang, E. D. Grimley, C. Niu, D. L. Irving and J. M. LeBeau, *Appl. Phys. Lett.*, 2015, **1016**, 061913.

[28] T. Lunkenbein, F. Girgsdies, A. Wernbacher, J. Noack, G. Auffermann, A. Yasuhara, A. Klein-Hoffman, W. Ueda, M. Eichelbaum, A. Trunschke, R. Schlögl and M. G. Willinger, *Angew. Chem. Int. Ed.*, 2015, **54**, 1.

[29] K. Kimoto, T. Asaka, T. Nagai, M. Saito, Y. Matsui and K. Ishizuka, *Nature*, 2007, **450**, 702.

[30] J. Verbeeck, O. I. Lebedev, G. V. Tendeloo, J. Silcox, B. Mercey, M. Haervieu and A. M. Haghiri-Gosnet, *Appl. Phys. Lett.*, 2001, **79**, 2037.
[31] R. Sayers, N. L. O. Flack, J. Alaria, P. A. Chater, R. G. Palgrave, S. R. C. McMitchell, S. Romani, Q. M. Ramasse, T. J. Pennycook and M. J. Rosseinsky, *Chem. Sci.*, 2013, **4**, 2403.
[32] F. Azough, D. Kepaptsoglou, Q. M. Ramasse, B. Schaffer and R. Freer, *Chem. Mater.*, 2015, **27**, 497.
[33] S. Turner, J. Verbeeck, F. Ramezanipour, J. E. Greedan, G. V. Tendeloo and G. A. Botton, *Chem. Mater.*, 2012, **24**, 1904.
[34] P. K. Davies, H. Wu, A. Y. Borisevich, I. E. Molodetsky and L. Farber, *Annu. Rev. Mater. Res.*, 2008, **38**, 369.
[35] C. J. Howard and Z. Zhang, *Acta Cryst. B*, 2004, **60**, 249.
[36] Y. Harada, T. Ishigaki, H. Kawai and J. Kuwano, *Solid State Ionics*, 1998, **108**, 407.
[37] F. Millange, V. Caignaert, B. Domengès and B. Raveau, *Chem. Mater.*, 1998, **10**, 1974.
[38] T. Nakajima, H. Kageyama, M. Ichihara, K. Ohoyama, H. Yoshizawa and Y. Ueda, *J. Solid State Chem.*, 2004, **177**, 987.
[39] J. Spooren, R. I. Walton and F. Millange, *J. Mater. Chem.*, 2005, **15**, 1542.
[40] S. V. Trukhanov, V. V. Fedotova, A. V. Trukhanov, H. Szymczak and C. E. Botez, *Tech. Phys.*, 2008, **53**, 49.
[41] S. V. Trukhanov, L. S. Lobanovski, M. V. Bushinsky, V. V. Fedotova, I. O. Troyanchuk, A. V. Trukhanov, V. A. Ryzhov, H. Szymczak, R. Szymczak and M. Baran, *J. Phys.: Condens. Matter*, 2005, **17**, 6495.
[42] S. V. Trukhanov, V. A. Khomchenko, L. S. Lobanovski, M. V. Bushinsky, D. V. Karpinksy, V. V. Fedotova, I. O. Troyanchuk, A. V. Trukhanov, S. G. Stepin, R. Szymczak, C. E. Botez and A. Adair, *J. Exp. Theor. Phys.*, 2006, **103**, 398.
[43] A. A. Belik, Y. Matsushita, M. Tanaka and E. Takayama-Muromachi, *Chem. Mater.*, 2012, **24**, 2197.
[44] J. Spooren and R. I. Walton, *J. Solid State Chem.*, 2005, **178**, 1683.
[45] Z. Zeng, F. Calle-Vallejo, M. B. Mogensen and J. Rossmeisl, *Phys. Chem. Chem. Phys.*, 2013, **15**, 7526.

Chapter 6

Conclusions & Future Work

The three results chapters above have dealt with the synthesis of new complex mixed-metal oxides, and the studies of their structures and properties. The work provides a good illustration of how hydrothermal synthesis allows the production of materials that are not accessible through conventional solid state synthesis, such as metastable pyrochlore and layered rare-earth chromium perovskite phases. Several of the synthesised materials contain disorder over various length scales, and it has been the study of this using techniques such as total scattering and EELS, and the subtle effects that this has on the properties, that provides the overarching theme of the reported work.

6.1 New Metastable Bi-Fe-Mn Pyrochlores

The syntheses of two new pyrochlore materials were discovered, and involved combining both iron and manganese within the pyrochlore structure alongside bismuth. It was found that the alkali metals, originating from the mineraliser used in each reaction, were necessary for the formation of these pyrochlore phases; the alkali metals are incorporated into the structure, and it is not possible to produce these materials from reactions in water alone or other alkali media.

Non-ambient diffraction measurements performed above room temperature illustrated an important advantage of hydrothermal chemistry; the production of metastable phases.[1] These pyrochlores break down at approximately 400 °C, showing that it would not be possible to synthesise these phases through traditional high-temperature solid state methods.

The average structures of these materials, determined through diffraction, were shown to adopt the cubic space group $Fd\overline{3}m$, whilst refinement of structural

models against the data indicated that a portion of A site bismuth was substituted by alkali metals, and the remaining bismuth was present on the B site of the structure. This site mixing of bismuth was shown by XANES to involve Bi^{3+} on the A site, and Bi^{5+} on the smaller, symmetrical octahedral B site. Refinement of these models against both X-ray and neutron data suggest the presence of the inherent disorder in these materials, with static displacements of both the A site and O′ site atoms away from their ideal positions, towards their nearest neighbours.

This work involving the synthesis, analysis of average structures, XANES, thermal behaviour, and magnetic properties of the pyrochlores has been published.[2]

The disorder in the pyrochlores was further studied by utilising the method of total neutron scattering, which revealed that on the very local scale (within the unit cell), the deviation of the atoms away from their ideal sites was sufficient enough that it was not accounted for by the average structural models. It was not possible to fit the short range disorder whilst the model was constrained by the symmetry operators of the space group. This level of local disorder was not unexpected, given the presence of the stereochemically active Bi^{3+} cation on the A site, and also the incorporation of three different metals on the B site of the structure.

The use of RMC modelling to study this disorder resulted in excellent fits to the short-range structure of both pyrochlores, whilst simultaneously agreeing with the long-range average structure. The probability densities of the A and O′ sites almost mirror those of the Rietveld model, showing that an accurate model of the disorder requires only a slight deviation away from the average structure, resulting in more realistic bond valence sums for each cation.

Further study of the configurations resulting from each pyrochlore will be performed through analysis of bond length and bond angle distributions. This will allow for the coordination environments of the different B site metals to be compared, which are assumed to be perfectly octahedral, however, this information was not obtained through the analysis of Bragg data alone. Further modelling could be performed using atom-swap algorithms that would reveal any preferential clustering of metal cations or vacancies.

The inclusion of X-ray total scattering data within this RMC study would provide further information on the local coordination of bismuth cations, and could be used to determine if any correlated displacements exist where the cations prefer to be displaced in certain directions over others. Correlated displacements were observed from such analysis of lead-free piezoelectric $Na_{0.5}Bi_{0.5}TiO_3$,[3] and it was

possible to observe the different local coordination preferences of sodium and bismuth, highly relevant to the current study.

The possibility of iron migration from the B site onto the A site of the pyrochlores was discussed in Chapter 3, following the observations of increased edge energies from XANES and broad doublet components present in Mössbauer data. Whilst these are both likely due to the inherent disorder in these systems, it was not possible to dismiss the potential for A site iron. Further work could involve EXAFS analysis of data not only from the Fe K-edge, but also the Mn K-edge. Comparison of the local coordination environments of iron and manganese would prove useful as they should be very similar if both metals are on the B site. If the data were different, then this would indicate that further modelling is required to confirm the mixing of iron across both the A and B sites.

Whilst the EXAFS analysis could be performed separately, it is now possible to include EXAFS data within RMC simulations.[4] The inclusion of this alongside total scattering and Bragg data, would allow for the possibility of A site iron to be tested completely.

Further exploration of the synthesis could be made, as preliminary results suggest that a different pyrochlore phase is produced when the manganese reagent is omitted from the synthesis. Contrarily, exploratory reactions indicate that a fluorite-type phase is produced from reactions where the iron reagent is omitted. It is possible that this is the δ-phase of Bi_2O_3, stabilised by the addition of manganese.

6.2 New $La_xSm_{1-x}CrO_3$ Perovskite Solid Solutions

The formation of orthochromite perovskites, with mixed La^{3+} and Sm^{3+} on the A site, was performed using high-temperature hydrothermal synthesis, providing a single-step route to these materials. These compositions were previously unreported, and hydrothermal treatment for just 6 hours at 370 °C leads to more crystalline and homogeneous products compared to those produced through solid state synthesis at 1200 °C for 12 hours. The immense variation in particle size and morphology of crystallites from the solid state sample are shown in Figure 6.1, compared against the much more homogeneous particles prepared hydrothermally.

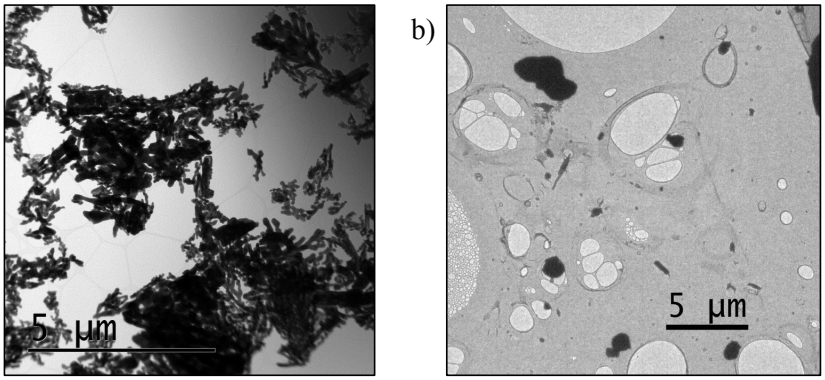

Figure 6.1: TEM images of a) dendritic crystallites from hydrothermal $La_{0.5}Sm_{0.5}CrO_3$ and b) those from solid state sample, which wildly vary in size and shape.

The orthorhombic distortion of each solid solution (x = 1.0, 0.875, 0.75, 0.625, 0.5, 0.25, 0.0) was studied in detail through analysis of high-resolution X-ray diffraction and Raman scattering data. Solution of the structures allowed for the calculation of accurate octahedral tilt angles that were directly compared against octahedral soft Raman modes. The use of shell model calculations, based upon the structures obtained from Rietveld analysis, proved effective in the assignment of phonon modes in the low wavenumber region (< 250 cm^{-1}), revealing complex mode-mixing between bands of the same symmetry. The existence of this behaviour was suggested by a previous study that included single rare-earth chromites RCrO$_3$.[5] Through the production of several $La_xSm_{1-x}CrO_3$ solid solutions, it was possible to closely follow and analyse the complex mode interactions.

The subtle structural distortions that accompany slight changes in x were shown to have a significant effect on the magnetic properties of the material; the ordering Néel temperature exhibits a shift of almost 100 °C from one end member to the other, whilst anisotropic exchange interactions result in coupling effects between the B site Cr^{3+} and A site Sm^{3+}, leading to greatly varied low-temperature behaviour across the series.

These results on the synthesis, and the study of structural effects on the magnetic properties have been published.[6]

The investigation into possible magnetoelectric effects in $La_{0.25}Sm_{0.75}CrO_3$ follows the observation of such behaviour observed in end member SmCrO$_3$.[7,8] The observations of a switchable polarisation and spin-phonon couplings suggest that these materials would be classified as type II multiferroics, where magnetic

interactions drive the observed spontaneous ferroelectric properties. However, further work is needed to complete the study of potential magnetoelectric effects within these materials, and to understand truly the mechanisms that lead to these interactions. This could include the measurement of Raman scattering data across the low-temperature spin reorientation transition T_{SR} at approximately 40 K, in order to study the effect that this has on the structure.

Future work could involve this one-step synthesis method being applied to other B site metals, including Co^{3+}, Ni^{3+}, Ga^{3+}, In^{3+}, and Fe^{3+}. Although the orthorhombic structures and magnetic properties of rare-earth ferrites have been extensively studied, there have been no previous reports of a hydrothermal synthesis route to RFeO$_3$. It is likely that the preferential formation of $R(OH)_3$ under basic hydrothermal conditions hinders the production of the ferrites, however, the direct synthesis route reported in this thesis could be explored. The study of a mixed B site solid solution, RFe$_{1-x}$Cr$_x$O$_3$, may also be a feasible approach.

6.3 Radius Variance Effects in Mixed Rare-Earth Orthochromites

Two new mixed rare-earth chromite solid solutions, $Y_xHo_{1-x}CrO_3$ and $La_xTb_{1-x}CrO_3$, were synthesised from high-temperature hydrothermal methods and included in a study of A site cation size variance, alongside the $La_xSm_{1-x}CrO_3$ materials mentioned above. Analyses using XRD and Raman scattering were performed to study their orthorhombic distorted structures, and the results were correlated to the observed magnetic properties of each material.

Close inspections of HAADF-STEM images from $La_{0.5}Sm_{0.5}CrO_3$ crystallites showed intensity variations between neighbouring A site atomic columns, suggesting inhomogeneous distributions of the two rare-earth cations. Atomically-resolved EELS was used to investigate the degree of rare-earth mixing within the perovskite solid solutions, and revealed different levels of inhomogeneity in each, with greater separation observed in the largest variance system of $La_{0.5}Tb_{0.5}CrO_3$. The increased variance, due to the difference between their ionic radii, resulted in the formation of an almost layered-like distribution of lanthanum and terbium, an effect that was observed from several separate crystallites of the material. The preference for the formation of this layered-like phase could result from strain reduction between the different octahedral tilts surrounding lanthanum-rich and terbium-rich layers. This showed that the rare-earth mixing is not simply random, but is influenced by ionic radii variance effects, resulting from

the size disparity of the two lanthanides present. To the best of the author's knowledge, local A site layering effects of this kind have previously only been observed in $NaLaBB'O_6$ (where B = Mn or Fe, and B′ = Nb or Ta) double perovskite materials through HAADF-STEM and X-ray PDF analysis.[9] Whilst these observations support the current study of radius variance within $La_{0.5}Tb_{0.5}CrO_3$, it is noted that charge ordering effects would also exist between La^{3+} and Na^{+}. The much larger scattering contrast between sodium and lanthanum allowed for these effects to be observed directly through imaging alone, whilst the comparative scattering contrast between lanthanum and terbium is much more subtle, prompting the requirement for EELS in the current study.

The structural distortion within these perovskites is generated by the size mismatch of the A site rare-earth and B site chromium ions. The inhomogeneous distributions of the lanthanides would lead to local deviations of the distortions and octahedral tilts such that the short-range structure of these materials would not be accurately described by a regular orthorhombic tilt system.

All three materials displayed magnetic behaviour that agreed well with the properties of the other solid solutions and end members of their respective series. The measurements confirmed the materials were genuine solid solutions, and revealed an increased ordering temperature for the Tb^{3+}–Tb^{3+} interactions in $La_{0.5}Tb_{0.5}CrO_3$ compared to end member $TbCrO_3$, likely due to the layered distributions of the lanthanides.

The effect of synthesis on the degree of rare-earth mixing was explored by preparing the same materials through solid state methods, which were then compared against those produced hydrothermally. Similar results were obtained through all analysis methods for the two $La_{0.5}Sm_{0.5}CrO_3$ samples, including XRD, Raman spectroscopy, EELS and magnetometry. However, such agreement was not seen between the two $La_{0.5}Tb_{0.5}CrO_3$ materials as the layered, but well-mixed distributions of the hydrothermal sample were not observed in the solid state material. Instead, a solid solution was not formed, and the material consisted of crystallites with large domains of phase-separated $LaCrO_3$ and $TbCrO_3$, observed through EELS. These large La-rich and Tb-rich regions show that the conventional solid state technique does not provide the same level of homogeneity as the hydrothermal method, despite the precursor being the same mixed-metal amorphous hydroxide gel that was used for both techniques.

The phase separation of the $La_{0.5}Tb_{0.5}CrO_3$ solid state material was evident in the magnetic data, with separate transitions corresponding to the solid solution and

end members, as well as greatly varied low-temperature behaviour, being observed. It was shown through the measurement of magnetic data that annealing the hydrothermal material to high temperatures resulted in what appears to be an irreversible decomposition of the layered-like structure, due to the magnetic behaviour being more consistent with that of the solid state material post-annealing.

It is possible that the repeated process of firing and grinding (total time at 1400 °C of 48 hours) for the solid state material was not sufficiently long enough to produce a genuine mixed solid solution. The rare-earth mixing may improve upon further annealing, however, both the observed separation of the solid state material, and the effect of annealing the hydrothermal sample indicate that it may not be possible to produce a solid solution of this material through traditional ceramic methods. This highlights an important benefit of the hydrothermal method that was also observed with doped rare-earth manganites;[10] the ability to produce unique and metastable phases, allowing for subtle ways of controlling the properties of materials.

The work involving several mixed rare-earth chromium perovskites made it possible to study the effects of radius variance as well as tolerance factor on the synthesis of these systems, resulting in a *synthesis map* of tolerance factor plotted against variance. This refers to the difficulty encountered in synthesising distorted materials, with low tolerance factors and high variance, whilst high tolerance factor (least distorted) and low-variance materials were the easiest to produce. Data from the hydrothermal investigation of doped manganite perovskites,[10] are combined with those from the current chromite study in Figure 6.2, providing further insight into the synthesis-structure relationships of distorted perovskites.

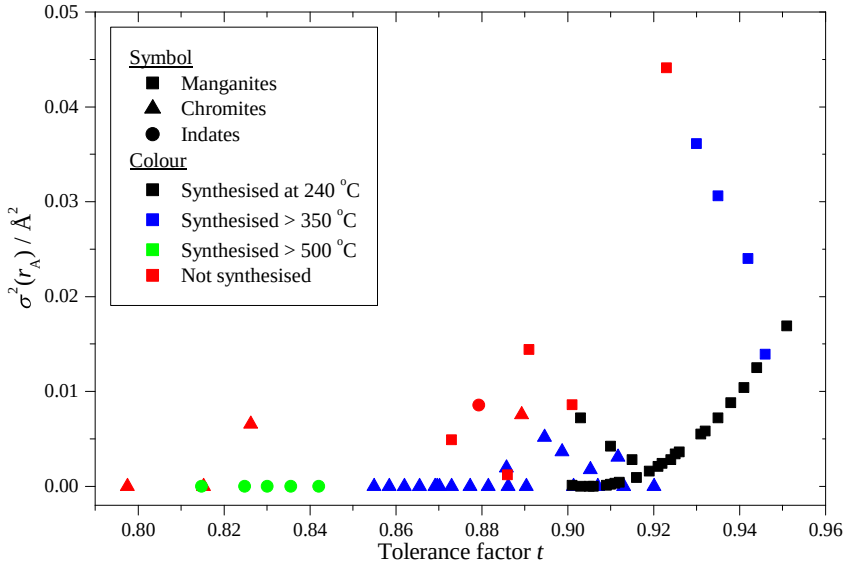

Figure 6.2: Plot of tolerance factor against A site radius variance for mixed rare-earth manganites, chromites, and indates, that have been hydrothermally synthesised. Different symbol-types refer to different B site metals, whilst symbol-colour refers to their synthesis conditions, as shown by the legend. Red shows materials that have not yet been made via hydrothermal methods.

The plot is supported by the measured enthalpies of formation which show linear dependencies on t for doped chromites and manganites, and structures with tolerance factors closer to unity give the most exothermic values.[11,12] This shows that the energetics of formation for the studied perovskites are affected by structural distortion and composition, providing support that the figure can act as a *synthesis map*. The previous investigation into doped manganites, from which the data were taken,[10] performed hydrothermal syntheses at temperatures lower than 270 °C; it may be possible to produce some of the manganites which were labelled as unsuccessful in the plot, using higher temperatures.

It would be interesting to investigate whether variance limits, discussed in Chapter 5, show a dependence on the tolerance factor of the system. For example, would the variance limit differ for a heavily-distorted perovskite with $t = 0.8$, compared to one with $t = 0.95$? The limited evidence available from Figure 6.2 suggests that the maximum variance possible for a structure might decrease with tolerance factor, however, much more data are required to be able to conclude this with absolute certainty. It would be possible to do this by the careful selection of certain A and B site metals in order to achieve desired values of tolerance factor and variance.

Preliminary analysis performed by the author indicates that it is possible to produce several rare-earth indate perovskites $R\mathrm{InO_3}$ through hydrothermal synthesis at 500 °C. These materials could be used to explore a range of the plot (i.e. with $0.8 < t < 0.85$), shown by green points in Figure 6.2, that is inaccessible through the present study of rare-earth chromites. This study may provide extra or new knowledge about the effects of variance on the properties exhibited by mixed-metal systems.

Further information regarding the magnetic behaviour exhibited by these materials could be obtained through specific heat measurement, or even low-temperature neutron scattering. Difficulties could arise from performing neutron diffraction measurements on mixed rare-earth chromites due to the high neutron absorption cross sections of the lanthanides. This, however, could be exploited through anomalous dispersion neutron scattering, which utilises the imaginary parts of scattering lengths in order to isolate exclusively the R–R correlations, as reported for samarium phosphate glasses.[13] Alternatively, magnetic difference neutron diffraction methods provided detailed insight into the different Tb–Tb correlations within terbium phosphate glass.[14] Such techniques would provide PDFs with which to study the local disorder in A site radius variance-affected chromite perovskites.

References

[1] K. Byrappa and M. Yoshimura, *Handbook of Hydrothermal Technology*, Noyes Publications: Park Ridge, New Jersey, USA, 2001.

[2] L. M. Daniels, H. Y. Playford, J.-M. Grenèche, A. C. Hannon and R. I. Walton, *Inorg. Chem.*, 2014, **53**, 13197.

[3] D. S. Keeble, E. R. Barney, D. A. Keen, M. G. Tucker, J. Kreisel and P. A. Thomas, *Adv. Funct. Mater.*, 2013, **23**, 185.

[4] H. Y. Playford, L. R. Owen, I. Levin and M. G. Tucker, *Annu. Rev. Mater. Res.*, 2014, **44**, 429.

[5] M. C. Weber, J. Kreisel, P. A. Thomas, M. Newton, K. Sardar and R. I. Walton, *Phys. Rev. B*, 2012, **85**, 054303.

[6] L. M. Daniels, M. C. Weber, M. R. Lees, M. Guennou, R. J. Kashtiban, J. Sloan, J. Kreisel and R. I. Walton, *Inorg. Chem.*, 2013, **52**, 12161.

[7] B. Rajeswaran, D. I. Khomskii, A. K. Zvezdin, C. N. R. Rao and A. Sudaresan, *Phys. Rev. B*, 2012, **86**, 214409.

[8] V. S. Bhadram, B. Rajeswaran, A. Sundaresan and C. Narayana, *EPL*, 2013, **101**, 17008.

[9] W. Dachraouti, T. Yang, L. Chang, G. King, J. Hadermann, G. Van Tendeloo, A. Llobet and M. Greenblatt, *Chem. Mater.*, 2011, **23**, 2398.

[10] J. Spooren and R. I. Walton, *J. Solid State Chem.*, 2005, **178**, 1683.

[11] J. Cheng and A. Navrotsky, *J. Solid State Chem.*, 2005, **178**, 234.

[12] C. Laberty, A. Navrotsky, C. N. R. Rao and P. Alphonse, *J. Solid State Chem.*, 1999, **145**, 77.

[13] J. M. Cole, A. C. Wright, R. J. Newport, R. N. Sinclair, H. E. Fischer, G. J. Cuello and R. A. Martin, *J. Phys.: Condens. Matter*, 2007, **19**, 056002.

[14] J. M. Cole, A. C. Hannon, R. A. Martin and R. J. Newport, *Phys. Rev. B*, 2006, **73**, 104210.

Appendix A

STEM images & EELS maps of mixed rare-earth orthochromites

Shown below are EELS maps recorded from the various mixed rare-earth orthochromite materials that are discussed in Chapter 5. The elemental maps were recorded from several separate crystallites throughout each sample, to ensure that the observations correspond to the bulk sample.

Hydrothermal $La_{0.5}Sm_{0.5}CrO_3$ HAADF-STEM & EELS

The majority of the EELS maps were recorded from crystallites aligned along the [101] direction, as this projection provided the largest spacing between rare-earth and chromium atomic columns.

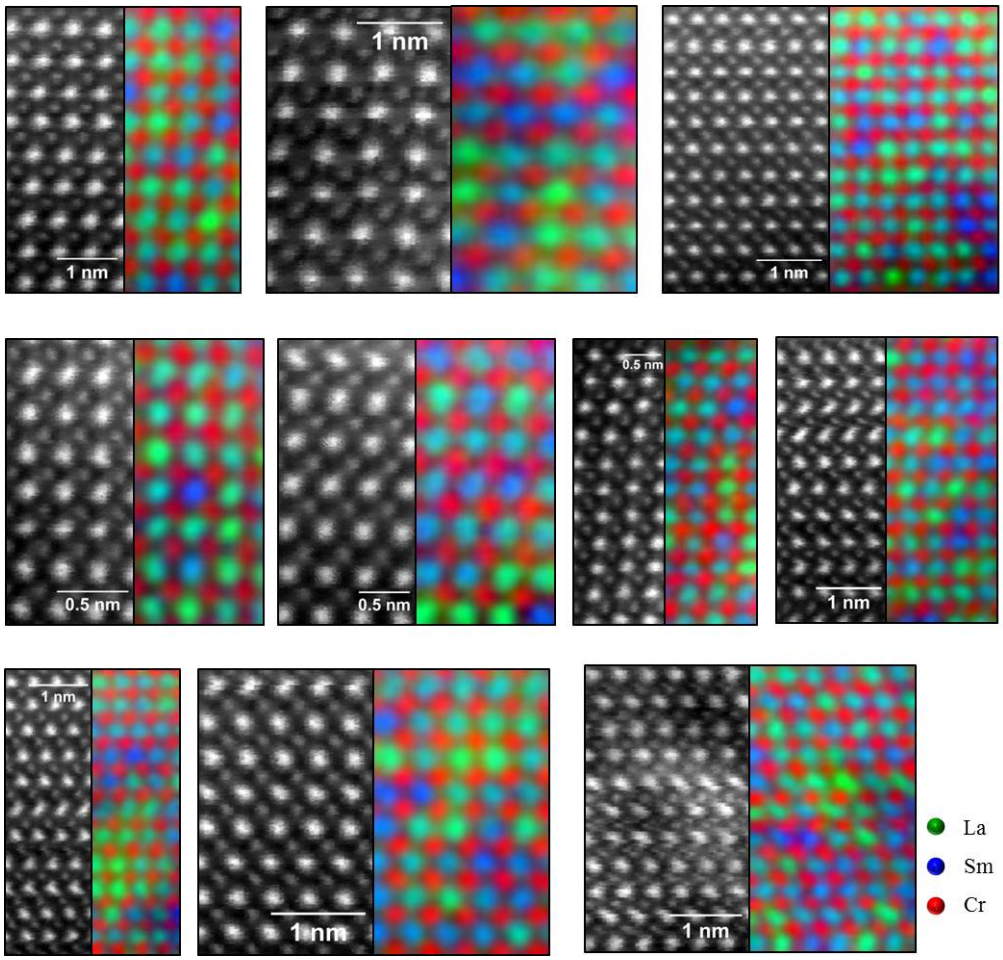

Several EELS maps were recorded from crystallites aligned along the [301] direction of the hydrothermally-prepared $La_{0.5}Sm_{0.5}CrO_3$ material.

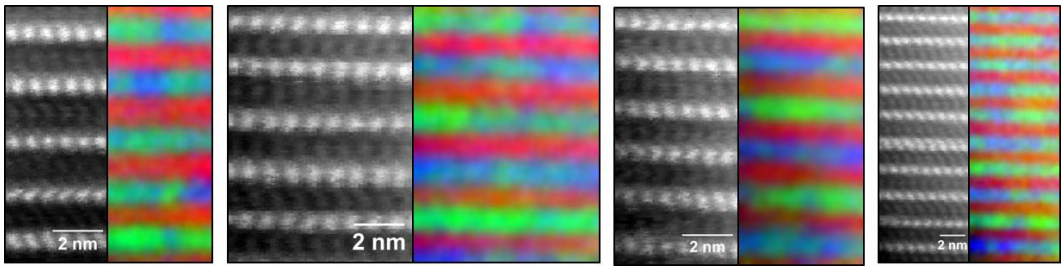

Solid state $La_{0.5}Sm_{0.5}CrO_3$ HAADF-STEM & EELS

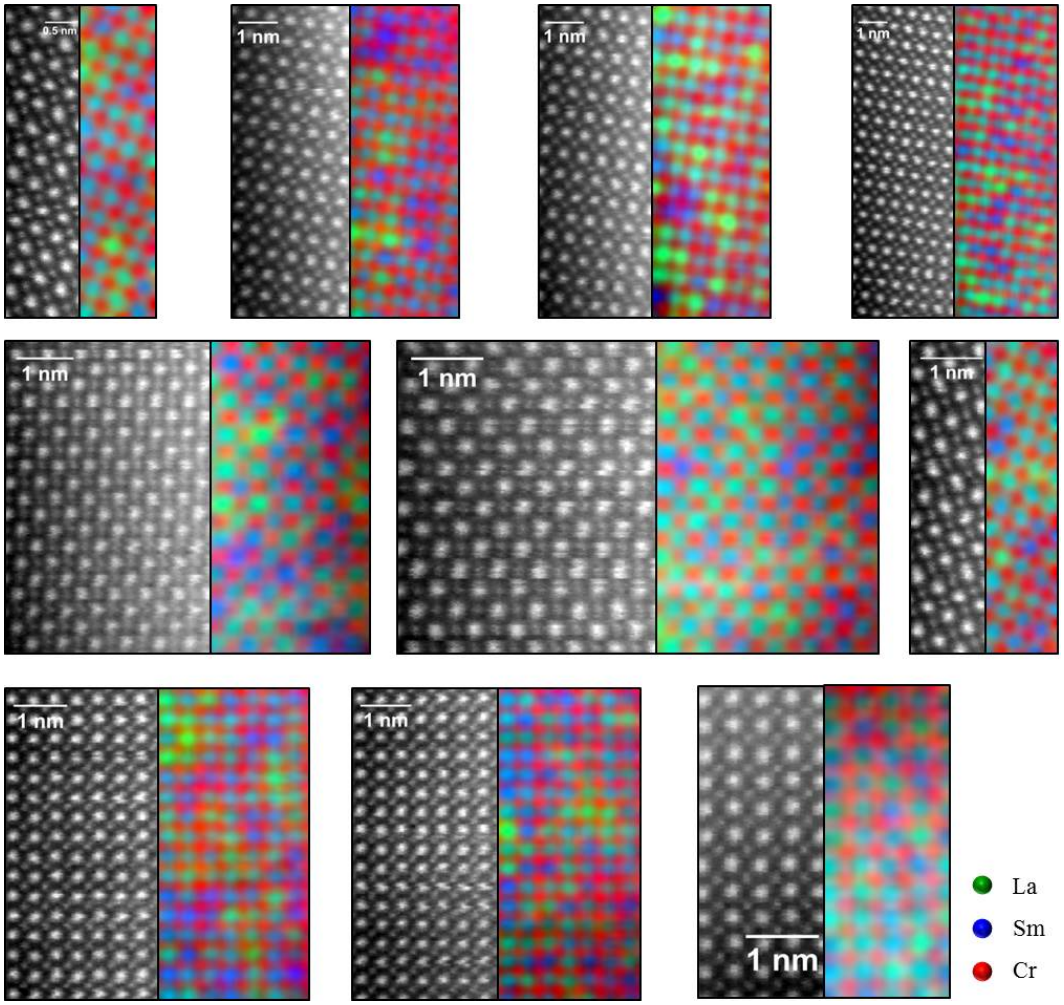

Hydrothermal $La_{0.5}Tb_{0.5}CrO_3$ HAADF-STEM & EELS

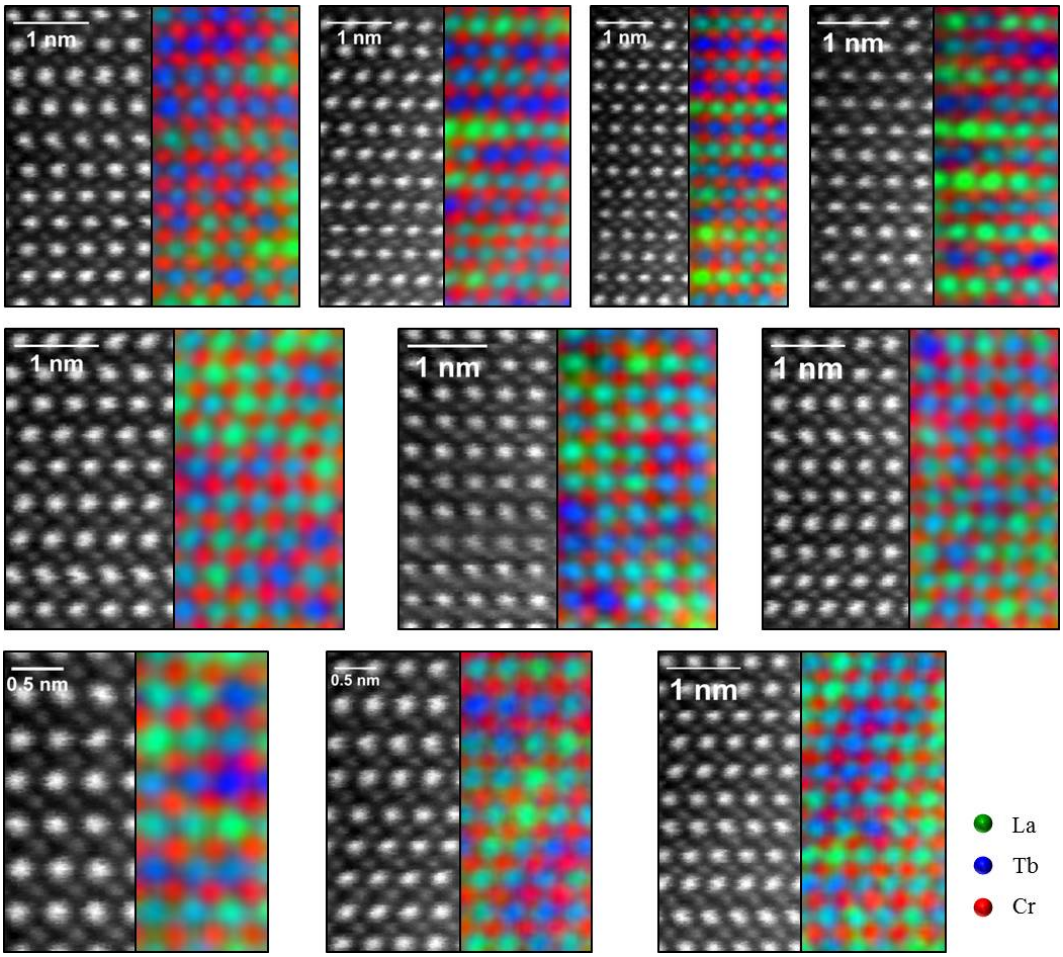

Solid state $La_{0.5}Tb_{0.5}CrO_3$ HAADF-STEM & EELS

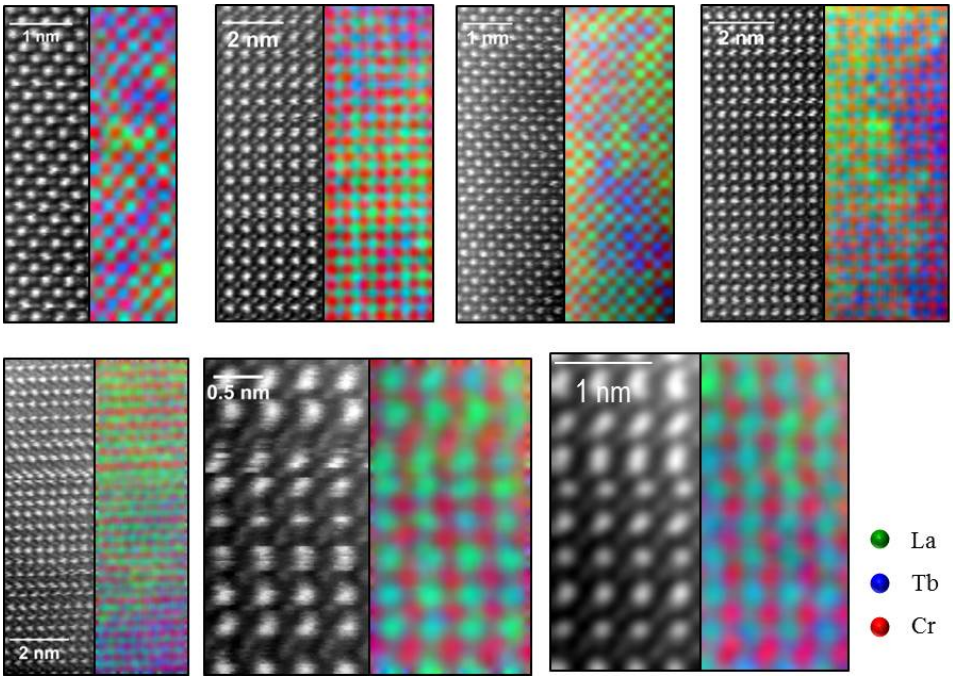

Boundaries between large regions of La-rich and Tb-rich structure were observed and mapped using EELS.

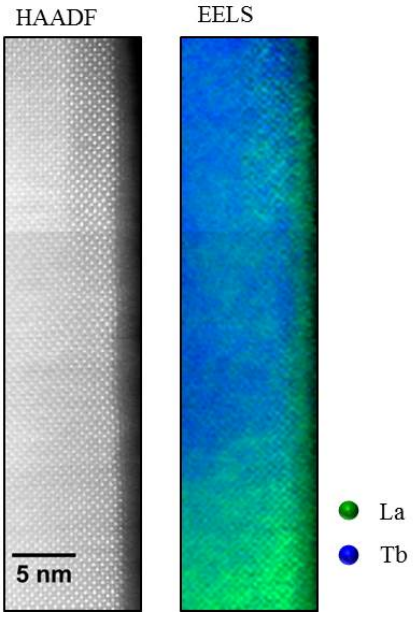

Hydrothermal $Y_{0.5}Ho_{0.5}CrO_3$ HAADF-STEM & EELS

Closer inspection of the images recorded from the hydrothermally-prepared $Y_{0.5}Ho_{0.5}CrO_3$ solid solution revealed that the crystallites were oriented along the [010] zone axis, rather than the [101] axis that was expected. When viewing the crystal structure, the two axes appear very similar, however, periodic offsets of the rare-earth cations are observed in the former. These offsets were observed in the images as a slight smearing of the individual rare-earth atomic columns in different directions.

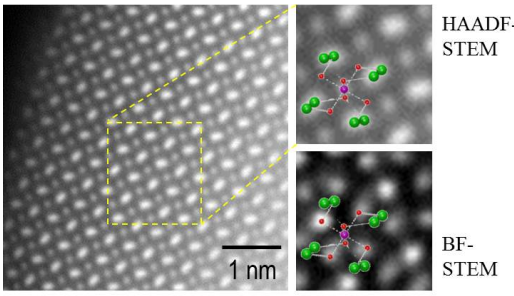

It was described in Chapter 5 that the K-edge of holmium completely dominates that of yttrium, so it was not possible to obtain accurate maps from integrating the yttrium K-edge. A few EELS spectra were obtained for yttrium, and although they are not atomically resolved, it is possible to observe variations that complement the corresponding holmium maps. Yttrium and holmium maps are grouped and compared below; HAADF-STEM images (left), holmium maps (centre), and yttrium maps (right).

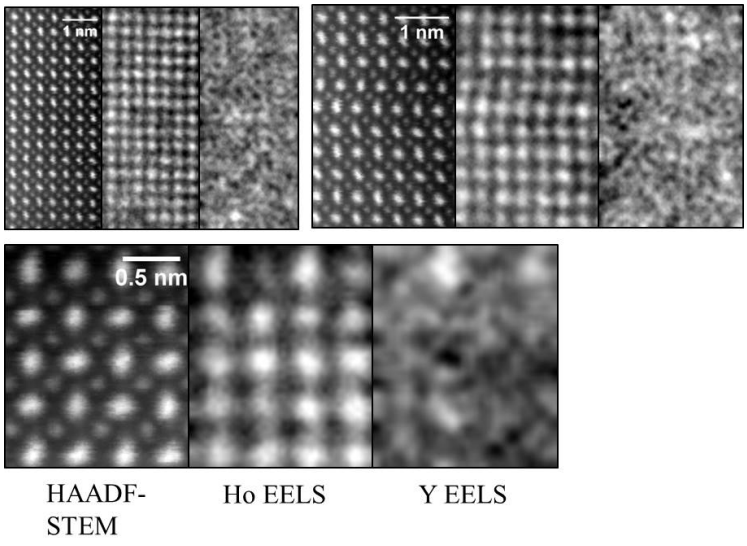

Most of the EELS maps integrated from yttrium spectra were of inadequate quality, however, it was possible to observe variations in the maps produced from the holmium K-edge. Holmium (right), chromium (centre) maps, are compared alongside HAADF-STEM images (left).